The Dissertation Committee for Ryoichi Miyamoto
certifies that this is the approved version of the following dissertation:

Diagnostics of the Fermilab Tevatron Using an AC Dipole

Committee:

Sacha E. Kopp, Supervisor

Michael J. Sypher

Michael J. Syphers

Jack L. Ritchie

Jack L. Ritchie

Karol Lang

Eiichiro Komatsu

Diagnostics of the Fermilab Tevatron Using an AC Dipole

by

Ryoichi Miyamoto, B.S.

Dissertation

Presented to the Faculty of the Graduate School of

The University of Texas at Austin

in Partial Fulfillment

of the Requirements

for the Degree of

Doctor of Philosophy

The University of Texas at Austin

August 2008

"Some investigators have gone so far as to assert
that nature is loath to give up her secrets
without a considerable expenditure of effort on our part,
and that it is a fundamental fact of life
that first steps in experimentation are bound to fail."

Philip R. Bevington

Acknowledgments

This document summarizes what I learned, enjoyed, and also struggled to as a graduate student of the University of Texas at Austin. I could complete my Ph.D. research simply because of tremendous supports and encouragements from many people, and I cannot possibly thank enough.

First of all, I would like to thank my supervisor Prof. Sacha Kopp who supported me in many ways and taught me all the aspects of being a scientist. I was very fortunate that I could work closely with Mike Syphers of Fermilab, a co-auther of a famous book of accelerator physics. I always enjoyed to learn from his great knowledge and insight of accelerator physics. I also thank to supports of my other committee members, Prof. Jack Ritchie, Prof. Karol Lang, and Prof. Eiichiro Komatsu.

At Fermilab, Andreas Jansson always helped my experiments, despite most of them being very late night. I also thank all the other members of the Tevatron Department at Fermilab, who always supported my work. I would also like to thank Suzanne Gysin who let me stay in her house almost three years when I worked at Fermilab.

When I lived in Austin, Prof. and Mrs. Udagawa helped me in many occasions. Without their help, especially in first few months, my life in Austin had been much tougher. I must also thank Prof. Akira Suzuki of the Tokyo

Science University who showed me the opportunity to come to the United States. If I did not meet him, I have never come to the United States. I am proud to be one of Japanese physics graduate students in the University of Texas at Austin. It was such an interesting group of people and I was very encouraged by the group.

Finally, I cannot forget my parents who are waiting return of their "prodigal son". Without their support and understanding, I could never come this far.

RYOICHI MIYAMOTO

The University of Texas at Austin
August 2008

Diagnostics of the Fermilab Tevatron Using an AC Dipole

Publication No. ____________________

Ryoichi Miyamoto, Ph.D.
The University of Texas at Austin, 2008

Supervisor: Sacha E. Kopp

The Fermilab Tevatron is currently the world's highest energy colliding beam facility. Its counter-rotating proton and antiproton beams collide at 2 TeV center-of-mass. Delivery of such intense beam fluxes to experiments has required improved knowledge of the Tevatron's beam optical lattice. An oscillating dipole magnet, referred to as an AC dipole, is one of such a tool to non-destructively assess the optical properties of the synchrotron.

We discusses development of an AC dipole system for the Tevatron, a fast-oscillating (f $\sim$ 20 kHz) dipole magnet which can be adiabatically turned on and off to establish sustained coherent oscillations of the beam particles without affecting the transverse emittance. By utilizing an existing magnet and a higher power audio amplifier, the cost of the Tevatron AC dipole system became relatively inexpensive. We discuss corrections which must be applied to the driven oscillation measurements to obtain the proper interpretation of beam optical parameters from AC dipole studies. After successful operations of the Tevatron AC dipole system, AC dipole systems, similar to that in the Tevatron, will be build for the CERN LHC. We present several measurements of linear optical parameters (beta function and phase advance) for the Tevatron, as well as studies of non-linear perturbations from sextupole and octupole elements.

Contents

Chapter 1

The Fermilab Tevatron

Charged particle accelerators have been used as probes to study structures and interactions of subatomic particles, governed by the laws of quantum physics. Because of the subatomic particles' wave nature, for instance described by the de Broglie's equation of matter waves $\lambda = h/p$, observing phenomena in a small quantum system requires large momentum particles with small wavelengths. Figure 1.1 summarize historical growth of charged particles' energy achieved by the succession of accelerators, enabling research of the physics of smaller structures.

In early history of elementary particle physics, some particles, such as positrons, muons, and pions, were discovered in cosmic rays. The most energetic particles in cosmic rays have energies higher than 1 J [2], and even the highest energy accelerator of the present day cannot accelerate particles to such a high energy. However, the fluence of high energy cosmic rays is insufficient to observe rare events, such as the production of the long-sought Higgs particle.

Hence, in addition to achieving a high energy, another important aspect

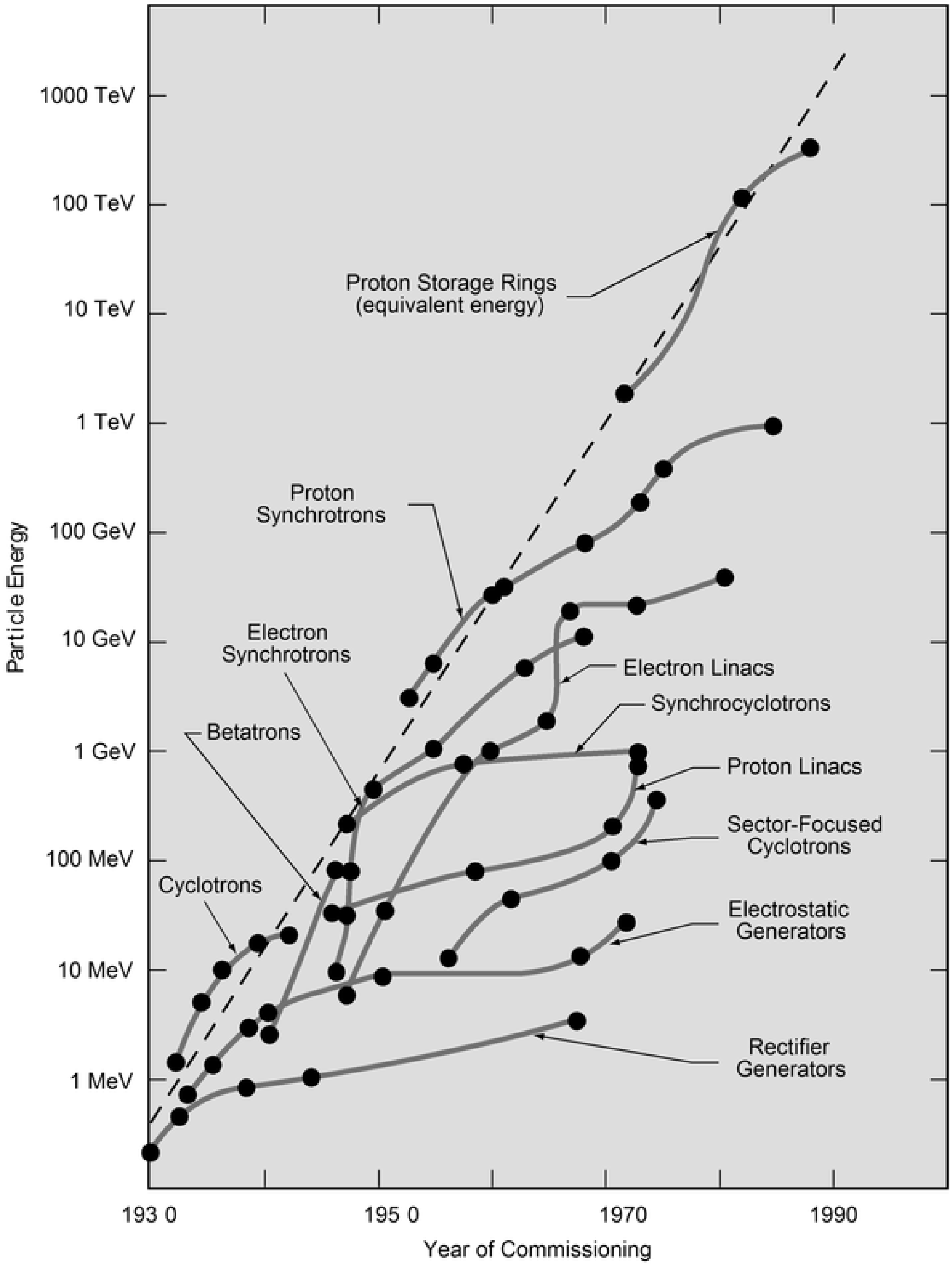

Figure 1.1: Livingston's plot [1], showing historical growth in beam particles' energies in various accelerators.

of an accelerator is to produce extremely intense beams, whose collision rates are sufficiently high to observe statistically rare processes. Today's highest energy collisions are studied at so-called "colliding beam" accelerators, where counter-rotating beams are made to collide head-on. Such collisions of diffuse clouds of beam particles requires extremely good control of the beams' motion and spatial size. One of the important subjects of accelerator physics is the measurement of the beam particles' properties to test whether they are controlled as desired. This dissertation discusses measurements the beam particles' properties in the Fermilab Tevatron [3], using a type of a magnet referred to as an AC dipole [4].

1.1 Luminosity

In the present day, there are many types of accelerators for various purposes (see for instance Chapters 1 and 13 of [5]). In this dissertation, we mainly discuss one type of circular accelerators, referred to as a collider synchrotron. In a circular accelerator, charged particles undergo circular motions guided by dipole magnetic fields and are repeatedly accelerated by longitudinal electric fields of radio frequency. When a charged particle circulates in a uniform magnetic field $\vec{B}$, radius of the circular motion ρ, charge of the particle e, and momentum of the particle p satisfy the following equation:

$$\frac{1}{\rho} = \frac{e|\vec{B}|}{p} = \frac{|\vec{B}|}{(B\rho)} \ , \tag{1.1}$$

where $(B\rho)$ denotes the ratio p/e and is referred to as magnetic rigidity, describing hardness to bend the charged particle. When the momentum is given in units of GeV/c, the magnetic rigidity satisfies

$$(B\rho) = \frac{10}{2.997} p \ \mathrm{T\,m} \ . \tag{1.2}$$

In the synchrotrons, the guiding magnetic field is adjusted along with acceleration of the beam particles, so that the circulation radius of the particles remains the same throughout processes of the acceleration. This makes the synchrotrons more compact, compared to other types of circular accelerators. The collider synchrotron, such as the Fermilab Tevatron, is a type of synchrotrons where two counter-rotating beams of charged particles are accelerated and collided head-on, producing higher center-of-mass energy for physics experiments than smashing the beam particles to a target (Figure 1.2).

Besides the beam energy, an important parameter of a collider is the number of produced particle collisions. In a collider, rate of the particle collisions R, with dimensions $(\text{time})^{-1}$, is proportional to the total cross-section of the counter-rotating particles Σ (see for instance [7, 8]):

$$R = \mathcal{L}\Sigma \ , \tag{1.3}$$

where the prefactor $\mathcal{L}$ has units of $(\text{area})^{-2}(\text{time})^{-1}$, is referred to as luminosity of the collider, and is a measure of the intensity of the colliding beams. We suppose that each of the counter-rotating beam includes N particles, transverse distributions of the particles within the beams are Gaussian with a standard deviation σ, and frequency of the beams' collisions is f. Then, with these parameters, the luminosity is given by [7, 8]

$$\mathcal{L} = \frac{fN^2}{4\pi\sigma^2} = \frac{fN^2}{4\pi\epsilon\beta^*} \ . \tag{1.4}$$

We note that the luminosity is determined only by parameters of the collider and that it increases with the number of particles and decreases with the cross-section of the beams. In modern synchrotrons, in addition to bending dipole magnets, quadrupole magnets are used to produce linear restoring forces and to focus the beam particles around the ideal trajectory. In the

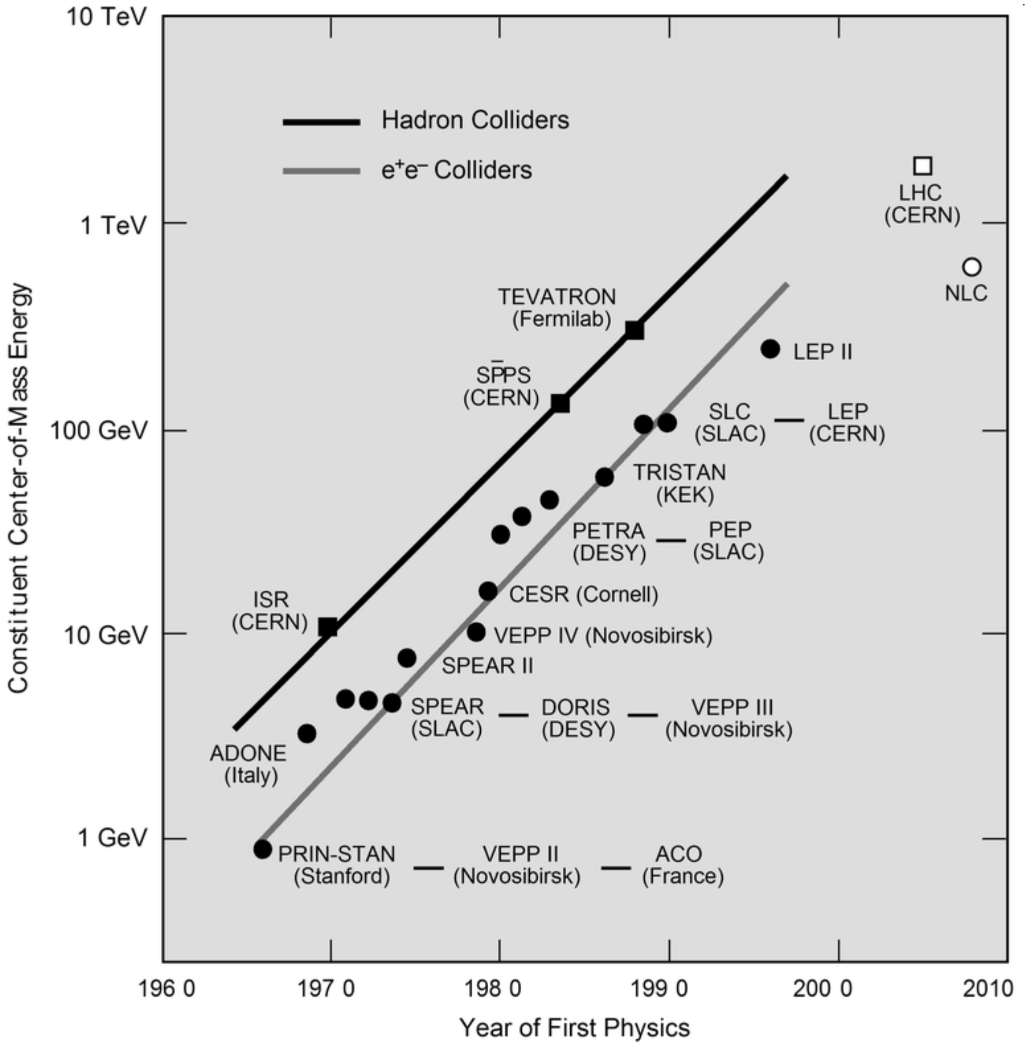

Figure 1.2: Livingston's plot modified by Panofsky and Breidenbach [6], describing historical growth of center-of-mass energies produced by accelerators which collide beams head-on, so-called colliding beam facilities..

second expression of Equation 1.4, the cross-section of the beams is rewritten with a parameter related to the lattice of such focusing quadrupole magnets β^*, referred to as amplitude function. The other parameter ϵ, referred to as emittance, describes the beams' qualities determined from the initial conditions of the beam particles. (We will discuss about the amplitude function and the emittance in detail in Chapter 2.) Once a collider is constructed, it is very hard to raise its beam energy. However, we can often improve the luminosity [9] by increasing the number of particles as well as by improving the lattice of quadrupole magnets and the beams' qualities. Hence, when applied to a collider, the goal of accelerator physics is to improve the luminosity to produce more particle collisions for experiments.

Figure 1.3 shows historical growth in the integrated luminosity of the Tevatron since the year 2001. Because of various improvements [10], the integrated luminosity has been growing better than a linear function of time. Figure 1.4 shows historical growths in the peak luminosity and the number of antiprotons of the Tevatron since the year 2001. During this time period, growth in the number of protons has been negligible. While it is true that the number of antiprotons has increased by a factor of 4 to 5, it is interesting to note that the peal luminosity has increased by more than a factor of ten. This indicates that the luminosity growth is also due to reductions of the beam sizes from improvements of the beams' qualities and the lattice of the focusing quadrupole magnets. Hence, to maximize a collider's luminosity, it is desired to constantly diagnose (and, if possible, improve) the lattice of the quadrupole magnet in the collider .

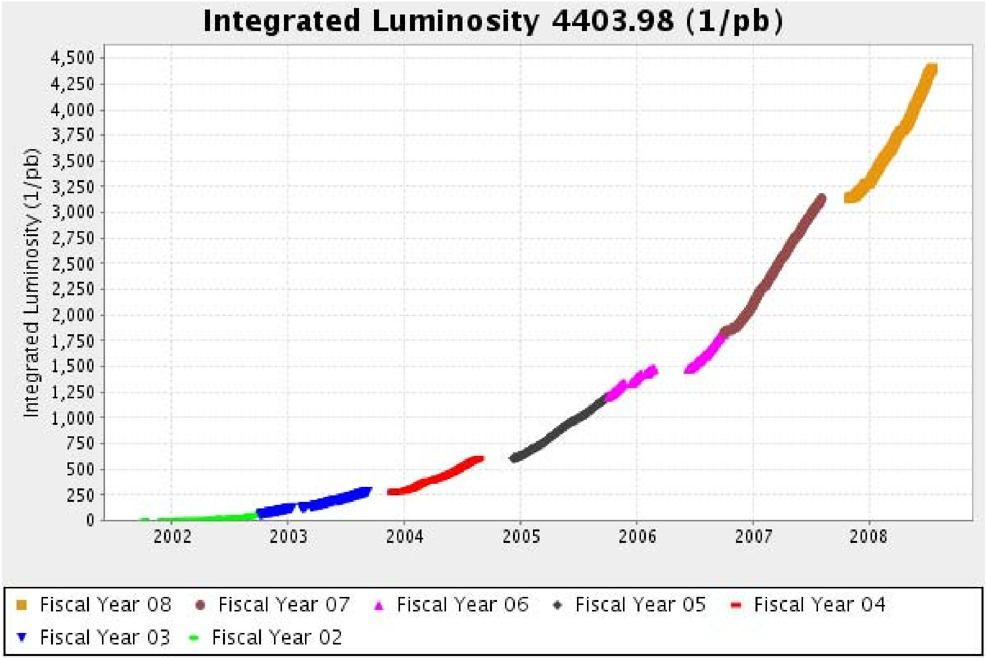

Figure 1.3: The integrated luminosity of the Tevatron since the year 2001. The vertical axis is given by units of inverse picobarn, where barn is a unit of area 1 b = 10^{-28} m^2. Because of various improvements, the luminosity growth has been growing better than a linear function of time.

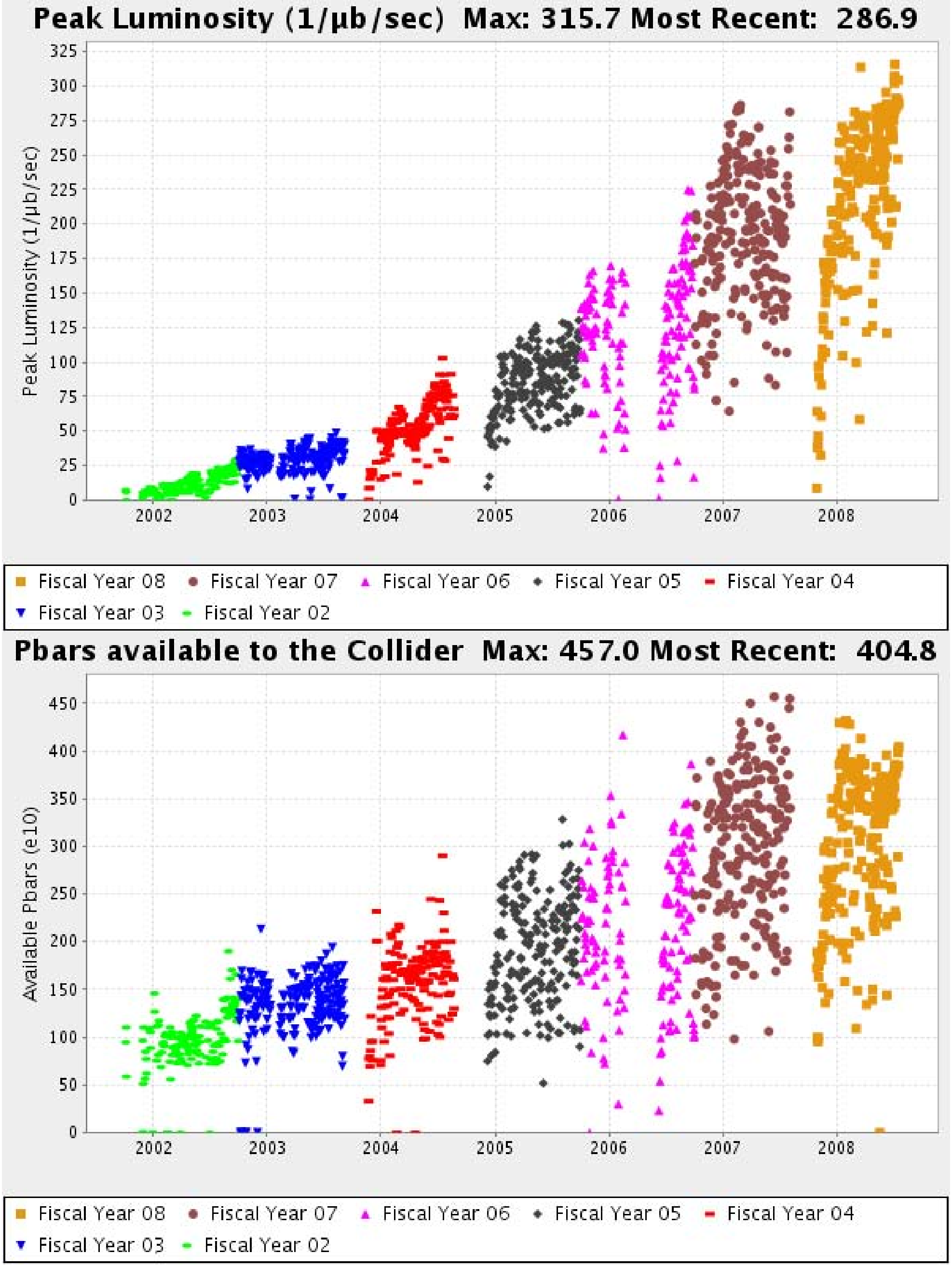

Figure 1.4: Growths of the peak luminosity and the number of antiprotons since the year 2001. The luminosity has been improved not only by increasing number of the particles but also by improving the qualities of the beams and the lattice of the magnetic elements.

1.2 The Fermilab Tevatron

The Fermilab Tevatron [3] is a collider synchrotron, which accelerates the counter-rotating proton and antiproton beams from 150 GeV to about 1 TeV, producing particle collisions of 2 TeV center-of-mass energy, which is the world's highest center-of-mass energy at present[1]. Figure 1.5 shows an aerial photograph of the Fermilab Tevatron with its preaccelerators. The beam particles in the Tevatron are guided by superconducting dipole magnets with the maximum field strength of 4.4 T. Even with such strong dipole magnets, the radius of the Tevatron must be at least 750 m to form a circular trajectory for the 1 TeV beam particles (Equations 1.1 and 1.2). Because an accelerator requires space for components other than the bending dipole magnets, the actual radius of the Tevatron is 1 km.

Table 1.1 lists preaccelerators of the Tevatron. All the accelerators are synchrotrons except the Cockcroft-Walton and the Linac (see [7] for details of these two types of accelerators). In one cycle of the Tevatron, first, negatively charged hydrogen ions are produced from the source and are accelerated to 400 MeV with the Cockcroft-Walton and the Linac. When injected to the Booster the electrons of the hydrogen ions are stripped, and then the protons are accelerated to 150 GeV with the Booster and Main Injector and are sent to a target to produce antiprotons. This process to produce antiprotons is repeated until a sufficient number of antiprotons is prepared, which takes about one day. In the Accumulator and Recycler, the antiprotons are stored and the sizes of the antiproton beam are slowly shrunk down through the processes referred to as stochastic cooling [11] or electron cooling [12]. The proton and

---

[1] The Large Hadron Collider (LHC), which has been constructed at CERN and is turned on soon, will collider counter-rotating proton beams and produce particle collisions of 14 TeV center-of-mass energy.

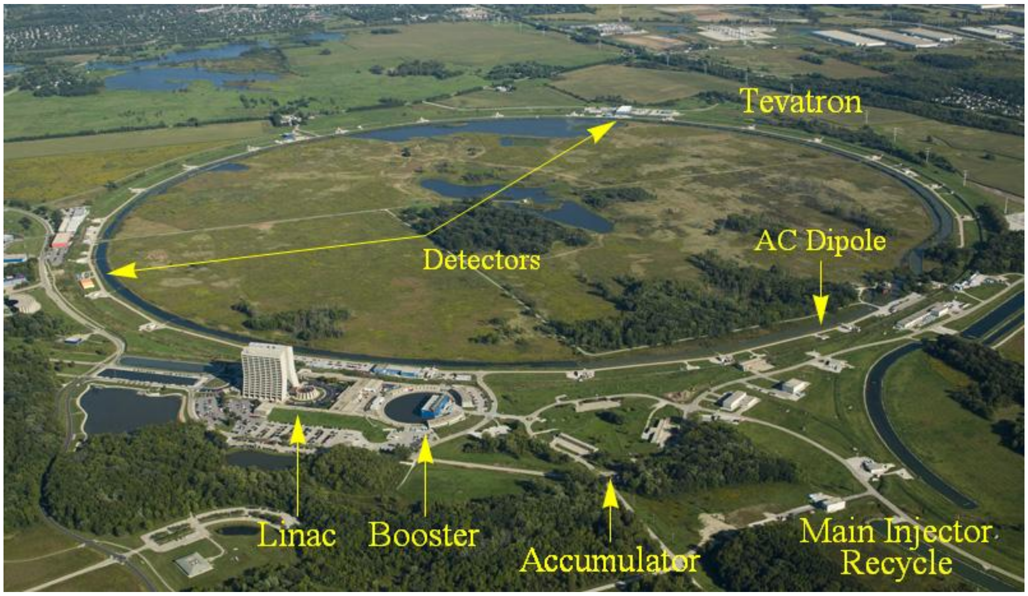

Figure 1.5: Aerial photograph of the Fermilab Tevatron and its preaccelerators. Even with superconducting bending dipole magnets of 4.4 T, the radius of the Tevatron must be as large as 1 km to make a circular path for ∼1 TeV beam particles.

Table 1.1: Preaccelerators of the Tevatron. Negatively charged hydrogen ions are produced from the source and accelerated to 400 MeV with the Cockcroft-Walton and Linac. When injected into the Booster, the electrons are stripped. The Booster and Main Injector accelerate protons up to 150 GeV for the antiproton production. The Main Injector is also used to accelerate protons and antiprotons to 150 GeV and to inject them into the Tevatron. The Accumulator and Recycler store and cool the antiproton beam.

Accelerator	Particle type(s)	Injection energy	Extraction energy
Cockcroft-Walton	H^-	-	750 keV
Linac	H^-	750 keV	400 MeV
Booster	p^+	400 MeV	8 GeV
Main Injector	p^+/p^-	8 GeV	150 GeV
Accumulator	p^-	-	8 GeV
Recycler	p^-	8 GeV	8 GeV

antiproton beams are accelerated to 150 GeV and injected into the Tevatron separately. In the Tevatron, the both beams are accelerated simultaneously and, once the energy reaches the maximum 980 GeV, the collisions are initiated. The two beams continue circulating and colliding usually about one day until the next batch of antiprotons are prepared. This cycle of about one day is called one store. In the Tevatron, the proton and antiproton beams circulate in a single beam vacuum pipe without colliding each other except at two designated collision points, inside the physics detectors. This is achieved by separating the orbits of the two beams with electric fields produced by pairs of high voltage plates (electric separators). Such orbits of the two beams are referred to as helical orbits or simply helices.

Table 1.2 lists the main parameters of the Tevatron which determine its luminosity. As seen in Figure 1.4, the parameters such as the beam intensities and the beam emittances, determining quality of the beams, vary over stores. In addition, in a large collider like the Tevatron, the lattice of the quadrupole magnets also changes in a long period of time, changing the parameters like the amplitude function β^* and affecting the luminosity. Hence, to maximize its performance, it is ideal to constantly diagnose the lattice of the quadrupole magnets in the collider.

Table 1.3 lists types of additional magnets in the Tevatron, referred to as correctors [3, 13]. These magnets are used to make small corrections when errors are found in a diagnosis. The dipole and normal quadrupole correctors are used for to compensate errors in bending dipole magnets and focusing quadrupole magnets. In the Tevatron, motions in the two transverse planes are uncoupled by design since coupling may affect the luminosity and the beam's stability. When the coupling occurs, for instance due to a rolled quadrupole magnet, the skew quadrupole correctors are used to fix it. To compensate

Table 1.2: Main parameters of the Tevatron. As seen in Figure 1.4, some parameters are not constants and the luminosity differs over the stores. Even parameters related to the quadrupole magnet lattice, such as the amplitude function β^*, may change and affect the luminosity. To maximize performance of a large accelerator like the Tevatron, we have to constantly perform the machine diagnoses.

Injection energy	150 GeV
Collision energy	980 GeV
Maximum peak luminosity	300 $\mu\mathrm{b}^{-1}\mathrm{sec}^{-1}$
Number of collision points	2
Circumference	$2\pi \times 1000$ m
Revolution frequency	47.7 kHz
Number of bunches	36
Typical proton bunch intensity	2.75×10^{11}
Typical antiproton bunch intensity	0.75×10^{11}
β_{max} in arc	100 m
β_{min} in arc	25 m
β^* at collision points	28 cm
Tune	20.58
Phase advance per cell	68 deg
Typical proton emittance (95% normalized)	20π mm mrad
Typical antiproton emittance (95% normalized)	10π mm mrad
Number of bend magnets	774
Bending dipole field (980 GeV)	4.4 T
Number of quadrupole magnets (except low-β)	204
Focal length (980 GeV)	25 m
Standard half-cell length	30 m

Table 1.3: List of corrector magnets in the Tevatron. The second column shows the maximum strength of one of each collector magnets, The third column shows the errors/effects compensated by each collector magnets.

Collector	Maximum strength	Collection/Compensation
Dipole	0.46 T m	Central orbit
Quadrupole (normal)	7.5 T m/m	Focusing
Quadrupole (skew)	7.5 T m/m	Transverse coupling
Sextupole (chromaticity)	450 T m/m^2	Tune spread due to momentum spread
Sextupole (feeddown)	350 T m/m^2	Orbits and focusings on helices
Octupole	31000 T m/m^3	Instability due to high intensity

certain multi particle effects, the Tevatron also has magnets to produce higher order nonlinear fields, such as sextupole and octupole magnets. We discuss the effects of these nonlinear fields on the motion of the beam particles in Chapter 3.

1.3 Diagnostics with an AC Dipole

Under the influence of the linear restoring forces of the quadrupole magnets, the beam particles undergo oscillations in the transverse planes around the ideal orbit. The oscillations are analogous to simple harmonic oscillations in classical mechanics and are referred to as betatron oscillations. As reviewed in Chapter 2, the function of a quadrupole magnet on the particle beam is analogous to a thin focusing lens in ray optics. Hence, the parameters associated to the betatron oscillations, which are determined from the lattice of the focusing quadrupole magnets, are referred to as beam optical parameters (or just optical parameters). The parameter β^* in Equation 1.4 is one of the beam optical parameters. To maximize the luminosity of a collider, we have to monitor the beam optical parameters and maintain them at their optimum values.

This dissertation discusses measurements of the beam optical parameters, using a diagnostic magnet referred to as an AC dipole. Synchrotron diagnostics using the AC dipole was first tested in BNL AGS [4]. The AC dipole has been also employed in the BNL RHIC [14, 15], the CERN SPS [16, 17], and the FNAL [18, 19, 20, 21] and will be used in CERN LHC [22]. The AC dipole, located at one point on the synchrotron, has a weak sinusoidally-varying dipole field which deflects the beam particles slightly. The AC dipole's field oscillates at a frequency nearly equal to the natural frequency of beam particles' transverse oscillations, as they go around the synchrotron. Thus, the AC dipole excites a resonant motion of all the beam particles which is readily measured, providing detailed information about the beam optical parameters of the synchrotron.

The resonant motion of the beam particles excited by the AC dipole is monitored with devices referred to as beam position monitors (BPM's). The Tevatorn has 236 BPM's around the ring to measure transverse positions of the beam particles. Figure 1.6 shows a schematic cross-section of a BPM in the Tevatron [23, 24]. When the beam goes through the BPM, the beam's image charges are detected by the two conducting plates forming a shunt capacitance to ground. If the signals on the left and right plates are L and R, the beam's horizontal displacement x from the center of the BPM is given by

$$x = \frac{\frac{b}{2}\sin\phi\sin(\pi\frac{R-L}{I_b})}{\cos\frac{\phi}{2}\cos(\pi\frac{R-L}{I_b}) - \cos(\pi\frac{R+L}{I_b} + \frac{\phi}{2})} \simeq \frac{b\phi}{4\sin\frac{\phi}{2}}\frac{R-L}{R+L} \ , \tag{1.5}$$

where I_b is the total current of the beam and the geometric angle of the conducting plates ϕ and the radius to the conducting plates b are defined in Figure 1.6. This formula, which is exact, was derived by the author in [25].

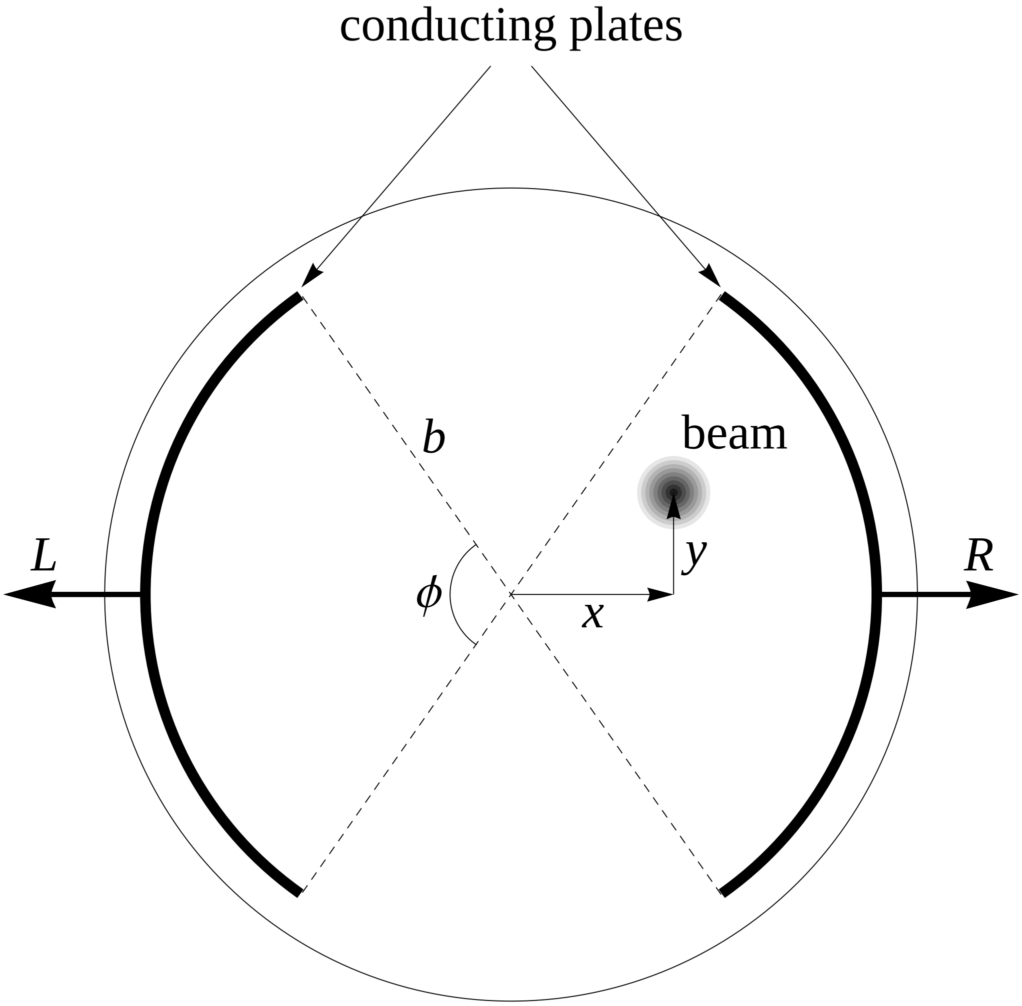

Figure 1.6: Schematic cross-section of a BPM in the Tevatron. The beam's image charges are detected by the two conducting plates. The horizontal position of the beam centroid x, measured from the center of the BPM, is determined from the signals on the two plates, L and R, and geometry of the BPM, b and ϕ.

The approximate formula and Taylor series corrections to it (see for instance [26, 27]) are commonly used at accelerator laboratories. We note that this type of a BPM can measure only position of the beam centroid and does not give us any information of the particles' distribution within the beam. As explained in Chapter 4, this is why we have to excite motion of all the beam particles to acquire information of the beam optical parameters.

1.4 Outline of This Dissertation

In Chapter 2, we review basics of the betatron oscillations in the synchrotron and define linear optical parameters of the charged particle beam. A synchrotron can never be perfect and it always has error magnetic fields perturbing the ideal betatron oscillations. Chapter 3 summarizes such perturbative effects of the betatron oscillations and it also discusses nonlinear motions of the beam particles. In Chapter 4, we discuss measurement of linear optical parameters, using the AC dipole. We compare the measurement using the AC dipole to the other conventional measurement techniques, to show advantages to the measurement with the AC dipole. In Chapter 5, we discuss the AC dipole system used in the Tevatron. In Chapter 6, we discuss the formalism to describe the motion of the charged particle beam excited by the AC dipole. Chapter 7 shows measurements of the linear optical parameters using the AC dipole, performed in the Tevatron. In Chapter 8, we show measurements of the nonlinear effects, discussed in Chapter 3, performed in the Tevatron using the AC dipole. Chapter 9 gives conclusions of this dissertation.

Chapter 2

Particle Motion in an Ideal Synchrotron

While the ideal particles in a synchrotron will move in a circular orbit guided by dipole magnetic fields and accelerated by longitudinal electric fields of resonant cavities, few particles circulate in ideal orbit. Instead, the cloud of the beam particles tends to diverge due to the angular spread and the momentum spread of the beam. In order to achieve a substantial collision rate for experiments, we must contain the circulating beam to a finite size (see the luminosity formula, Equation 1.4). We use quadrupole magnets to produce restoring forces and confine the particles around the ideal trajectory or, in other words, to focus the beam.

The importance of beam focusing can be demonstrated with a couple of simple numerical examples. When a particle moves in a uniform vertical magnetic field in the absence of focusing, if the initial momentum of the particle is perfectly horizontal, it undergoes a circular motion in the horizontal plane. However, if the particle has a vertical angular divergence, it spirals up or

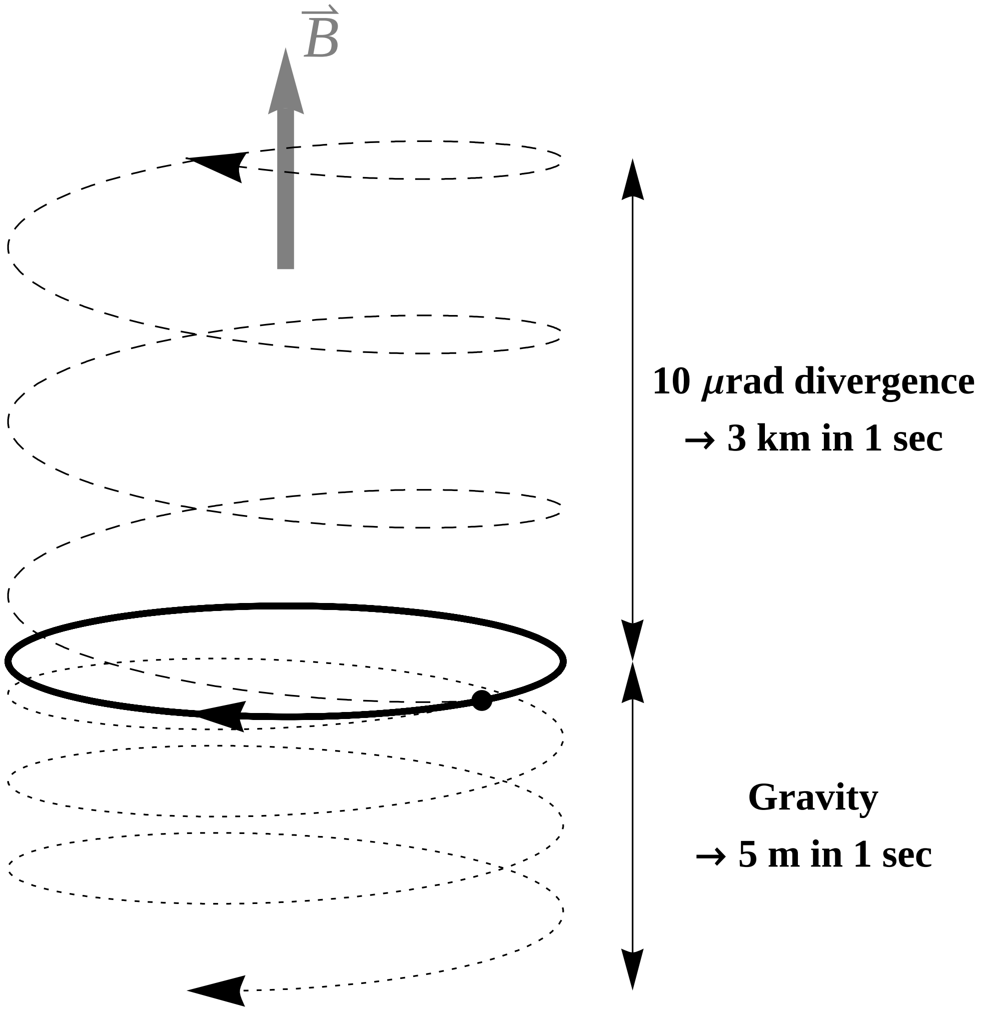

Figure 2.1: Motion of a particle in a uniform magnetic field. A particle with the speed of light and angular divergence as little as 10 μrad moves up or down 3 km just in one second. Even the perfect beam with no divergence is pulled down 5 m in 1 sec by the gravitational force, without any restoring forces.

down and soon hits the beam vacuum pipe in a synchrotron. For instance, a 1 TeV/c proton with as little as 10 μrad vertical angular divergence moves up or down 3 km in just 1 sec. Such is indicated in Figure 2.1. A real synchrotron has billions of particles, about 10^{13} in the case of the Tevatron, and it is impossible to perfectly control the initial conditions of all the particles. Even if we could have perfect control of the protons' initial conditions, there is still the gravitational force which pulls the particles down by 5 m in 1 sec.

In this chapter, we discuss the focusing properties of quadrupole magnets and their implementation in typical synchrotrons. As well, we develop the formalism of calculating particles' trajectories around the synchrotron under the influence of quadrupole magnets' restoring forces. In Section 2.1, we discuss the properties of quadrupole magnets as thin focusing/defocusing lenses. In Section 2.2, we discuss the fundamental unit of a modern synchrotron, the FODO lattice, which consists of a pair of focusing and defocusing quadrupole magnets. We show a simple simulation of a particle motion in such a system and introduce basic concepts of a particle's transverse motion in a synchrotron, referred to as betatron oscillations. Section 2.3 gives the mathematical formalism of betatron oscillations in detail. We introduce Hill's equation and the Courant-Snyder parameters to characterize the particles' trajectories in a synchrotron.

2.1 Quadrupole Magnets

2.1.1 Field and Force

Figure 2.2 shows the magnetic field and force of a typical quadrupole magnet. The force vectors are shown for a positive charge coming out of the page.

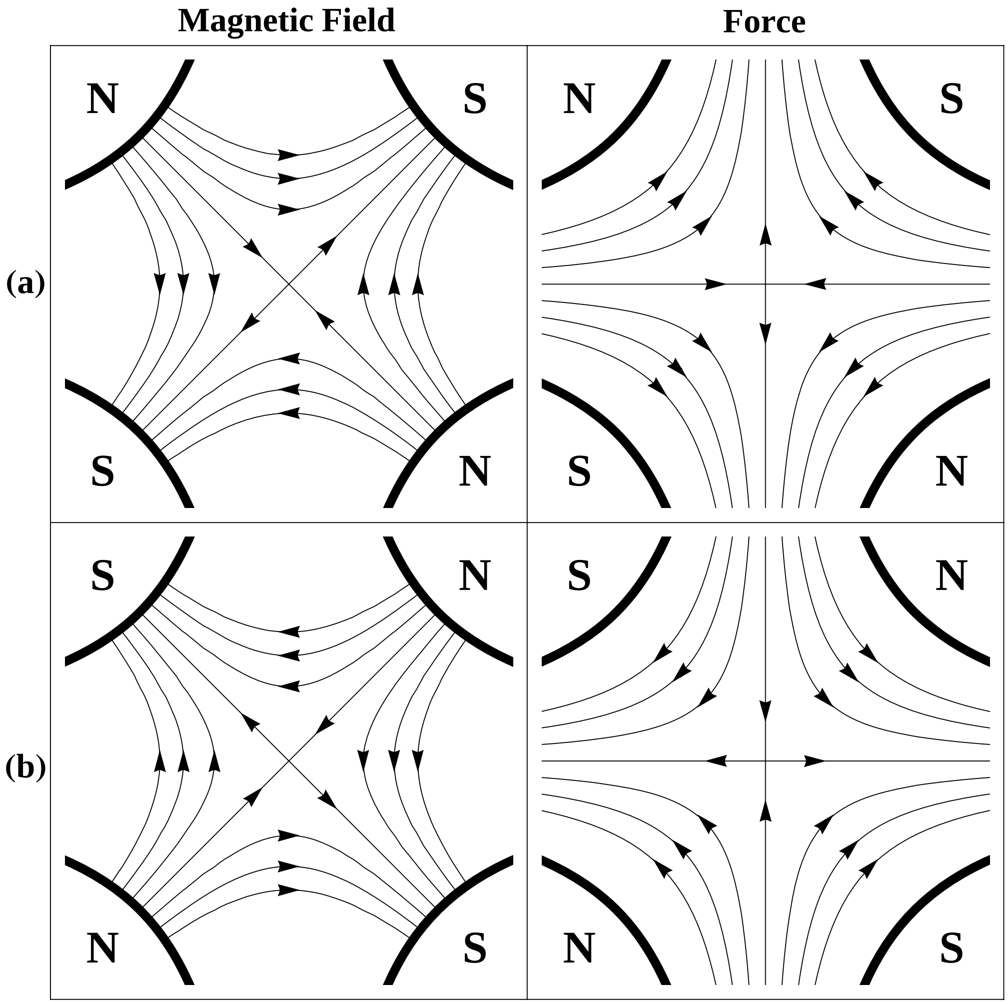

Figure 2.2: Magnetic field and force of a quadrupole magnet. For a positive charge coming out of the page, the quadrupole magnet (a) produces an attractive force in the horizontal direction and repulsive force in the vertical direction. The quadrupole magnet (b), whose pole faces are rotated by 90 degrees compared to (a), has the opposite effect on the same charge.

The field of the quadrupole magnet is linearly proportional to position of the particle, (x, y), and given by

$$B_y(x, y) = B_{y,1}x \ , \tag{2.1}$$

$$B_x(x, y) = B_{y,1}y \tag{2.2}$$

where the origin of the coordinate is the center of the quadrupole magnet and the constant parameter $B_{y,1}$, referred to as gradient of the quadrupole magnet, is a shorthand notation of

$$B_{y,1} \equiv \left.\frac{\partial B_y}{\partial x}\right|_{x=y=0} \ . \tag{2.3}$$

The quadrupole magnet shown in Figure 2.2(a) produces an attractive force in the horizontal direction and a repulsive force in the vertical direction. Rotation of the pole faces by 90 degrees produces the opposite effect, as in Figure 2.2(b). In any case, a quadrupole magnet produces a restoring force only in one of the transverse directions. Hence, to stabilize the particle's motions in both of the transverse planes, a pair of quadrupole magnets, one of which is rotated 90 degrees or has opposite polarity, is required.

2.1.2 Thin Lens Approximation

The length of a typical quadrupole magnet is much less than its bending radius. In such a case, we can approximate the function of a quadrupole magnet as a thin lens, which deflects a particle but does not change its position (thin lens approximation). Figure 2.3 is a schematic of a particle deflected by a generic thin magnetic element with length ℓ. In a thin element, the magnetic field seen by the particle is approximately uniform and the particle moves on an arc with radius ρ ($\rho \gg \ell$). The deflection angle is equal to the arc angle and

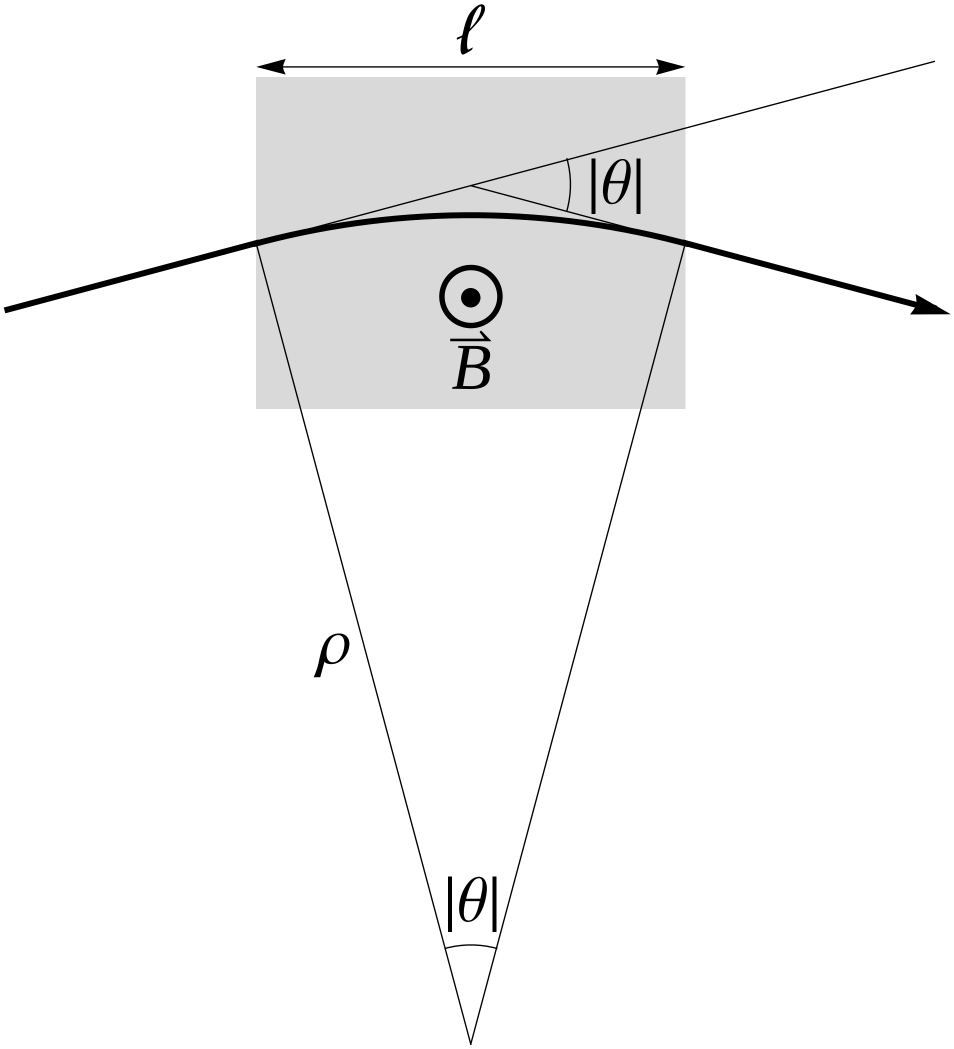

Figure 2.3: Schematic of a particle deflected by a thin magnetic element with length ℓ (shaded area). In the thin element, the deflection angle is approximated by $|\theta| \simeq \ell/\rho = |\vec{B}|\ell/(B\rho)$.

satisfies

$$|\theta| \simeq \frac{\ell}{\rho} = \frac{|\vec{B}|\ell}{(B\rho)} \ , \tag{2.4}$$

where the curvature $1/\rho$ is rewritten by using Equation 1.2. We note that we allow a negative deflection angle. From Equations 2.1, 2.2, and 2.4, for a thin quadrupole magnet, deflection angles in the horizontal and vertical planes, θ_x and θ_x, are given by

$$\theta_x \simeq -\frac{B_{y,1}\ell}{(B\rho)}\,x \tag{2.5}$$

$$\theta_y \simeq \frac{B_{y,1}\ell}{(B\rho)}\,y \ . \tag{2.6}$$

Here, x and y are the horizontal and vertical displacements of the particle relative to the ideal trajectory, which is also equal to the horizontal and vertical distances from the center of the quadrupole magnet. We choose the outward and upward directions as positive directions of x and y. The negative sign for the horizontal case is a convention related to this coordinate system. Because the deflection angles θ_x and θ_y are linearly proportional to the displacements x and y, the quadrupole acts on a particle as a linear focusing or defocusing lens in a optical system. Figure 2.4 is a schematic of particles focused in the horizontal plane and defocused in the vertical plane by a thin quadrupole magnet. As in the case of geometrical optics, we assume the charged particles are paraxial. Focal lengths of this quadrupole magnet F_x and F_y are given by

$$\begin{aligned} \frac{1}{F_x} &\simeq \frac{\theta_x}{x} \simeq -\frac{B_{y,1}\ell}{(B\rho)} \\ \frac{1}{F_y} &\simeq \frac{\theta_y}{y} \simeq \frac{B_{y,1}\ell}{(B\rho)} \ . \end{aligned} \tag{2.7}$$

Here, magnitudes of the focal lengths in both planes are the same, $|F_x| = |F_y|$, but their signs are different, indicating the quadrupole focuses the beam only in one plane. Reciprocal of focal length is referred to as effective strength of a quadrupole and is denoted with q.

The function of a linear focusing or defocusing lens can be expressed with a 2×2 matrix. In the paraxial approximation, the angle of a particle is equal to the slope of the particle's trajectory $x' \equiv dx/ds$. Here, s is the distance from a reference point measured along the ideal trajectory and is referred to as the longitudinal coordinate. When the particle goes through a thin focusing or defocusing lens, transformation of the particle's position and angle, (x, x'), is given by

$$\begin{pmatrix} x \\ x' \end{pmatrix}_f = \begin{pmatrix} 1 & 0 \\ \frac{1}{F} & 1 \end{pmatrix} \begin{pmatrix} x \\ x' \end{pmatrix}_i , \tag{2.8}$$

where $F < 0$ and $F > 0$ corresponds to the thin focusing lens and defocusing lens for each, and subscripts i and f denote the initial and final states of a particle.

Particle motion in a magnet free straight region, referred to as drift space, can be also expressed with a 2×2 matrix. When a particle moves in a drift space of length L, its angle remains the same but its transverse position changes by Lx'. Hence, the transformation is given by

$$\begin{pmatrix} x \\ x' \end{pmatrix}_f = \begin{pmatrix} 1 & L \\ 0 & 1 \end{pmatrix} \begin{pmatrix} x \\ x' \end{pmatrix}_i . \tag{2.9}$$

2.2 FODO Lattice

2.2.1 System with a Focusing and Defocusing Lenses

In Section 2.1, we discussed that a pair of quadrupole magnets can focus particles' motions in both of the transverse planes. By using the matrices of

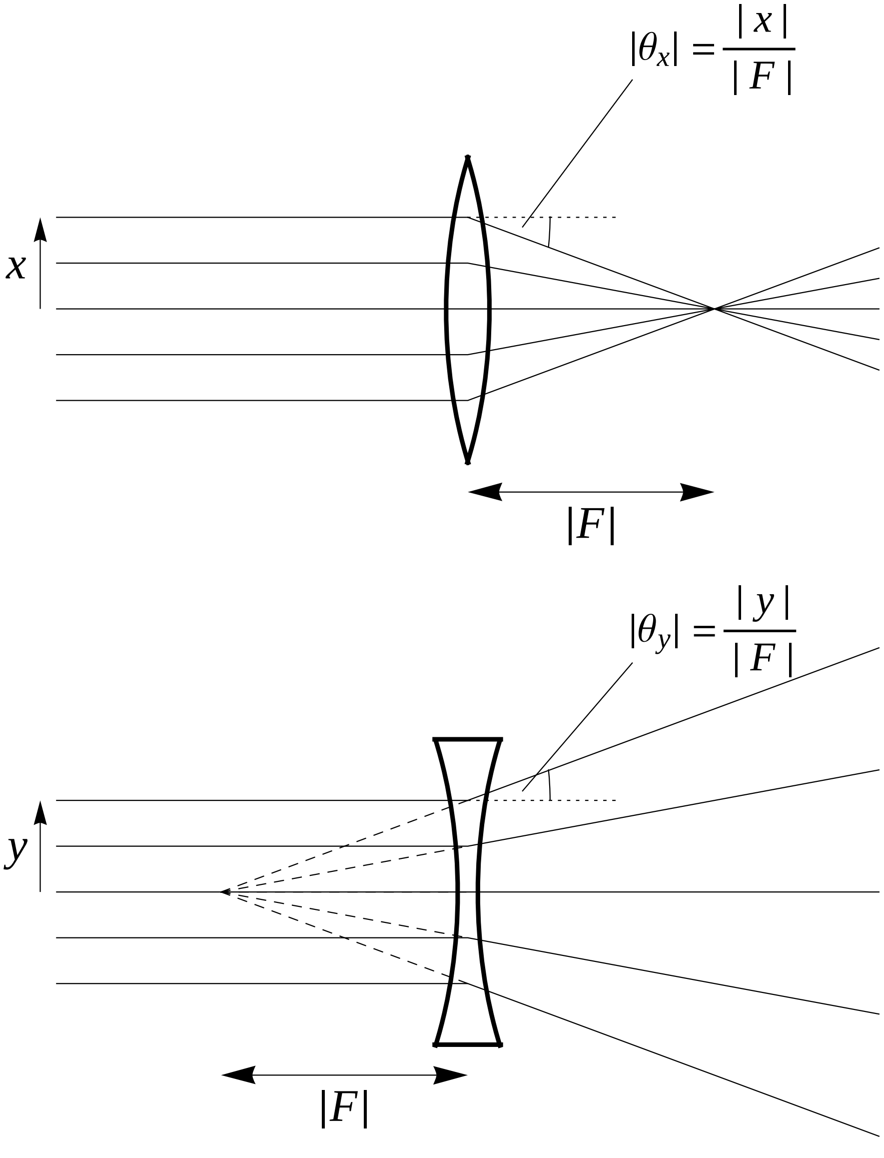

Figure 2.4: Schematic of a thin quadrupole magnet focusing particles in the horizontal plane and defocusing particles in the vertical plane. Because the deflection angles θ_x and θ_y are linearly proportional to the displacements x and y, the particles moving parallel to the axes are focused to the focal points. The coil lengths F_x and F_y are given by Equation 2.7.

thin lenses and a drift space in Section 2.1.2, we can easily check this statement. Figures 2.5(a) and 2.5(b) show trajectories of particles going through a system consisting of a thin focusing and defocusing lenses with focal lengths $-|F|$ and $|F|$. Here, the trajectories of the particles are calculated by multiplying the matrices of the thin lenses and drift space. The difference between Figures 2.5(a) and 2.5(b) is that magnitude of the focal lengths $|F|$ is larger than the distance between the two lenses L ($|F| > L$) in 2.5(a) and the relation is opposite ($|F| < L$) in 2.5(b). In Figure 2.5(b), when $|F| < L$, we can see particles cross the axis before the deflections of the defocusing lens and diverge away after they exit the system. Figure 2.5(c) and Figure 2.5(d) show trajectories of particles going through the systems similar to Figures 2.5(a) and 2.5(b), where the order of the focusing and defocusing lenses are flipped. Because a quadrupole magnet has the opposing focusing properties in the two transverse planes, Figures 2.5(c) and 2.5(d) can be interpreted as the same systems at Figures 2.5(a) and 2.5(b) observed in the other plane. In both cases, the net effects are focusing when the condition $|F| > L$ is satisfied.

The conclusion of the previous paragraph can be analytically derived by using the matrices of the thin lenses and a drift space. When the initial state of a particle is $(x, x')_i = (x, 0)$, the state of the particle when it exits a pair of lenses, $(x, x')_f$, can be calculated by the following matrix multiplications:

$$\begin{aligned}
\begin{pmatrix} x \\ x' \end{pmatrix}_f &= \begin{pmatrix} 1 & 0 \\ \pm\frac{1}{|F|} & 1 \end{pmatrix} \begin{pmatrix} 1 & L \\ 0 & 1 \end{pmatrix} \begin{pmatrix} 1 & 0 \\ \mp\frac{1}{|F|} & 1 \end{pmatrix} \begin{pmatrix} x \\ 0 \end{pmatrix} \\
&= \begin{pmatrix} 1 \mp \frac{L}{|F|} & L \\ -\frac{L}{|F|^2} & 1 \pm \frac{L}{|F|} \end{pmatrix} \begin{pmatrix} x \\ 0 \end{pmatrix} = \begin{pmatrix} (1 \mp \frac{L}{|F|})x \\ \frac{L}{|F|^2}x \end{pmatrix} \quad , \qquad (2.10)
\end{aligned}$$

where the upper set of signs represents the case when a particle passes through a focusing, then defocusing lens ("FD") and the lower set of signs represents

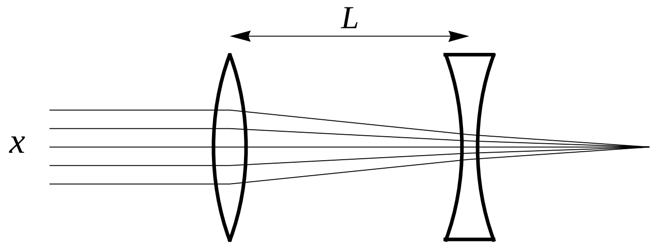

(a) $|\mathtt{F}| > \mathtt{L}$

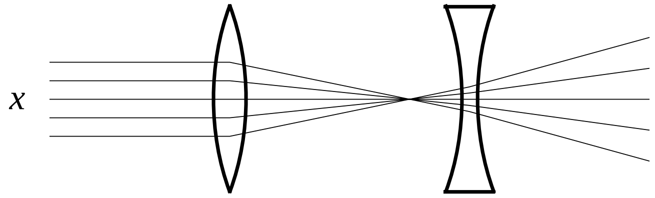

(b) $|\mathtt{F}| < \mathtt{L}$

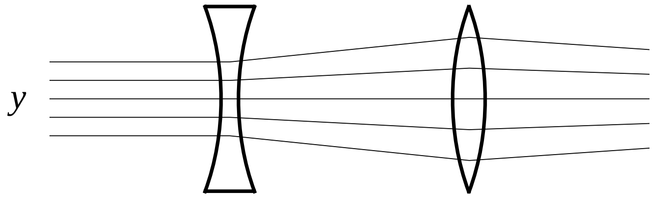

(c) $|\mathtt{F}| > \mathtt{L}$

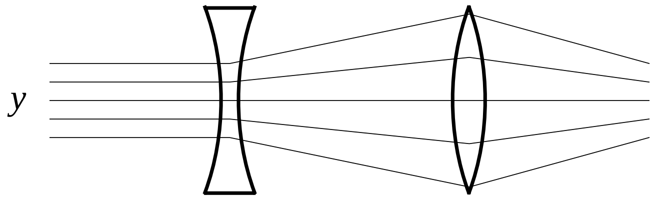

(d) $|\mathtt{F}| < \mathtt{L}$

Figure 2.5: Systems consisting of a focusing and defocusing lens. When particles enter the focusing lens and exit from the defocusing lens, the net effect is focusing when $|F| > L$, (a), and defocusing when $|F| < L$, (b),. When the order of the focusing and defocusing lenses are flipped, the net effect is always focusing, (c) and (d).

the opposite case ("DF"). From this equation, magnitude of the focal lengths $|F|$ must be larger than the drift space length L for parallel particles to be focused for both the FD and DF cases. Hence, if we adjust focal lengths properly, a pair of quadrupole magnets can focus transverse motions in both planes.

A system consisting of a pair of equally spaced quadrupole magnets, with the same magnitude of focal lengths $|F|$, is called the FODO lattice. Here, F and D represent the focusing and defocusing lenses and O represents the drift space. This system, focusing the beam in both of the transverse planes, is a fundamental unit of modern synchrotrons. If the order is first the focusing lens, the matrix of the FODO lattice $\mathbf{M}_{\mathrm{FODO}}$ is given by

$$\begin{aligned}\mathbf{M}_{\mathrm{FODO}} &= \begin{pmatrix}1 & L\\ 0 & 1\end{pmatrix}\begin{pmatrix}1 & 0\\ \frac{1}{|F|} & 1\end{pmatrix}\begin{pmatrix}1 & L\\ 0 & 1\end{pmatrix}\begin{pmatrix}1 & 0\\ -\frac{1}{|F|} & 1\end{pmatrix}\\ &= \begin{pmatrix}1-\frac{L}{|F|}-\frac{L^2}{|F|^2} & 2L+\frac{L^2}{|F|}\\ -\frac{L}{|F|^2} & 1+\frac{L}{|F|}\end{pmatrix}. \qquad (2.11)\end{aligned}$$

2.2.2 Structure of a Synchrotron

Figure 2.6 is a schematic diagram of a small synchrotron. Focusing and defocusing quadrupole magnets are evenly spaced and interleaved with the bending dipole magnets. To describe motion of circulating particles, we use the coordinate system known as Frenet-Serret's curvilinear coordinates (see for instance page 3 of [28]). In Figure 2.6, the closed loop is the trajectory of an ideal particle. The longitudinal coordinate s is the distance measured along this ideal trajectory. The two transverse coordinates x and y describe the horizontal and vertical deviations from the ideal trajectory. The positive directions of x and y are outward and upward directions, and the combination (x, y, s)

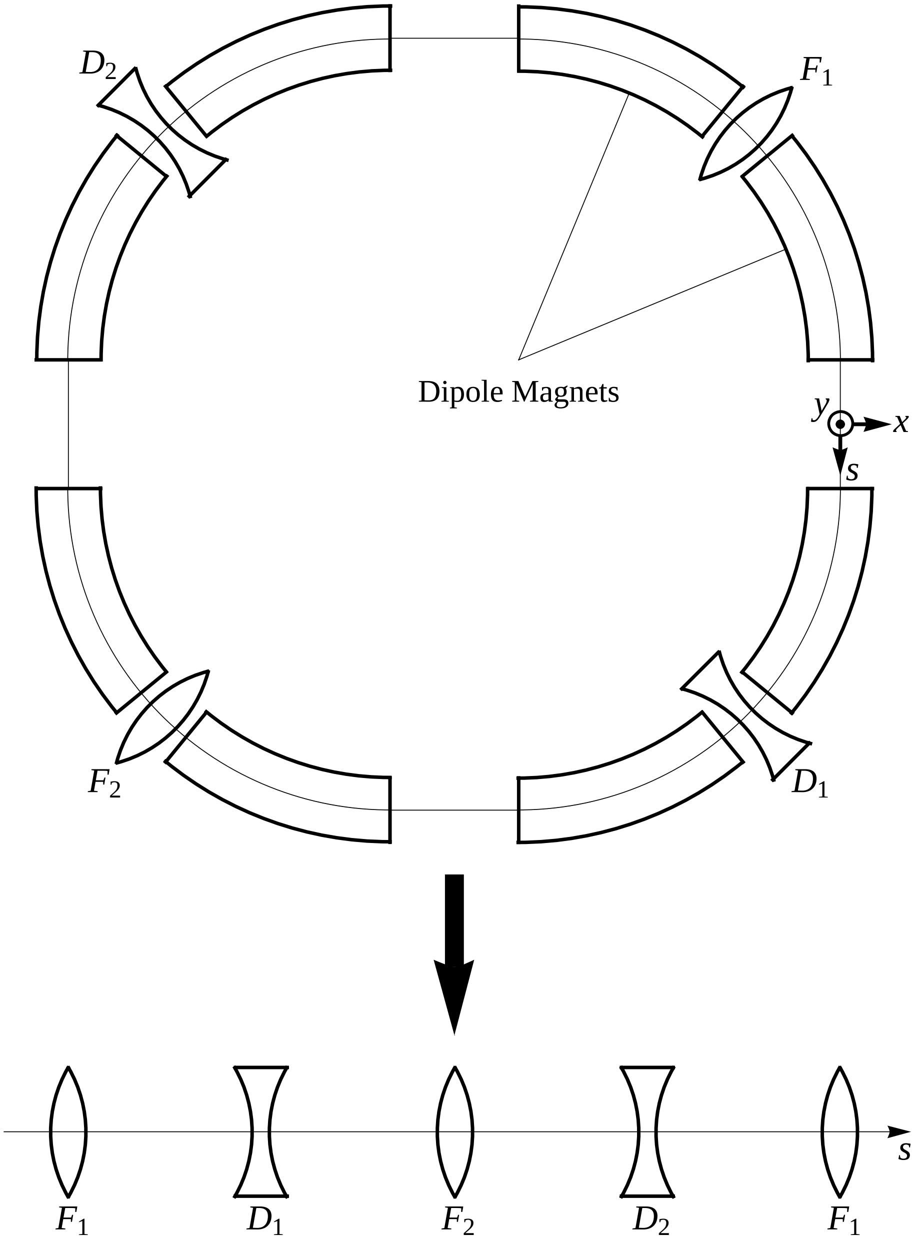

Figure 2.6: Schematic diagram of a small synchrotron. A modern synchrotron consists of the bending dipole magnets, focusing quadrupole magnets, and straight sections in-between. In the Frenet-Serret's curvilinear coordinates moving along the ideal trajectory, the space of the bending dipole magnet is equivalent to the drift space and the synchrotron is reduced to a system of FODO lattices with the periodic boundaries.

forms a right-hand coordinate system. In this coordinate system, the spaces of the bending dipole magnets become effectively free spaces and a synchrotron becomes equivalent to a straight system of FODO lattices with the periodic boundaries[1]. Hence, we can understand the transverse motions of particles in a synchrotron by studying particles' motion in the FODO lattices.

2.2.3 Simulation of a FODO Lattice System

This section shows simple model of a particle's motion in the FODO lattices. Through this model, we can learn basic concepts of betatron oscillations. In brief, the particles which diverge from the ideal orbit experience restoring forces from the quadrupole magnets in the synchrotron. As a result, the particles undergo transverse oscillations around the ideal trajectory, referred to as betatron oscillations. Mathematical details of betatron oscillations are discussed in the next section.

Trajectory

Figure 2.7 shows the calculated trajectory of the particle in a model system of two FODO lattices, like the small synchrotron in Figure 2.6. In the calculation, we chose the focal length $F = 25$ m and drift distance $L = 30$ m as the FODO lattices in the Tevatron. A particle with initial conditions $x = 1$ mm and $x' = 0$ mrad enters the system from the location of the focusing lens F_1 and proceeds rightward. The position and angle of the particle are tracked by multiplying the matrices of lenses (Equation 2.8) and the drift space (Equation 2.9), as we did in Equation 2.10. We note, in our coordinate system, the particle's

---

[1] This statement is true only for a particle with the ideal longitudinal momentum. The bending dipole magnets cannot be ignored for off-momentum particles even in the Frenet-Serret's coordinates.

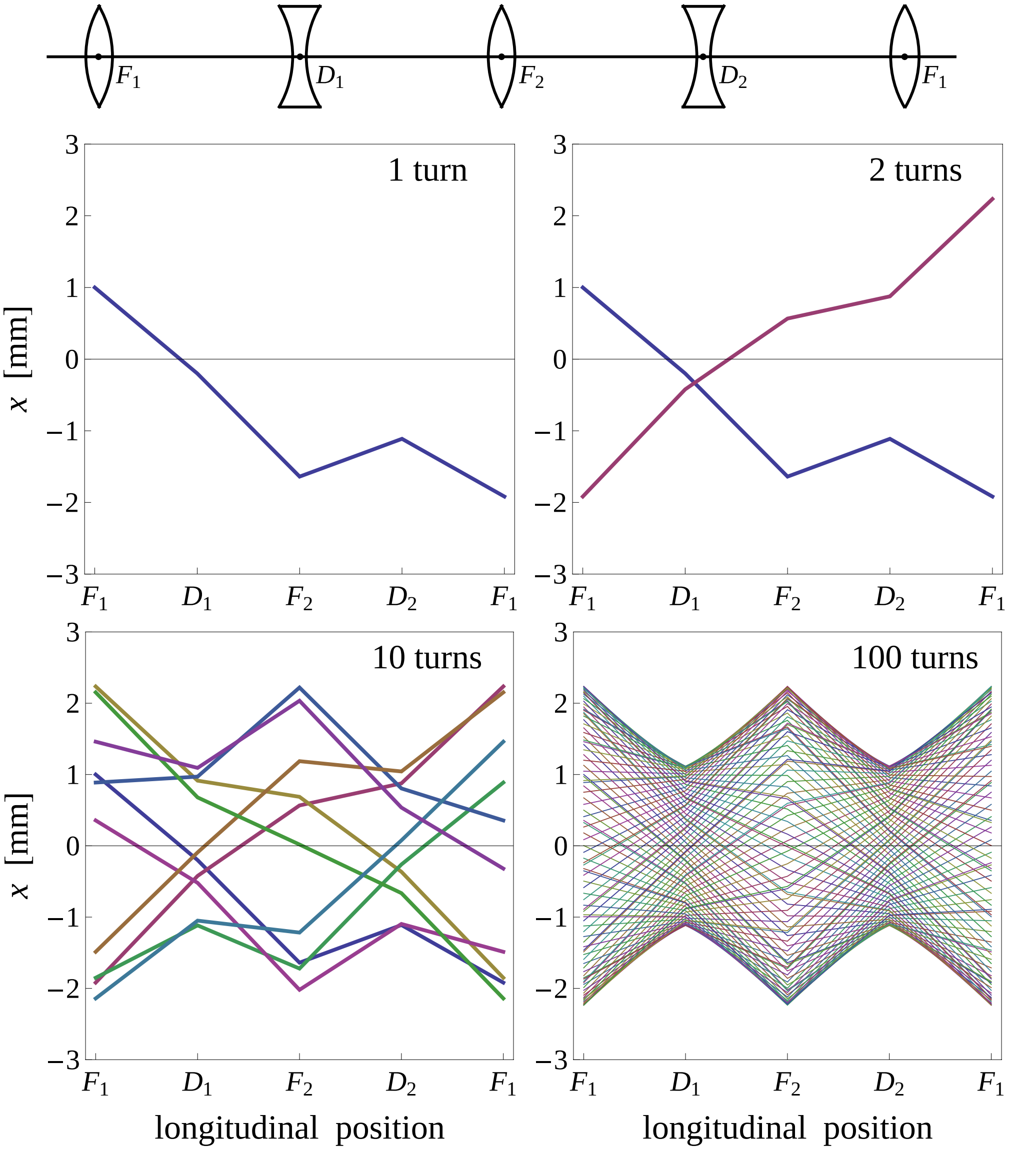

Figure 2.7: Trajectory of a particle in a system of two FODO lattices. In the Frenet-Serret's coordinates, the particle moves on straight lines between thin lenses. The periodicity of the system returns the particle from the right end to the left end. After many turns, the trajectory shows the envelope structure, whose shape and scale are determined by the amplitude function $\beta(s)$ and emittance ϵ. If trajectories of multiple particles are traced in a single revolution, there appears the same envelope structure, determining the beam size in this case.

motion is a combination of straight motions between lenses and instantaneous deflections by lenses. The betatron oscillations are such zigzag motions in this coordinate system. Because of the periodicity in the system, once the particle reaches the right end, it wraps back to the left end and begins the next revolution. Because there are two complete FODO lattices in our model synchrotron, the position and angle after the first revolution, $(x, x')_1$, is given by multiplying the matrix $(\mathbf{M}_{\text{FODO}})^2$ to the initial state, $(1, 0)$:

$$\begin{pmatrix} x \\ x' \end{pmatrix}_1 = (\mathbf{M}_{\text{FODO}})^2 \begin{pmatrix} 1 \\ 0 \end{pmatrix} \quad . \tag{2.12}$$

More generally, the position and angle after n revolutions, $(x, x')_n$, is given by multiplying $(\mathbf{M}_{\text{FODO}})^{2n}$:

$$\begin{pmatrix} x \\ x' \end{pmatrix}_n = (\mathbf{M}_{\text{FODO}})^{2n} \begin{pmatrix} 1 \\ 0 \end{pmatrix} \quad . \tag{2.13}$$

In Figure 2.7, we can see that, after many revolutions, the motion has an envelope structure. The shape of the envelope is determined by a function of the longitudinal position s, referred to as the (betatron) amplitude function or β-function and denoted by $\beta(s)$. The particle's maximum deviation from the ideal trajectory is proportional to square root of the amplitude function at each longitudinal position. Obviously, the maximum deviation from the ideal trajectory also depends on the particle's initial condition. We use a constant parameter, referred to as the emittance and denoted by ϵ, to describe the scale of the maximum deviation. Although this figure shows the trajectory of a single particle in multiple revolutions, we can also interpret it as trajectories of multiple particles within the beam in a single revolution. In the interpretation of multiple particles, the envelope of the particles' trajectories is of significance, defining the beam size in the transverse direction.

Turn-by-turn Position

Figure 2.8 shows the particle's positions observed at two fixed locations, F_1 and D_1, in the same model as Figure 2.7. When observed at one location, the particle undergoes sinusoidal oscillations as a function of revolution number. This is the other aspect of the betatron oscillations. Such oscillations observed at one location in a synchrotron is referred to as turn-by-turn oscillations. The amplitude of the turn-by-turn oscillations is proportional to square root of the amplitude function $\beta(s)$ at the location. The frequency of the turn-by-turn oscillations is the same at any location in the synchrotron but relative phases of the turn-by-turn oscillations at any two locations are obviously different. The betatron tune, denoted by ν, is the frequency of the turn-by-turn oscillations in units of the revolution number. The betatron phase advance, denoted by $\psi(s_2|s_1)$, is the relative phase difference between two locations in the synchrotron, s_1 and s_2. A schematic definition of the phase advance, for example, between F_1 and D_1 is given in Figure 2.8.

Phase Space

As we have seen in this chapter, the horizontal deviation from the ideal trajectory x and the angle $x' = dx/ds$ are convenient coordinates to describe the particle's horizontal motion in the synchrotron. Hence, instead of momentum, we use the angle x' as the second coordinate of the phase space to characterize the horizontal motion. Similarly, the phase space of the vertical motion is characterized by the pair (y, y'), where $y' \equiv dy/ds$. Figure 2.9 shows the evolution of particle's phase space in the same model as Figures 2.7 and 2.8. Here, points with the same color represent values of (x, x') for the particle at a specific location in the FODO lattice. For instance, yellow points represent

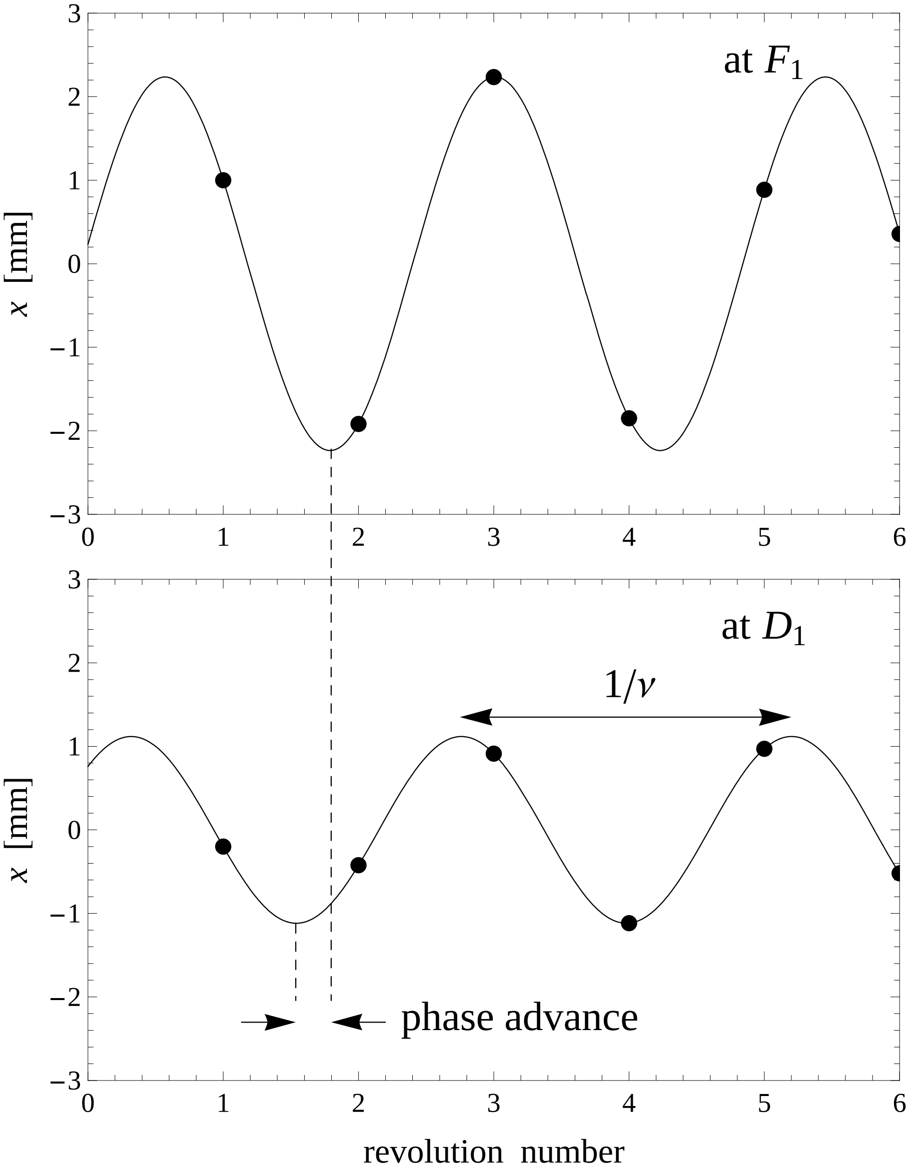

Figure 2.8: Turn-by-turn positions at F_1 and D_1 of Figure 2.7. The amplitude of the turn-by-turn oscillations is proportional to square root of the amplitude function $\beta(s)$. The difference of the amplitudes at F_1 and D_1 is due to the difference of the amplitude functions at these locations. The betatron tune ν is the frequency of the turn-by-turn oscillations, which is a global parameter, and the betatron phase advance $\psi(s_2|s_1)$ is the oscillations' relative phase difference between two locations.

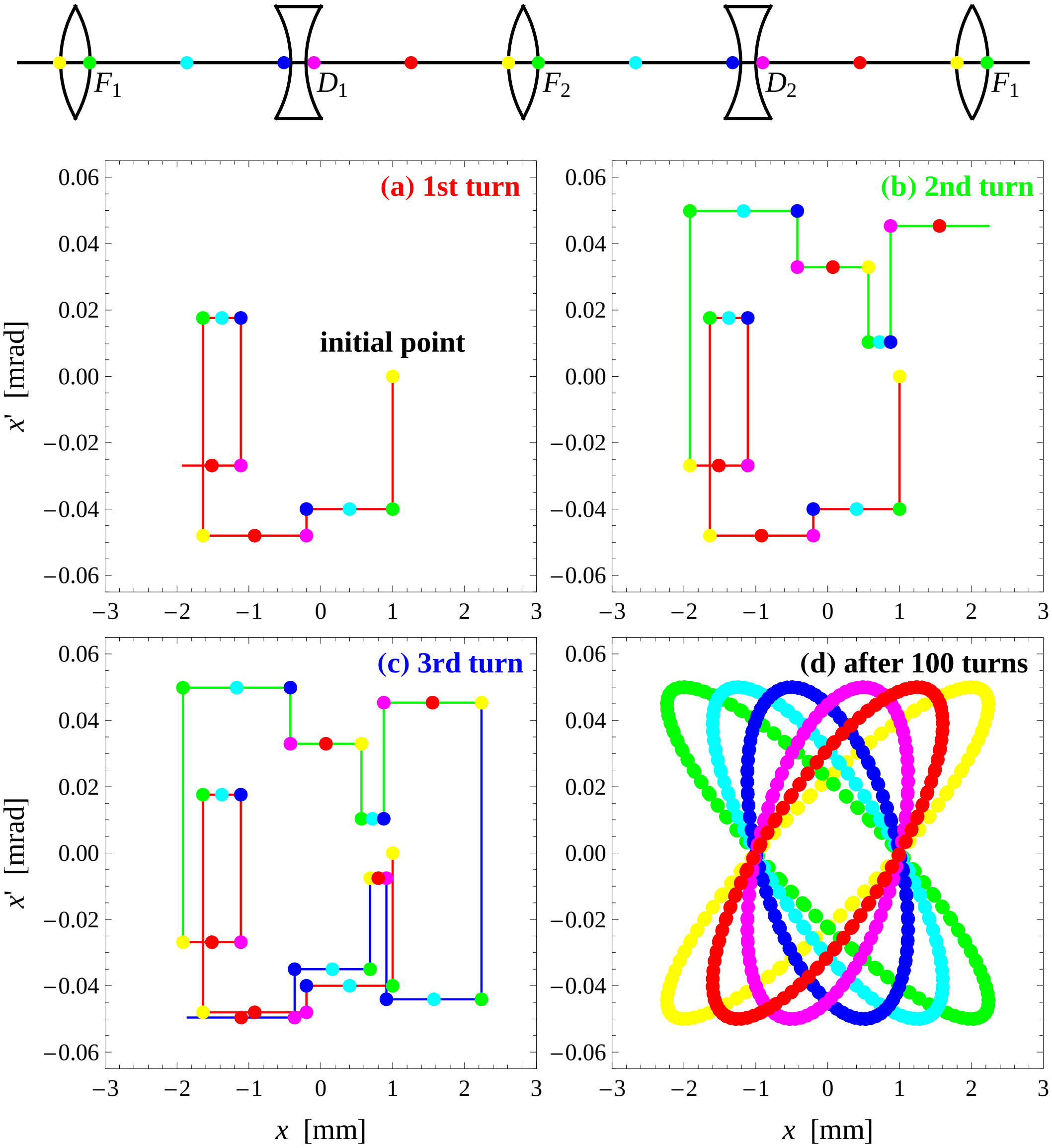

Figure 2.9: Phase space of a system consisting of the FODO lattices. The colors of the points represent the locations in the FODO lattice. Corresponding to the zigzag trajectory of the particle, only the angle changes in the lenses and only the position changes in the drift spaces. If observed at one location of the system, the particle moves on one ellipse. The area of the ellipses, the emittance, is a constant of motion and the shapes of the ellipses are determined by the amplitude function.

the phase space positions when the particle is in front of the focusing lenses, F_1 and F_2. Referring to Figure 2.9(a), the series of plotted points give the particle's position at the various longitudinal position in the FODO lattice, indicated above. For instance, as the particle moves right to left through lens D_1, indicated in colors by the transition from blue to pink, the plotted coordinate x does not change but the angle x' becomes increasingly negative, as expected for a defocusing lens at the location. In contrast, the drift region between D_1 and F_2, characterized by the color from pink to yellow, shows no change in the angle x' but shows an increase in the position x as the particle drifts away from the central orbit. Figures 2.9(b) and 2.9(c) continue to follow the particle through additional revolutions around this model system.

As seen in Figure 2.9, if observed at one location of the FODO lattice, the particle's motion can be seen to follow an ellipse. The area enclosed by these ellipses is a constant of motion and it is the emittance. The shapes of these ellipses are determined by the amplitude function and its slope at each locations. The turn-by-turn oscillations in Figure 2.8 are the projections of such motions on the phase space ellipses onto the position axes. As we did for Figure 2.7, we can imagine the case of multiple particles from this figure. If we assume these ellipses are of the outermost particle, they can be interpreted as the shapes of the particle distributions at each locations. We can see the transverse beam size varies depending on the amplitude function of the location, in this interpretation as well.

Simulation of Free Straight Regions

Figure 2.10 shows the trajectories of the particles coming out of the system of the FODO lattices in Figure 2.7 and traveling in a drift space. In the model,

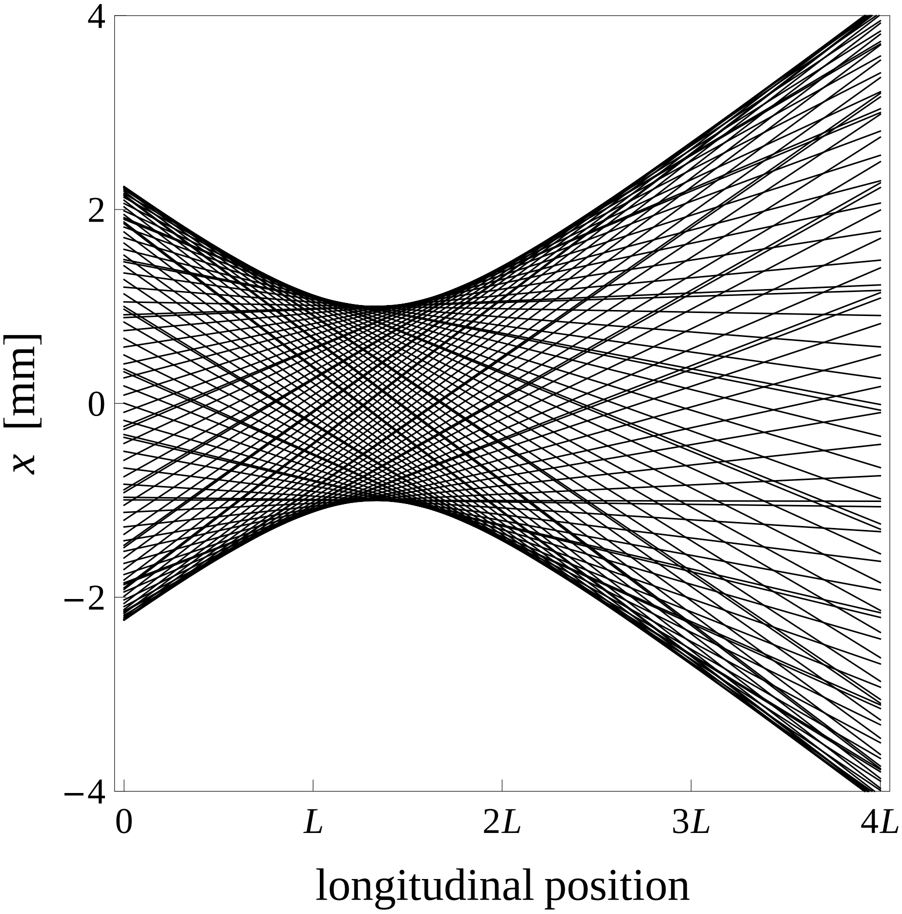

Figure 2.10: Particles' trajectories in a drift space. The beam looks like this in a collision straight section of a collider. We adjust the beam so that its size become minimum at the center of the physics detector.

the particles are coming out of a focusing lens of the FODO lattices. In a drift space, the amplitude function is a parabolic function of the longitudinal position s. The location where the amplitude function and the beam size become minimum is referred to as the (beam) waist. In a collider, a physics detector sits in a magnet free straight region, referred to as collision straight section, and the beam looks like Figure 2.10 near the detector. To maximize the event rate, we adjust the collider's lattice so that the beam waists in both of the plains are at the center of the detector[2]

2.3 Betatron Oscillations

In the previous section, through simple models, we learned basic properties of the betatron oscillations and also introduced parameters such as the amplitude function, emittance, tune, and phase advance. In this section, we discuss the mathematical formalism of the betatron oscillations.

2.3.1 Hill's Equation of Motion

In this section, we discuss the equation of motion to describe the betatron oscillations. When a charged particle goes through a thin magnetic element, the deflection angle is given by Equation 2.4. From this equation, when a particle is deflected by a short magnetic element with field $(B_x(x, y, s), B_y(x, y, s))$ and length Δs, located at the longitudinal position s, the changes of the transverse

---

[2] In this simulation, the beam has no waist in the other plane since the last quadrupole magnet defocus the beam in the other plane. To arrange the beam waists in both of the planes at the center of the detector, we need a set of quadrupole magnets, referred to as quadrupole triplets (see for instance [29]), at both ends of a collision straight section.

angles, $\mathit{\Delta} x'$ and $\mathit{\Delta} y'$, are given by

$$\mathit{\Delta} x' = -\frac{B_y(x,y,s)\mathit{\Delta} s}{(B\rho)} \tag{2.14}$$

$$\mathit{\Delta} y' = \frac{B_x(x,y,s)\mathit{\Delta} s}{(B\rho)} \ . \tag{2.15}$$

Here, the signs in the right-hand-sides are from the choice of the Frenet-Serret's coordinate system. By taking the limit $\mathit{\Delta} s \to 0$, we get the following two equations:

$$x'' = -\frac{B_y(x,y,s)}{(B\rho)} \tag{2.16}$$

$$y'' = \frac{B_x(x,y,s)}{(B\rho)} \ . \tag{2.17}$$

We note that, because the transverse positions x and y are the deviations from the ideal trajectory, the angles x' and y' are not changed by the bending dipole magnets. Hence, in our coordinate system, the magnetic field $(B_x(x,y,s), B_y(x,y,s))$ should not include that of the bending dipole magnets.

In Equations 2.16 and 2.17, we usually perform the multipole expansion of the field $(B_x(x,y,s), B_y(x,y,s))$ and separate the dipole and quadrupole field components from the rest. The general multipole expansion of two dimensional magnetic field is given by

$$B_x(x,y,s) = B_{x,0}(s) + B_{x,1}(s)x + B_{y,1}(s)y + \dots \tag{2.18}$$

$$B_y(x,y,s) = B_{y,0}(s) + B_{y,1}(s)x - B_{x,1}(s)y + \dots \ . \tag{2.19}$$

Here, $B_{x,n}(s)$ and $B_{y,n}(s)$ $(n = 0, 1, 2, \dots)$ are shorthand notations similar to Equation 2.3:

$$B_{x,n}(s) \equiv \left. \frac{\partial^n B_x(x,y,s)}{\partial^n x} \right|_{x=y=0} \tag{2.20}$$

$$B_{y,n}(s) \equiv \left. \frac{\partial^n B_y(x,y,s)}{\partial^n x} \right|_{x=y=0} \tag{2.21}$$

and the two dimensional Maxwell's equations in vacuum are used:

$$\frac{\partial B_x(x,y,s)}{\partial x} + \frac{\partial B_y(x,y,s)}{\partial y} = 0 \tag{2.22}$$

$$\frac{\partial B_y(x,y,s)}{\partial x} - \frac{\partial B_x(x,y,s)}{\partial y} = 0 \ . \tag{2.23}$$

In this expansion, $B_{y,0}(s)$ denotes the dipole field component. As we already discussed in this section, $B_{y,0}(s)$ is zero by design in our coordinate system. The term $B_{x,0}(s)$ is referred to as skew dipole component which bends the beam particles vertically. Because we are thinking planar synchrotrons, $B_{x,0}(s)$ is also zero by design. As we defined in Section 2.1, the terms proportional to $B_{y,1}(s)$ represent the field of the quadrupole magnets. The terms proportional to $B_{x,1}(s)$ represent the field referred to as skew quadrupole field. The skew quadrupole field has an undesired effect of coupling the motions in the two transverse planes, which is often undesired, and so $B_{x,1}(s)$ is zero in the designs of most accelerators. Hence, by keeping only the quadrupole field, we rewrite Equations 2.18 and 2.19 in the following way:

$$B_x(x,y,s) = B_{y,1}(s)y + \mathit{\Delta} B_x(x,y,s) \tag{2.24}$$

$$B_y(x,y,s) = B_{y,1}(s)x + \mathit{\Delta} B_y(x,y,s) \ , \tag{2.25}$$

where $\mathit{\Delta} B_x(x,y,s)$ and $\mathit{\Delta} B_y(x,y,s)$ represent perturbative fields including the error dipole fields, error quadrupole fields, skew dipole fields, skew quadrupole fields, and the other higher order fields. By using Equations 2.24 and 2.25, Equations 2.16 and 2.17 can be written as

$$x'' + K(s)x = -\frac{\mathit{\Delta} B_y(x,y,s)}{(B\rho)} \tag{2.26}$$

$$y'' - K(s)y = \frac{\mathit{\Delta} B_x(x,y,s)}{(B\rho)} \ , \tag{2.27}$$

where the quantity $K(s)$, defined as

$$K(s) \equiv \frac{B_{y,1}(s)}{(B\rho)} \ , \tag{2.28}$$

is referred to as effective gradient of the quadrupole magnets and is analogous to the spring constant of a harmonic oscillator.

Because of the synchrotron's periodicity, $K(s)$ is a periodic function of the longitudinal coordinate s, satisfying $K(s) = K(s + C)$. This type of a second order differential equation, with spring constant of a periodic function, is known as Hill's equation [30]. In the ideal synchrotron, the right-hand-sides of Equations 2.26 and 2.27 are zero and, then, the equations are homogeneous. In this case, transverse motions of the beam particles are linear and uncoupled. The fields $\mathit{\Delta} B_x(x, y, s)$ and $\mathit{\Delta} B_y(x, y, s)$ produce perturbative effects on such ideal motions. In Chapter 3, we discuss details of such perturbative effects on the ideal motions.

2.3.2 A Closed Form Solution of the Hill's Equation

Hill's equation (in homogeneous form) has a closed form solution which is similar to the solution of a simple harmonic oscillator:

$$x(s) = A\sqrt{\beta(s)}\cos(\psi(s|s_0) + \chi) \ . \tag{2.29}$$

Here, A is a constant of the integral with dimensions of $(\text{length})^{1/2}$ and χ is a constant phase. As we discussed in Section 2.2.3, the square root of the amplitude function $\beta(s)$ determines the amplitude of the betatron oscillations. The amplitude function has dimensions of length and is a periodic function of the longitudinal coordinate s, satisfying $\beta(s + C) = \beta(s)$. The amplitude function is determined from the effective gradient $K(s)$ through the following differential equation:

$$\frac{1}{2}\beta(s)\beta''(s) - \frac{1}{4}\beta'(s)^2 + \beta(s)^2 K(s) = 1 \ . \tag{2.30}$$

Instead of solving this differential equation, we discuss a method to determine the amplitude function using matrices, later in Section 2.3.4. The phase of the betatron oscillations is determined by the phase advance $\psi(s|s_0)$, introduced in Section 2.2.3. We note that the phase advance is always defined from a reference point, in this case s_0. When the reference point is the origin of the longitudinal coordinate s, namely $s_0 = 0$, we sometimes use the following shorthand notation: $\psi(s) \equiv \psi(s|0)$. An important difference between betatron oscillations and simple harmonic oscillations is the following correlation between the amplitude and phase, given by

$$\psi(s|s_0) \equiv \int_{s_0}^{s} \frac{d\bar{s}}{\beta(\bar{s})} \ , \tag{2.31}$$

where $\bar{s}$ is a variable of integration. From this relation, the amplitude function can be interpreted as the local wavelength of the betatron oscillations (divided by 2π). The betatron tune ν is the phase advance of a single revolution measured in units of 2π:

$$2\pi\nu \equiv \psi(s + C|s) = \int_{s}^{s+C} \frac{d\bar{s}}{\beta(\bar{s})} \ , \tag{2.32}$$

where s is an arbitrary longitudinal position in the synchrotron. Because of the amplitude function's periodicity, the tune is a global parameter, independent of the starting point s.

In a real synchrotron, we cannot trace the entire trajectory of the betatron oscillations. Rather, we can only observe the turn-by-turn oscillations at locations of the BPM's. When we observe turn-by-turn oscillations, it is convenient to rewrite Equation 2.29. First, we express the longitudinal position s

with the circumference C, revolution number n, and a parameter $\tilde{s}$ which is in the range $0 \le \tilde{s} < C$: $s = nC + \tilde{s}$. Similarly we rewrite the longitudinal position of the reference: $s_0 = nC + \tilde{s}_0$. We note that the amplitude function and betatron phase advance satisfy $\beta(s) = \beta(\tilde{s})$ and $\psi(s|s_0) = 2\pi\nu(n - n_0) + \psi(\tilde{s}|\tilde{s}_0)$. Then, Equation 2.29 can be also written as

$$x(nC + \tilde{s}) = A\sqrt{\beta(\tilde{s})}\cos(2\pi\nu n + \psi(\tilde{s}|\tilde{s}_0) + \bar{\chi}) \ , \tag{2.33}$$

where $\bar{\chi} \equiv \chi - 2\pi\nu n_0$ is a constant phase. This equation describes the sinusoidal oscillations as a function of revolution number n, as we saw in the model of Figure 2.8. In this equation, we can see that the tune and phase advance are the frequency (in units of the revolution number) and relative phase differences between different locations, as discussed in Section 2.2.3.

2.3.3 Courant-Snyder Parameters and Emittance

By differentiating Equation 2.29 with respect to the longitudinal coordinate s, the slope is given by

$$\begin{aligned} x'(s) &= -\frac{A}{\sqrt{\beta(s)}}\sin(\psi(s|s_0) + \chi) - \frac{A\alpha(s)}{\sqrt{\beta(s)}}\cos(\psi(s|s_0) + \chi) \qquad (2.34) \\ &= -A\sqrt{\gamma(s)}\sin(\psi(s|s_0) + \chi + \arctan(\alpha(s))) \ , \qquad (2.35) \end{aligned}$$

where we introduced the two new parameters $\alpha(s)$ and $\gamma(s)$:

$$\begin{aligned} \alpha(s) &\equiv -\frac{1}{2}\frac{d\beta(s)}{ds} \qquad (2.36) \\ \gamma(s) &\equiv \frac{1 + \alpha(s)^2}{\beta(s)} \ . \qquad (2.37) \end{aligned}$$

A set of parameters $\beta(s)$, $\alpha(s)$, and $\gamma(s)$ are referred to as Courant-Snyder parameters [31]. We note, just as the β-function determines the amplitude of the position oscillations, the γ-function determines the amplitude of the angle oscillations. The differential equation to determine the amplitude function, Equation 2.30, is simplified with the Courant-Snyder parameters:

$$K(s)\beta(s) = \gamma(s) + \alpha'(s)\ . \tag{2.38}$$

Mathematical expressions of the betatron oscillations is often simplified by using normalized conjugate momentum, $p_x \equiv \alpha(s)x + \beta(s)x'$, instead of the angle x'. The space spanned by x and p_x is called the normalized phase space, as opposed to the ordinary phase space spanned by x and x'. From Equations 2.29 and 2.34, when a particle undergoes the betatron oscillations, the normalized conjugate momentum is given by

$$p_x(s) = -A\sqrt{\beta(s)}\sin(\psi(s|s_0) + \chi)\ . \tag{2.39}$$

A relation referred to as Courant-Snyder invariance can be easily verified from Equations 2.29 and 2.39:

$$\frac{1}{\beta(s)}\left[x(s)^2 + p_x(s)^2\right] = \gamma(s)x(s)^2 + 2\alpha(s)x(s) + \beta(s)x'(s)^2 = A^2\ . \tag{2.40}$$

This relation is analogous to the energy conservation of a simple harmonic oscillator. This equation indicates that, if observed at one location in the synchrotron, the mapping in the normalized phase space (x, p_x) forms a circle and the mapping in the ordinary phase space (x, x') forms an ellipse. Figure 2.11 shows schematic examples of mappings in the normalized and ordinary phase spaces, observed at one location in the synchrotron. Because the Courant-Snyder parameters varies over the longitudinal position s, the shape of the ellipse is different at each location in the synchrotron. Such a phenomenon is also seen in Figure 2.9. In this sense, the Courant-Snyder parameters can be interpreted as the parameters to determine the shape of the phase space

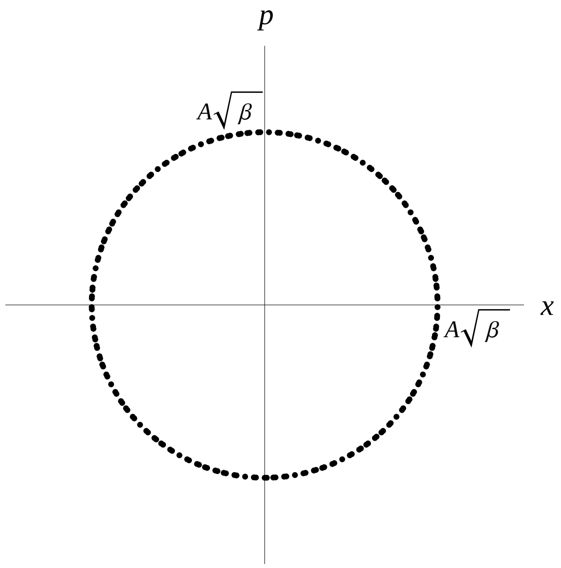

(a) Normalized phase space

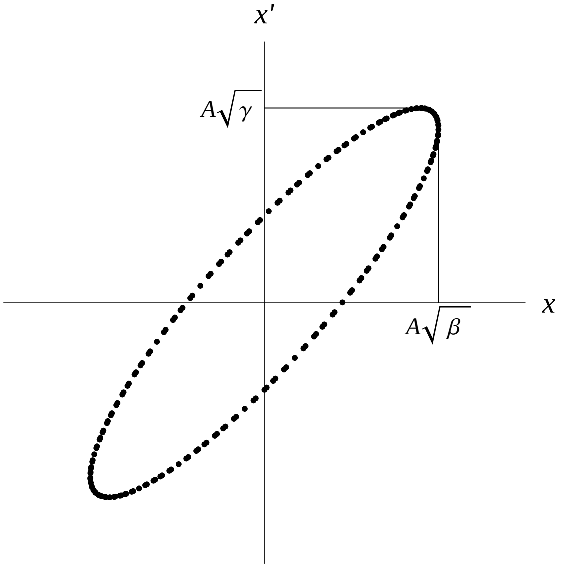

(b) Phase space

Figure 2.11: The mapping in the normalized phase space (x, p) and ordinary phase space (x, x'), observed at one location in the synchrotron. In the normalized phase space, the mapping forms a circle with area $\pi A\beta(s)$. In the ordinary phase space, the mapping forms an ellipse with area πA^2. The emittance ϵ is the area of the ellipse in the ordinary phase space and is a constant of motion.

ellipse at each location in the synchrotron. In contrast, the area of the ellipse in the ordinary phase space is a constant of motion, given by

$$\epsilon = \frac{\pi A^2}{\sqrt{\beta(s)\gamma(s) - \alpha(s)^2}} = \pi A^2 \ , \tag{2.41}$$

where we used an identity of the Courant-Snyder parameters: $\beta(s)\gamma(s) - \alpha(s)^2 = 1$. This area ϵ is the emittance defined in Section 2.2.3. The emittance is analogous to the energy of a simple harmonic oscillator.

When we read articles of accelerator physics, depending on authors and institutions, the definition of the emittance is different. In the following, when we consider a single particle, the emittance denotes the area of the ellipse in the ordinary phase space. This emittance is sometimes referred to as single particle emittance. When we consider multiple particles in a synchrotron, we use the definition referred to as 95% convention. In this case, the emittace is defined as the area enclosed by the outermost particle, inside which 95% of the particles are included (Figure 2.12). This is a typical convention for proton synchrotrons. Details about various conventions of the emittance can be seen in pages 81-83 of [7]. As discussed in Section 2.2.3, what is important for the synchrotron is that the beam size is determined by the amplitude function $\beta(s)$ and emittance.

2.3.4 Transfer Matrix

The matrix to describe a particle's propagation in a synchrotron is referred to as transfer matrix. The matrices of the thin lenses and drifting in Equations 2.8 and 2.9 are the simplest examples of the transfer matrix. In principle, we know all the elements of the synchrotron and so the transfer matrix between any two locations can be calculated by multiplying the matrices of the all

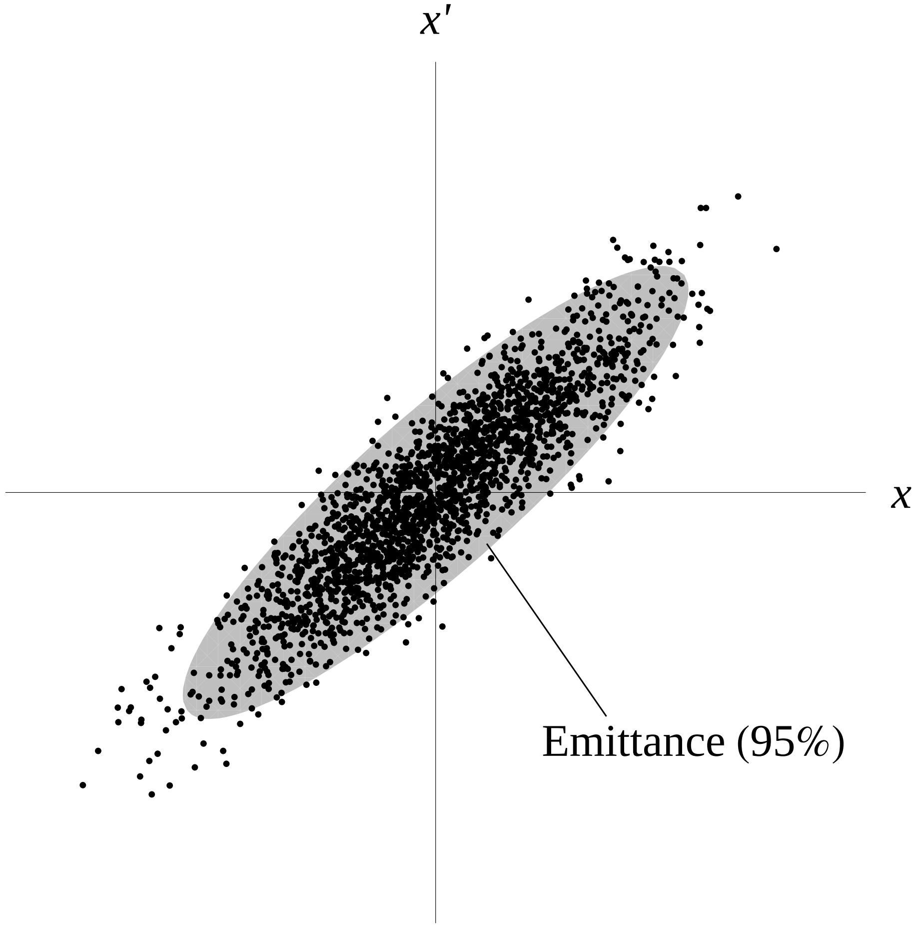

Figure 2.12: Beam emittance. Each black point represents a particle and the shaded are shows the emittance of the 95% convention which encloses 95% of the particles. The beam size is determined by the emittance and the amplitude function at the location.

elements in-between, one after the other. By using properties of the closed form solution of the betatron oscillations, the transfer matrix can be also expressed with the betatron tune and Courant-Snyder parameters. In this section, we discuss the relation among the transfer matrix, the betatron tune, and the Courant-Snyder parameters.

Transfer Matrix of a Single Revolution

Suppose a particle's position and normalized conjugate momentum are $x(s)$ and $p_x(s)$ at the longitudinal position s. After a single revolution, from Equations 2.29 and 2.39, the state of the particle becomes

$$\begin{aligned}\begin{pmatrix} x(s+C) \\ p_x(s+C) \end{pmatrix} &= \begin{pmatrix} \cos(2\pi\nu) & \sin(2\pi\nu) \\ -\sin(2\pi\nu) & \cos(2\pi\nu) \end{pmatrix} \begin{pmatrix} x(s) \\ p_x(s) \end{pmatrix} \\ &= \mathbf{R}(-2\pi\nu) \begin{pmatrix} x(s) \\ p_x(s) \end{pmatrix} \quad , \end{aligned} \tag{2.42}$$

where $\mathbf{R}(\theta)$ is the two dimensional rotational matrix with angle θ. In the normalized phase space, the single turn transfer matrix is the rotational matrix with angle $-2\pi\nu$ and independent of the longitudinal position s. This corresponds to the fact that, if observed at one location in the synchrotron, the mapping in the normalized phase space forms a circle (Figure 2.11). Suppose $\mathbf{M}(s+C|s)$ is the single-turn transfer matrix in the ordinary phase space, defined by

$$\begin{pmatrix} x(s+C) \\ x'(s+C) \end{pmatrix} = \mathbf{M}(s+C|s) \begin{pmatrix} x(s) \\ x'(s) \end{pmatrix} \quad . \tag{2.43}$$

Because the ordinary phase space is related to the normalized phase space by a matrix $\mathbf{N}(s)$:

$$\begin{pmatrix} x \\ p_x \end{pmatrix} = \begin{pmatrix} 1 & 0 \\ \alpha(s) & \beta(s) \end{pmatrix} \begin{pmatrix} x \\ x' \end{pmatrix} \equiv \mathbf{N}(s) \begin{pmatrix} x \\ x' \end{pmatrix} , \qquad (2.44)$$

the single turn transfer matrix $\mathbf{M}(s+C|s)$ in the ordinary phase space can be calculated from $\mathbf{R}(-2\pi\nu)$ and $\mathbf{N}(s)$:

$$\begin{aligned} &\mathbf{M}(s+C|s) \\ &\quad = \mathbf{N}(s)^{-1}\mathbf{R}(-2\pi\nu)\mathbf{N}(s) \\ &\quad = \begin{pmatrix} \cos(2\pi\nu) + \alpha(s)\sin(2\pi\nu) & \beta(s)\sin(2\pi\nu) \\ -\gamma(s)\sin(2\pi\nu) & \cos(2\pi\nu) - \alpha(s)\sin(2\pi\nu) \end{pmatrix} . \end{aligned} \qquad (2.45)$$

We note that the matrix $\mathbf{M}(s + C|s)$ can be also written in the following compact form:

$$\mathbf{M}(s+C|s) = \mathbf{I}\cos(2\pi\nu) + \mathbf{J}(s)\sin(2\pi\nu) , \qquad (2.46)$$

where $\mathbf{I}$ is the identity matrix and $\mathbf{J}(s)$ is a matrix given by the Courant-Snyder parameters:

$$\mathbf{J}(s) \equiv \begin{pmatrix} \alpha(s) & \beta(s) \\ -\gamma(s) & -\alpha(s) \end{pmatrix} . \qquad (2.47)$$

In contrast to the normalized phase space, the single turn transfer matrix in the ordinary phase space depends on the longitudinal position s. This corresponds to the fact that, if observed at one location, the mapping in the ordinary phase space forms an ellipse and its shape depends on the longitudinal position s (Figure 2.11).

As we discussed earlier, the single turn transfer matrix can be calculated by multiplying the matrices of the all elements, one after the other. For instance, if the system consists of N FODO lattices, the single turn transfer matrix in front of the focusing lens is given by $(\mathbf{M}_{\mathrm{FODO}})^N$. Hence, by comparing the elements of the known single turn transfer matrix with those of Equation 2.45, we can determine the betatron tune and the Courant-Snyder parameters at the location. This is a standard procedure to determine the Courant-Snyder parameters, rather than solving the differential equation 2.30.

Transfer Matrix of Two Arbitrary Positions

In the normalized phase space, the general transfer matrix between two arbitrary longitudinal positions, s_0 and s, is the composite of the rotational matrix with angle $-\psi(s|s_0)$ and the scaling related to the amplitude function:

$$\begin{pmatrix} x(s) \\ p_x(s) \end{pmatrix} = \sqrt{\frac{\beta(s)}{\beta(s_0)}}\,\mathbf{R}(-\psi(s|s_0)) \begin{pmatrix} x(s_0) \\ p_x(s_0) \end{pmatrix} \quad . \tag{2.48}$$

Here, the scaling factor $(\beta(s)/\beta(s_0))^{1/2}$ corresponds to the fact that the area enclosed by the mapping depends on $\beta(s)$ in the normalized phase space (Figure 2.11). As in the case of the single turn transfer matrix, the transfer matrix from s_0 to s in the ordinary phase space, $\mathbf{M}(s|s_0)$, is calculated from the corresponding matrix in the normalized phase space and Equation 2.44:

$$\begin{aligned} &\mathbf{M}(s|s_0) \\ &\quad = \sqrt{\frac{\beta(s)}{\beta(s_0)}}\,\mathbf{N}(s)^{-1}\mathbf{R}(-\psi(s|s_0))\mathbf{N}(s_0) \\ &\quad = \begin{pmatrix} \sqrt{\frac{\beta}{\beta_0}}(\cos\varDelta\psi + \alpha_0 \sin\varDelta\psi) & \sqrt{\beta\beta_0}\sin\varDelta\psi \\ -\frac{1+\alpha\alpha_0}{\sqrt{\beta\beta_0}}\sin\varDelta\psi - \frac{\alpha-\alpha_0}{\sqrt{\beta\beta_0}}\cos\varDelta\psi & \sqrt{\frac{\beta_0}{\beta}}(\cos\varDelta\psi - \alpha\sin\varDelta\psi) \end{pmatrix} \quad , \end{aligned} \tag{2.49}$$

where, in the last expression, we used the following shorthand notations: $\beta \equiv \beta(s)$, $\beta_0 \equiv \beta(s_0)$, $\alpha \equiv \alpha(s)$, $\alpha_0 \equiv \alpha(s_0)$, and $\varDelta\psi \equiv \psi(s|s_0)$. As discussed previously, the transfer matrix is calculated by multiplying the matrices of the all elements between the two positions. This equation indicates that, if the Courant-Snyder parameters and the betatron phase advance are known at these two positions, we can construct the transfer matrix between these two points without performing the matrix multiplications.

Propagation of the Courant-Snyder Parameters

So far, we have been discussing the propagation of the phase space coordinates. There is also a similar law of propagation for the Courant-Snyder parameters. The matrix $\mathbf{J}(s)$'s at two longitudinal positions s_0 and s are related through the transfer matrix between these two positions $\mathbf{M}(s|s_0)$ in the following way:

$$\mathbf{J}(s) = \mathbf{M}(s|s_0)\mathbf{J}(s_0)\mathbf{M}(s|s_0)^{-1} \ . \tag{2.50}$$

From this equation, we can determine behavior of the Courant-Snyder parameters of a region, where magnetic elements and transfer matrices are known.

For instance, if the space between $s = 0$ and s is a drift space, from Equation 2.9, its transfer matrix is given by

$$\mathbf{M}(s|0) = \begin{pmatrix} 1 & s \\ 0 & 1 \end{pmatrix} \ . \tag{2.51}$$

From Equation 2.50, the Courant-Snyder parameters at $s = 0$ and s are related by the following equation:

$$\begin{aligned} \begin{pmatrix} \alpha(s) & \beta(s) \\ -\gamma(s) & -\alpha(s) \end{pmatrix} &= \begin{pmatrix} 1 & s \\ 0 & 1 \end{pmatrix} \begin{pmatrix} \alpha(0) & \beta(0) \\ -\gamma(0) & -\alpha(0) \end{pmatrix} \begin{pmatrix} 1 & -s \\ 0 & 1 \end{pmatrix} \\ &= \begin{pmatrix} \alpha(0) - \gamma(0)s & \beta(0) - 2\alpha(0)s + \gamma(0)s^2 \\ -\gamma(0) & -\alpha(0) + \gamma(0)s \end{pmatrix} \ . \end{aligned} \tag{2.52}$$

By comparing the 2-1 element of the both sides, we can see the γ-function is a constant in the drift space. From the 1-2 elements of the both sides, the amplitude function $\beta(s)$ satisfies

$$\begin{aligned}\beta(s) &= \beta(0) - 2\alpha(0)s + \gamma(0)s^2 \\ &= \beta^* + \frac{1}{\beta^*}(s - s^*)^2 \ , \end{aligned} \tag{2.53}$$

where, in the second expression, we used the two new parameters:

$$\beta^* \equiv \frac{1}{\gamma(0)} \tag{2.54}$$

$$s^* \equiv \frac{\alpha(0)}{\gamma(0)} = \alpha_0 \beta^* \ . \tag{2.55}$$

As seen in the simulation of Figure 2.10, the amplitude function is a parabolic function of the longitudinal position s in the drift space. If $s^* > 0$ ($\alpha(0) > 0$), the amplitude function has the waist at $s = s^*$ and its value becomes $\beta(s^*) = \beta^*$. We note that the β^* in the luminosity formula, Equation 1.4, is this quantity. Hence, the Courant-Snyder parameters in the collision straight section is particularly important since they are directly related to its luminosity.

Chapter 3

Perturbations to the Ideal Motion in a Synchrotron

In chapter 2, we discussed the transverse oscillatory motion of particles in the restoring forces around the ideal trajectory of a synchrotron. A real synchrotron consists of many magnets with imperfections and such imperfections produce perturbative fields to the ideal betatron oscillations. This is particularly important for a large accelerator consisting of many magnets, like the Tevatron. For instance, if the restoring force is changed due to errors in quadrupole magnets, the betatron amplitude function is modified and the luminosity may be degraded. Perturbative fields also drive certain oscillation modes. The phenomena are similar to classical driven oscillations: for certain values of the tunes, a given mode may be sufficiently large to cause losses of the beam particles. Furthermore, in modern synchrotrons, we sometimes use higher order magnets producing nonlinear fields, such as sextupole and octupole magnets, to compensate some phenomena related to multiple particle effects. We also treat these higher order fields as perturbations. In

Table 3.1: Effects of the perturbative fields to one dimensional betatron oscillations. Each column represents list of effects due to each field. For instance, a sextupole field causes a central orbit distortion and also drives a mode with tune 2ν. Magnitudes of these two effects depend on the constant A of the solution of the homogeneous Hill's equation in Equation 2.29. We note that higher order perturbations include the effects of lower order perturbations. When the tune is close to one of the resonant condition listed in the last row, where N is an arbitrary positive integer, the corresponding field may cause large motion leading to particle losses (resonance).

Magnet type	Dipole	Quadrupole	Sextupole	Octupole
Order	1st	2nd	3rd	4th
Force	$\propto x^0$	$\propto x^1$	$\propto x^2$	$\propto x^3$
Potential	$\propto x^1$	$\propto x^2$	$\propto x^3$	$\propto x^4$
Central orbit distortion	$\propto A^0$ (Eq. 3.36)	-	$\propto A^2$ (Eq. 3.56)	-
Tune shift	-	$\propto A^0$ (Eq. 3.45)	-	$\propto A^2$ (Eq. 3.61)
Beta-beat	-	$\propto A^0$ (Eq. 3.48)	-	$\propto A^2$ (Eq. 3.64)
New Modes	-	-	$\propto A^2$ (at 2ν) (Eq. 3.56)	$\propto A^3$ (at 2ν) (Eq. 3.64)
Resonant conditions	$\nu = N$	$2\nu = N$	$3\nu = N$ $\nu = N$	$4\nu = N$ $2\nu = N$

this chapter, we discuss perturbations due to dipole field errors, quadrupole field errors, sextupole fields, and octupole fields. The effects of these perturbations are summarized in Table 3.1. The main goal of this chapter is to understand these effects listed on this table. Figure 3.1 shows magnetic field lines of dipole, quadrupole, sextupole, and octupole magnets. As reviewed previously, the dipole magnet produces a constant force and the quadrupole magnet produces a linearly growing restoring force, which is proportional to the transverse positon of a beam particle x, much like a harmonic oscillator in classical mechanics. In the horizontal plane, the sextupole produces a force proportional to x^2, corresponding to a potential proportional to x^3, and the octupole produces a force proportional to x^3, corresponding to the potential proportional to x^4. If these forces are small compared to the linear restoring forces of the quadrupole magnets, then these higher higher order fields may be treated as perturbations to the ideal oscillations.

This chapter proceeds as follows. In Section 3.1, we review perturbations to a simple classical oscillator. By considering perturbations similar to the perturbative fields listed in Table 3.1, we can have better ideas about the effects of these perturbative fields. In Section 3.2, we discuss details of perturbative effects listed in Table 3.1.

3.1 Review of Simple Oscillatory Systems

Perturbative fields in the synchrotron produce forces given by polynomials of position x. Hence, in this section, we review perturbations to a classical simple oscillator, whose forces are also given by similar polynomials of position x. Through such simple examples, we can more easily interpret the perturbations to betatron oscillations. As seen in Section 2.3.1, the betatron oscillations of

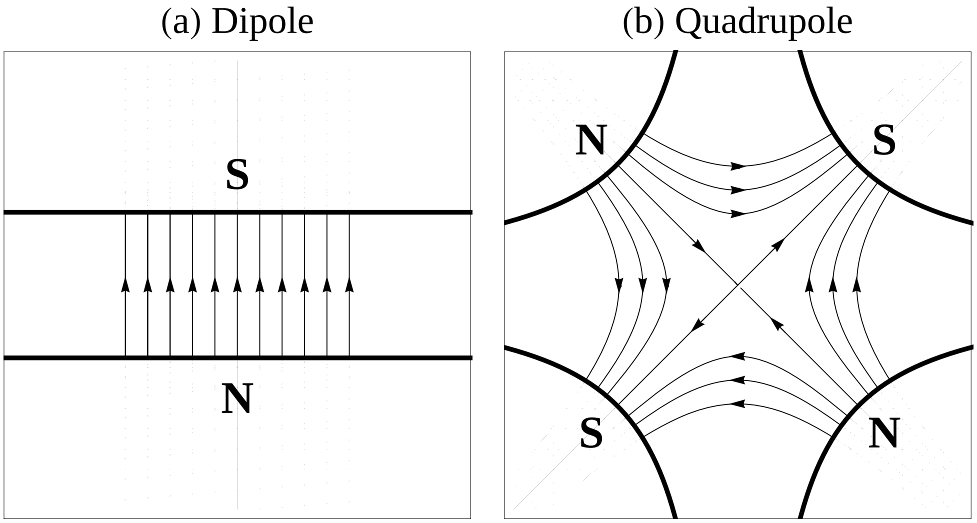

(a) Dipole

(b) Quadrupole

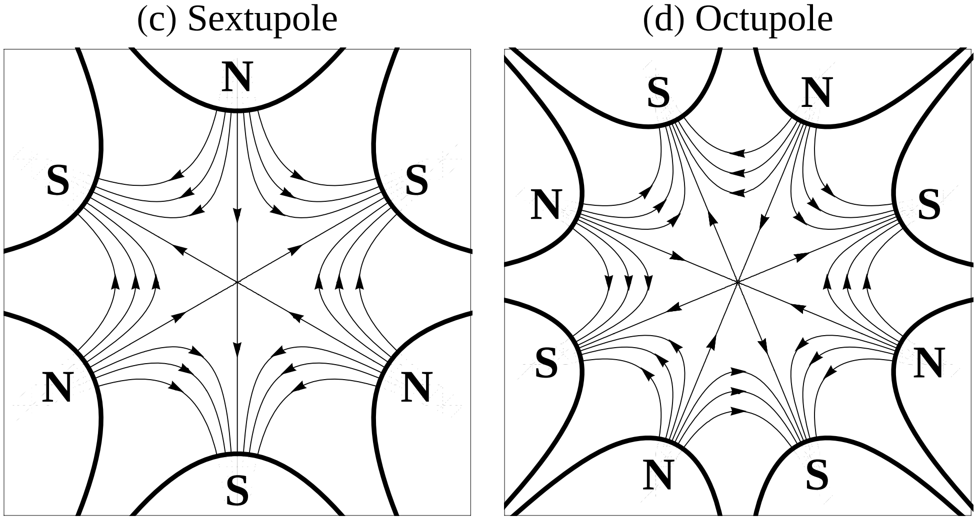

(c) Sextupole

(d) Octupole

Figure 3.1: Schematic cross-sections and magnetic fields of a dipole, quadrupole, sextupole, and octupole magnet. In the horizontal plane, each magnet produce a force proportional to x^0, x^1, x^2, and x^3.

beam particles are determined by Equations 2.26 and 2.27. Hence, we consider an analogous classical system described by the following equation of motion:

$$\frac{d^2x}{dt^2} + \omega_0^2 x = -f(x) \ , \tag{3.1}$$

where ω_0 is the intrinsic angular frequency of the system and the function $f(x)$ describes the perturbation. We suppose the solution of the homogeneous part, the case corresponding to zero perturbation $f(x) = 0$, is given by

$$x_0(t) = a\cos(\omega_0 t) \ , \tag{3.2}$$

where a is a constant amplitude.

When the oscillator is driven by a periodic external force $f(t) = -\kappa_d \cos(\omega_d t)$, the equation of motion for the driven oscillator is given by

$$\frac{d^2x}{dt^2} + \omega_0^2 x = -\kappa_d \cos(\omega_d t) \ , \tag{3.3}$$

where κ_d and ω_d are the strength and angular frequency of the driving force. A perturbation which is a polynomial of x may be approximated by such an external force. The particular solution of this equation, $x_d(t)$, is given by

$$\begin{aligned} x_d(t) &= \frac{\kappa_d}{\omega_d^2 - \omega_0^2}\cos(\omega_d t) \\ &= \frac{\kappa_d}{2\omega_d}\left[\frac{1}{\omega_d - \omega_0} + \frac{1}{\omega_d + \omega_0}\right]\cos(\omega_d t) \ . \end{aligned} \tag{3.4}$$

Because the angular frequencies ω_0 and ω_d are positive, resonances occur only when $\omega_d = \omega_0$. For betatron oscillations, ω_d and ω_0 correspond to the driving tune and the intrinsic tune of the system. As we will see in Section 6.1, for the driven particles in the synchrotron, resonances occur at more than one frequencies because of the synchrotron's periodicity.

3.1.1 First Order Perturbation

Suppose the system is under a perturbation of a constant force: $f(x) = \kappa_1$, corresponding to the potential $V(s) = \kappa_1 x$. Here, the index 1 denotes the first order. In a synchrotron, the first order perturbations are due to errors of the dipole fields. The equation of motion is given by

$$\frac{d^2x}{dt^2} + \omega_0^2 x = -\kappa_1 \ . \tag{3.5}$$

The particular solution of this equation, $x_1(t)$, is also a constant:

$$x_1(t) = -\frac{\kappa_1}{\omega_0^2} \ , \tag{3.6}$$

and the full solution is given by the sum of $x_0(t)$ and $x_1(t)$:

$$x(t) = x_0(t) + x_1(t) = a\cos(\omega_0 t) - \frac{\kappa_1}{\omega_0^2} \ . \tag{3.7}$$

Hence, the first order perturbation to the simple harmonic oscillator shifts the equilibrium position of the oscillations. This effect can be seen by comparing the potentials with and without this perturbation. Figure 3.2(a) shows schematic potentials of a harmonic oscillator with no perturbation (solid), $V(x) = \frac{1}{2}\omega_0^2 x^2$, and with the first order perturbation, $V(x) = \frac{1}{2}\omega_0^2 x^2 + \kappa_1 x^2$. In the figure, we can see the first order perturbation simply translates the potential[1]. The classical system described by Equation 3.6 is quite analogous to the case of a dipole field error in a synchrotron. Such an error shifts the equilibrium of the betatron oscillations and distorts the central orbit by an amount that linearly grows with the perturbation strength κ_1.

---

[1] Here, we ignored the constant change of the potential, which makes no impact on dynamics of the system.

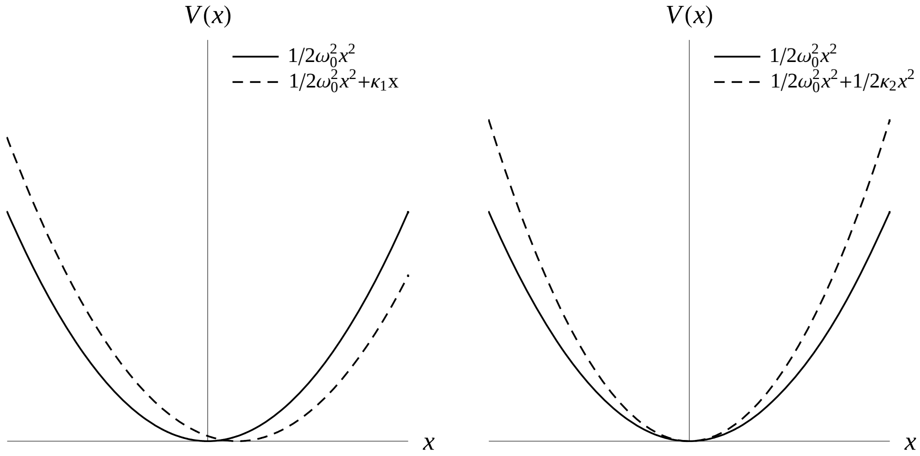

(a) Potential with a 1st order perturbation (b) Potential with a 2nd order perturbation

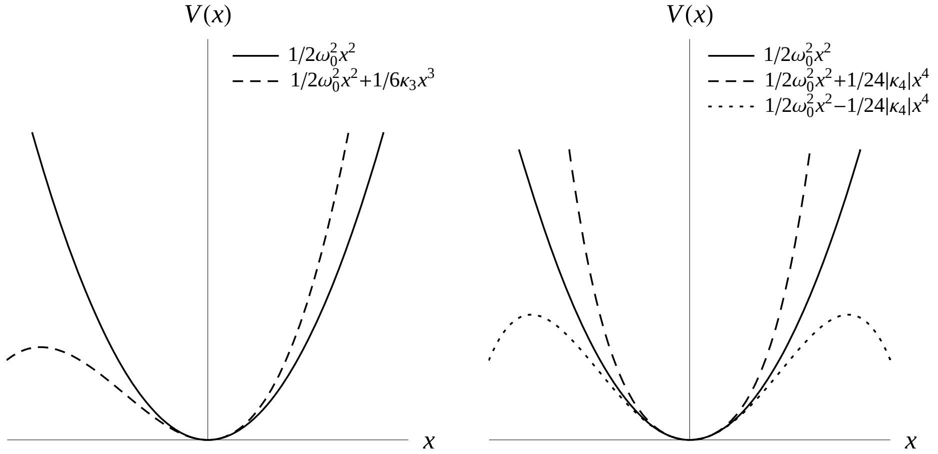

(c) Potential with a 3rd order perturbation (d) Potentials with 4th order perturbations

Figure 3.2: Distortions of a harmonic potential $V_0(x) = \frac{1}{2}\omega_0^2x^2$ (black curve) by various perturbations (dashed curves). These potentials correspond to potentials of magnets in the synchrotron, described in Figure 3.1. (a) The first order perturbation translate the potential and shifts the equilibrium position of the oscillations. (b) The second order perturbation changes the potential to a different quadratic form and changes the system's frequency. (c) Depending on the oscillation amplitude, the third order perturbation drives a mode with the angular frequency $2\omega_0$ and shifts the equilibrium point. (d) Depending on the oscillation amplitude, the fourth order perturbation changes the frequency of the system and drives a mode with the angular frequency $3\omega_0$.

3.1.2 Second Order Perturbation

A second order perturbative force $f(x)$ is linearly proportional to x, corresponding to a potential $V(x) = \frac{1}{2}\omega_0^2 x^2 + \frac{1}{2}\kappa_2 x^2$ (Figure 3.2(b)). Here, κ_2 is a constant to describe the strength of the second order perturbation. The equation of motion is given by

$$\frac{d^2x}{dt^2} + \omega_0^2 x = -\kappa_2 x \ . \tag{3.8}$$

This perturbation changes the angular frequency of the system from ω_0 to an another value ω:

$$\omega = \sqrt{\omega_0^2 + \kappa_2} \simeq \omega_0 + \frac{\kappa_2}{2\omega_0} \ , \tag{3.9}$$

If the perturbation is small and $\omega_0^2 \gg \kappa_2$, ω is approximated by the second expression. Figure 3.2(b) shows schematic potentials of the cases with and without the second order perturbation. The perturbation changes the coefficient of the quadratic potential from ω_0^2 to $\omega_0^2 + \kappa_2$ and, hence, changes the frequency of the system. In a synchrotron, the second order perturbations are due to quadrupole field errors and we can expect such errors change the betatron tune. As discussed later in Section 3.2, a change of the betatron tune may have a significant impact on operations of a synchrotron.

When the second order perturbation is small, a naive way to solve Equation 3.8 is to expand $x(t)$ around the solution of the homogeneous part $x_0(t)$ from Equation 3.2, such as $x(t) = x_0(t) + x_2(t)$, and to solve for the difference $x_2(t)$. Here, the difference $x_2(t)$ is of the order of κ_2. Up to the first of order of κ_2, the equation to determine $x_2(t)$ is given by

$$\frac{d^2x_2}{dt^2} + \omega_0^2 x_2 = -\kappa_2 x_0 = -\kappa_2 a \cos(\omega_0 t) \ . \tag{3.10}$$

The right-hand-side of this equation indicates that, on the first order of κ_2, the second order perturbation reduces to an external force with the angular frequency ω_0. If we use the solution of the driven oscillator in Equation 3.4, the second order position x_2 becomes infinitely large. This result is quite different from the true effect of the second order perturbation, changing the frequency of the system. When a perturbation changes the frequency of the system, the naive perturbation like this always ends up infinity and we must use a modified perturbation technique [32]. The essence of such a modified perturbation technique is the following. First, from the coefficient of the external force giving divergence, in this case $\kappa_2 a$, we can predict the frequency change of Equation 3.9. Once we know the new angular frequency ω, we replace all the intrinsic angular frequency ω_0 to this new frequency ω. Then, the leading order position $x_0(t)$ is changed to

$$x_0(t) = a\cos(\omega t) \ . \tag{3.11}$$

After this replacement of the angular frequency, we can drop the external force giving the divergence, in this case $[-\kappa_2 a\cos(\omega_0 t)]$. Here, there is no external force for the second order position $x_2(t)$ and so $x_2(t) = 0$. Hence, the modified perturbation technique also gives

$$x(t) = x_0(t) = a\cos(\omega t) \ . \tag{3.12}$$

This modified perturbation technique will be used for the fourth order perturbations to a simple harmonic oscillator and the betatron oscillations in Sections 3.1.4 and 3.2.4.

3.1.3 Third Order Perturbation

We next consider third and fourth order perturbations to a simple harmonic oscillator, as examples of nonlinear perturbations. In contrast to the first and second order perturbations, closed form solutions do not always exist under the presence of the nonlinear perturbations. Here, we consider only the leading order effects of these perturbations.

For a third order perturbation, the perturbative force $f(x)$ is proportional to square of x, corresponding the potential $V(x) = \frac{1}{2}\omega_0^2 x^2 + \frac{1}{6}\kappa_3 x^3$ (Figure 3.2(c)). Here, κ_3 is a constant to describe the strength of the third order perturbation. Then, the equation of motion is given by

$$\frac{d^2x}{dt^2} + \omega_0^2 x = -\frac{1}{2}\kappa_3 x^2 \ . \tag{3.13}$$

Figure 3.2(c) shows schematic potentials of oscillators with and without the third order perturbation. The figure indicates that, when the oscillation amplitude (or the energy) increases, the equilibrium point of the oscillations shifts from the origin, in this case leftward. When the oscillation amplitude increases, the potential deviates farther from the quadratic form $\frac{1}{2}\omega_0^2 x^2$ and, as we learn next, this indicates that the perturbation drives modes with different angular frequencies from the intrinsic angular frequency ω_0.

We can solve Equation 3.13 perturbatively by expanding $x(t)$ around the solution of the homogeneous part $x_0(t)$ from Equation 3.2. By substituting $x(t) = x_0(t) + x_3(t)$ into Equation 3.13, up to the first order of the parameter κ_3, the equation to determine the third order position $x_3(t)$ is given by

$$\begin{aligned} \frac{d^2x_3}{dt^2} + \omega_0^2 x_3 &\simeq -\frac{1}{2}\kappa_3 x_0^2 \\ &= -\frac{1}{4}\kappa_3 a^2 - \frac{1}{4}\kappa_3 a^2 \cos(2\omega_0 t) \ , \end{aligned} \tag{3.14}$$

where we used a formula of the trigonometric functions to rewrite $x_0(t)^2 = a^2\cos^2(\omega_0 t)$:

$$\cos^2(\omega_0 t) = \frac{1}{2} + \frac{1}{2}\cos(2\omega_0 t)\ . \tag{3.15}$$

As derived in Equation 3.5, the constant term in Equation 3.14 simply shifts the equilibrium point of the oscillations. The right-hand-side of Equation 3.14 also contains a term proportional to $\cos(2\omega_0 t)$ which corresponds to the case of the driven harmonic oscillator with the angular frequency $\omega_d = 2\omega_0$. From Equations 3.3 and 3.4, this term drives a mode with the angular frequency $2\omega_0$. The full solution $x(t) = x_0(t) + x_3(t)$ is given by the sum of these three contributions:

$$x(t) = a\cos(\omega_0 t) - \frac{\kappa_3 a^2}{4\omega_0^2} + \frac{\kappa_3 a^2}{12\omega_0^2}\cos(2\omega_0 t)\ . \tag{3.16}$$

We note that the magnitudes of both of the perturbative effects depend on the amplitude of the leading order oscillations a, which makes this a nonlinear perturbation.

In a synchrotron, the third order perturbations are due to sextupole magnetic fields. From these discussions, we can expect that the presence of sextupole fields in a synchrotron will distort the central orbit of the beam and will also drive modes whose tunes are twice of the intrinsic betatron tune.

3.1.4 Fourth Order Perturbation

For a fourth order perturbation, the perturbative force $f(x)$ is proportional to cube of x, corresponding to the potential $V(x) = \frac{1}{2}\omega_0^2 x^2 + \frac{1}{24}\kappa_4 x^4$ (Figure 3.2(d)). Here, the parameter κ_4 describes the strength of the fourth order perturbation. Then, the equation of motion is given by

$$\frac{d^2x}{dt^2} + \omega_0^2 x = -\frac{1}{6}\kappa_4 x^3\ , \tag{3.17}$$

As in the case of the third order perturbation, when the oscillation amplitude increases, the potential deviates from the quadratic form $\frac{1}{2}\omega_0^2 x^2$. This indicates that the perturbation drives a mode whose frequency is different from the system's intrinsic frequency.

We again try to solve Equation 3.17 perturbatively by expanding $x(t)$ around the solution of the homogeneous part, such as $x(t) = x_0(t) + x_4(t)$. Up to the first order of the constant parameter κ_4, $x_4(t)$ is determined by

$$\begin{aligned} \frac{d^2 x_4}{dt^2} + \omega_0^2 x_4 &\simeq -\frac{1}{6}\kappa_4 x_0^3 \\ &= -\frac{1}{8}\kappa_4 a^3 \cos(\omega_0 t) - \frac{1}{24}\kappa_4 a^3 \cos(3\omega_0 t) \ , \end{aligned} \tag{3.18}$$

where we used a formula of the trigonometric functions to rewrite $x_0(t)^3$:

$$\cos^3(\omega_0 t) = \frac{3}{4}\cos(\omega_0 t) + \frac{1}{4}\cos(3\omega_0 t) \ . \tag{3.19}$$

We note that the two terms on the right-hand-side of Equation 3.18 drive modes whose angular frequencies are ω_0 and $3\omega_0$. As we discussed about the second order perturbation in Section 3.1.2, the term $[-\frac{3}{24}\kappa_4 a^3 \cos(\omega_0 t)]$ makes the fourth order position x_4 infinitely large and we have to use the modified perturbation technique in such a case. Here, we follow the procedure discussed in Section 3.1.2. First, by comparing Equations 3.9, 3.10, and 3.18, we can expect that the new frequency of the system ω is given by

$$\omega \simeq \omega_0 + \frac{\kappa_4 a^2}{16\omega_0} \ . \tag{3.20}$$

After this frequency change, the leading order solution $x_0(t)$ is given by

$$x_0(t) = a\cos(\omega t) \ . \tag{3.21}$$

Once the frequency is changed, the influence of the term $[-\frac{3}{24}\kappa_4 a^3 \cos(\omega_0 t)]$ is included and we can drop this term from Equation 3.18. The fourth order position $x_4(t)$ is now determined by

$$\frac{d^2x_4}{dt^2} + \omega^2 x_4 = -\frac{1}{24}\kappa_4 a^3 \cos(3\omega t) \ , \tag{3.22}$$

where the intrinsic angular frequency ω_0 is replaced by the new angular frequency ω. Hence, from Equation 3.4, the full solution $x(t) = x_0(t) + x_4(t)$ is given by

$$x(t) = a\cos(\omega t) + \frac{\kappa_4 a^3}{192\omega^2}\cos(3\omega t) \ . \tag{3.23}$$

In this way, the fourth order perturbation changes the oscillator's frequency and drives a mode with the angular frequency 3ω. We note that both of these effects depend on the amplitude of the leading order solution a, again making this a nonlinear perturbation.

In a synchrotron, the fourth order perturbations are due to octupole magnetic fields. From these discussions, we can expect presence of the octupole fields in a synchrotron changes the betatron tune and also drives modes whose tunes are three times of the tune of the leading order solution, and the effects grow as the particles' oscillation amplitude increases.

3.1.5 Remarks on a Perturbation of an Arbitrary Order

From the discussions of the third and fourth order perturbations, we can see that a higher order perturbation includes effects of lower order perturbations. For a system with the intrinsic angular frequency ω_0, we can make the following general statement.

- A perturbation of an odd order $2n+1$ shifts the equilibrium point of the oscillations and also drives modes with angular frequencies $2n\omega_0$, $(2n-2)\omega_0$, …, and $2\omega_0$.

- A perturbation of an even order $2n$ changes the angular frequency to a new value ω and also drives modes with angular frequencies $(2n-1)\omega$, $(2n-3)\omega$, …, and 3ω.

When a system has perturbations of the first and nth ($n \geq 2$) orders, the combination produces perturbations of all the orders less than n. The equation of motion for this system is given by

$$\frac{d^2x}{dt^2} + \omega_0^2 x = -\kappa_1 - \frac{1}{(n-1)!}\kappa_n x^{n-1} \ , \tag{3.24}$$

where κ_1 and κ_n are parameters to describe the strengths of the first and nth order perturbations. If we expand $x(t)$ around κ_1/ω_0^2, such as $x(t) = -\kappa_1/\omega_0^2 + \bar{x}(t)$, the equation of motion for the difference $\bar{x}$ is given by

$$\frac{d^2\bar{x}}{dt^2} + \omega_0^2 \bar{x} = -\frac{\kappa_n}{(n-1)!}\left(\bar{x} - \frac{\kappa_1}{\omega_0^2}\right)^{n-1} \ . \tag{3.25}$$

We note that the right-hand-side includes the terms of all the powers of $\bar{x}$ up to $n-1$. Hence, the nth order perturbation combined with the first order perturbation effectively produces perturbations of all the orders up to nth. In accelerator physics, this phenomenon is called feeddown effect: when a particle passes off center through an nth order magnet, it feels multipole fields of all the order up to nth. For instance, when a particle goes through a quadrupole magnet and the particle's mean position is off the center of the magnet, the quadrupole magnet produces an effective dipole field and bends the mean trajectory of the particle (Figure 3.3). The strength of this effective dipole fields depend on the mean offset from the center of the quadrupole magnet. Such an offset could be caused by the orbit change due to dipole field errors or misalignments of the quadrupole magnets.

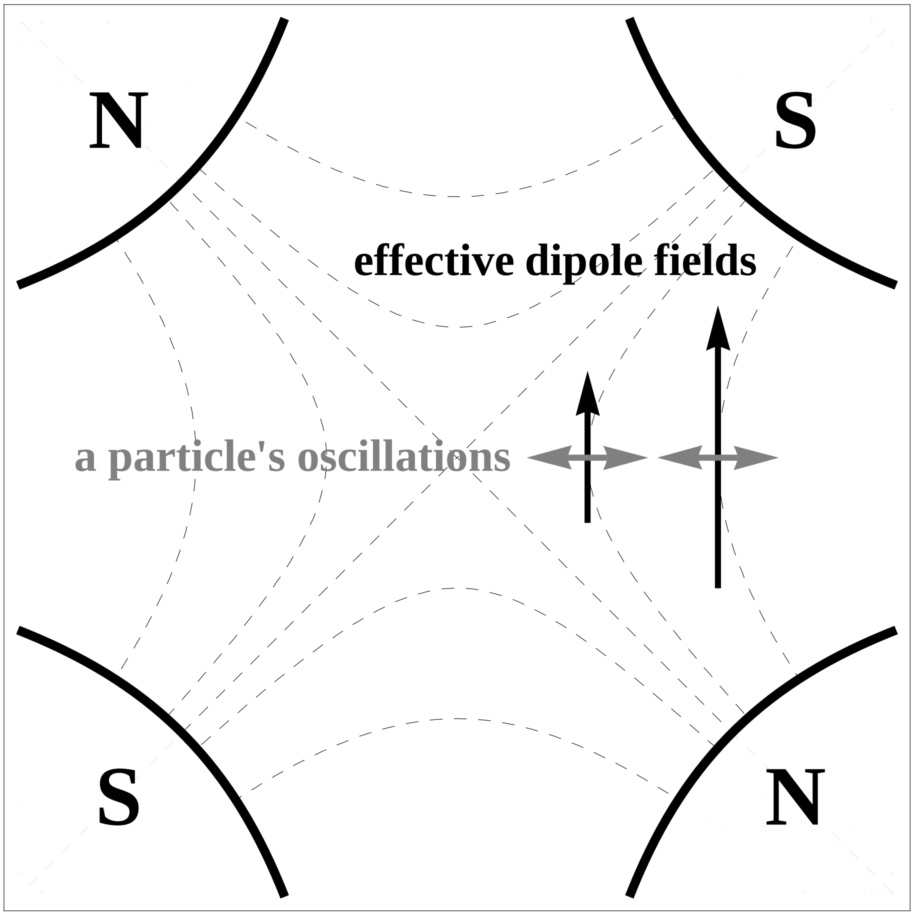

Figure 3.3: A feeddown dipole field produced by a quadrupole magnet. When a particle's mean position is off the center of the quadrupole magnet, the quadrupole magnet produces an effective dipole field whose strength depends on the mean offset from the center of the magnet.

3.1.6 Summary

In this section, we have reviewed particle motion in a simple oscillatory system, which is under the perturbations of polynomial forces. By choosing perturbations with similar mathematical forms as perturbative magnetic fields in a synchrotron, we have derived a relatively clear understanding about the effects due to such perturbative fields, which are summarized in Table 3.1.

3.2 Perturbations to Betatron Oscillations

In this chapter, so far, we have studied classical systems of simple oscillators, which have perturbative forces similar to the forces of the magnets in the synchrotron. In this section, we discuss various effects of perturbative magnetic fields on beam particles' motions. As will be seen, such considerations will reproduce the results in Table 3.1. In particular, we study perturbations due to a single thin magnetic element. From Hill's equation (Equation 2.26), the equation of motion in such a case is given by

$$x'' + K_0(s)x = -\frac{\mathit{\Delta} B_y(x, \tilde{s}_0)\ell}{(B\rho)} \sum_{\bar{n}=-\infty}^{\infty} \delta(s - \tilde{s}_0 - \bar{n}C) \ , \tag{3.26}$$

where K_0 is the effective gradient of the unperturbed case, $\mathit{\Delta} B_y(x, \tilde{s}_0)$ is magnetic field of the perturbation, $\tilde{s}_0$ $(0 \leq \tilde{s}_0 < C)$ is location of the perturbation, ℓ is longitudinal length of the perturbation, $\bar{n}$ is a dummy variable of the summation, C is circumference of the synchrotron and $\delta(s - \tilde{s}_0 - \bar{n}C)$ is the Dirac δ-function. We note that the Dirac δ-function indicates the perturbative field is in a thin region and the summation describes periodicity of the system. The Dirac δ-functions summed over all the revolution number is referred to as periodic δ-function. In the following, from Equation 2.33, we denote the solution of homogeneous Hill's equation by

$$x_0(s) = A\sqrt{\beta_0(\tilde{s})}\cos(2\pi\nu_0 n + \psi_0(\tilde{s}) + \chi) \ , \tag{3.27}$$

where $\beta_0(s)$, $\psi_0(s)$, and ν_0 are the amplitude function, phase advance, and tune when there is no perturbation. Discussions of the simple classical oscillators indicate that the perturbative fields may change these parameters and may also add additional terms to this solution x_0.

3.2.1 Dipole Field Errors

In a synchrotron, dipole field errors produce first order perturbations to the betatron oscillations. Major sources of the dipole field errors are construction errors of the magnets, errors of magnets' power supplies, tilts of the dipole magnets, and the feeddown effects of higher order magnets such as a misaligned quadrupole magnet in Figure 3.3. From the discussion of the simple oscillator with the first order perturbation, in Section 3.1.1, we expect the dipole field errors change the mean trajectories of the beam particles.

Simulation of a FODO Lattice System with a Dipole Error

To study influence of a thin dipole field error, we again use the simulation of the FODO lattice system, which we discussed about in Section 2.2.3. Figure 3.4 shows simulated trajectory of a particle in a system of FODO lattices with a dipole field error. In the figure, a thin dipole field error is at the location of the focusing lens F_5. When the particle goes through a thin dipole field, the angle is changed by a constant value, in this case 10 μrad, but the position remains the same. Red and blue lines represent the particle's trajectories with and without the dipole field error. The green line represents the average of

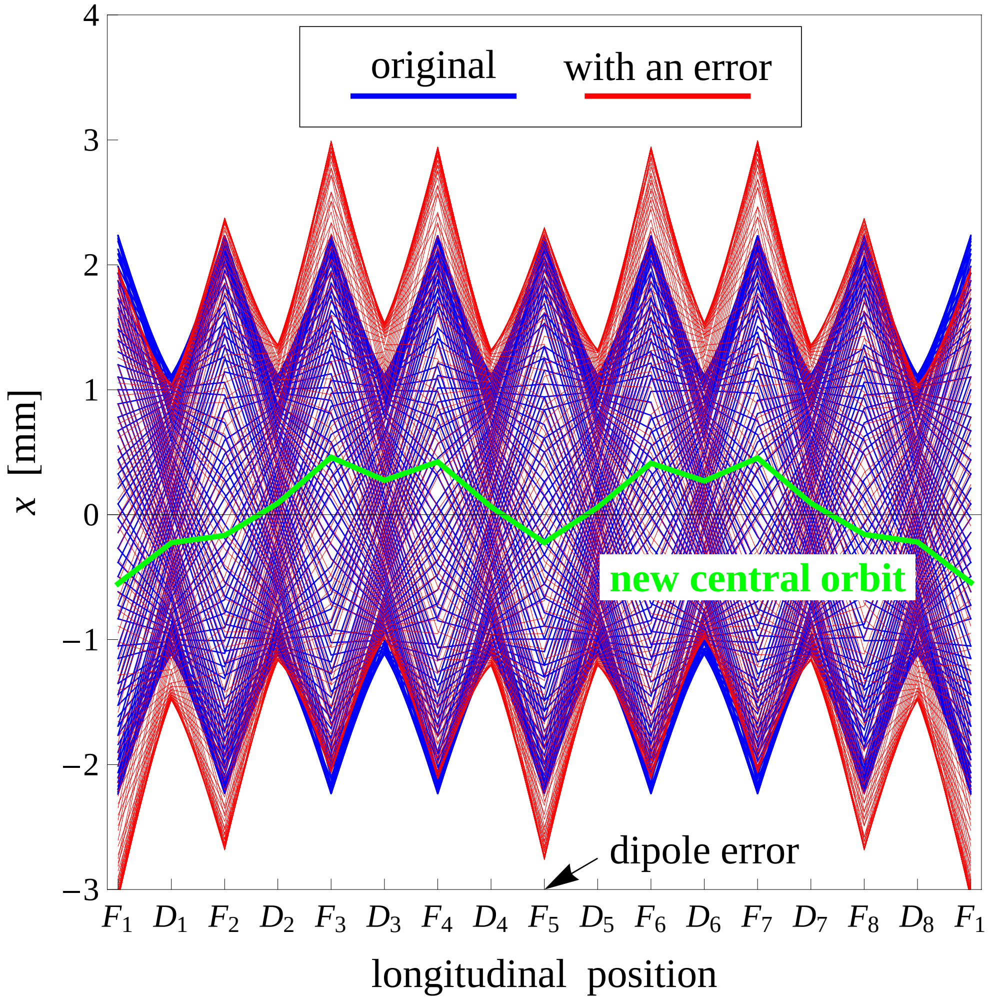

Figure 3.4: A simulation of a particle's trajectory in a system of the FODO lattices with a dipole field error. When there is a dipole field error, the particle undergoes betatron oscillations around a new central orbit (green line). The new central orbit oscillates around the synchrotron but undergoes a sudden change at the location of the error.

the red lines. The green line indicates that, under the influence of the thin dipole field error, the beam particles have a new central orbit and they undergo betatron oscillations around this new central orbit. The situation is similar to the discussion in Section 3.1.1. The change of the central orbit is a periodic function of the longitudinal position, oscillating roughly one and half times with a sudden change at the location of the dipole field error. The deviation of the new central orbit from $x = 0$ tends to be large at locations where the betatron amplitude function $\beta(s)$ is large. We note that such a change of the central orbit can be directly measured by BPM's. Hence, compared to the other higher order perturbations, dipole field errors could be found and corrected relatively easily.

Solution Using Green's Functions of Hill's Equation

Here, we discuss mathematical details of the central orbit change due to a thin dipole field error. When there is a thin dipole field error, from Equation 3.26, the equation of motion is given by

$$x'' + K_0(s)x = -\theta \sum_{\bar{n}=-\infty}^{\infty} \delta(s - \tilde{s}_1 - \bar{n}C) \ , \tag{3.28}$$

where $\theta = \Delta B_{y,0}(\tilde{s}_1)\ell/(B\rho)$ is bend angle of the dipole field error located at $\tilde{s}_1$ $(0 \leq \tilde{s}_1 < C)$. One way to solve this equation is to use the matrix formalism discussed in Section 2.3.4 (see for instance [7]). Here, instead, we review a solution using Green's function of Hill's equation. By using the Green's function, calculation of the orbit change becomes straight forward. The Green's function is also useful later when we calculate driven motion of the beam particles in Section 6.1.

The retarded Green's function of Hill's equation, $G_\infty(s|s_0)$, is defined by the following differential equation:

$$G''_{\infty}(s|s_0) + K_0(s)G_{\infty}(s|s_0) = \delta(s - s_0) \ . \tag{3.29}$$

We can construct the retarded Green's function $G_{\infty}(s|s_0)$ from the solution of homogeneous Hill's equation [33]:

$$G_{\infty}(s|s_0) = \Theta(s - s_0)\sqrt{\beta_0(s)\beta_0(s_0)}\,\sin(\psi_0(s|s_0)) \ , \tag{3.30}$$

where $\Theta(s)$ is the Heaviside step function:

$$\Theta(s) = \begin{cases} 0 & (s < 0) \\ \frac{1}{2} & (s = 0) \\ 1 & (s > 0) \end{cases} \ . \tag{3.31}$$

We note that derivative of the Heaviside step function is the Dirac δ-function:

$$\frac{d\Theta(s)}{ds} = \delta(s) \ . \tag{3.32}$$

Given this property of the Heaviside step function, it is a straight forward calculation to check the function in Equation 3.30 satisfies Equation 3.29. When the external force is a periodic function, like the case of the thin dipole field error in Equation 3.28, the equation of motion can be also solved by using periodic Green's function $G_C(s|s_0)$, defined by

$$G''_C(s|s_0) + K_0(s)G_C(s|s_0) = \sum_{\bar{n}=-\infty}^{\infty} \delta(s - s_0 - \bar{n}C) \ , \tag{3.33}$$

where the subscript C denotes the period of the system. The periodic Green's function $G_C(s|s_0)$ is constructed with the retarded Green's function $G_{\infty}(s|s_0)$ [34]:

$$\begin{aligned} G_C(s|s_0) &= \sum_{\bar{n}=-\infty}^{\infty} G_{\infty}(s|s_0 + \bar{n}C) \\ &= \frac{\sqrt{\beta_0(\tilde{s})\beta_0(\tilde{s}_0)}}{2\sin(\pi\nu_0)} \cos(\psi_0(\tilde{s}|\tilde{s}_0) - \pi\nu_0 \,\mathrm{sgn}(\tilde{s} - \tilde{s}_0)) \ , \end{aligned} \tag{3.34}$$

where sgn(s) is sign function defined by

$$\operatorname{sgn}(s) = \begin{cases} -1 & (s < 0) \\ 0 & (s = 0) \\ 1 & (s > 0) \end{cases} \quad , \tag{3.35}$$

and $\tilde{s}$ and $\tilde{s}_0$ denote s and s_0 modulo the circumference C as in Section 2.3.2. From Equation 3.34, the periodicity of $G_C(s|s_0)$, $G_C(s|s_0) = G_C(s + C|s_0) = G_C(s|s_0 + C)$, can be easily checked.

Given the Green's functions, the particular solution of Equation 3.28, $x_1(s)$, is calculated from the following integral:

$$\begin{aligned} x_1(s) &= \int_{-\infty}^{\infty} ds_0 \, G_\infty(s|s_0) \left[-\theta \sum_{\bar{n}=-\infty}^{\infty} \delta(s_0 - \tilde{s}_1 - \bar{n}C) \right] \\ &= \int_0^C ds_0 \, G_C(s|s_0) \left[-\theta \delta(\tilde{s}_0 - \tilde{s}_1) \right] \\ &= -\frac{\theta \sqrt{\beta_0(\tilde{s}_1)\beta_0(\tilde{s})}}{2 \sin(\pi\nu_0)} \cos(\psi_0(\tilde{s}|\tilde{s}_1) - \pi\nu_0 \operatorname{sgn}(\tilde{s} - \tilde{s}_1)) \ . \end{aligned} \tag{3.36}$$

We note that, when we use the retarded Green's function, we have to integrate the influence of the dipole field error from $-\infty$ to ∞. Whereas, when we use the periodic Green's function, the same solution is given by the integral within one period. From Equations 3.33 and 3.36, the orbit change due to a thin dipole field error has the same functional form as the periodic Green's function. Hence, the properties of the new central orbit seen in Figure 3.4, such as the dependence of the amplitude function and the sudden change at the location of the source, come from the periodic Green's function $G_C(s|s_0)$. In Equation 3.36, the sudden change of the new central orbit at the error location is described by the term $[-\pi\nu_0 \operatorname{sgn}(\tilde{s} - \tilde{s}_1)]$. We will see the similar sudden changes of parameters at the error sources in the cases of the higher order perturbations, as well. We note that the new central orbit is inversely proportional to $\sin(\pi\nu_0)$. Hence, the orbit change gets larger when the tune ν gets close to an integer. In bad cases, we may lose particles if the new central orbit is deviated too far from the ideal one. This is an example of phenomenon referred to as resonance and is due to the periodicity of the system. The resonance driven by the dipole field errors are referred to as integer resonance or the first order resonance. When we design and operate synchrotrons, we avoid the tune being too close to integers.

Multipole Dipole Field Errors

In a real synchrotron consisting of many elements, there are usually multiple number of errors. When there are N_1 dipole field errors at locations of $\tilde{s}_{1,j}$ ($j = 1, 2, \ldots, N_1$) and their bend angles are given $\theta_j = \mathit{\Delta} B_{y,0}(\tilde{s}_{1,j})\ell/(B\rho)$, the equation of motion (Equation 3.28) is modified to

$$x'' + K_0(s)x = -\sum_{j=1}^{N_1} \theta_j \sum_{\bar{n}=-\infty}^{\infty} \delta(s - \tilde{s}_{1,j} - \bar{n}C) \ . \tag{3.37}$$

The particular solution of this equation is superposition of the orbit changes due to all the dipole field errors. From Equation 3.36,

$$\begin{aligned} x_1(s) &= -\sum_{j=1}^{N_1} \frac{\theta_j \sqrt{\beta_0(\tilde{s}_{1,j})\beta_0(\tilde{s})}}{2\sin(\pi\nu_0)} \cos(\psi_0(\tilde{s}|\tilde{s}_{1,j}) - \pi\nu_0 \operatorname{sgn}(\tilde{s} - \tilde{s}_{1,j})) \\ &\to -\int_0^C d\tilde{s}_1 \, \frac{\mathit{\Delta} B_{y,0}(\tilde{s}_1)\sqrt{\beta_0(\tilde{s}_1)\beta_0(\tilde{s})}}{2(B\rho)\sin(\pi\nu_0)} \cos(\psi_0(\tilde{s}|\tilde{s}_1) - \pi\nu_0 \operatorname{sgn}(\tilde{s} - \tilde{s}_1)) \ . \end{aligned} \tag{3.38}$$

Here, the second expression is useful for a case when the dipole field errors are distributed almost continuously. This equation indicates that, when there are multiple dipole field errors, the net effect is determined by the error strengths, the amplitude functions at the error locations, and the relative phase differences among the error locations.

3.2.2 Quadrupole Field Errors

In a synchrotron, quadrupole field errors produce second order perturbations to the betatron oscillations. The sources of the quadrupole field errors are construction errors of the magnets, errors of magnets' power supplies, and the feeddown effects of higher order magnets. From the discussion of the second order perturbation to a simple classical oscillator in Section 3.1.2, we can predict the quadrupole field errors change the betatron tune. In addition, because of the correlation between the amplitude function and phase advance given in Equation 2.31, the quadrupole field errors change the amplitude function of a synchrotron, as well.

Tune Shift

Here, we discuss the change of the betatron tune (referred to as tune shift in accelerator physics) due to a thin quadrupole field error. When there is a thin quadrupole field error, the equation of motion is given by

$$x'' + K_0(s)x = -qx \sum_{\bar{n}=-\infty}^{\infty} \delta(s - \tilde{s}_2 - \bar{n}C) \ , \tag{3.39}$$

where $\tilde{s}_2$ $(0 \leq \tilde{s}_2 < C)$ is location of the error and $q = \mathit{\Delta} B_{y,1}\ell/(B\rho)$ is the effective strength of the quadrupole field error. From Equations 2.7 and 2.8, the error corresponds to the transfer matrix

$$\mathbf{M}_q = \begin{pmatrix} 1 & 0 \\ -q & 1 \end{pmatrix} \ . \tag{3.40}$$

Suppose the single turn transfer matrices of the location $\tilde{s}_2$ are $\mathbf{M}_0(\tilde{s}_2 + C|\tilde{s}_2)$ without this quadrupole field error and $\mathbf{M}(\tilde{s}_2 + C|\tilde{s}_2)$ with this quadrupole field error. With the transfer matrix of the quadrupole field error $\mathbf{M}_q$, these two matrices are related by

$$\mathbf{M}(\tilde{s}_2 + C|\tilde{s}_2) = \mathbf{M}_0(\tilde{s}_2 + C|\tilde{s}_2)\mathbf{M}_q \ . \tag{3.41}$$

From Equation 2.45, the matrix elements of $\mathbf{M}_0(\tilde{s}_2 + C|\tilde{s}_2)$ and $\mathbf{M}(\tilde{s}_2 + C|\tilde{s}_2)$ are given by

$$\begin{aligned} &\mathbf{M}_0(\tilde{s}_2 + C|\tilde{s}_2) \\ &\quad = \begin{pmatrix} \cos(2\pi\nu_0) + \alpha_0(\tilde{s}_2)\sin(2\pi\nu_0) & \beta_0(\tilde{s}_2)\sin(2\pi\nu_0) \\ -\gamma_0(\tilde{s}_2)\sin(2\pi\nu_0) & \cos(2\pi\nu_0) - \alpha_0(\tilde{s}_2)\sin(2\pi\nu_0) \end{pmatrix} \end{aligned} \tag{3.42}$$

and

$$\begin{aligned} &\mathbf{M}(\tilde{s}_2 + C|\tilde{s}_2) \\ &\quad = \begin{pmatrix} \cos(2\pi\nu) + \alpha(\tilde{s}_2)\sin(2\pi\nu) & \beta(\tilde{s}_2)\sin(2\pi\nu) \\ -\gamma(\tilde{s}_2)\sin(2\pi\nu) & \cos(2\pi\nu) - \alpha(\tilde{s}_2)\sin(2\pi\nu) \end{pmatrix} \ , \end{aligned} \tag{3.43}$$

where $\beta_0()$, $\alpha_0(s)$, $\gamma_0(s)$, and ν_0 are the Courant-Snyder parameters and tune without this quadrupole field error and $\beta(s)$, $\alpha(s)$, $\gamma(s)$, and ν are those under the influence of this quadrupole field error. By substituting these two equations into Equation 3.41, we can get the relations among the old and new Courant-Snyder parameters and tunes. By comparing the traces of the both sides in Equation 3.41, we get

$$\cos(2\pi\nu) = \cos(2\pi\nu_0) - \frac{1}{2}q\beta_0(\tilde{s}_2)\sin(2\pi\nu_0) \ . \tag{3.44}$$

Hence, up to first order of the effective quadrupole strength q, the tune shift $\varDelta\nu$ is given by

$$\varDelta\nu \equiv \nu - \nu_0 \simeq \frac{q\beta_0(\tilde{s}_2)}{4\pi} \ . \tag{3.45}$$

We note that, when the intrinsic tune ν_0 is close to an integer or a half-integer, the new tune determined by Equation 3.44 may not be real, depending on magnitude and sign of $q\beta_0(\tilde{s}_2)$. If the quadrupole field error is large enough to make the new tune imaginary, the particle's motion becomes unstable. Such instability driven by quadrupole field errors are referred to as half-integer resonance or second order resonance. Not only when the tune is exactly an integer or a half integer, there are ranges of the initial tune around integers or half-integers, in which the new tune become imaginary and the particle's motion becomes unstable. Such a region in space of the tune is referred to as a stopband. The width of the stopband is determined by strengths of errors.

So far, we have discussed that the particle's motion may be unstable when the tune is close to an integer of a half-integer. If we consider higher order perturbations, there are more resonances. We also note that, due to a finite spread of longitudinal momenta, particles within the beam have slightly different tunes. Hence, the significance of the quadrupole field errors lies in that, even if we design a synchrotron so that the tune is off the dangerous values such as integers and half-integers, these errors may shift the tunes of some particles into a undesired region, making those particles' motions unstable. Measurement and control of the tune is crucial for stability of the beam in a synchrotron.

When there are N_2 quadrupole field errors, whose locations and effective gradients are given by $\tilde{s}_{2,j}$ $(j = 1, 2, \ldots, N_2)$ and $q_j = \mathit{\Delta} B_{y,1}(\tilde{s}_{2,j})\ell/(B\rho)$, up to first order of the effective gradients q_j, the net tune shift is a superposition of the tune shifts due to all the quadrupole errors:

$$\mathit{\Delta}\nu \simeq \sum_{j=1}^{N_2} \frac{q_j \beta_0(\tilde{s}_{2,j})}{4\pi} \rightarrow \int_0^C d\tilde{s}_2 \, \frac{\mathit{\Delta}B_{y,1}(\tilde{s}_2)\beta_0(\tilde{s}_2)}{4\pi(B\rho)} \ . \tag{3.46}$$

In contrast to the central orbit change due to multiple dipole field errors, given in Equation 3.38, the net tune shift is determined by this simple superposition is independent of the relative phase differences among the errors.

Simulation of a FODO Lattice System with a Quadrupole Error

Compared to the simple harmonic oscillations, one difference of the betatron oscillations is the correlation between the amplitude and phase, given by Equation 2.31. Because of this correlation, the quadrupole field error, causing the tune shift, changes the amplitude function and also phase advance. This can be foreseen from the equation to determine the amplitude function, Equation 2.30. The quadrupole field error modified the effective gradient $K_0(s)$ and, hence, changes the amplitude function which is determined from $K_0(s)$. To study such influences of the quadrupole field error on the beam particles, we again use the simulation of the FODO lattice system, similar to those in Section 2.2.3.

Figure 3.5 shows a simulation of a particle's trajectory in a system consisting of FODO lattices, where the strength of the quadrupole magnet F_5 is intentionally decreased by 5%. Red and blue lines represent the trajectories with and without the influence of this quadrupole error, when the particle starts from the same initial condition. The central orbit remains at $x = 0$ but the envelope of the particle's positions is modified, indicating the change of the amplitude function.

The middle plot of Figure 3.5 shows the normalized change of the amplitude function as a function of the longitudinal position, $(\mathit{\Delta}\beta/\beta_0)(\tilde{s}) \equiv$

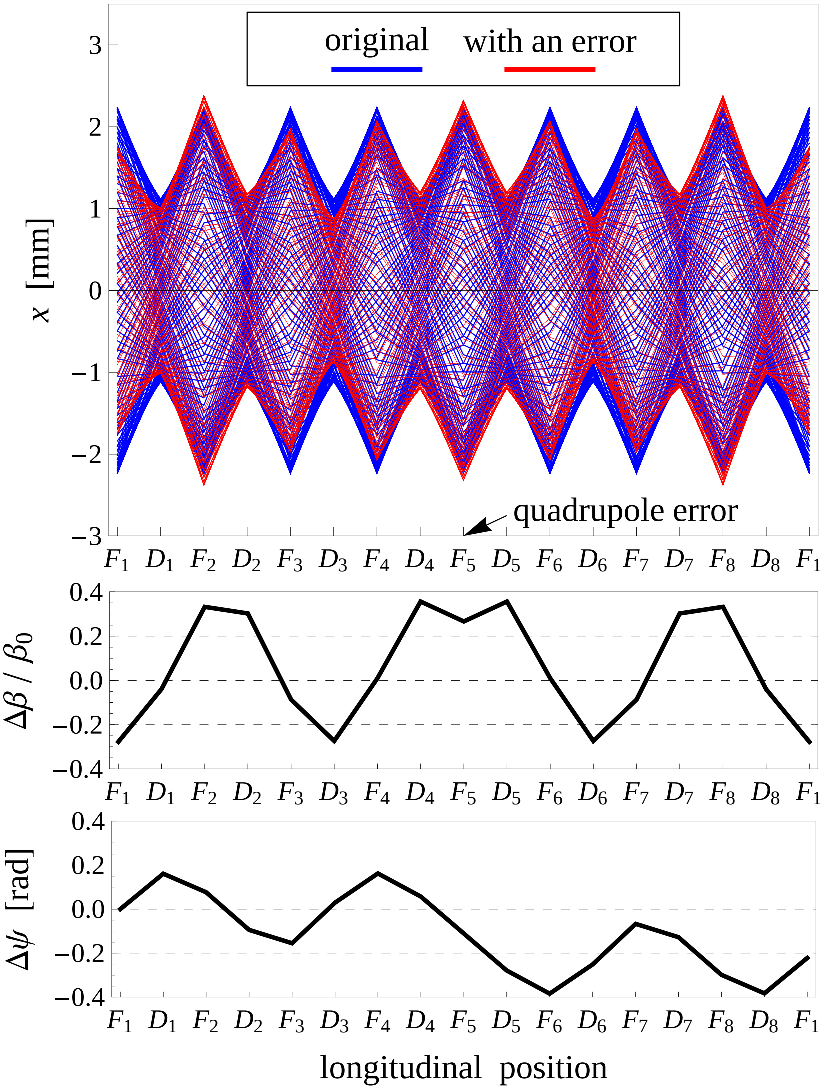

Figure 3.5: A simulation of a particle's trajectory in a system of the FODO lattices with a quadrupole field error. A quadrupole field error changes the amplitude function and, hence, changes the envelope of the trajectory. In the case of multiple particles, quadrupole field errors change the transverse beam sizes. The middle and bottom plots show the normalized change of the amplitude function $(\Delta\beta/\beta_0)(\tilde{s})$ and the change of the phase advance $\Delta\psi(\tilde{s})$. Much like the central orbit change due to dipole field errors, these quantities oscillate along the system. We note that $(\Delta\beta/\beta_0)(\tilde{s})$ undergo a sudden change at the error location. Whereas, $\Delta\psi(\tilde{s})$ is shifted by a constant value at the error location.

$(\beta(\tilde{s}) - \beta_0(\tilde{s}))/\beta_0(\tilde{s})$. This quantity is referred to as beta-beat. The beta-beat $(\mathit{\Delta}\beta/\beta_0)(\tilde{s})$ oscillates along the system and undergoes a sudden change at the location of the quadrupole error. We note that the number of the oscillations of the beta-beat is about three[2]. As we discussed in Section 2.2.3, the maximum deviation of a single particle can be interpreted as the outermost particle within the beam, determining the beam size. Hence, the quadrupole field errors alter the beam size and may influence the luminosity of the collider.

The bottom plot of Figure 3.5 shows the change of the phase advance as a function of the longitudinal position, $\mathit{\Delta}\psi(\tilde{s}) \equiv \psi(\tilde{\tilde{s}}) - \psi_0(\tilde{s})$. Here, the reference point of the phase advance is in front of the quadrupole F_1. Similar to the beta-beta $(\mathit{\Delta}\beta/\beta_0)(\tilde{s})$, we call the quantity $\mathit{\Delta}\psi(\tilde{s})$ phase-beat. Much like the beta-beat, the phase-beat oscillates along the system and the number of the oscillations is roughly three in this simulation. In contrast to the beta-beat, the phase-beat has a constant difference between its upstream and downstream values.

We note that these changes of the amplitude function and phase advance cannot be measured with BPM's in a naive manner. To measure such changes, we have to excite and observe a certain mode of particles' motion. An AC dipole is one of such a tool to excite a mode of beam particles. This makes a quite contrast to the change of the central orbit due to dipole field errors, which can be directly measured with BPM's. We discuss the measurement based on the excitation of the beam particles' motion in Chapter 4.

---

[2] Behaviors of the beta-beat, such as the sudden change at the error location, are quite similar to the behaviors of the central orbit change due to a dipole field error, seen in Figure 3.4. However, the number of the oscillations along the system is twice for the beta-beat, compared to the central orbit change.

Beta-beat and Phase-beat

In this section, we discuss mathematical expressions of the beta-beat $(\Delta\beta/\beta_0)(\tilde{s})$ and phase beat $\Delta\psi(\tilde{s})$, due to a thin quadrupole field error. Some equations in this section are also used when we discuss driven oscillations of the beam particles in Chapter 6.

When we derived the tune shift due to a thin quadrupole field error, we compared the single turn transfer matrices of the error location with and without the influence of the quadrupole field error, $\mathbf{M}(\tilde{s}_2+C|\tilde{s}_2)$ and $\mathbf{M}_0(\tilde{s}_2+C|\tilde{s}_2)$ given in Equations 3.42 and 3.43. From these two matrices, we can also get a relation between the perturbed and unperturbed amplitude function of the error location, $\beta(\tilde{s}_2)$ and $\beta_0(\tilde{s}_2)$. By repeating the same process at all the locations in the synchrotron[3], we get a relation between the perturbed and unperturbed amplitude functions of an arbitrary location $\tilde{s}$:

$$\begin{aligned}&\beta(\tilde{s})\sin(2\pi\nu)\\ &=\begin{cases}\beta_0(\tilde{s})\big[\sin(2\pi\nu_0)-q\beta_0(\tilde{s}_2)\sin(\psi_0(\tilde{s}+C|\tilde{s}_2))\sin(\psi_0(\tilde{s}_2|\tilde{s}))\big] & (\tilde{s}<\tilde{s}_2)\\ \beta_0(\tilde{s})\big[\sin(2\pi\nu_0)-q\beta_0(\tilde{s}_2)\sin(\psi_0(\tilde{s}|\tilde{s}_2))\sin(\psi_0(\tilde{s}_2+C|\tilde{s}))\big] & (\tilde{s}>\tilde{s}_2)\end{cases}.\end{aligned} \tag{3.47}$$

From this equation and Equation 3.44, giving the new tune ν, up to first order of the effective quadrupole strength q, the beta-beat is given by

$$\left(\frac{\Delta\beta}{\beta_0}\right)(\tilde{s})\simeq-\frac{q\beta_0(\tilde{s}_2)}{2\sin(2\pi\nu_0)}\cos(2\psi_0(\tilde{s}|\tilde{s}_2)-2\pi\nu_0\,\mathrm{sgn}(\tilde{s}-\tilde{s}_2))\ . \tag{3.48}$$

---

[3] Suppose we know the unperturbed Courant-Snyder parameters of an arbitrary location, $\beta_0(s)$, $\alpha_0(s)$, and $\gamma_0(s)$. By propagating these two matrices to the other location $\tilde{s}$ with Equation 2.50, we can calculate the perturbed and unperturbed single turn transfer matrices of the new location $\tilde{s}$, $\mathbf{M}(\tilde{s}+C|\tilde{s})$ and $\mathbf{M}_0(\tilde{s}+C|\tilde{s})$. Relations among the perturbed and unperturbed Courant-Snyder parameters are determined by comparing the matrix elements of these two matrices.

Here, in the second expression, we rewrote $q\beta_0(\tilde{s}_2)$ with the tune shift Δ by using Equation 3.45. The equation indicates that, when the betatron tune is close to an integer or a half-integer, a quadrupole field error may diverge particle motion in the synchrotron. This is another aspect of the second order resonance. The sudden change of the beta-beat at the error location, seen in Figure 3.5, is due to the term $[-2\pi\nu_0\,\mathrm{sgn}(\tilde{s}-\tilde{s}_2)]$ in the phase. We also note that the phase of the the beta-beat is twice of the central orbit change in Equation 3.36. This is from the orders of the perturbations.

The new betatron phase advance including the influence of the quadrupole field error, $\psi(\tilde{s}|\tilde{s}_0)$, can be calculated from the definition of the phase advance, Equation 2.31:

$$\begin{aligned}\psi(\tilde{s}|\tilde{s}_0) &= \int_{\tilde{s}_0}^{\tilde{s}} \frac{d\bar{s}}{\beta(\bar{s})} \\ &\simeq \int_{\tilde{s}_0}^{\tilde{s}} \frac{d\bar{s}}{\beta_0(\bar{s})}\left[1-\left(\frac{\Delta\beta}{\beta_0}\right)(\bar{s})\right] \\ &= \psi_0(\tilde{s}|\tilde{s}_0) - \int_{\psi_0(\tilde{s}_0|\tilde{s}_2)}^{\psi_0(\tilde{s}|\tilde{s}_2)} d\bar{\psi}\left(\frac{\Delta\beta}{\beta_0}\right)(\bar{s}(\bar{\psi}))\ , \end{aligned} \tag{3.49}$$

where, in the last expression, we used the relation $\psi_0(\tilde{s}|\tilde{s}_0)=\int_{\tilde{s}_0}^{\tilde{s}} d\bar{s}/\beta_0(\bar{s})$ and changed the dummy variable from the longitudinal position $\bar{s}$ to the phase $\bar{\psi}\equiv\psi_0(\bar{s}|\tilde{s}_2)$. By performing this integral with the explicit form of the beta-beat, given in Equation 3.48, the phase-beat due the quadrupole field error, $\Delta\psi(\tilde{s}|\tilde{s}_0)\equiv\psi(\tilde{s}|\tilde{s}_0)-\psi_0(\tilde{s}|\tilde{s}_0)$, is given by

$$\begin{aligned}\Delta\psi(\tilde{s}|\tilde{s}_0) = \frac{q\beta_0(\tilde{s}_2)}{4\sin(2\pi\nu_0)}&\big[\sin(2\psi_0(\tilde{s}|\tilde{s}_2)-2\pi\nu_0\,\mathrm{sgn}(\tilde{s}-\tilde{s}_2)) \\ &\qquad -\sin(2\psi_0(\tilde{s}_0|\tilde{s}_2)2\pi\nu_0\,\mathrm{sgn}(\tilde{s}_0-\tilde{s}_2))\big] \\ &+\frac{q\beta_0(\tilde{s}_2)}{4}\big[\mathrm{sgn}(\tilde{s}-\tilde{s}_2)-\mathrm{sgn}(\tilde{s}_0-\tilde{s}_2)\big]\ . \end{aligned} \tag{3.50}$$

We note that the amplitude of the phase-beat is half of the amplitude of the beta-beat. The term $\frac{1}{4}q\beta_0(\tilde{s}_2)[\cdots]$ make the step structure of the phase-beat between the upstream and downstream of the error location, seen in the simulation of Figure 3.5. From Equation 3.45, the step size $\frac{1}{2}q\beta_0(\tilde{s}_2)$ is equal to $2\pi\mathit{\Delta}\nu$. When we measure the phase advance and compared to the ideal case, such a step structure indicates the location of the quadrupole field error. These results are summarized in Table 3.1.

Remarks on the Solution Using the Perturbative Expansion

Here, we try to solve Equation 3.39 by expanding the position $x(s)$ around the solution of the homogeneous Hill's equation $x_0(s)$ (Equation 3.27): $x(s) \equiv x_0(s) + x_2(s)$. Up to the first order of the effective gradient q, the equation to determine $x_2(s)$ is given by

$$\begin{aligned} & x_2'' + K(s)x_2 \\ & \quad = -qx_0 \sum_{\bar{n}=-\infty}^{\infty} \delta(s - \tilde{s}_2 - \bar{n}C) \\ & \quad = -qA\beta_0(\tilde{s}_2)^{1/2} \sum_{\bar{n}=-\infty}^{\infty} \delta(s - \tilde{s}_2 - \bar{n}C)\cos(2\pi\nu_0\bar{n} + \psi_0(\tilde{s}_2) + \chi) \ . \end{aligned} \tag{3.51}$$

The right-hand-side is a driving force with the same tune as the intrinsic tune of the system ν_0. Such a force gives a diverging solution, indicating the perturbative solution must be modified. Procedure of the modified perturbative solution is similar to the case of the simple classical oscillator in Section 3.1.2. When we have such a driving force to give a diverging solution, we first change the tune, amplitude function, and phase advance based on Equations 3.45, 3.48and 3.50. After these changes, we can drop the term of the driving force from the equation to determine the higher order position. Another example will be discussed in Section 3.2.4

3.2.3 Sextupole Fields

In this section, we discuss third order perturbation to the betatron oscillations due to sextupole magnetic fields. So far, we have considered motion of a single particle within the beam, assuming the particle has the ideal longitudinal momentum. However, distribution of the beam particles' longitudinal momenta has a finite spread (momentum spread of the beam). Because the restoring force of the effective gradient $K_0(s)$ depends on the magnetic rigidity $(B\rho) = p/e$, such deviations of the longitudinal momenta cause the tune shifts and make distribution of the particles' tunes finite (tune spread of the beam). This phenomenon is referred to as Chromatic aberration (See for instance [7, 8]). In the synchrotrons, Sextupole magnets are used to compensate the tune spread due to the momentum spread. A synchrotron may also have sextupole fields due to errors. From the discussion of the simple classical oscillator in Section 3.1.3, we can expect that the sextupole fields change the central orbit and also drive modes whose tunes are twice of the intrinsic betatron tune.

The magnetic field of a sextupole magnet is given by

$$B_x(x, y) = B_{y,2}xy \tag{3.52}$$

$$B_y(x, y) = \frac{1}{2}B_{y,2}(x^2 - y^2) \; . \tag{3.53}$$

Schematic field lines of a sextupole magnet is shown in Figure 3.1(c). These equations indicate that a sextupole magnetic field couples motions in the two transverse planes. Here, we only consider the simplest case of $y = 0$ and, then, a sextupole magnet produces a force proportional to square of x in the horizontal plane. When there is a thin sextupole field, the equation of motion is given by

$$x'' + K_0(s)x = -\frac{1}{2}k_3 x^2 \sum_{\bar{n}=-\infty}^{\infty} \delta(s - \tilde{s}_3 - \bar{n}C) \ , \tag{3.54}$$

where $k_3 \equiv B_{y,2}\ell/(B\rho)$ is effective strength of the sextupole magnet and $\tilde{s}_3$ is location of the sextupole magnet. We again solve this equation perturbatively by expanding the position $x(s)$ around the solution of homogeneous Hill's equation, $x_0(s)$ in Equation 3.27, $x(s) \equiv x_0(s) + x_3(s)$. Up to the first order of the sextupole magnet's effective strength k_3, the equation to determine $x_3(s)$ is given by

$$\begin{aligned} & x_3'' + K_0(s)x_3 \\ & = -\frac{1}{2}k_3 x_0(s)^2 \sum_{\bar{n}=-\infty}^{\infty} \delta(s - \tilde{s}_3 - \bar{n}C) \\ & = -\frac{1}{4}k_3 A^2 \beta_0(\tilde{s}_3) \sum_{\bar{n}=-\infty}^{\infty} \delta(s - \tilde{s}_3 - \bar{n}C) \\ & \quad - \frac{1}{4}k_3 A^2 \beta_0(\tilde{s}_3) \sum_{\bar{n}=-\infty}^{\infty} \delta(s - \tilde{s}_3 - \bar{n}C) \cos(2\pi(2\nu_0)\bar{n} + 2\psi_0(\tilde{s}_3) + 2\chi) \ , \end{aligned} \tag{3.55}$$

where we used the formula in Equation 3.15 to rewrite $x_0(s)^2$. We note that the first term of the right-hand-side is effectively a thin dipole field error in Equation 3.28. From the solution of the thin dipole field error, Equation 3.36, and also the solution of the driven betatron oscillations discussed in Section

6.1, Equation 6.2, the full solution, $x(s) = x_0(s) + x_3(s)$, is given by

$$\begin{aligned} x(s) &= A\sqrt{\beta_0(\tilde{s})}\cos(2\pi\nu_0 n + \psi_0(\tilde{s}) + \chi) \\ &\quad - \frac{k_3 A^2 \beta_0(\tilde{s}_3)^{3/2}\sqrt{\beta_0(\tilde{s})}}{8\sin(\pi\nu_0)}\cos(\psi_0(\tilde{s}) - \psi_0(\tilde{s}_3) - \pi\nu_0\,\mathrm{sgn}(\tilde{s} - \tilde{s}_3)) \\ &\quad + \frac{k_3 A^2 \beta_0(\tilde{s}_3)^{3/2}\sqrt{\beta_0(\tilde{s})}}{16\sin(\pi\nu_0)} \\ &\qquad \times \cos(2\pi(2\nu_0)n + \psi_0(\tilde{s}) + \psi_0(\tilde{s}_3) + \pi\nu_0\,\mathrm{sgn}(\tilde{s} - \tilde{s}_3) + 2\chi) \\ &\quad - \frac{k_3 A^2 \beta_0(\tilde{s}_3)^{3/2}\sqrt{\beta_0(\tilde{s})}}{16\sin(3\pi\nu_0)} \\ &\qquad \times \cos(2\pi(2\nu_0)n - \psi_0(\tilde{s}) + 3\psi_0(\tilde{s}_3) + 3\pi\nu_0\,\mathrm{sgn}(\tilde{s} - \tilde{s}_3) + 2\chi)\,. \end{aligned} \tag{3.56}$$

Hence, similar to the case of the simple classical oscillator in 3.1.3, the sextupole changes the central orbit and drives modes with the tune $2\nu_0$. We note that the amplitude of the last mode is proportional to $1/\sin(3\pi\nu_0)$. Hence, the particle's position may diverge when the tune is close to the condition $3\nu_0 = N$, where N is an arbitrary positive integer. This is third order resonance. Because of the second and third terms, the sextupole magnet may also cause the first order resonance like dipole magnets. These results are summarized in Table 3.1.

3.2.4 Octupole Fields

Fourth order perturbations to the betatron oscillations are due to octupole magnetic fields. From the discussions of the simple classical oscillator in Section 3.1.4, we can expect that the octupole magnets cause the tune shift and drive a mode with a tune $3\nu_0$. Octupole magnets are employed in modern synchrotrons to compensate for beam instabilities due to coherent motion of beam particles, which can occur at very high intensity [35]. A synchrotron may also have octupole magnetic fields due to error.

The magnetic field of an octupole is given by

$$B_x(x,y) = \frac{1}{6}B_{y,3}(3x^2y - y^3) \tag{3.57}$$

$$B_y(x,y) = \frac{1}{6}B_{y,3}(x^3 - 3xy^2) \ , \tag{3.58}$$

whose schematic field lines are shown in Figure 3.1(d). We again consider only the horizontal motion and, then, an octupole field produces a force proportional to cube of x. The equation of motion is given by

$$x'' + K_0(s)x = -\frac{1}{6}k_4x^3 \sum_{\bar{n}=-\infty}^{\infty} \delta(s - \tilde{s}_4 - \bar{n}C) \ , \tag{3.59}$$

where $k_4 \equiv B_{y,3}\ell/(B\rho)$ is the effective octupole strength and $\tilde{s}_4$ is location of the octupole magnet. We again try to solve this equation perturbatively by expanding the position $x(s)$ around the solution of homogeneous Hills equation $x_0(s)$ in Equation 3.27: $x(s) \equiv x_0(s) + x_4(s)$. Up to the first order of the parameter k_4, the equation to determine the fourth order position $x_4(s)$ is given by

$$\begin{aligned} & x_4'' + K_0(s)x_4 \\ & = -\frac{1}{6}k_4x_0(s)^3 \sum_{\bar{n}=-\infty}^{\infty} \delta(s - \tilde{s}_4 - \bar{n}C) \\ & = -\frac{1}{8}k_4A^3\beta_0(\tilde{s}_4)^{3/2} \sum_{\bar{n}=-\infty}^{\infty} \delta(s - \tilde{s}_4 - \bar{n}C)\cos(2\pi\nu_0\bar{n} + \psi_0(\tilde{s}_4) + \chi) \\ & \quad - \frac{1}{24}k_4A^3\beta_0(\tilde{s}_4)^{3/2} \sum_{\bar{n}=-\infty}^{\infty} \delta(s - \tilde{s}_4 - \bar{n}C)\cos(2\pi(3\nu_0)\bar{n} + 3\psi_0(\tilde{s}_4) + 3\chi) \ , \end{aligned} \tag{3.60}$$

where we used a formula of the trigonometric function, Equation 3.19, to rewrite $x_0(s)^3$. The first term in right-hand-side is an external force with the intrinsic tune, indicating the perturbation changes the tune and the solution must be modified. By comparing this equation and Equation 3.51, the thin octupole field effectively behaves like a thin quadrupole field with the strength $q = \frac{1}{8} k_4 A^2 \beta_0(\tilde{s}_4)$, causing the tune shift, beta-beat, and phase beat. For instance, the tune shift due to this octupole field is given by

$$\mathit{\Delta}\nu = \frac{k_4 A^2 \beta_0(\tilde{s}_4)^2}{32\pi} \ . \tag{3.61}$$

The beta-beat and phase-beat due to this octupole field are also given by simply substituting the $q = \frac{1}{8} k_4 A^2 \beta_0(\tilde{s}_4)$ into 3.48, and 3.50. We note that these changes depend on the parameter A, which describes the oscillation amplitude of the leading order solution x_0. This indicates that, for the beam particles with different values of A, the octupole field acts differently and, for instance, cause the tune spread. Because of the changes of the tune, amplitude function, and phase advance, the leading order solution x_0 is modified to

$$x_0(s) = A\sqrt{\beta(\tilde{s})} \cos(2\pi\nu n + \psi(\tilde{s}) + \chi) \ , \tag{3.62}$$

where $\nu = \nu_0 + \mathit{\Delta}\nu$, $\beta(\tilde{s}) = \beta_0(\tilde{s})(1 + (\mathit{\Delta}\beta/\beta_0)(\tilde{s}))$, and $\psi(\tilde{s}) = \psi_0(\tilde{s}) + \mathit{\Delta}\psi(\tilde{s})$ denote the new tune, amplitude function, and phase advance. Once these changes are included, we can drop the first term in the right-hand-side of Equation 3.60 and, now, the fourth order position $x_4(s)$ is determined by

$$\begin{aligned} & x_4'' + K(s) x_4 \\ & \quad = -\frac{1}{24} k_4 A^3 \beta(\tilde{s}_4)^{3/2} \sum_{\bar{n}=-\infty}^{\infty} \delta(s - \tilde{s}_4 - \bar{n}C) \cos(2\pi(3\nu)\bar{n} + 3\psi(\tilde{s}_4) + 3\chi) \ , \end{aligned} \tag{3.63}$$

where $K(s) \equiv K_0(s) + \frac{1}{8} k_4 A^2 \beta_0(\tilde{s}_4) \sum_{-\infty}^{\infty} \delta(s - \tilde{s}_4 - \bar{n}C)$ is a modified effective gradient. Again, by using the solution of the driven betatron oscillations in

Equation 6.2, the full solution, $x(s) = x_0(s) + x_4(s)$, is given by

$$\begin{aligned}
x(s) = {} & A\sqrt{\beta(\tilde{s})}\cos(2\pi\nu n + \psi(\tilde{s}) + \chi) \\
& + \frac{k_4 A^3 \beta(\tilde{s}_4)^2 \sqrt{\beta(\tilde{s})}}{96\sin(2\pi\nu)} \\
& \quad \times \cos(2\pi(3\nu)n + \psi(\tilde{s}) + 2\psi(\tilde{s}_4) + 2\pi\nu\,\mathrm{sgn}(\tilde{s} - \tilde{s}_4) + 3\chi) \\
& - \frac{k_4 A^3 \beta(\tilde{s}_4)^2 \sqrt{\beta(\tilde{s})}}{96\sin(4\pi\nu)} \\
& \quad \times \cos(2\pi(3\nu)n - \psi(\tilde{s}) + 4\psi_0(\tilde{s}_4) + 4\pi\nu_0\,\mathrm{sgn}(\tilde{s} - \tilde{s}_4) + 3\chi) \ . \qquad (3.64)
\end{aligned}$$

Hence, similar to the case of the simple classical oscillator in 3.1.4, the octupole field changes the tune, amplitude function, phase advance, and also drives modes with the tune 3ν. We note that the amplitude of the last mode is proportional to $1/\sin(4\pi\nu)$. Hence, the octupole field may diverge the particle's position, if the tune is close to the condition $4\nu = N$, where N is an arbitrary positive integer. The phenomenon is referred to as fourth order resonance. Because of the second term, which is proportional to $1/\sin(2\pi\nu)$, the octupole magnet may also cause the second order resonance like quadrupole magnets. These results are summarized in Table 3.1.

3.3 Summary

In this section, we reviewed the perturbations to the ideal betatron oscillations, due to dipole field errors, quadrupole fields, sextupole fields, and octupole fields. We saw the quadrupole field errors change the amplitude function and may affect the luminosity of the collider. We also saw that perturbative fields drive certain oscillation modes associated to their orders. Similar to a classical driven oscillator, for a certain value of the tune, one of such mode may diverge and cause particle losses. Such phenomena are referred to as resonances. To avoid resonances, it is ideal to measure distribution of the perturbative fields and, if possible, make corrections. The features derived in this chapter and summarized in Table 3.1 will be crucial for their diagnosis. As seen in Chapters 6, 7, and 8, by exciting beam motion with an AC dipole, it is possible to observe the various phenomena in Table 3.1 due to the perturbative fields.

Chapter 4

Synchrotron Diagnostics with an AC Dipole

Perturbative magnetic fields in a synchrotron due to imperfections and higher order magnets, could degrade performance of a collider both in terms of its ultimate luminosity and stability of the circulating beam. It is therefore desired to constantly diagnose the synchrotron and find the sources of such perturbations. The simplest magnetic field error, namely, the dipole field error simulated in Figure 3.4 can change the particles' central orbit and such a change can be directly observed by using the BPM system in the synchrotron. The effects due to most other perturbative magnetic fields, however, cannot be detected directly with a BPM system, which measures only the average position, or central orbit, of the beam particle. Imperfections like quadrupole field error, simulated in Figure 3.5 may significantly perturb the collider's amplitude function and thus impact its luminosity (Equation 1.4), while leaving the central orbit unchanged. As indicated schematically in Figure 4.1, the difficulty in a synchrotron's diagnosis arises because the particles' betatron oscillations are

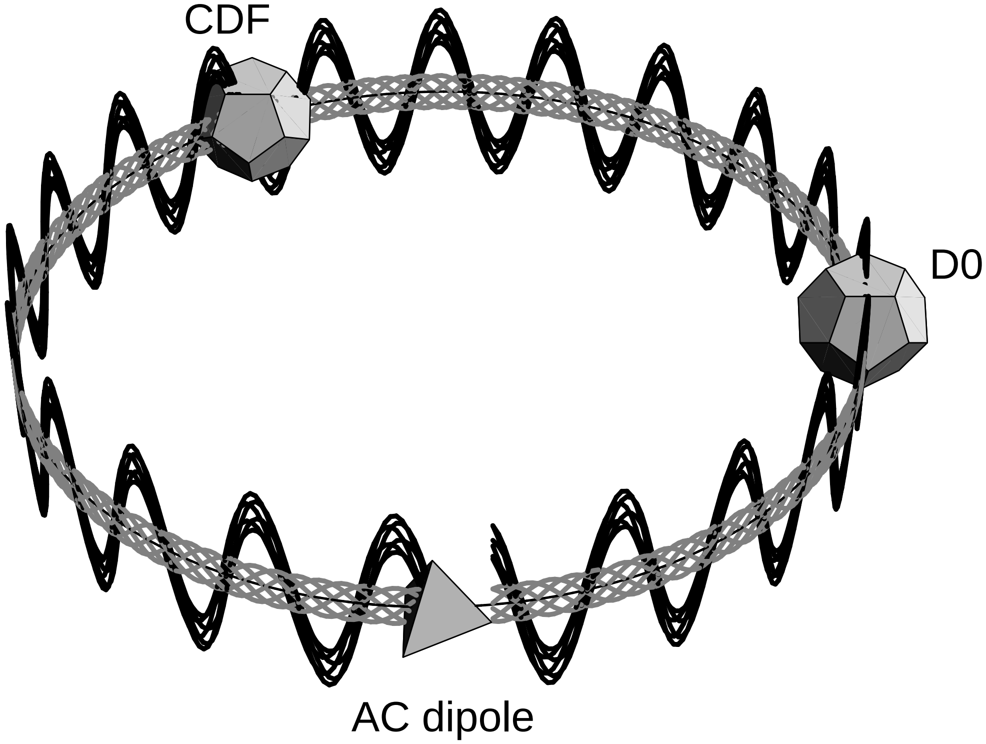

Figure 4.1: Incoherent free oscillations (gray) and excited coherent oscillations (black) of charged particles in the Tevatron. When coherent oscillations are excited, the beam centroid oscillates like a single particle and the oscillations can be observed by a BPM. An AC dipole is one of such tools to excite coherent oscillations of the beam.

"incoherent": each beam particle undergoes transverse oscillations around the synchrotron, which are at random phase differences compared to other beam particles. Thus, while the amplitude function may be perturbed, central orbit measured by a BPM system is unaffected.

The solution for successful diagnosis of synchrotron's errors, such as the beta-beat, is to excite coherent oscillations of the beam, as indicated in Figure 4.1. For instance, a kicker magnet, which produces an instantaneous dipole field, gives an impulse to the particles and excites all beam particles into transverse oscillations with the same initial phases, as the particles are perturbed by the kick and then subsequently given restoring forces of the quadrupole magnets (Figure 4.1). By observing such coherent oscillations, we can measure various parameters of the synchrotron. Examples of the measurements based on the kicked beam can be seen in Section 2.7 of [36]. Application of the kicker based measurements to the Tevatron is discussed in [37] and, in fact, such kicker magnet systems are widely used in high energy synchrotrons [38, 39, 40].

An AC dipole is another instrument to excite coherent beam oscillations for the synchrotron diagnosis [4]. It produces a sinusoidally-varying dipole field in phase with the beam particles' betatron oscillations and excites coherent driven oscillations of the beam. An AC dipole can produce sustained oscillations for many revolutions of the beam around the synchrotron, enabling more accurate measurements than oscillations available in fewer revolutions after an instantaneous kick. Perhaps equally important, the AC dipole field can be adiabatically ramped to full strength, introducing much smaller growth in the beam emittance and the beam size compared to the excitation of the kicker magnet. These properties of the AC dipole makes it a useful diagnostic tool of a synchrotron. AC dipoles have been employed in the AGS and RHIC in BNL [4, 14, 15], CERN SPS [16, 17], and FNAL Tevatron [18, 19, 20]. There is an ongoing project to develop AC dipoles for LHC as well [22]. In this chapter, we discuss the synchrotron diagnosis, mainly measurement of the betatron amplitude function, using the kicker and AC dipole magnets and compare these two magnets. Subsequent Chapters 6, 7, and 8 will demonstrate more advanced measurements using the AC dipole.

4.1 Kick Excitation

Simulation of a Perfectly Linear Synchrotron

A conventional and common method to excite coherent oscillations is to use a kicker magnet which produces an instantaneous dipole field and gives a single impulse to the particles. Figure 4.2 shows a simulation of the particles' motions after being excited by the kicker magnet, observed in the phase space at the location of the kicker magnet. In the figure, the black points represent individual beam particles and the white triangle represents the beam centroid (the center of the charges), whose position is the only quantity we can measure with a BPM. Before the excitation, each particle moves on an ellipse in this phase space, as described in Figures 2.9 and 2.11. The shape of the particles' phase space ellipse is determined by the Courant-Snyder parameters and, hence, all the particles are on ellipses with the same shape. However, areas of the ellipses and phases are different between particles and it is worth mentioning that the beam centroid stays at the same location, $(x, x') = (0, 0)$. When a particle is deflected by a thin magnetic element, its angle is changed but its position remains the same, and hence the particle are displaced vertically

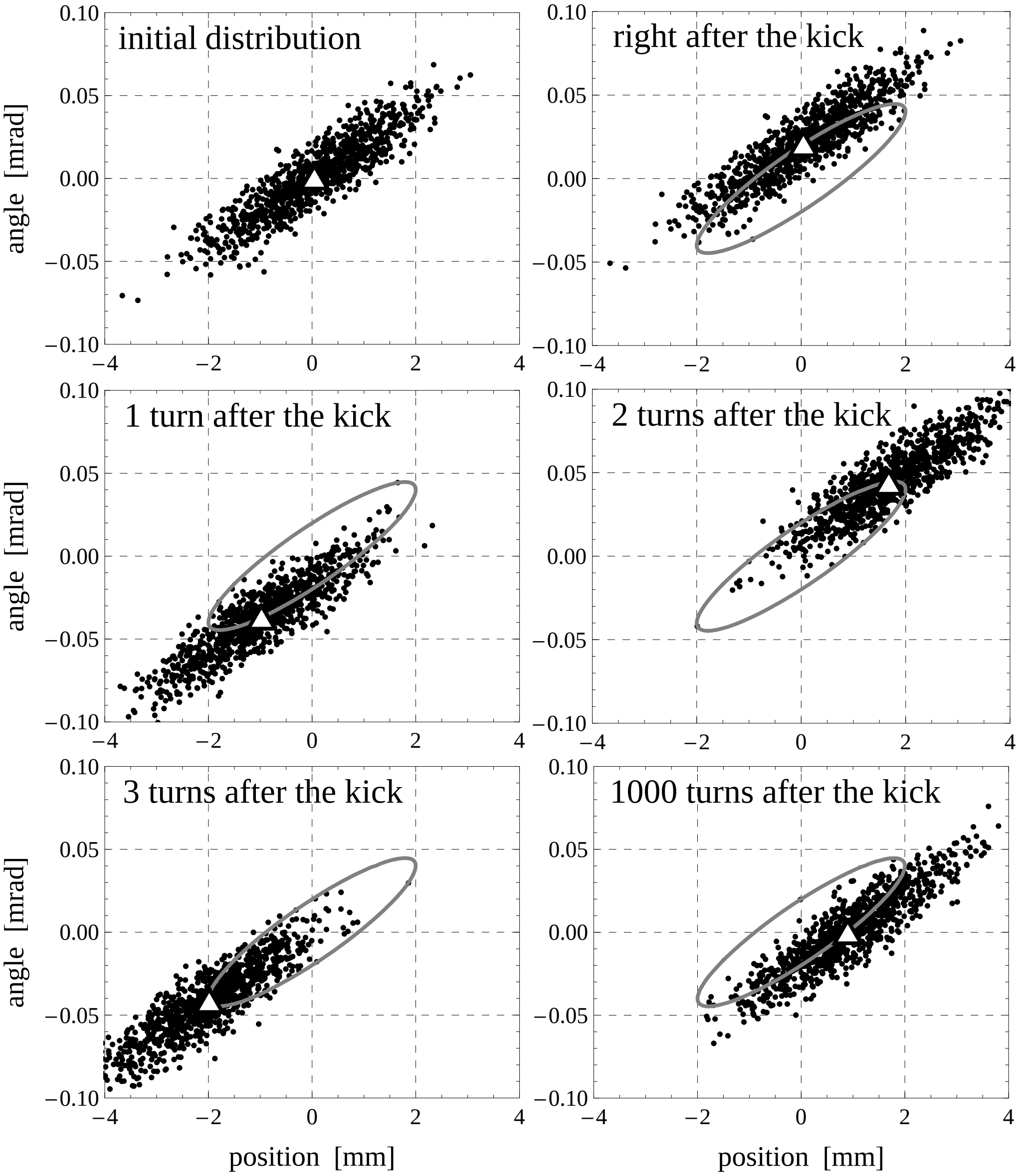

Figure 4.2: A simulation of kicked particles in a perfectly linear synchrotron. The figures show snap shots of particles' phase positions observed at the location of the kicker magnet. The particles move coherently after the kick and the beam centroid undergoes the elliptic motion like a single particle. The amplitude function and phase advance can be determined from the amplitude and phase of the beam centroid's oscillations.

in the phase space[1]. Because the kicker magnet's dipole field is independent of the particle's position, it displaces all the particles vertically by the same amount in phase space (compare the two plots on the top row). After the excitation, each particle restarts elliptic motion from its new phase space position, and the beam centroid also undergoes the elliptic motion (gray ellipse) as a single particle. At each BPM location, we can observe the turn-by-turn oscillations of the beam centroid and determine the amplitude function (up to a constant) and relative phase advances between BPM's.

Simulation of a Synchrotron with a Tune Spread

In the simulation Figure 4.2, we assumed all the particles have the same tune before and after the excitation. We note that, because of this assumption, the particles did not lose the coherence of their motion and consequently the beam's elliptical motion in phase space could be observed over many revolutions around the synchrotron. However, in real synchrotrons, this is never a case. The particles within the beam have the tune spread due to the momentum spread and/or the octupole fields. As a result, the kicked beam with a finite tune spread will eventually lose its coherence among the particles (decoherence). Figure 4.3 shows the same simulation of the kicked beam as Figure 4.2 except one octupole field. As we discussed in Section 3.2.4, the octupole field induces the amplitude dependent tune shift. Because of the octupole field, the outer particles have smaller tunes. As seen in the figure, due to the lags of the outer particles, the coherence of the particles is gradually lost and the motion of the beam centroid damps down. Obviously, the speed of the decoherence depends on the strength of the octupole field. In this simulation,

---

[1] The same argument was applied in the analysis of Section 2.1.2

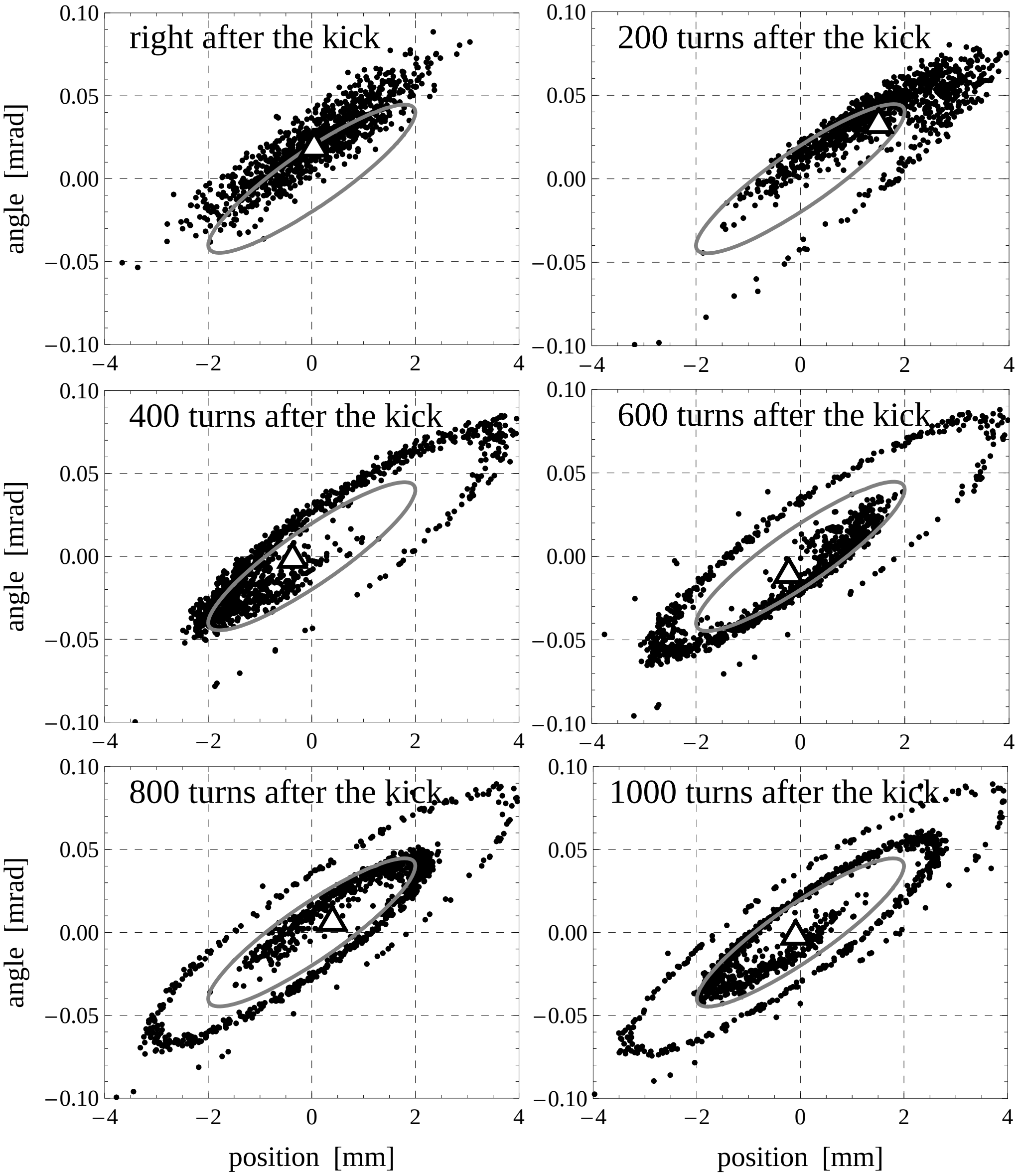

Figure 4.3: A simulation of kicked particles when there is an octupole field. Because of the amplitude dependent tune shift due to the octupole field, the particles gradually lose the coherence (decoherence). Due to the decoherence, the oscillations of the beam centroid damp down and the beam size increases.

we chose a value $\frac{1}{6}B_{y,3}\ell\beta/(B\rho) \simeq 2 \times 10^{-3}$ mm^{-2}, which is on the same order as the total octupole field strength in the Tevatron at its injection energy. We also note that, due to the decoherence, the particles occupy larger area in the phase space and the beam's transverse size increases. When the beam with the initial rms size σ_0 undergoes a kick excitation with (coherent) oscillation amplitude a_k, the rms beam size after the kick σ_k is given by (see for instance Chapter 7 of [7])

$$\sigma_k^2 = \sigma_0^2 + \frac{1}{2}a_k^2 \ . \tag{4.1}$$

Because of such a growth in beam size, we cannot use the kicked beam for physics experiments requiring high luminosity. The beam size growth also makes it impossible to make consecutive excitations of the same beam, more than a few times. To make measurements using the kicker magnet more than a few times, we have to repeat injection and ejection of the beam every two or three kick excitations. This process may be lengthy, particularly in a large synchrotron like the Tevatron, where it takes a few minutes to accelerate the beam to the highest energy.

Decoherence of Turn-by-turn Oscillations

Figure 4.4 shows turn-by-turn oscillations of the kicked beam, measured by one BPM in the Tevatron. Because the BPM observes the position of the beam centroid, as predicted from the simulation of Figure 4.3, the oscillations damp down due to the decoherence. In Figures 4.4(a) and 4.4(b), we can see the speed of the decoherence varies depending on the synchrotron's condition. Figure 4.4(c) shows the case when the envelope has an additional oscillatory structure. As discussed in [41], the damping speed of the decoherence is determined by strengths of nonlinear fields (mostly octupole fields) and

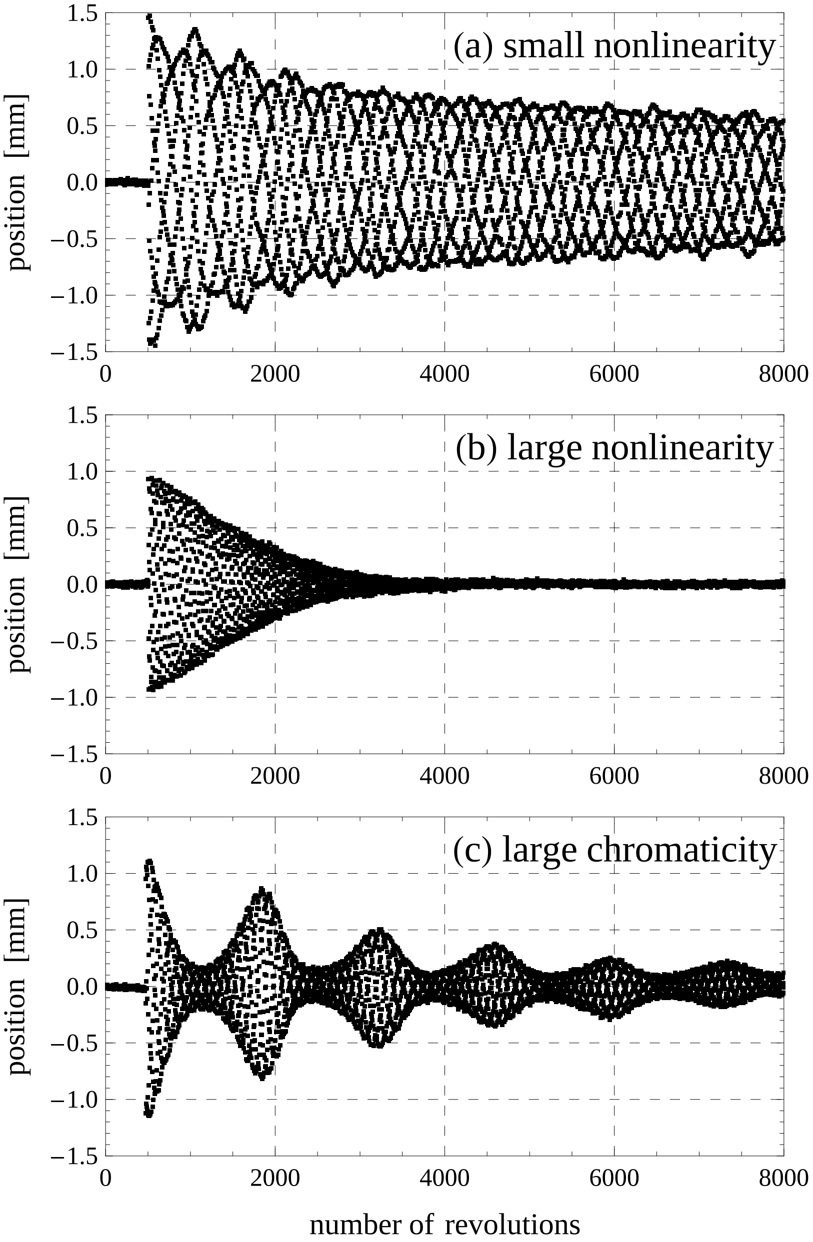

Figure 4.4: Turn-by-turn oscillations excited by a kicker magnet in the Tevatron under three different conditions. As expected from the simulation of Figure 4.3, the oscillations of the beam centroid damps down (decoherence). The speed of the decoherence depends on the strength of the nonlinearity. When the chromaticity is non-zero, the envelope also has the oscillatory structure.

the oscillatory structure of the envelope, seen in Figure 4.4, is due to spread of longitudinal momenta[2].

The important point to emphasize here is that beam excitation measurements, such as Figure 4.4 are performed in order to learn the optical parameters of the synchrotron. However, to extract information of the optical parameters from the significantly modulated data in Figure 4.4, we must consider other effects such as the nonlinear fields and even the momentum spread of beam particles, which defines a quality of the beam and has nothing to do with the synchrotron's magnet lattice[3]. Thus, the diagnostic tool can yield ambiguous results because both beam and synchrotron effects are combined.

A Simple Model of Decoherence

We conclude this section with discussion about a simple mathematical model of the kicked particles, giving an explanation to decoherence due to a tune spread. When the particle is under the influence of the kicker magnet, the equation of motion is given by

$$x'' + K(s)x = -\theta_k \delta(s - \tilde{s}_k) \ , \tag{4.2}$$

where θ_k is the kick angle of the kicker magnet and $\tilde{s}_k$ $(0 \leq \tilde{s}_k < C)$ denotes the location of the kicker magnet. Because the particle is deflected only in one revolution, the right-hand-side has only one delta function[4]. By integrating the right-hand-side with the retarded Green's function $G_\infty(s|s_0)$ in Equation

---

[2] As we discussed in Section 3.2.3, the effective gradient $K(s)$ depends on the magnetic rigidity $(B\rho) = p/e$ and so the spread of the longitudinal momenta affects transverse motion of an each beam particle differently.

[3] Although the decoherence is not desired when we measure parameters such as the amplitude function and phase advance, we can measure the chromaticity and the net octupole field strength from the envelope of the turn-by-turn oscillations[41].

[4] The present circumstance is in contrast to that in Equation 3.28

3.30, the particular solution after the kick ($s \geq \tilde{s}_k$) is given by

$$x_k(nC + \tilde{s}) = -\theta_k \sqrt{\beta(\tilde{s})\beta(\tilde{s}_k)} \sin(2\pi\nu n + \psi(\tilde{s}|\tilde{s}_k)) \ . \tag{4.3}$$

We rewrite the solution of the homogeneous part, given in Equation 2.33, into the following way:

$$x_0(nC + \tilde{s}) = A_0 \sqrt{\beta(\tilde{s})} \cos(2\pi\nu n + \psi(\tilde{s}|\tilde{s}_k) + \chi_0) \ , \tag{4.4}$$

where we chose the location of the kicker magnet $\tilde{s}_k$ as the reference of the phase advance and A_0 and χ_0 are constants. The position of the particle $x(nC+\tilde{s})$ is the sum of these two terms: $x(nC+\tilde{s}) = x_k(nC+\tilde{s})+x_0(nC+\tilde{s})$. Hence, the particle undergoes the betatron oscillations $x_0(nC+\tilde{s})$ around the coherent oscillations $x_k(nC+\tilde{s})$, as depicted in Figure 4.1. As emphasized in the introduction of this chapter, a BPM will be sensitive to only the coherent oscillations, expressed by $x_k(nC+\tilde{s})$, and not the betatron motion.

When we consider the particles within the beam, the distribution of the constant phase χ_0 is uniform. Hence, without the term of the coherent oscillations $x_k(nC+\tilde{s})$, the average position of the particles is zero. We note that the total position $x(nC+\tilde{s}) = x_k(nC+\tilde{s})+x_0(nC+\tilde{s})$ can be also written in the following way:

$$x(nC + \tilde{s}) = A \sqrt{\beta(\tilde{s})} \cos(2\pi\nu n + \psi(\tilde{s}|\tilde{s}_k) + \chi) \ , \tag{4.5}$$

where the constants A and χ are given by

$$\begin{aligned} A &\equiv \sqrt{A_0^2 + \theta_k^2\beta(\tilde{s}_k) + 2\theta_k A_0 \sqrt{\beta(\tilde{s}_k)} \sin\chi_0} \\ \chi &\equiv \chi_0 + \arctan\frac{\theta_k\sqrt{\beta(\tilde{s}_k)}\cos\chi_0}{A_0 + \theta_k\sqrt{\beta(\tilde{s}_k)}\sin\chi_0} \ . \end{aligned} \tag{4.6}$$

If we again consider multiple particles, here, the distribution of the constant phase χ is not uniform because of the second term, even for the uniform distribution of χ_0. This corresponds to the fact that the beam centroid oscillates after the kick. When the beam particles have a non-zero tune-spread due to the nonlinear fields or the spread of longitudinal momenta, then the total position $x(nC + \tilde{s})$ is modified to

$$x(nC + \tilde{s}) = A\sqrt{\beta(\tilde{s})}\cos(2\pi(\nu + \mathit{\Delta}\nu(A))n + \psi(\tilde{s}|\tilde{s}_k) + \chi) \ , \tag{4.7}$$

where $\mathit{\Delta}\nu(A)$ is the deviation of the particle's tune from the average tune ν and each particle has a different value of $\mathit{\Delta}\nu(A)$. Hence, for the beam particles with a tune spread, the distribution of the phase is modified from χ to $2\pi\mathit{\Delta}\nu(A)n + \chi$ and it evolves with the revolution number n. Eventually, when n is large enough, the distribution of the phases becomes uniform and, at this asymptotic limit, the particles completely lose the coherence. This simple derivation explains the behavior of the simulation in Figure 4.3, in which the decoherence of particles in phase space was shown. In this way, with a single turn kicker magnet, it is inherently impossible to perform measurements of coherent oscillations over a larger period of time, and often measurement accuracy is compromised. The ability of the experiments to fit data such in Figure 4.4 for information of synchrotron's parameters can be limited by such short available measurement times.

4.2 AC Dipole Excitation

In this section, we discuss basic properties the AC dipole excitation and explain advantages of the AC dipole over the kicker magnet. The AC dipole produces a sinusoidally-varying dipole magnetic field, where sinusoidally-varying kick of the field tuned to be in phase with betatron oscillations of the circulating beam particles. The situation is analogous to a simple harmonic oscillator driven by an external force, discussed in Section 3.1. From Equation 3.4, when a general oscillator is driven by an external force, the frequency of the resultant oscillations is that of the external force and is independent of the intrinsic frequency of the system[5]. Similarly, when the particles within the beam are driven by the AC dipole, all the particles have the same oscillation tune, the tune of the AC dipole. Hence, the driven beam does not have the problem of the decoherence and the AC dipole can produce sustained oscillations without increasing the beam size.

Turn-by-turn Oscillations of an AC Dipole Excitation

Figure 4.5 shows the turn-by-turn oscillations of the beam driven by the AC dipole, measured by one BPM in the Tevatron. In contrast to the kicked beams in Figure 4.4, the particles driven by the AC dipole do not have the decoherence effect. With the AC dipole, we can produce sustained excitations in any conditions of the synchrotron. As discussed earlier in Section 4.1, the amplitude function and phase advance are determined from the amplitudes and phases of the turn-by-turn oscillations observed by BPM's. Hence, for the measurements of these parameters, this ability of the AC dipole to produce sustained oscillations is useful because more measurement time is available.

Figure 4.6 shows discrete Fourier spectra of the turn-by-turn data from Figures 4.5 and 4.4(a). When calculating the discrete Fourier transformation, we used 2,000 revolutions of data points for each cases. Here, the vertical axes are scaled so that the peak hight represents the amplitude when the signal is a pure sine wave. The horizontal axis is also scaled to represent the tune or, equivalently, the frequency in unit of the revolution frequency of the beam. The Fourier spectrum of the sinusoidally driven beam with an AC dipole is like

---

[5] Here, we are assuming the external force is adiabatically turned on and, as a result, the mode corresponding to the solution of the homogeneous part is negligibly small.

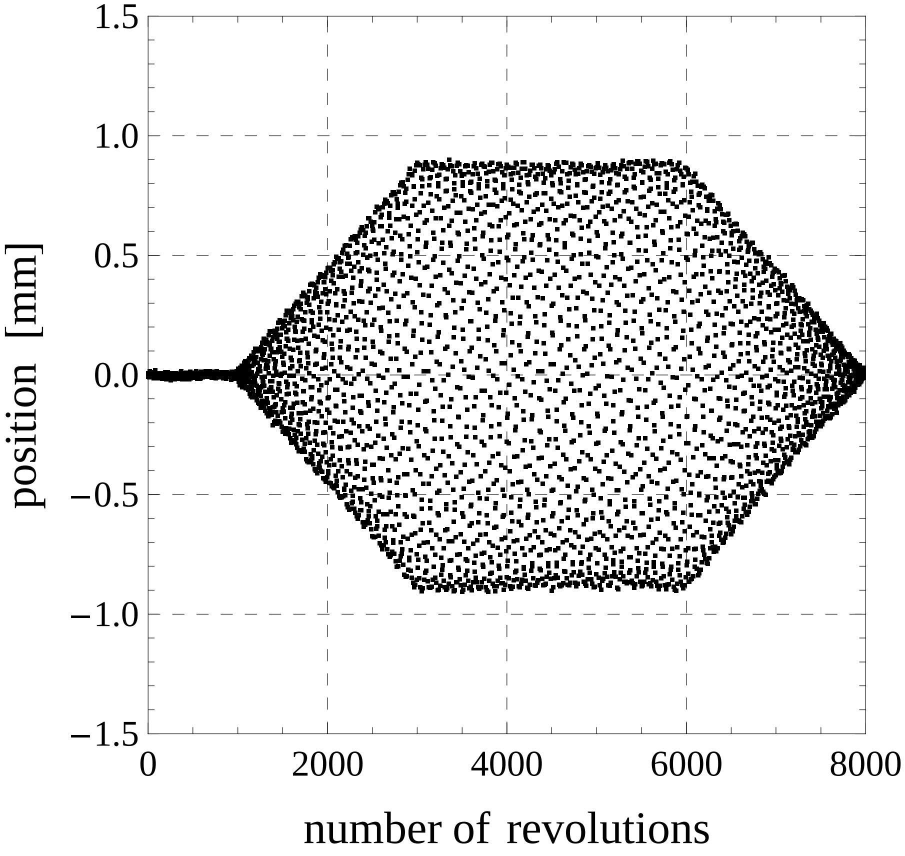

Figure 4.5: Measured turn-by-turn oscillations of the beam driven by an AC dipole in the Tevatron. In contrast to the kicked beam in Figure 4.4, the driven particles do not lose the coherence. By adiabatically ramping up and down the amplitude of the AC dipole's field, we can produce an excitation without increasing the beam size.

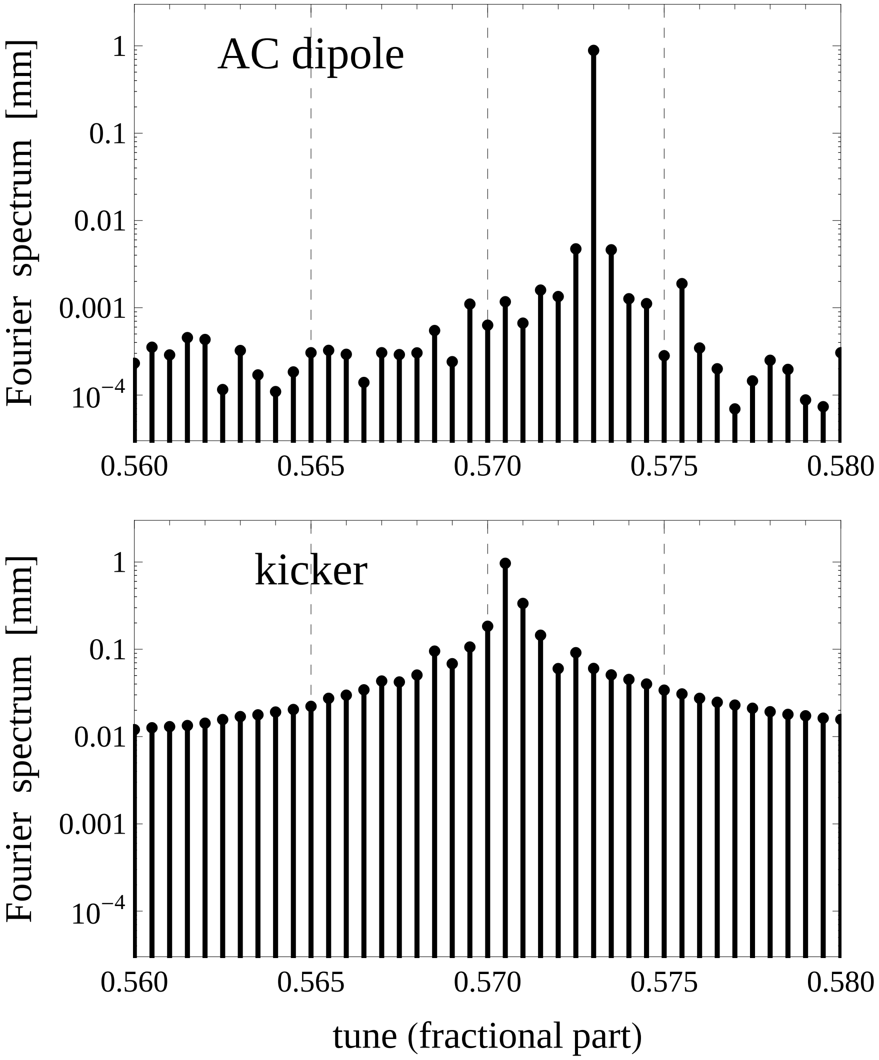

Figure 4.6: Measured discrete Fourier spectra of the driven beam with the AC dipole (Figure 4.5) and kicked beam (Figure 4.4). The particles within the driven beam has the same tune and so its Fourier spectrum is like the delta function. Whereas the particles within the kicked beam has the tune spread and so its Fourier spectrum has a finite width around the peak.

the Dirac δ-function, whereas that of the kicked beam has a finite spread. Such may be expected because the decoherence of the kicked beam is cause by a finite tune spread. As discussed in Section 3.2, it is possible to detect existence of sextupole and octupole errors in a synchrotron by detecting the presence of tunes besides the nominal betatron tune. Such errors due to nonlinear fields would present themselves as new frequency peaks in the Fourier spectrum. For such an analysis, the clean spectrum of the driven oscillations is more useful than the spectrum of the kicked beam.

AC Dipole Excitation as Driven Harmonic Oscillations

As well known in classical mechanics and also seen in Equation 3.4, for a particle beam, the amplitude of a driven oscillator depends on the difference between the driving frequency and intrinsic frequency. The amplitude grows as the driving frequency approaches the intrinsic frequency and it diverges when the two frequencies are identical. Figure 4.7 shows the measured amplitudes of the turn-by-turn oscillations, observed with one BPM in the Tevatron, for several different tunes of the AC dipole. The data points in the figure are acquired using an AC dipole in the Tevatron, excited at several different frequency. Here, the tune of the AC dipole, denoted by ν_{ac}, is the ratio between the AC dipole's frequency and the beam's revolution frequency. In the Tevatron, the frequency of the AC dipole is about 20 kHz and the revolution frequency of the beam is about 47.7 kHz and so the tune of the AC dipole is about 0.425. In this case, the amplitude is roughly proportional to $1/\sin|\pi(\nu_{\mathrm{ac}} - \nu)|$ [4]. The curve represents the fit of this function to the data. As can be seen, the AC dipole can produce large amplitude oscillations by moving its tune toward the intrinsic tune. The achievement of large amplitudes is particularly important

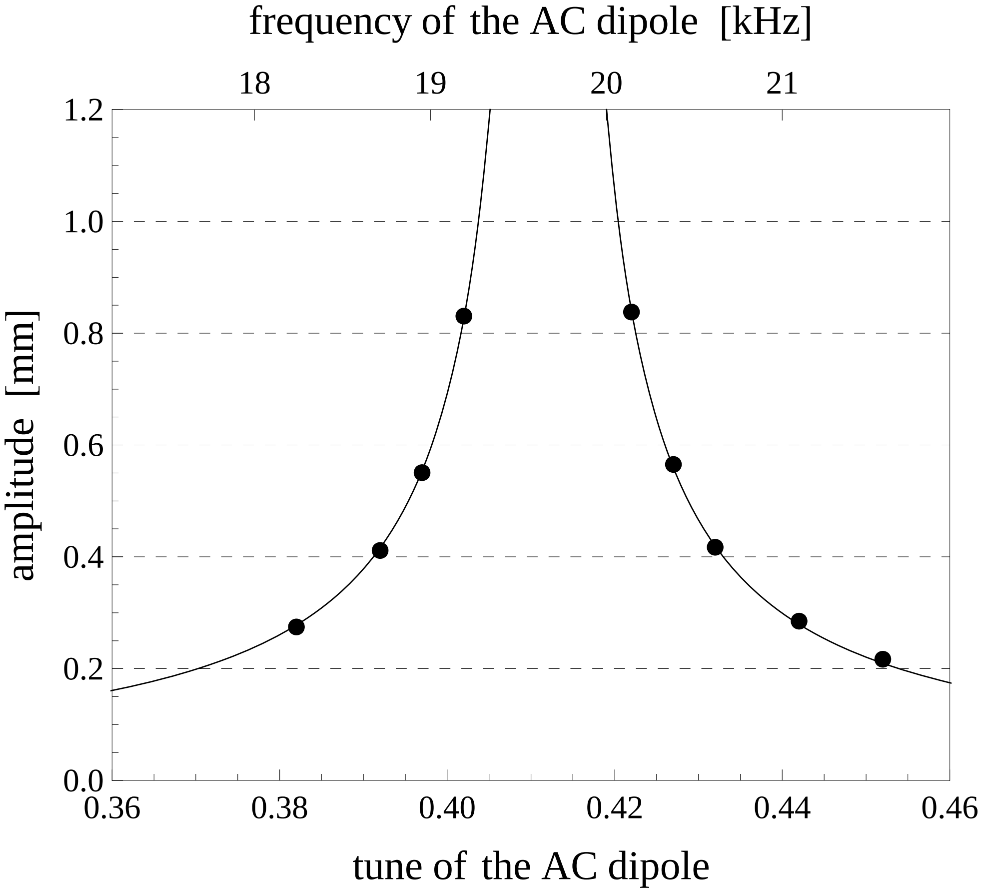

Figure 4.7: Measurement of the amplitude vs. the tune of the AC dipole observed by one BPM in the Tevatron. Similar to the classical system of a driven oscillator, the amplitude gets larger when the tune of the AC dipole gets closer to the intrinsic tune of the system. The amplitude is roughly proportional to the factor $1/\sin|\pi(\nu_{\rm ac}-\nu)|$.

to measure effects of nonlinear fields, as in Chapter 8.

Beam Size Growth Due to an AC Dipole Excitation

In Figure 4.5, the amplitude of the AC dipole's field is linearly ramped up and down. If these ramp up and ramp down are adiabatic, the beam size is preserved during the excitation. Figure 4.8 shows measurements of the beam profiles in the Tevatron after an AC dipole excitation followed by a kick excitation. In this measurements, we made vertical excitations of the 150 GeV proton beam in the Tevatron, first with the AC dipole and next with the kicker magnet. After the each excitations, beam profiles are recorded with the flying wire profile monitors[6]. The first row of the figure shows the initial profiles of the proton beam in both horizontal and vertical planes. The second row shows the profiles after the vertical excitation with an AC dipole. The amplitude of the excited oscillations was about 4 mm at the BPM locations in the Tevatron's arc, where the amplitude function is about $\beta(s) \simeq 100$ m. The amplitude of the AC dipole's field is ramped up and down in about 2,000 revolutions, as the data in Figure 4.5. The figure indicates no beam size growth in this case. The third row of the figure shows the profiles after the same beam is vertically excited with a kicker magnet. The amplitudes of the excited oscillations was roughly the same as the case of the AC dipole, about 4 mm. As expected, the vertical beam size increased after the excitation, in this case.

Here, we estimate the adabatic condition of the ramp up speed of the AC dipole's field. Further details of the following discussion can be seen in [43]. Suppose the amplitude of turn-by-turn oscillations excited by an AC

---

[6] The flying wire system measures the transverse beam profile [42]. The collisions of the beam particles with the moving wire produce a spray of secondary particles. The beam profile is determined by observing the intensity distribution of the secondary particles with a scintillator.

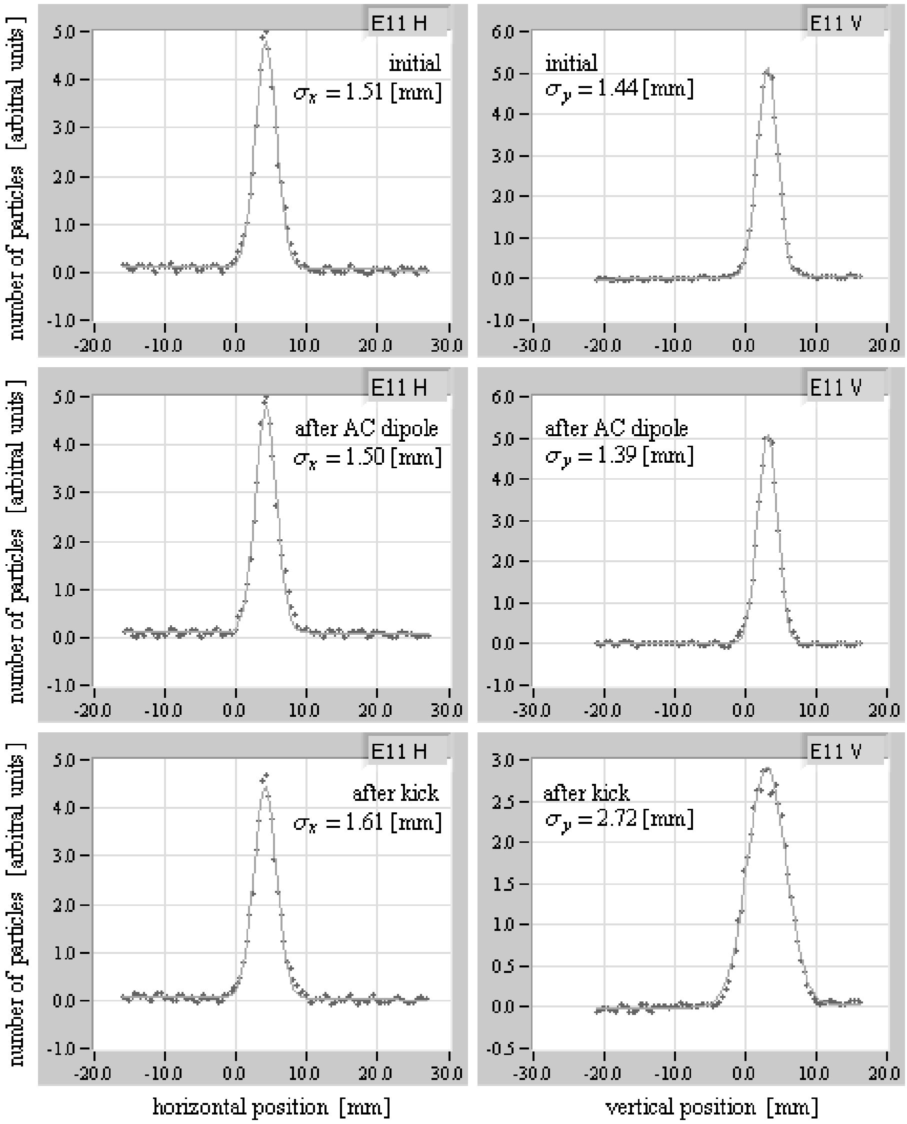

Figure 4.8: Measured proton beam profiles in the Tevatron after an AC dipole excitation followed by a kick excitation. The amplitudes of the excited oscillations are about 4 mm (in the Tevatron's arc) in both cases. The first row shows the initial profiles of the beam, and the second and third rows show the profiles after the excitations with the AC dipole and kicker magnet. The left column shows the beam profiles measured in the horizontal plane and the right column shows the profiles measured in the vertical plane. The AC dipole and kicker both applied excitations in the vertical plane. In contrast to the kick excitation, the AC dipole excitation preserves the beam size.

dipole is a_d, when observed by one BPM. Then, the AC dipole also excites a small mode with the tune of the free oscillations ν, which is referred to as transient mode. When the amplitude of the AC dipole's field is ramped up in n_r revolutions,the amplitude of the transient mode is estimated by [43]

$$a_{\text{trans}} \equiv \frac{1}{\pi n_r |\delta_d|} a_d \ , \tag{4.8}$$

where δ_d is the difference between the tune of the AC dipole and the tune of the free oscillations[7]. Because the transient mode has the free oscillation tune, the mode undergoes the decoherence and increases the beam size as the kick excitation. Hence, the beam size growth due to an AC dipole excitation can be also calculated from Equation 4.1, replacing the amplitude of the kick excitation a_k by a_{trans}. If the original rms beam size is σ_0, the rms beam size after the AC dipole excitation σ_{ac} is given by

$$\sigma_{\text{ac}}^2 = \sigma_0^2 + \frac{1}{2} a_{\text{trans}}^2 = \sigma_0^2 + \frac{1}{2\pi^2 n_r^2 \delta_d^2} a_d^2 \ . \tag{4.9}$$

We solve this equation for normalized beam size growth due to an AC dipole:

$$\frac{\Delta\sigma_{\text{ac}}}{\sigma_0} \equiv \frac{\sigma_{\text{ac}} - \sigma_0}{\sigma_0} \simeq \left(\frac{a_d/\sigma_0}{2\pi n_r \delta_d} \right)^2 \ . \tag{4.10}$$

Figure 4.9 shows the numerical calculation of this equation. Because diameters of beam vacuum pipes vary over synchrotrons, depending on their rms transverse beam sizes, we usually use the rms transverse beam size σ_0 as a scale of the AC dipole excitation. Measurements of a synchrotron's nonlinear fields typically require large excitations with 2-4σ_0 amplitudes. Hence, AC dipoles are usually designed to produce such large amplitude oscillations (Table 5.2).

---

[7] The amplitude of the transient mode is also proportional to $\sin(\pi\delta_d n_r)$. Because this is a fast-oscillating term in a typical operational condition of the Tevatron's AC dipole, $\delta_d n_r \gtrsim 10$, we simply assume the worst case, $\sin(\pi\delta_d n_r) = 1$, in our estimate.

For instance, from Table 5.2, the maximum amplitude produced by the Tevatron's AC dipole is about $3\sigma_0$. In the Tevatron, a typical value of $|\delta_d|$ is about 0.01. When $|\delta_d|$ is smaller than 0.01, some particles within the beam may have too large amplitudes and thus we may loose a part of the beam. Figure 4.9 indicates that, with these conditions $a_d = 3\sigma_0$ and $|\delta_d| = 0.01$, the ramp up of 1,000 revolutions corresponds to the beam size growth of less than 0.3%. Hence, in the Tevatron, the ramp up of 1,000-2,000 revolutions is adiabatic enough to ignore the beam size growth due to the AC dipole excitation.

4.3 Summary

In this chapter, we discussed the tools necessary to measure linear beam optical parameters, such as the amplitude function and phase advance, by exciting coherent oscillations of the beam particles and observing motion of the beam centroid with a BPM system. With the AC dipole, we can produce sustained coherent oscillations without increasing the beam size, independent of conditions such as strengths of nonlinear fields and a longitudinal momentum spread. This makes a contrast to an excitation with a kicker magnet, which undergoes the decoherence and increases the beam size, depending on such conditions. An available long measurement time of the AC dipole excitation helps data analyses. The non-destructive nature of the AC dipole is also useful because the measurement interfere less with operations of a synchrotoron. Applications of the AC dipole technique will be discussed in Chapters 7 and 8.

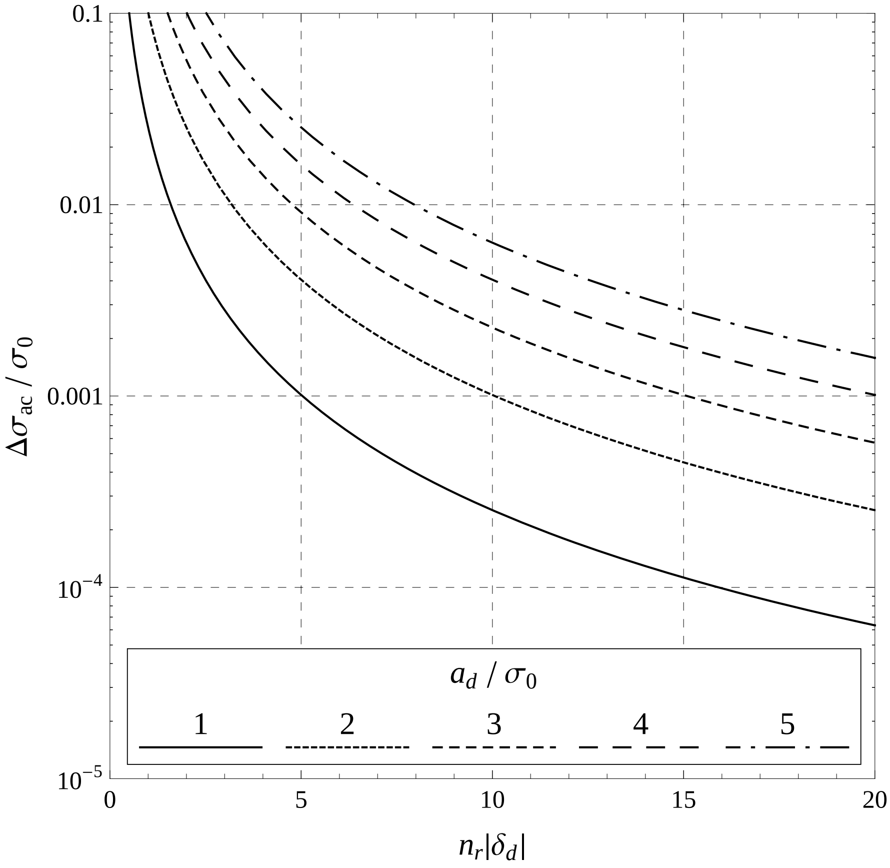

Figure 4.9: Calculation of the beam size growth due to an AC dipole excitation (Equation 4.10). This simple model predicts that 1,000 revolutions of the ramp up is slow enough to suppress the beam size growth to less than 1% when $|\delta_d| \simeq 0.01$ and the excited amplitude is $a_d \lesssim 5\sigma_0$.

Chapter 5

Tevatron AC Dipole System

In Chapter 4, we discussed diagnosis of a synchrotron by observing coherent oscillations of the beam particles excited by an AC dipole. The AC dipole excites coherent oscillations with its sinusoidally oscillating dipole magnetic field, in phase with the betatron oscillations of the beam particles. In the present chapter, we discuss the AC dipole system design for the Fermilab Tevatron, which has become the model for the CERN LHC.

5.1 System Overview

The essence of the Tevatron AC dipole system is the combination of an existing magnet and a low-cost audio amplifier. In the Tevatron, a vertical kicker magnet has been utilized as a vertical AC dipole [20]. We desire excited oscillations at a frequency near the tune of the free betatron oscillations ν. Here, as discussed in Section 4.2, the tune of the AC dipole is the ratio between the AC dipole's frequency f_{ac} and the revolution frequency of the beam f_{rev}: $\nu_{\mathrm{ac}} \equiv f_{\mathrm{ac}}/f_{\mathrm{rev}}$. Because of the synchrotron's periodicity, however, the am-

Table 5.1: Parameters related to the AC dipole excitation in the Tevatron.

Parameter	Injection	Collision
Beam Energy [GeV]	150	980
RMS beam size in arcs [mm]	1.3	0.6
Minimum $\lvert\nu_{\mathrm{ac}} - \nu\rvert$	0.015	0.01
Maximum deflection angle [μrad]	15	3.5
Maximum amplitude in arcs [mm]	8.7	1.8
Maximum amplitude in arcs [σ]	7	3

plitude of the AC dipole excitation also grows when the AC dipole tune ν_{ac} approaches $N + \nu$ or $N - \nu$, where N is an arbitrary positive integer (see Section 6.1). In the Tevatron, the fractional part of the free oscillation tune ν is about 0.58. Hence, we can make a large excitation with an AC dipole when its tune ν_{ac} is close to 0.58, 1.58, 2.58, $\cdots$ or 0.42, 1.42, 2.42, $\cdots$. Because the revolution frequency of the beam is about 47.7 kHz, the lowest operational frequency of the Tevatron AC dipole is 0.42×47.7 kHz $\simeq 20$ kHz.

The fact that the lowest allowed driving frequency is 20 kHz permits us to use a high power consumer audio amplifier to power the AC dipole magnet. Further, our design utilizes an existing iron-core kicker magnet in the Tevatron, which, though of relatively high inductance, is able to respond at the required 20 kHz frequency. This may be contrasted with AC dipole systems in the BNL RHIC which, because of the RHIC's higher revolution frequency of 78 kHz, must employ custom-built amplifiers and custom-built air-core dipole magnets which can respond at such high frequency [14].

The maximum current of the Tevatron AC dipole is about 380 A and it produces integrated field of 115 G m. At the injection and collision energies of Tevatron, 150 GeV and 980 GeV, the integrated field of 115 G m is able to deflect the beam by 15 μrad and 3.5 μrad and to produce oscillations with amplitudes of about 8.7 mm (6.7σ beam size) and 1.8 mm (3σ beam size) in the Tevatron's arcs (Table 5.1). The minimum difference between the AC dipole's tune and the free betatron oscillation tune, $|\nu_{\mathrm{ac}} - \nu|$, at which the AC dipole may be safely operated, is determined by the tune spread. At the injection and collision energies of the Tevatron, typical limits of $|\nu_{\mathrm{ac}} - \nu|$ are 0.015 and 0.01, below which beam losses may occur.

Our audio amplifier system expects to drive a ∼8 Ω load, far greater than the impedance of our kicker magnet. Therefore, the magnet must be incorporated into a resonant circuit to achieve the ∼8 Ω load and maximize the current through the magnet. In this chapter, we discuss the AC dipole magnet, the audio amplifier, and the resonant circuit. We compare the predicted performance of this system with measurements in the Tevatron. Finally, we conclude the chapter with comparison of AC dipoles in high energy hadron colliders: the Tevatron, RHIC, and LHC. The AC dipole design adopted here can be readily utilized at the LHC [22].

5.2 Review of AC Circuits

In the present section, we use the so called phasor representation of an AC circuit [44], to represent an AC amplifier, tuning circuit, and the load of the dipole magnet. We derive some general considerations of how to match the impedance of the existing dipole magnet in the Tevatron to that required for the typical commercial audio amplifier.

A sinusoidal voltage $V(t)$ and current $I(t)$ can be expressed as the real part of complex functions $\tilde{V}$ and $\tilde{I}$ called phasors:

$$V(t) = \Re\{\tilde{V}e^{i\omega t}\} = |\tilde{V}|\cos(\omega t + \arg\tilde{V}) \tag{5.1}$$

$$I(t) = \Re\{\tilde{I}e^{i\omega t}\} = |\tilde{I}|\cos(\omega t + \arg\tilde{I}) \ . \tag{5.2}$$

Here, the angular frequency ω represents the frequency of the system. The absolute values $|\tilde{V}|$ and $|\tilde{I}|$ represent the measured amplitudes of the voltage and the current. When we consider voltage and current of a circuit element, one of the phases, $\arg\tilde{V}$ or $\arg\tilde{I}$, is arbitrary and we choose $\arg\tilde{V} = 0$. In this case, the phase $\arg\tilde{I}$ represents the phase lag of the current relative to the voltage. In the same manner as for the DC resistance, the AC impedance phasor $\tilde{Z}$ is defined as the ratio of $\tilde{V}$ and $\tilde{I}$:

$$\tilde{Z}(\omega) \equiv \frac{\tilde{V}}{\tilde{I}} \ , \tag{5.3}$$

which, in general, depends upon the circuit's angular frequency ω.

The impedance of a general circuit can be considered as the sum of resistive, inductive, and capacitative impedances. For a single resistor, inductor, and capacitor, the phasor impedances are given by

$$\tilde{Z}_R = R \tag{5.4}$$

$$\tilde{Z}_L = i\omega L = iX_L \tag{5.5}$$

$$\tilde{Z}_C = \frac{1}{i\omega C} = -iX_C \ , \tag{5.6}$$

where $X_L = \omega L$ and $X_C = 1/\omega C$ are inductive and capacitative reactances. When $\Re\{\tilde{Z}\} \gg \Im\{\tilde{Z}\}$, the impedance is called resistive and when $\Im\{\tilde{Z}\} \gg \Re\{\tilde{Z}\}$, the impedance is called reactive. When N impedances $\tilde{Z}_j$ ($j = 1, 2, \cdots, N$) are connected in series or parallel, the effective impedances $\tilde{Z}_{\text{series}}$ and $\tilde{Z}_{\text{parallel}}$

can be calculated in the same ways as DC resistances:

$$\tilde{Z}_{\text{series}} = \sum_{j=1}^{N} \tilde{Z}_j \tag{5.7}$$

$$\tilde{Z}_{\text{parallel}} = \left[\sum_{j=1}^{N} \frac{1}{\tilde{Z}_j} \right]^{-1} \tag{5.8}$$

In the phasor representation, the time averaged power P is given by

$$P = \frac{1}{2}\,\Re\{\tilde{V}\tilde{I}^*\} = \frac{1}{2}|\tilde{V}||\tilde{I}|\cos(\arg\tilde{I}) \ . \tag{5.9}$$

Here, $\cos(\arg\tilde{I})$ is called the power factor. The power delivered to an impedance $\tilde{Z}$ is increased either when the current amplitude $|\tilde{I}|$ is increased or when the power factor $|\cos(\arg\tilde{I})|$ approaches unity (i.e, the current is in phase with the voltage).

In connecting a dipole magnet to an amplifier, it is often desirable to do so through the transformer, as indicated in Figure 5.1. In the application of the AC dipole, the transformer has the benefit of stepping down the voltage, while keeping the power constant, and thus the current into the magnet can be increased, which achieves a higher magnetic field in the magnet and a larger beam deflection. In the phasor representation, the transformer's equations are also the same as for a DC circuit. A transformer with winding ratio N_1:N_2 transforms voltage, current, and impedance in the following way:

$$N_1\tilde{I}_1 = N_2\tilde{I}_2 \tag{5.10}$$

$$\frac{\tilde{V}_1}{N_1} = \frac{\tilde{V}_2}{N_2} \tag{5.11}$$

$$\frac{\tilde{Z}_{\text{eff}}}{N_1^2} = \frac{\tilde{Z}}{N_2^2} \ , \tag{5.12}$$

where indices 1 and 2 denote the primary (source) and secondary (load) sides and $\tilde{Z}$ and $\tilde{Z}_{\text{eff}}$ are the impedance of the system and the effective impedance seen by the source (Figure 5.1).

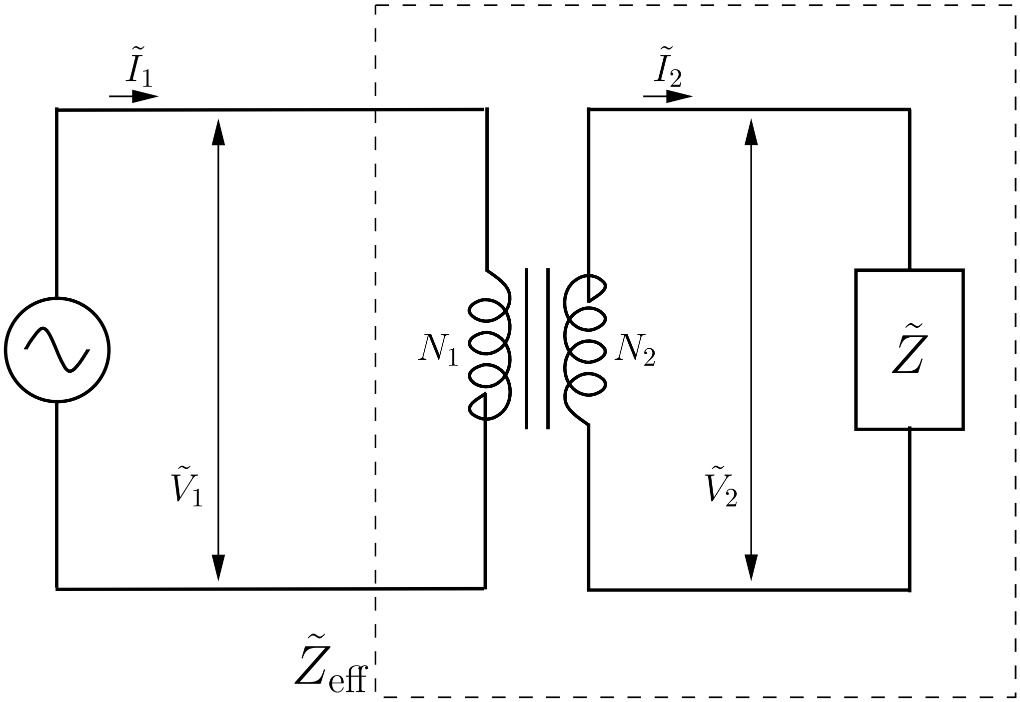

Figure 5.1: A magnet connected to a power supply through a transformer. By a transformer with winding ratio N_1:N_2, the effective impedance seen by the power supply is changed from the original impedance of the magnet $\tilde{Z}$ to $\tilde{Z}_{\mathrm{eff}}$.

In Section 5.5, we discuss methods to maximize the current $|\tilde{I}_2|$ into the magnet by utilizing a transformer and an impedance matching resonant circuit.

5.3 AC Dipole Magnet

The Tevatron AC dipole is a single turn magnet with an iron core and a ceramic beam pipe. Figure 5.2 is the design drawing of the magnet's cross section. Because the gap between the pole faces is $g = 7.91$ cm (3.125 inch), the conductors' number of turns is $N = 1$, and the length of the magnet is $\ell = 1.89$ m, from the ampère's law (see for instance Section 4.3.1 of [45]), the integrated field strength $B\ell$ for magnet current I is given by

$$B\ell = \frac{\mu_0 N I \ell}{g} = 0.30 I \ \mathrm{G\,m/A} \ . \tag{5.13}$$

The quality of the magnetic field dB/B is estimated about 1% in any location inside the magnet [46].

Figure 5.3 is the photograph of the Tevatron AC dipole magnet. As seen in the photograph, the magnet is connected to the other components of the system outside of the tunnel through two 22 m coaxial cables. Through in situ measurements of frequency dependent impedances when the magnet was connected to a voltage oscillator, we found that the combination of the magnet and two cables has inductance $L \simeq 8.0$ μH and resistance $R \simeq 90$ mΩ at $f = 20.5$ kHz. The inductive reactance of the combination is $X_L \simeq 1.0$ Ω at this frequency. Since $X_L \gg R$, the impedance of the magnet with the cables is reactive at 20.5 kH. Out of 8.0 μH and 90 mΩ, 2.8 μH and 25 mΩ are from the cables. At 20.5 kHz, the capacitative reactance of each cable is about 3.5 kΩ and parallel to the magnet. Compared to the magnet resistance $R \simeq 90$ mΩ

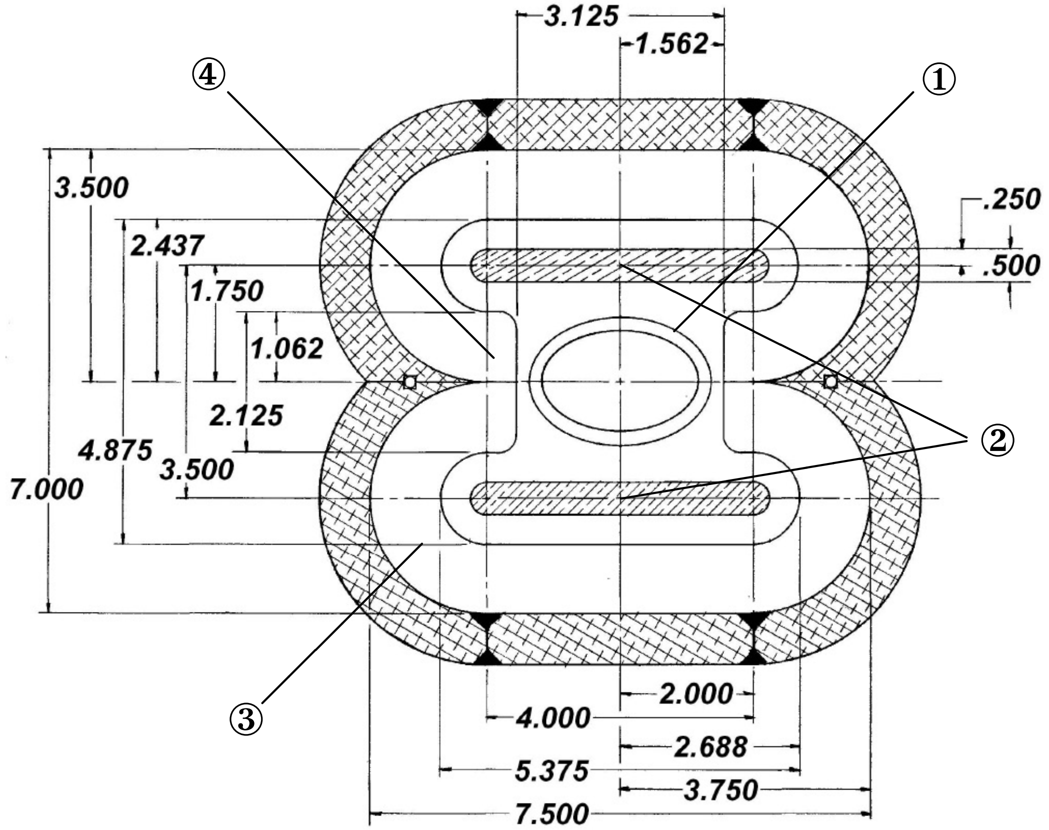

Figure 5.2: Cross section of the Tevatron AC dipole magnet. Dimensions are given in inches. ① Ceramic beam pipe. ② Current carrying conductors. Current in these conductors produces a horizontal magnetic field and deflects the beam vertically. ③ Iron yoke to improve the field quality. ④ Pole faces of the dipole magnet. The gap between the pole faces is 7.91 cm (3.125 inch).

Figure 5.3: Photograph of the Tevatron AC dipole magnet. The length of the magnet is 1.89 m. The other components of the system are outside of the tunnel and connected with two coaxial cables, shown at the center of the photograph. The proton beam goes from left to right in the photograph.

and inductive reactance $\omega L \simeq 1.0\ \Omega$, it is larger more than factor of 3 and effectively the same as an open. Hence, the capacitance of the cables can be ignored at this frequency.

5.4 Crown I-T8000 Audio Amplifier

The power supply of the Tevatron AC dipole is an 8 kW Crown I-T8000 audio amplifier [47]. Because the magnet and cable have resistance of $R \simeq 90$ mΩ, when the delivered current is $\tilde{I}$, they dissipate $\frac{1}{2}|\tilde{I}|^2 R$ of power. From energy conservation, this dissipation cannot be larger than the output power of the amplifier $P \simeq 8$ kW. Hence, the maximum magnet current of the Tevatron AC dipole system is $I_{\max} = \sqrt{2P/R} \simeq 420$ A.

The amplifier has limits in voltage and current. These limits depend on the load impedance and also frequency. According to the specification from the manufacturer [47], its output power becomes maximal when the load impedance is resistive and its magnitude is 8 Ω. Then, voltage and current limits are about 360 V and 45 A. These numbers indicate this amplifier is a source with high voltage and low current. Because the impedance of the AC dipole magnet and its cables is $(0.09) + i(1.0)\ \Omega$ at 20.5 kHz, the voltage and current phasors are almost perpendicular in the magnet. When voltage and current are not in phase, the power factor in Equation 5.9 decreases and the maximum voltage and current must increase to 1.5 kV and 150 A to produce 8 kW. It is therefore more practical to bring the voltage and current in phase and increase the power factor. That is, the magnet is integrated into a resonant circuit so that the load impedance matches the optimized value for the amplifier.

The output power of the amplifier also depends on the pulse duration.

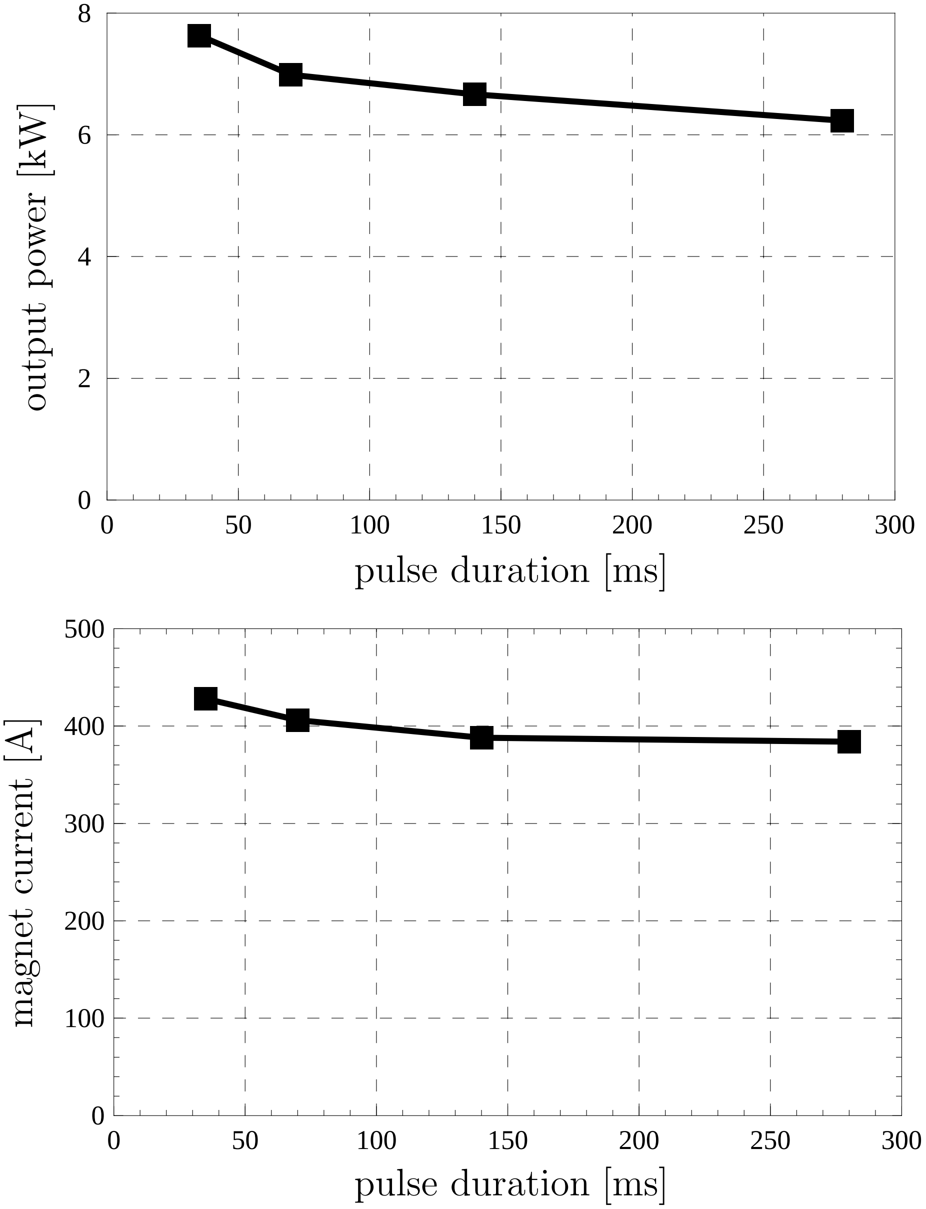

Figure 5.4: Our measurements of the Crown I-T8000 amplifier' output power [47] vs. pulse duration and the produced magnet current vs. pulse length. Both figures are for a 20.5 kHz sine wave. For the typical 140-150 ms measurement cycle of the Tevatron AC dipole, the output power of the amplifier and magnet current are about 6.5 kW and 380 A, a 19% decrease in power and 10% decrease in current relative to the maximum possible output from the amplifier.

Figure 5.4 shows our measurements of the output power and magnet current for different pulse durations. Because a typical measurement cycle with the Tevatron AC dipole is about 140-150 ms (Figure 5.8), the output power and magnet current are reduced to about 6.5 kW and 380 A.

5.5 Resonant Circuits

The Tevatron AC dipole magnet is integrated into a parallel resonant circuit to optimize the impedance matching of the system to the Crown audio amplifier. In this section we compare the optimizations with series and parallel resonant circuits. As will be shown, the best circuit for our particular magnet impedance and amplifier is a parallel resonant circuit.

5.5.1 Series Resonant Circuit

Figure 5.5 is the circuit diagram when an external capacitor is added in series to the resistive and inductive load of the dipole magnet to form an RLC series resonant circuit. The total impedance of the system is given by

$$\tilde{Z} = R + i(X_L - X_C) \ . \tag{5.14}$$

If the capacitor satisfies the resonant condition $X_L = X_C$, the total impedance is resistive and $Z = R \simeq 90$ mΩ. To adjust the effective impedance seen by the amplifier to the optimum 8 Ω, we have to use a transformer with large winding ratio $N_1/N_2 \simeq 9.4$:

$$\tilde{Z}_{\text{eff}} = \left(\frac{N_1}{N_2}\right)^2 R \simeq 8 \ \Omega \ . \tag{5.15}$$

Temporarily, we ignore the effect of the pulse length on the output power (see Figure 5.4) and assume the amplifier can actually produce 8 kW. From Ohm's

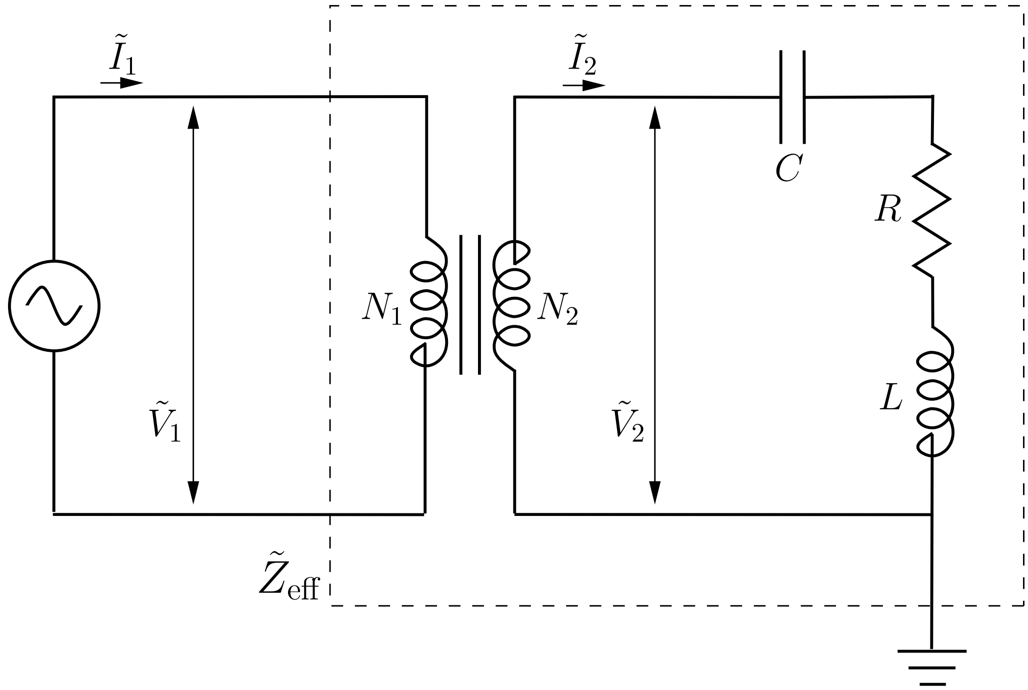

Figure 5.5: Circuit diagram of the series resonant circuit. When the capacitor satisfies the resonant condition $X_C = X_L \simeq 1\ \Omega$, the impedance is $\tilde{Z} = R \simeq 90\ \text{m}\Omega$. To adjust the effective impedance $\tilde{Z}_{\text{eff}}$ to the optimum 8 Ω, the transformer must have a large winding ratio $N_1/N_2 \simeq 9.4$. In general, a series resonant circuit is suited for a source with high current and low voltage.

law and the definition of the time averaged power Equation 5.9, the voltage and current phasors in the primary side, $\tilde{V}_1$ and $\tilde{I}_1$, satisfy

$$\tilde{V}_1 = \tilde{I}_1 \tilde{Z}_{\mathrm{eff}} \tag{5.16}$$

$$P = \frac{1}{2} \Re\{\tilde{V}_1 \tilde{I}_1^*\} \ . \tag{5.17}$$

By solving these two equations for $\tilde{V}_1$ and $\tilde{I}_1$,

$$\tilde{V}_1 = \frac{N_1}{N_2} I_{\mathrm{max}} R \simeq 360 \text{ V} \tag{5.18}$$

$$\tilde{I}_1 = \frac{N_2}{N_1} I_{\mathrm{max}} \simeq 45 \text{ A} \ . \tag{5.19}$$

Here, $I_{\mathrm{max}} = \sqrt{2P/R} \simeq 420$ A is the maximum current of the system and we chose the arbitrary phase of the voltage to be zero, $\arg \tilde{V} = 0$. From the transformer's equations 5.10 and 5.11, voltage and current phasors in the secondary side, $\tilde{V}_2$ and $\tilde{I}_2$, are given by

$$\tilde{V}_2 = I_{\mathrm{max}} R \simeq 38 \text{ V} \tag{5.20}$$

$$\tilde{I}_2 = I_{\mathrm{max}} \simeq 420 \text{ A} \ . \tag{5.21}$$

By comparing voltages and currents in both side, we can see high voltage and low current of the amplifier are converted to low voltage and high current in the magnet side. Although such a flip of high voltage to high current is possible by using a transformer with large winding ratio, $N_1/N_2 \simeq 9.4$, as a predictable manner, the effect of magnetic flux leakage changes the effective winding ratio and makes it difficult to reliably produce a transformer with a large winding ratio in a predictable manner. It is therefore desirable to choose a circuit design whose winding ratio is close to one-to-one.

5.5.2 Parallel Resonant Circuit

We repeat an exercise similar to the previous section but now for a parallel resonant circuit. As will be seen, this design can produce the same amount of magnet current, 420 A, by using a transformer whose winding ratio is close to unity. Figure 5.6 is the circuit diagram of the Tevatron AC dipole system. A capacitor $C \simeq 7.5\ \mu$F added in parallel to the magnet satisfies the resonant condition and makes the system a parallel resonant circuit. From Equation 5.8 the total impedance of R, L, and C is given by

$$\tilde{Z} = \left[\frac{1}{R + iX_L} + \frac{1}{-iX_C}\right]^{-1} = \frac{X_C^2 R + i[X_C^2 X_L - (R^2 + X_L^2)X_C]}{R^2 + (X_L - X_C)^2} \ . \tag{5.22}$$

As in the case of the series resonant circuit, the system becomes resonant when imaginary part of the impedance $\tilde{Z}$ is zero. Because $X_L \gg R$, the resonant condition is roughly the same as the series resonant circuit:

$$X_C = \frac{R^2 + X_L^2}{X_L} \simeq X_L \ . \tag{5.23}$$

When the resonant condition is satisfied, the total impedance is resistive and its magnitude is 12 Ω:

$$\tilde{Z} = \frac{R^2 + X_L^2}{R} \simeq \frac{X_L^2}{R} \simeq 12\ \Omega \ . \tag{5.24}$$

A second capacitor $C_{\text{filter}} \simeq 8\ \mu$F is added to filter low frequency noise of the amplifier. Since its impedance phasor is perpendicular and smaller in the magnitude compared to the total impedance $\tilde{Z}$, we ignore C_{filter} in the following analysis. When the AC dipole is integrated into the parallel resonant circuit, the total impedance is not very different from the optimum 8 Ω even without a transformer. The required winding ratio of the transformer to change the effective impedance seen by the amplifier to 8 Ω is much closer to one compared

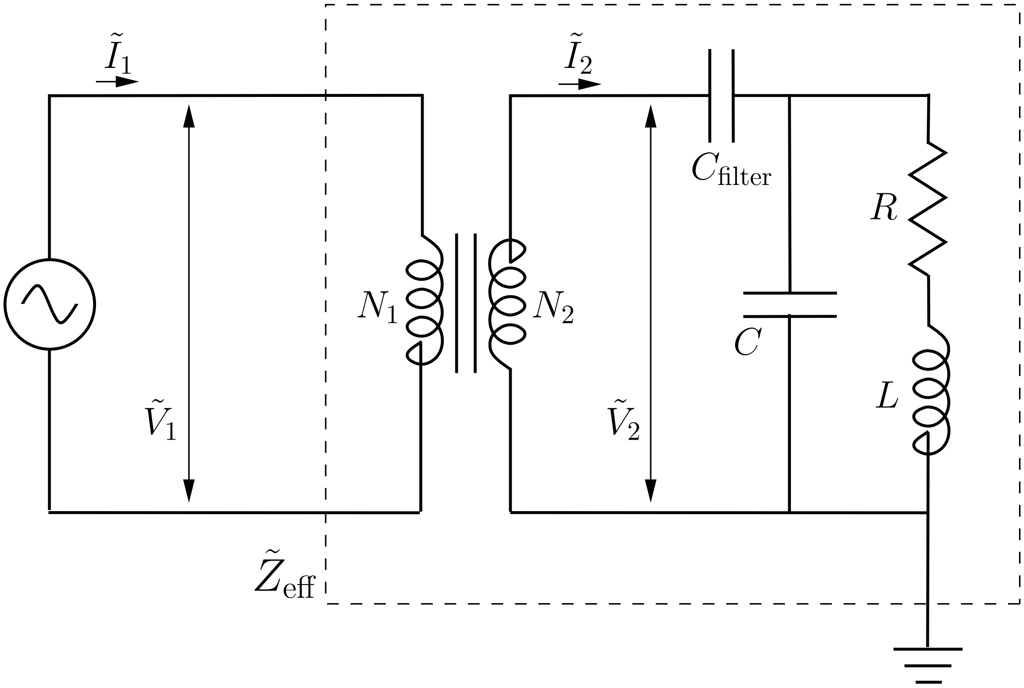

Figure 5.6: Circuit diagram of the Tevatron AC dipole system. The capacitor $C \simeq 7.5$ μF satisfies the resonant condition $X_C \simeq X_L \simeq 1.0$ Ω at 20.5 kHz and make the system a parallel resonant circuit. The other capacitor $C_{\text{filter}} \simeq 8.0$ μF filters low frequency noises from the amplifier and has virtually no impact on the system around the resonant frequency. The transformer has winding ratio $N_1 : N_2 = 40 : 50$ and converts the impedance from $X_L^2/R \simeq 12$ Ω to 8 Ω. Since most of the magnet current is enclosed in the loop of R, L, and C, the secondary side is high voltage and low current as the voltage and current limits of the amplifier.

to the case of the series resonant circuit, $N_1/N_2 \simeq 0.82$:

$$\tilde{Z}_{\text{eff}} \simeq \left(\frac{N_1}{N_2}\right)^2 \frac{X_L^2}{R} \simeq 8\ \Omega\ . \tag{5.25}$$

As in the previous section, we assume the amplifier outputs 8 kW and calculate voltage and current in the primary side, $\tilde{V}_1$ and $\tilde{I}_1$. Using Ohm's law (Equation 5.16) and the definition of the time averaged power (Equation 5.9), we have

$$\tilde{V}_1 \simeq \frac{N_1}{N_2} I_{\text{max}} X_L \simeq 360\ \text{V} \tag{5.26}$$

$$\tilde{I}_1 \simeq \frac{N_2}{N_1}\frac{R}{X_L} I_{\text{max}} \simeq 45\ \text{A}\ . \tag{5.27}$$

Because we match the load impedance to the amplifier by using a transformer, the voltage and current in the primary side $\tilde{V}$ and $\tilde{I}$ are the same in both the series and parallel resonant circuits. By using the transformer's equations 5.10 and 5.11, the voltage and current phasors in the secondary side, $\tilde{V}_2$ and $\tilde{I}_2$, are calculated:

$$\tilde{V}_2 \simeq I_{\text{max}} X_L \simeq 420\ \text{V} \tag{5.28}$$

$$\tilde{I}_2 \simeq \frac{R}{X_L} I_{\text{max}} \simeq 38\ \text{A}\ . \tag{5.29}$$

Here, $\tilde{I}_2$ is the current coming out of the loop of the magnet and capacitor. The magnet current $\tilde{I}_{\text{magnet}}$ is determined from the voltage $\tilde{V}_2$ and the impedance of the magnet with the cables $R + iX_L$:

$$|\tilde{I}_{\text{magnet}}| = \left|\frac{\tilde{V}_2}{R + iX_L}\right| \simeq \left|\left(\frac{R}{X_L} - i\right) I_{\text{max}}\right| \simeq 420\ \text{A}\ . \tag{5.30}$$

Hence, we can produce the maximum current defined by the amplifier (Section 5.4) with the parallel resonant circuit. Figure 5.7 shows phasors of the voltage and current in the series and parallel resonant circuit. In the parallel resonant

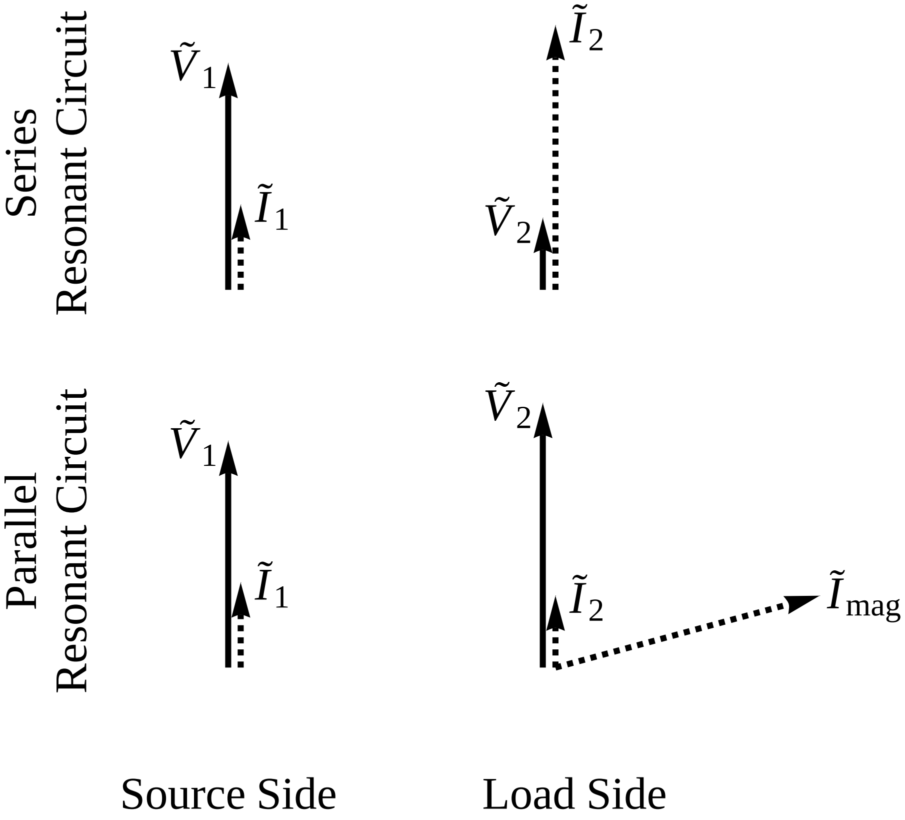

Figure 5.7: Voltage and current phasors in the series and parallel AC dipole circuits. In the series resonant circuit, high current is achieved by flipping high voltage of the amplifier with a transformer. In the parallel resonant circuit, voltage $\tilde{V}_2$ and magnet current $\tilde{I}_{\mathrm{magnet}}$ are almost perpendicular since the total impedance is resistive and impedance of the magnet is reactive. Hence, because of the power factor (Equation 5.9), we can produce high current without making large increase in power.

circuit, because the total impedance $\tilde{Z}$ is resistive and the impedance of the magnet is reactive, voltage and current in the magnet is almost perpendicular and the power factor (Equation 5.9) becomes very small: $\cos(\arg \tilde{I}) \simeq 0.09$. Most of the magnet current is enclosed inside the loop consisting of the magnet and the capacitor C, and only a component of $\tilde{I}_{\mathrm{magnet}}$ which is parallel to $\tilde{V}_2$, $\tilde{I}_2$, contributes to the power. This is why we can produce high current, maintaining the high voltage and keeping the power constant, in the parallel resonant circuit. Furthermore, because the transformer in the parallel resonant circuit has a winding ratio of 0.82, the parallel resonant circuit is easier to prepare than the series resonant circuit.

5.6 Performance of Tevatron AC Dipole

To adiabatically ramp up and ramp down the amplitude of the AC dipole field, the input to the amplifier is produced with two waveform generators. One (Stanford Research DS 345) produces a pure ∼20.5 kHz sine wave and the other (Agilent 33250A) modulates the amplitude by a trapezoidal function. Figure 5.8 shows the maximum current delivered to the AC dipole magnet and its input signal. The figure shows the case when the frequency is 20.5 kHz and the pulse duration is 150 ms. As seen in Figure 5.4, the maximum current is about 380 A. Figure 5.9 is the Fourier spectrum of the magnet current in Figure 5.8. The vertical axis is normalized so that the peak height represents the maximum current when the current is a pure sine wave. From the figure, the signal noise ratio is about 60 dB.

Until now, we have analyzed the system only at the resonant frequency $f_{\mathrm{res}} \equiv 20.5$ kHz. When frequency is off by Δf from the resonant frequency

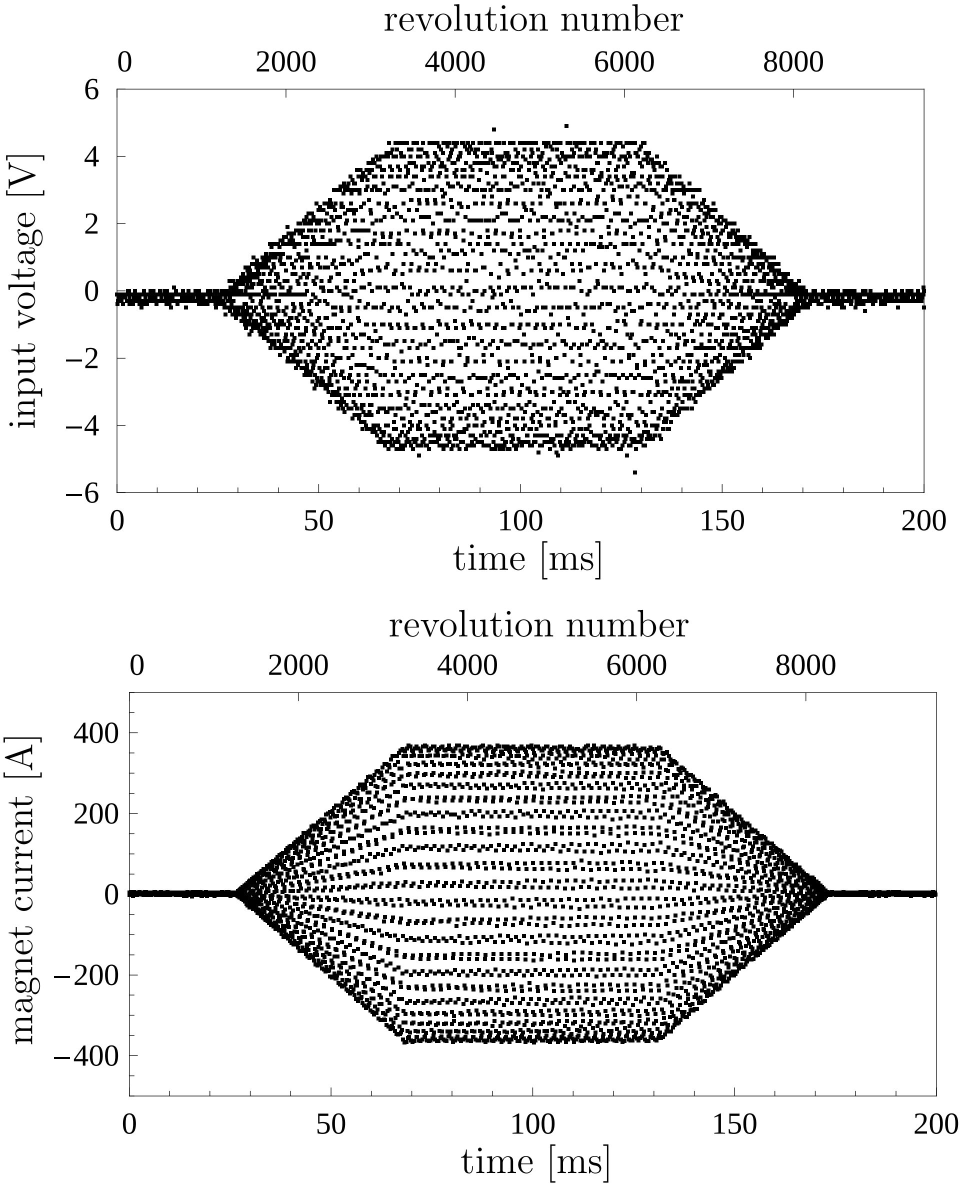

Figure 5.8: The input to the amplifier and magnet current. The figure shows the maximum current produced by the Tevatron AC dipole when frequency is 20.5 kHz and pulse length is 150 ms. The input is produced by modulating amplitude of a sine wave with a trapezoidal envelope. These linear ramp up and ramp down are adiabatic enough to preserve the beam size.

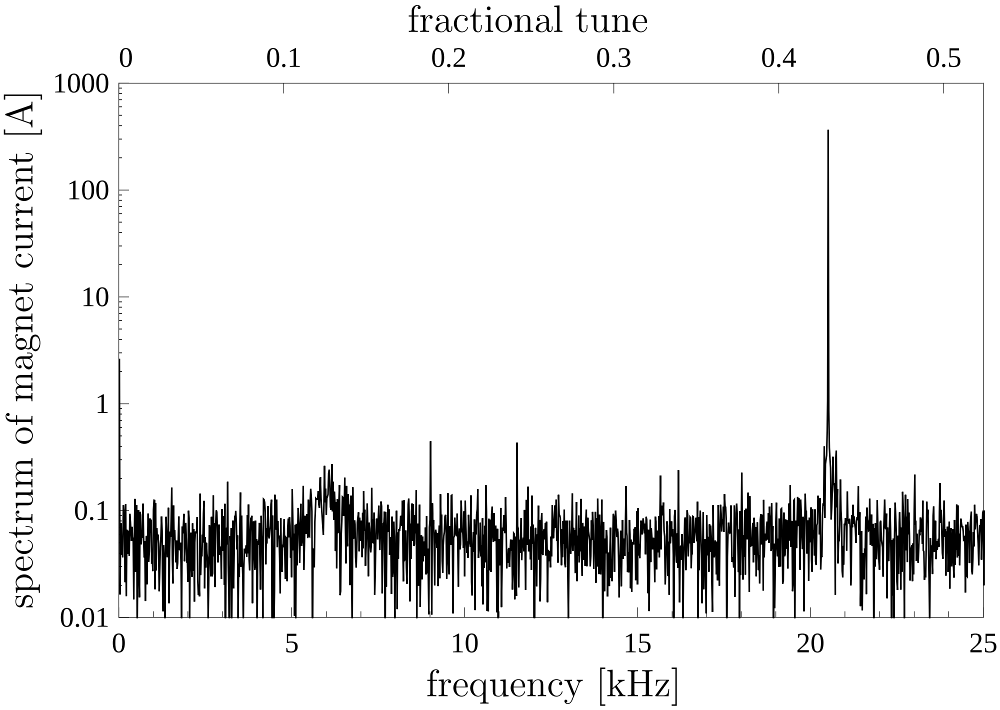

Figure 5.9: Measured Fourier spectrum of the magnet current in Figure 5.8. The spectrum is calculated from the data points when amplitude is maximum. The vertical axis is scaled so that the peak height represents the oscillation amplitude. The signal noise ratio is about 60 dB.

f_{res}, from Equation 5.22, the magnitude of the effective impedance is given by

$$|\tilde{Z}_{\text{eff}}(f_{\text{res}} + \Delta f)| \simeq \frac{\tilde{Z}_{\text{eff}}(f_{\text{res}})}{\sqrt{1 + 4Q^2(\Delta f / f_{\text{res}})^2}} \ , \tag{5.31}$$

where $\tilde{Z}_{\text{eff}}(f_{\text{res}}) \simeq 8\ \Omega$ is the effective impedance at the resonant frequency and $Q \equiv X_L/R \simeq 11$ is the quality factor of our parallel resonant circuit. The quality factor determines peak width of the impedance curve. For instance, when $\Delta f = \sqrt{3} f_{\text{res}}/2Q \simeq 1.6$ kHz, the magnitude of the effective impedance becomes half of the maximum value. In general, a system with high Q has high maximum current and a narrow frequency range and vice versa. Figure 5.10 shows measurements of the effective impedances and maximum magnet currents for different frequencies. Because of the low quality factor $Q \simeq 11$, the Tevatron AC dipole has a relatively wide operational frequency range, which is useful in many beam studies we wish to perform.

5.7 Tevatron, RHIC, and LHC

AC dipoles have been employed in the Tevatron and RHIC and there is also an ongoing project to build AC dipoles for the CERN LHC [22]. Since the LHC has larger circumference than the Tevatron, the lowest operational frequency of the LHC AC dipole is also in the audio range. Based on success of the Tevatron AC dipole, the LHC AC dipoles will follow the Tevatron's design and will utilize existing kicker magnets and audio amplifiers.

Table 5.2 shows the relevant beam and synchrotron parameters related to the AC dipoles in the RHIC, Tevatron, and LHC. From Equation 6.4, the oscillation amplitude produced by an AC dipole decreases linearly with the beam energy or the magnetic rigidity. This is significant because, for instance, beam energies of the RHIC and LHC are different by a factor 28. However,

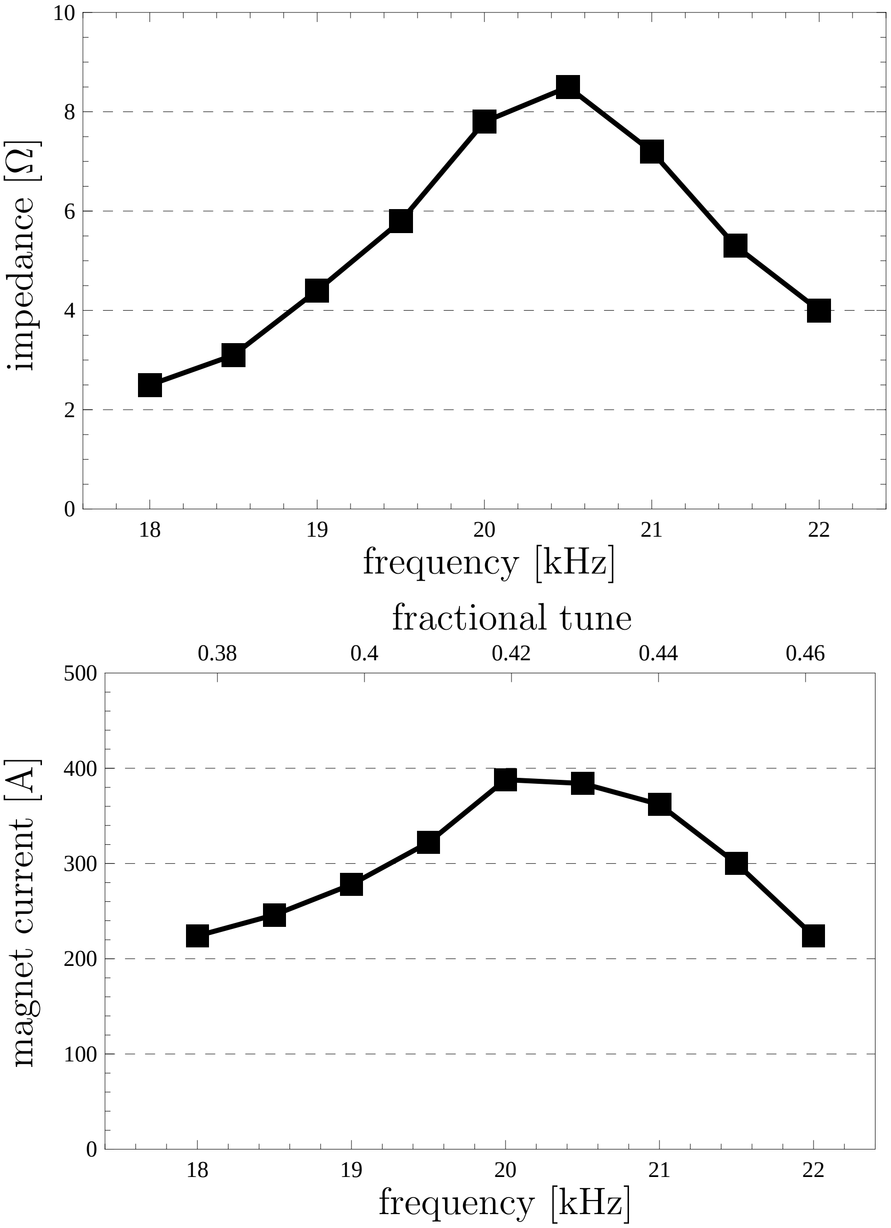

Figure 5.10: Impedance and magnet current vs. frequency. As expected, the impedance becomes maximum at 20.5 kHz and the peak value is about 8 Ω. The low quality factor of the resonant circuit, $Q \simeq 11$, makes the wide working frequency range. Between 18 and 22 kHz, the Tevatron AC dipole can produce 50% of its maximum magnet current. The range corresponds to between 0.38 and 0.46 (or 0.54 and 0.62) in tune of the Tevatron.

Table 5.2: Parameters related to the AC dipoles in the RHIC, Tevatron, and LHC. Parameters of the RHIC are for the proton-proton collider mode. The last row shows the required integrated field to produce oscillations with 4σ amplitude at the maximum beam energy of each collider under the condition when $|\nu_{\text{ac}} - \nu| = 0.01$. Because of the small beam size and the large amplitude function of their locations, the LHC AC dipoles are required only about 50% larger integrated fields, relateive to AC dipoles in the RHIC and Tevatron. As discussed in Section 5.1, there are more than one frequencies for an AC dipole to excite the beam. Because an LHC AC dipole can operate at four frequencies in audio range, 3, 8, 14, and 19 kHz, and also because the required integrated field is not far from that for the Tevatron, LHC AC dipole have similar designs to the Tevatron AC dipole.

Parameter	RHIC	Tevatron	LHC
Maximum beam energy [GeV]	250	980	7000
Revolution frequency [kHz]	78	48	11
RMS beam size in arcs [mm]	0.75	0.6	0.3
Fractional Tune	0.69	0.58	0.3
Maximum β in arcs [m]	49	100	180
β at the AC dipole [m]	11	47	260
Frequency of the AC dipole(s) [kHz]	54	20	
Integrated field (achieved) [G m]	105	115	
Amplitude (achieved)	3σ	3σ	
Possible frequencies of an AC dipole [kHz]	24, 54, $\cdots$	20, 28, $\cdots$	3, 8, $\cdots$
Integrated field for 4σ oscillation [G m]	135	140	200

because of various other factors such as the smaller beam sizes in higher energy synchrotrons and the amplitude function at the location of the AC dipole, the desired integrated field of an AC dipole does not necessarily grow linearly with the beam energy. In Section 4.2, we discussed a typical requirement an AC dipole is to produce oscillations with 2-4σ amplitudes to study nonlinear behavior of the beam. At the LHC, the typical transverse beam size is $\sigma \sim 0.3$ mm, to be compared with $\sigma \sim 0.75$ mm in the RHIC, which reduces the required oscillation amplitude by a factor of 2.5. Furthermore, because the oscillation amplitude produced by an AC dipole also depends on the amplitude function at the location of the AC dipole (see Equations 6.4 and 6.6), and because the LHC AC dipoles will be located at high β locations relative to the RHIC or Tevatron (see Table 5.2), the LHC AC dipoles gain a factor of $\sqrt{260 \text{ m}/11 \text{ m}} \simeq 4.9$ in the required integrated field. For these two reasons, the LHC AC dipoles require only about 50% larger integrated field than the AC dipoles in the RHIC and Tevatron.

As discussed in Section 5.1, the oscillation amplitude produced by an AC dipole also depends on the difference between the AC dipole's tune and the free oscillation tune $|\nu_{\text{ac}} - \nu|$. For purpose of comparison, in Table 5.2, we used $|\nu_{\text{ac}} - \nu| = 0.01$, which is the limit of the Tevatron at 980 GeV and a number easy to be scaled. If the LHC has a small tune spread in the beam and thus its AC dipoles can operate with $|\nu_{\text{ac}} - \nu|$ smaller than 0.01, the required integrated field decreases and vice versa.

Chapter 6

Driven Motion of a Charged Particle Beam

Because the circulating beam in a synchrotron experiences linear restoring forces from quadrupole magnets, it is appropriate to envision beam particles as simple harmonic oscillators, executing periodic motion in the transverse plane as they orbit the synchrotron, with a natural frequency defined by the magnet lattice and the longitudinal beam momentum. In such an analogy, the AC dipole introduced in Chapter 4 is a tool to resonantly drive this periodic motion, and we describe such beam's motion as a driven harmonic oscillator, with large amplitude motion possible when the driving frequency approaches the beam's natural frequency. When a beam particle is driven by an AC dipole, its motion is not completely identical to the free oscillation, instead the motion is analogous to the case when there is a thin quadrupole field error [21]. This difference between the beam particles' free and driven oscillations affects the diagnostics of a synchrotron. Hence, in this chapter, we discuss the beam particles' motions excited by an AC dipole in detail based on [21], in order to properly determine desired parameters from observations of driven motions.

6.1 Two Modes Driven by an AC Dipole

Because the beam sees an AC dipole only once in a revolution, the beam is driven by a pair of driving terms with driving tunes $\nu_{\rm ac}$ and $1-\nu_{\rm ac}$ (cf. Nyquist sampling theorem). The driving term closer to the machine tune ν has a bigger influence on a particle. Hence, in the following, the driving term closer to ν is called the primary and the other is called the secondary. A symbol ν_d is used for the primary driving tune (Figure 6.1):

$$\nu_d \equiv \begin{cases} \nu_{\rm ac} & \text{when} \quad |\nu_{\rm ac}-\nu| < |(1-\nu_{\rm ac})-\nu| \\ 1-\nu_{\rm ac} & \text{when} \quad |(1-\nu_{\rm ac})-\nu| < |\nu_{\rm ac}-\nu| \ . \end{cases} \tag{6.1}$$

For example, the frequencies of the AC dipole and beam revolution in the Tevatron are $f_{\rm ac} \simeq 20.5$ kHz and $f_{\rm rev} \simeq 47.7$ kHz and, hence, the tune of the AC dipole is $\nu_{\rm ac} = 20.5/47.7 \simeq 0.43$. Because the machine tune of the Tevatron is $\nu \simeq 0.58$, $1-\nu_{\rm ac} \simeq 0.57$ is the primary driving tune and $\nu_{\rm ac} \simeq 0.43$ is secondary. We note that machine tunes near 0.5 tend to exaggerate the influence of the secondary driving term. The difference between the primary driving tune and the machine tune, $\delta_d \equiv \nu_d - \nu$, is an important parameter of driven oscillations. As $\delta_d \to 0$, the influence of the primary driving term becomes dominant and the secondary driving term can be ignored. In the Tevatron, the typical value of $|\delta_d|$ is about 0.005-0.015 to prevent beam losses, and at this value of $|\delta_d|$, the secondary driving term a 6-18% effect on the amplitude function inferred from AC dipole measurements, so must be accounted for correctly.

After the AC dipole has adiabatically ramped to full field, position of

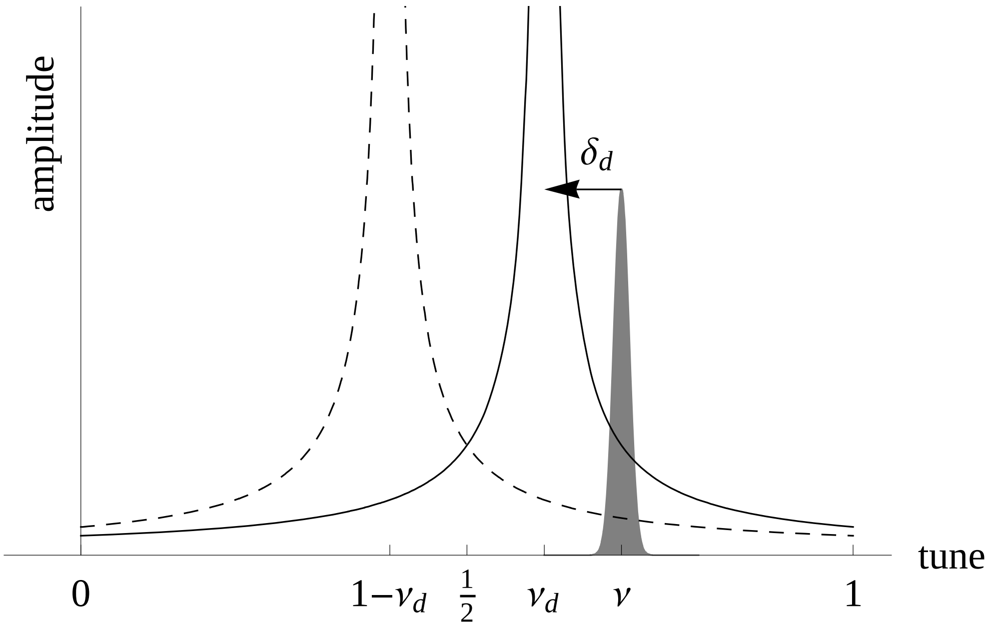

Figure 6.1: Two driving terms of an AC dipole. A circulating beam is driven by two driving terms of an AC dipole, ν_d and $1-\nu_d$. Solid and dashed lines represent amplitudes of modes driven by each driving terms. In typical operations of an AC dipole, realizable δ_d is limited by the tune spread of the beam (shaded area).

the driven beam $x_d(s)$ is given by[1].

$$\begin{aligned}
&x_d(nC+\tilde{s}) \\
&\simeq \frac{\theta_{\text{ac}}\sqrt{\beta_{\text{ac}}\beta(\tilde{s})}}{4\sin(\pi(\nu_d-\nu))} \\
&\qquad \times \cos(2\pi\nu_d n+\psi(\tilde{s}|\tilde{s}_{\text{ac}})+\pi(\nu_d-\nu)\text{sgn}(\tilde{s}-\tilde{s}_{\text{ac}})+\chi_d) \\
&\quad + \frac{\theta_{\text{ac}}\sqrt{\beta_{\text{ac}}\beta(\tilde{s})}}{4\sin(\pi(1-\nu_d-\nu))} \\
&\qquad \times \cos(2\pi(1-\nu_d)n+\psi(\tilde{s}|\tilde{s}_{\text{ac}})+\pi(1-\nu_d-\nu)\text{sgn}(\tilde{s}-\tilde{s}_{\text{ac}})-\chi_d)\,.
\end{aligned} \tag{6.2}$$

Derivation of this equation can be seen in [43, 48]. Here, θ_{ac} is the maximum kick angle of the AC dipole, β_{ac} is the amplitude function at the location of the AC dipole, and χ_d is a constant phase. We can see the two terms in Equation 6.2 are symmetric between ν_d and $1-\nu_d$. These two terms represent two modes excited by two driving terms of an AC dipole. In Equation 6.2, longitudinal position s is expressed with n, C, and $\tilde{s}$, because phases in Equation 6.2 cannot be expressed with one continuous function of the longitudinal position s. When a particle goes through the AC dipole, phases in each terms jump by $2\pi(\nu_d-\nu)$ and $2\pi(1-\nu_d-\nu)$.

To quantify the influence of the secondary driving term, we use a parameter to describe the ratio between magnitudes of two modes:

$$\lambda_d \equiv \frac{\sin(\pi(\nu_d-\nu))}{\sin(\pi(1-\nu_d-\nu))} = \frac{\sin(\pi\delta_d)}{\sin(2\pi\nu+\pi\delta_d)}\ . \tag{6.3}$$

As this parameter depends on not only δ_d but also the machine tune ν, the magnitude of the secondary mode, relative to the primary mode, depends on

---

[1] The exact expression of x_d includes transient modes which are inversely proportional to the ramp up time and oscillate with the machine tune ν. If the ramp up is slow enough, all of these modes are very small and decohere before the end of the ramp up. Hence, these ignored modes do not affect the motion of the beam centroid but they may affect the beam size.

the machine tune as well. For instance, when $|\delta_d| = 0.01$ and $\nu \simeq 0.58$ as in a typical condition in the Tevatron, $|\lambda_d| \simeq 0.06$. Whereas, when the machine tune is $\nu \simeq 0.3$ like the LHC, the same $|\delta_d| = 0.01$ gives about half of $|\lambda_d|$ compared to the Tevatron.

6.2 Optical Parameters of the Driven Motion

We note that Equation 6.2 can be written in the following compact form [21]:

$$x_d(s) = A_d\sqrt{\beta_d(s)}\cos(\psi_d(s|\tilde{s}_{\rm ac}) + \chi_d)\ . \tag{6.4}$$

When we observe turn-by-turn oscillations of the driven motion, the following equivalent form may be convenient:

$$x_d(nC + \tilde{s}) = A_d\sqrt{\beta_d(\tilde{s})}\cos(2\pi\nu_d n + \psi_d(\tilde{s}|\tilde{s}_{\rm ac}) + \chi_d)\ . \tag{6.5}$$

Because Equation 6.4 has the same mathematical form as the free betatron motion given in Equation 2.29, this expression is more convenient than Equation 6.2 when we compare the driven motion to the free betatron motion. Here, A_d is a constant parameter with dimensions of (length)$^{1/2}$, which is analogous to the constant parameter A in Equation 2.29:

$$A_d \equiv \frac{\theta_{\rm ac}}{4\sin(\pi\delta_d)}\sqrt{(1-\lambda_d^2)\beta(\tilde{s}_{\rm ac})}\ . \tag{6.6}$$

The quantity $\beta_d(s)$ is a newly defined amplitude function of the driven motion:

$$\beta_d(s) \equiv \frac{1+\lambda_d^2 - 2\lambda_d\cos(2\psi(\tilde{s}|\tilde{s}_{\rm ac}) - 2\pi\nu\,{\rm sgn}(\tilde{s}-\tilde{s}_{\rm ac}))}{1-\lambda_d^2}\beta(s)\ . \tag{6.7}$$

The quantity $\psi_d(s|\tilde{s}_{\rm ac})$ is a newly defined phase advance of the driven motion. Similar to the free betatron motion, for two arbitrary longitudinal positions s

and s_0, the phase advance of the driven motion is defined with the amplitude function

$$\psi_d(s|s_0) \equiv \int_{s_0}^{s} \frac{d\bar{s}}{\beta_d(\bar{s})} \ . \tag{6.8}$$

The following equation gives a relation between phase advances of the driven and free betatron motions, $\psi_d(\tilde{s}|\tilde{s}_{\mathrm{ac}})$ and $\psi(\tilde{s}|\tilde{s}_{\mathrm{ac}})$:

$$\begin{aligned} &\tan(\psi_d(\tilde{s}|\tilde{s}_{\mathrm{ac}}) - \pi\nu_d \,\mathrm{sgn}(\tilde{s} - \tilde{s}_{\mathrm{ac}})) \\ &\quad = \frac{1+\lambda_d}{1-\lambda_d} \tan(\psi(\tilde{s}|\tilde{s}_{\mathrm{ac}}) - \pi\nu \,\mathrm{sgn}(\tilde{s} - \tilde{s}_{\mathrm{ac}})) \\ &\quad = \frac{\tan(\pi\nu_d)}{\tan(\pi\nu)} \tan(\psi(\tilde{s}|\tilde{s}_{\mathrm{ac}}) - \pi\nu \,\mathrm{sgn}(\tilde{s} - \tilde{s}_{\mathrm{ac}})) \ . \end{aligned} \tag{6.9}$$

From this equation, we can see $\psi_d(\tilde{s}_{\mathrm{ac}} + C|\tilde{s}_{\mathrm{ac}}) = 2\pi\nu_d$ when $\psi(\tilde{s}_{\mathrm{ac}} + C|\tilde{s}_{\mathrm{ac}}) = 2\pi\nu$ after a single revolution. Compared to Equation 6.2, when we combine the two modes, the phase $\psi_d(s|\tilde{s}_{\mathrm{ac}})$ in Equation 6.4 is a continuous function of s and does not have a discrete change at the location of the AC dipole. By comparing the equations of the driven and free betatron motions, Equation 6.4 and 2.29, we can see the difference of these motions lies in the different amplitude functions, $\beta_d(s)$ and $\beta(s)$, and phase advances, $\psi_d(s|s_0)$ and $\psi(s|s_0)$. As expected, in the limit $\nu_d \to \nu$, λ_d becomes zero and $\beta_d(s)$ and $\psi_d(s|s_0)$ converge to $\beta(s)$ and $\psi(s|s_0)$.

Because Equation 6.4 for the driven motion has the same mathematical form as Equation 2.29 for the free betatron motion, in real measurements, we observe the driven motion's parameters, $\beta_d(s)$ and $\psi_d(s|s_0)$, instead of the free motion's parameters, $\beta(s)$ and $\psi(s|s_0)$. Thus, without careful interpretation of data obtained with an AC dipole, one might interpret the "driven particle" amplitude function as "free particle" amplitude function and is so doing 12% error in the measurement of the amplitude function. We also note the relation between δ_d and $\beta_d(s)$ is exactly the same as the relation between the tune shift and new $\beta(s)$ function when there is a thin gradient error [21]. Similarly, the relation between δ_d and $\psi_d(s|s_0)$ is exactly the same as the relation between the tune shift and the new phase advance when there is a thin quadrupole field error. Hence, the operation of an AC dipole in a synchrotron would be expected to excite a pattern of beam motion identical to the perturbation due to a thin quadrupole field error. Like a quadrupole field error, the AC dipole actually introduces a beta-beat pattern around the synchrotron whose amplitude is $2\lambda_d$ for the amplitude function and λ_d for the phase advance.

Figures 6.2 and 6.3 show numerical calculations of $\beta_d(s)/\beta(s)$ and $\psi_d(s|\tilde{s}_{\text{ac}})-\psi(s|\tilde{s}_{\text{ac}})$, based on Equations 6.7 and 6.9, for different $\psi(s|\tilde{s}_{\text{ac}})$ and δ_d. The two plots in each figure are for different machine tunes: $\nu = 0.58$ like the Tevatron and $\nu = 0.3$ like the LHC. In the figures, when $\nu = 0.58$ and $\delta_d = \pm 0.01$, we can see the beating amplitudes are roughly 10% for $\beta_d(s)$ and 5% for $\psi_d(s|\tilde{s}_{\text{ac}})$. When $\nu = 0.3$, the deviations of $\beta_d(s)$ and $\psi_d(s|\tilde{s}_{\text{ac}})$ from $\beta(s)$ and $\psi(s|\tilde{s}_{\text{ac}})$ are almost as half as when $\nu = 0.58$. We can see, when $\nu = 0.58$, curves are more asymmetric between positive and negative sides of δ_d. The curves in Figures 6.2 and 6.3 represent the potential error in experimental measurements when an AC dipole operated at a given δ_d is utilized.

Parameters corresponding to the other Courant-Snyder parameters, α and γ, can be also defined as for the free betatron oscillation:

$$\alpha_d(s) \equiv -\frac{1}{2}\frac{d\beta_d(s)}{ds} \ , \quad \gamma_d(s) \equiv \frac{1+\alpha_d(s)^2}{\beta_d(s)} \ . \tag{6.10}$$

The explicit forms of these parameters are given by

$$\begin{aligned}\alpha_d(s) = {} & \frac{1+\lambda_d^2-2\lambda_d\cos(2\psi(\tilde{s}|\tilde{s}_{\text{ac}})-2\pi\nu\,\text{sgn}(\tilde{s}-\tilde{s}_{\text{ac}}))}{1-\lambda_d^2}\,\alpha(s) \\ & - \frac{2\lambda_d\sin(2\psi(\tilde{s}|\tilde{s}_{\text{ac}})-2\pi\nu\,\text{sgn}(\tilde{s}-\tilde{s}_{\text{ac}}))}{1-\lambda_d^2}\end{aligned} \tag{6.11}$$

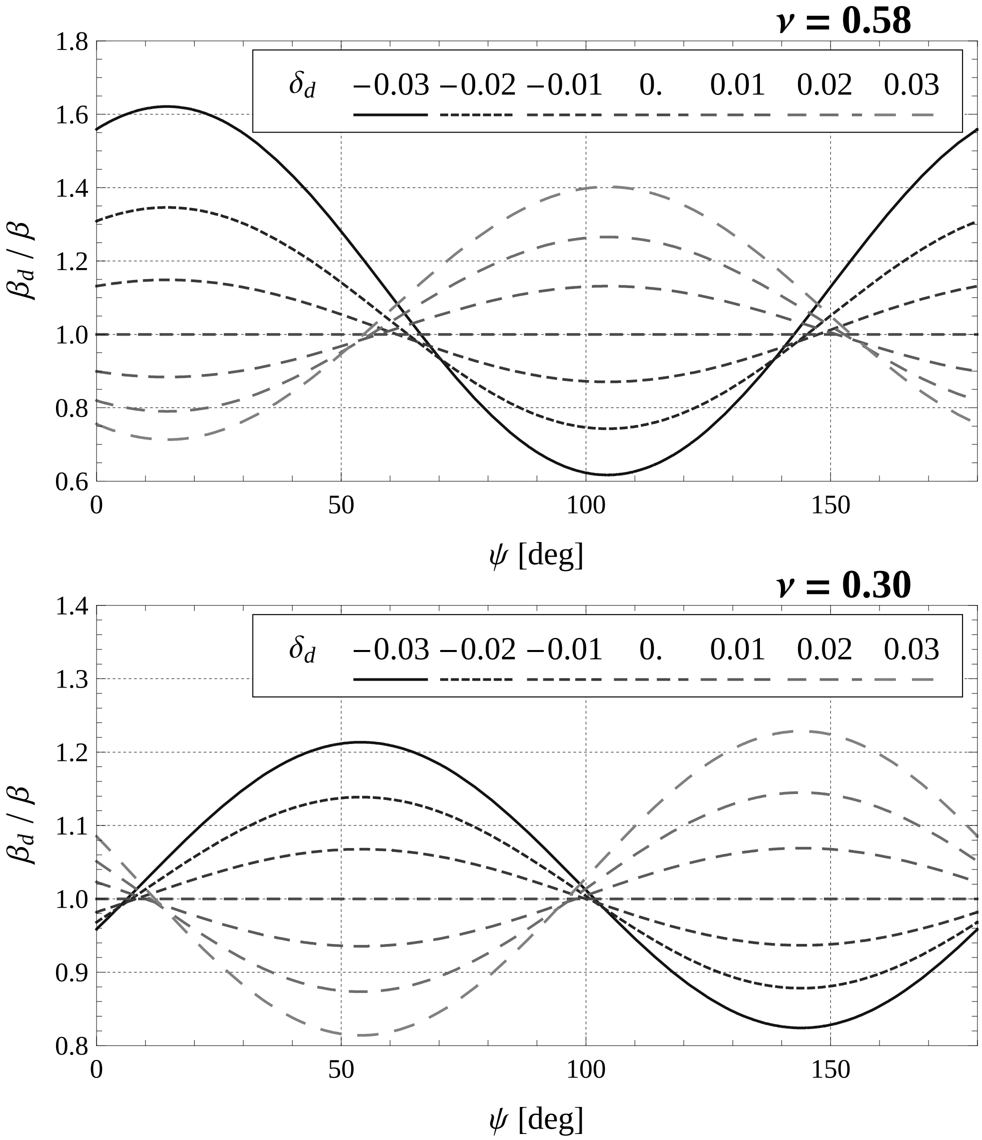

Figure 6.2: Calculated amplitude functions of the driven and free betatron motions, $\beta_d(s)$ and $\beta(s)$. The ratio $\beta_d(s)/\beta(s)$ is calculated based on Equation 6.7 for different phase advance $\psi(s|\tilde{s}_{\text{ac}})$ and $\delta_d = \nu_d - \nu$ when the machine tune is $\nu = 0.58$ like the Tevatron and $\nu = 0.30$ like the LHC. As in the beam influenced by a gradient error, $\beta_d(s)$ is beating relative to β. Compared to $\nu = 0.3$, when $\nu = 0.58$, the deviations from $\beta(s)$ is larger and curves are more asymmetric between positive and negative sides of δ_d.

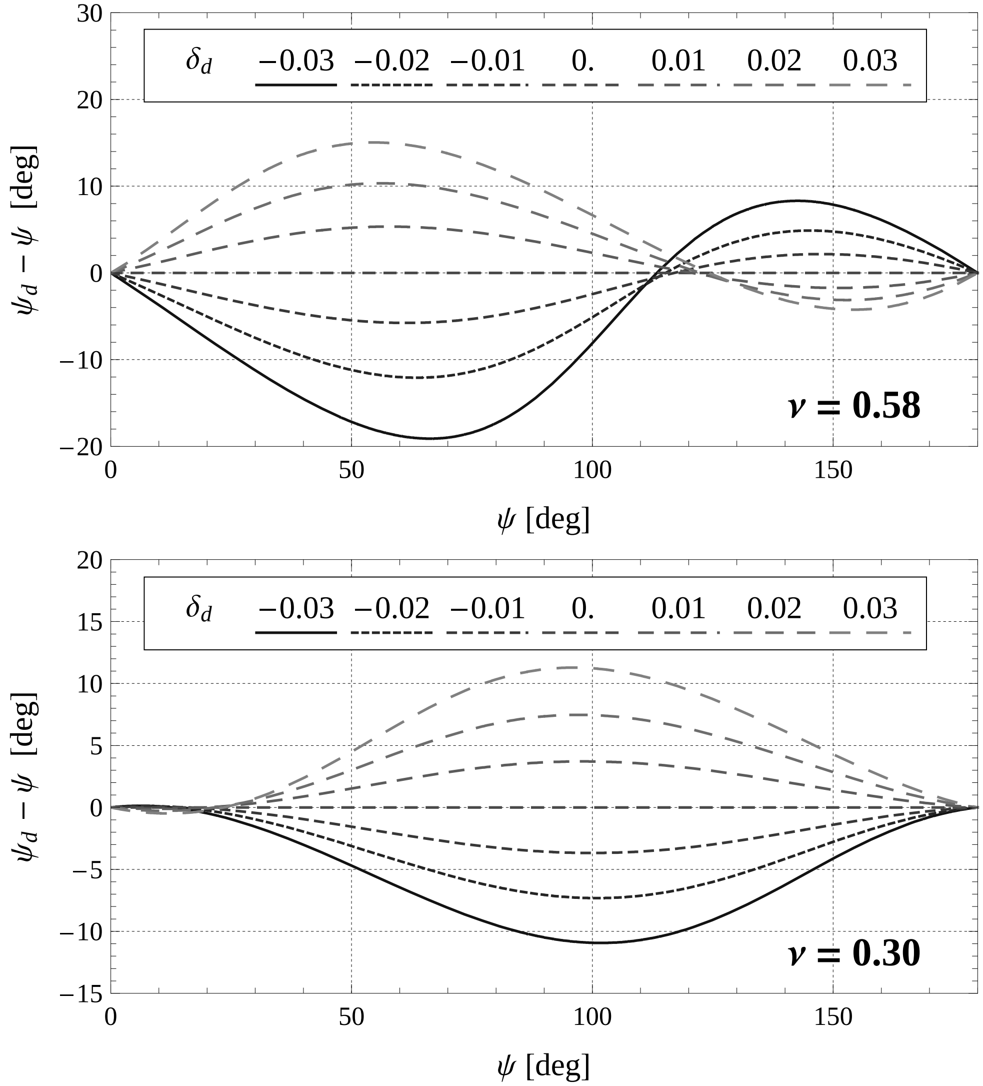

Figure 6.3: Calculated phase advances of the driven and free betatron motions, $\psi_d(s|\tilde{s}_{\mathrm{ac}})$ and $\psi(s|\tilde{s}_{\mathrm{ac}})$. The difference $\psi_d(s|\tilde{s}_{\mathrm{ac}}) - \psi(s|\tilde{s}_{\mathrm{ac}})$ is calculated based on Equation 6.9 for different phase advance $\psi(s|\tilde{s}_{\mathrm{ac}})$ and $\delta_d = \nu_d - \nu$ when the machine tune is $\nu = 0.58$ like the Tevatron and $\nu = 0.30$ like the LHC. As in the beam influenced by a gradient error, $\psi_d(s|\tilde{s}_{\mathrm{ac}})$ is beating relative to $\psi(s|\tilde{s}_{\mathrm{ac}})$. Compared to $\nu = 0.3$, when $\nu = 0.58$, the deviations from $\psi(s|\tilde{s}_{\mathrm{ac}})$ is larger and curves are more asymmetric between positive and negative sides of δ_d.

and

$$\gamma_d(s) = \frac{1+\lambda_d^2 + 2\lambda_d \cos(2\psi(\tilde{s}|\tilde{s}_{\mathrm{ac}}) - 2\pi\nu\,\mathrm{sgn}(\tilde{s}-\tilde{s}_{\mathrm{ac}}) + 2\arctan\alpha(s))}{1-\lambda_d^2}\,\gamma(s)\ . \tag{6.12}$$

When $\beta_d(s)$, $\alpha_d(s)$, $\gamma_d(s)$, and A_d are defined this way, they satisfy the Courant-Snyder invariance:

$$A_d^2 = \gamma_d(s)x_d(s)^2 + 2\alpha_d(s)x_d(s)x_d'(s) + \beta_d(s)x_d'(s)^2\ . \tag{6.13}$$

From this equation, in the phase space at one location of a circular accelerator, a particle driven by an AC dipole moves on an ellipse, as in the free betatron motion. However, since not only A_d but also $\beta_d(s)$, $\alpha_d(s)$, and $\gamma_d(s)$ depend on δ_d, both the area and shape of the ellipse changes along with δ_d for the driven motion. In the limit $\delta_d \to 0$, since $\beta_d(s)$, $\alpha_d(s)$, and $\gamma_d(s)$ converge to $\beta(s)$, $\alpha(s)$, and $\gamma(s)$, shapes of the ellipses for the driven and free betatron motions become identical. Fig 6.4 shows the several measurements of the phase space ellipses of the driven motions measured with a pair of such BPM's in the Tevatron when the AC dipole is operated at several values of δ_d. In the measurements, the beam is driven with different δ_d while the kick angle θ_{ac} is kept the same. As expected, shapes of the ellipses are different for different δ_d.

6.3 Amplitude Response

The secondary driving term can also be observed directly by its induced asymmetric amplitude response around the free oscillation tune. When the influence of the secondary driving term is negligible, by ignoring the smaller term of Equation 6.2 or taking the limit $\lambda_d \to 0$ in Equations 6.4, 6.6, and 6.7, the

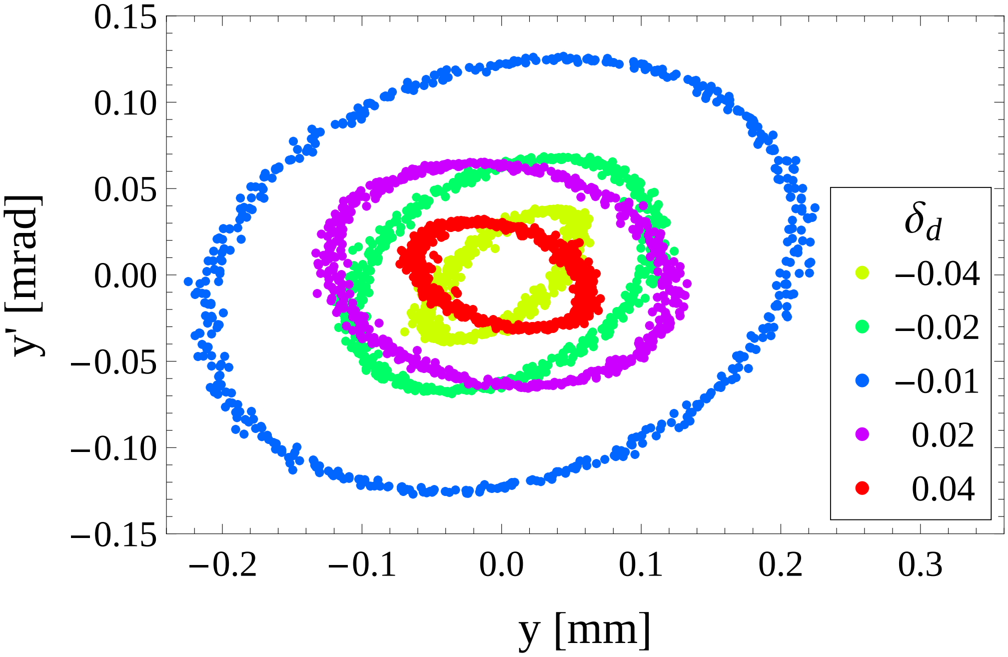

Figure 6.4: Phase space ellipses of the driven motion. The location is a low-β point (B0) of the Tevatron where $\alpha = 0$ by design. Since the Courant-Snyder parameters of the driven motion $\beta_d(s)$, $\alpha_d(s)$, and $\gamma_d(s)$ depend on δ_d, both area and shape of the ellipse change with δ_d for the driven motion.

amplitude of the driven motion is by

$$a_d^{(0)}(\tilde{s}) \equiv \left| A_d \sqrt{\beta_d(\tilde{s})} \right|_{\lambda_d \to 0} = \frac{\theta_{\mathrm{ac}} \sqrt{\beta(\tilde{s}_{\mathrm{ac}})\beta(\tilde{s})}}{4|\sin(\pi\delta_d)|} \ . \tag{6.14}$$

In this case, the amplitude depends on the primary driving tune ν_d only through the term $|\sin(\pi\delta_d)|$ and is symmetric around the free oscillation tune ν. Such would be the case for a simple driven harmonic oscillator, where the amplitude diverges as $1/(\omega_d^2 - \omega_0^2)$ (Equation 3.4). From Equations 6.4, 6.6, and 6.7, the amplitude fully including the influence of the secondary driving term $a_d(\tilde{s})$ is given by

$$a_d(\tilde{s}) = a_d^{(0)}(\tilde{s}) \sqrt{1 + \lambda_d^2 - 2\lambda_d \cos(2\psi(\tilde{s}|\tilde{s}_{\mathrm{ac}}) - 2\pi\nu \,\mathrm{sgn}(\tilde{s} - \tilde{s}_{\mathrm{ac}}))} \ . \tag{6.15}$$

Here, the amplitude $a_d(\tilde{s})$ depends on ν_d through the factor $[1 + \lambda_d^2 - 2\lambda_d \cos(2\psi(\tilde{s}|\tilde{s}_{\mathrm{ac}}) - 2\pi\nu \,\mathrm{sgn}(\tilde{s} - \tilde{s}_{\mathrm{ac}}))]^{1/2}$ as well. If we expand a_d to the first order of δ_d,

$$a_d(\tilde{s}) \simeq a_d^{(0)}(\tilde{s}) \left[1 - \frac{\pi \cos(2\psi(\tilde{s}|\tilde{s}_{\mathrm{ac}}) - 2\pi\nu \,\mathrm{sgn}(\tilde{s} - \tilde{s}_{\mathrm{ac}}))}{\sin(2\pi\nu)} \delta_d \right] \ . \tag{6.16}$$

Hence, the secondary driving term makes the ν_d dependence of the amplitude asymmetric around the machine tune ν. That is $a_d(\tilde{s})$ depends on whether we operate the AC dipole with $\delta_d < 0$ or $\delta_d > 0$. The magnitude of this asymmetry at each location is determined by the factor $\cos(2\psi(\tilde{s}|\tilde{s}_{\mathrm{ac}}) - 2\pi\nu \,\mathrm{sgn}(\tilde{s} - \tilde{s}_{\mathrm{ac}}))$.

Figure 6.5 shows the measured amplitude of the driven motion for different ν_d at three BPM locations in the Tevatron. In the measurements, only ν_d is changed and the current in the AC dipole magnet is kept the same and thus the maximum kick strength θ_{ac} is also kept the same. The dashed and solid curves are the fits of Equations 6.14 and 6.15 to the data. The fit parameters are the factor $\theta_{\mathrm{ac}}[\beta(\tilde{s}_{\mathrm{ac}})\beta(\tilde{s})]^{1/2}$ and the free oscillation tune ν for Equation 6.14 and $\theta_{\mathrm{ac}}[\beta(\tilde{s}_{\mathrm{ac}})\beta(\tilde{s})]^{1/2}$, ν, and the phase $\psi(\tilde{s}|\tilde{s}_{\mathrm{ac}})$ for Equation

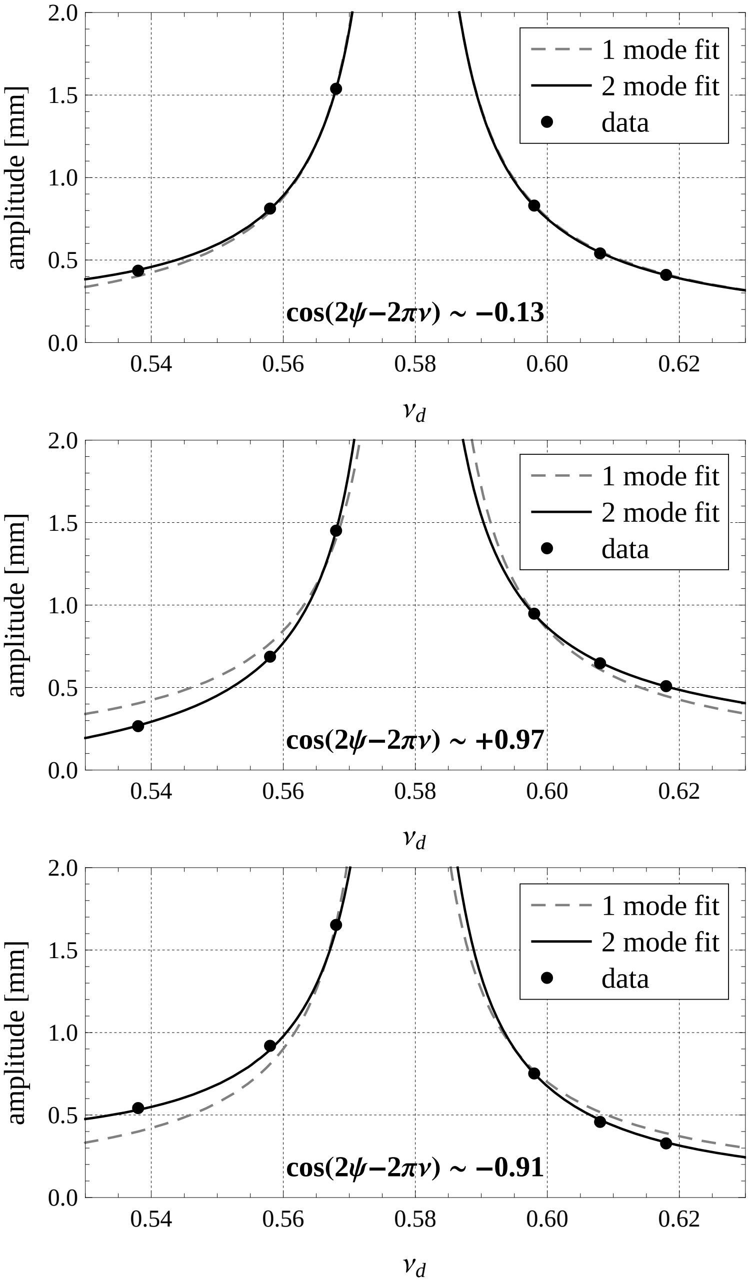

Figure 6.5: Measured amplitude of the driven motion vs. ν_d at three BPM locations in the Tevatron. The current in the AC dipole is kept constant while ν_d is changed. At locations where $\cos(2\psi(\tilde{s}|\tilde{s}_{\mathrm{ac}}) - 2\pi\nu\,\mathrm{sgn}(\tilde{s}-\tilde{s}_{\mathrm{ac}}))$ is not close to zero, the amplitude response is asymmetric around the free oscillation tune ν and the fits ignoring the secondary driving term (dashed curves) are not well matched to the data.

6.15. In the first plot, when the particular location around the synchrotron such that $\cos(2\psi(\tilde{s}|\tilde{s}_{\rm ac}) - 2\pi\nu\,\mathrm{sgn}(\tilde{s} - \tilde{s}_{\rm ac}))$ is close to zero, both fits are not far apart. However, in the second and third plots, close to locations around the synchrotron when $\cos(2\psi(\tilde{s}|\tilde{s}_{\rm ac}) - 2\pi\nu\,\mathrm{sgn}(\tilde{s} - \tilde{s}_{\rm ac}))$ is close to one, the asymmetry around the free oscillation tune ($\nu \simeq 0.5786$) is large and the fit ignoring the secondary driving term is not well matched to the data. We can also see, in the second plot, the amplitude in the side $\nu_d > \nu$ is larger than that of the side $\nu_d < \nu$ and the relation is inverted when the sign of $\cos(2\psi(\tilde{s}|\tilde{s}_{\rm ac}) - 2\pi\nu\,\mathrm{sgn}(\tilde{s} - \tilde{s}_{\rm ac}))$ is flipped in the third plot.

In the fits in Figure 6.5, the free oscillation tune ν is a fit parameter determined at each BPM location. Figure 6.6 shows the free oscillation tunes determined as fit parameters at all BPM locations around the Tevatron. In the figure, the solid curve is from the fits including the secondary driving term and the dashed curve is from the fits ignoring it. Since the free oscillation tune ν is a global parameter of a synchrotron accelerator, the variation of the determined machine tunes over BPM's shows inaccuracy of the measurements and data analyses. The fact that the free oscillation tune ν is now stably fit at a certain value when the two modes are included points to the validity of the secondary driving term formalism presented here.

Because one of the fit parameter is $\theta_{\rm ac}[\beta(\tilde{s}_{\rm ac})\beta(\tilde{s})]^{1/2}$, from these fits in Figure 6.5 including the secondary driving term, we can determine the amplitude function of the free oscillations at each BPM location (up to a constant). An advantage of this method is that we can also determine the free oscillation tune. On the other hand, for this method, we have to know the current in the AC dipole magnet accurately. Because the free oscillation tune is an important parameter of a synchrotron, we usually have other instruments to accurately measure the free oscillation tune [49]. If the free oscillation tune

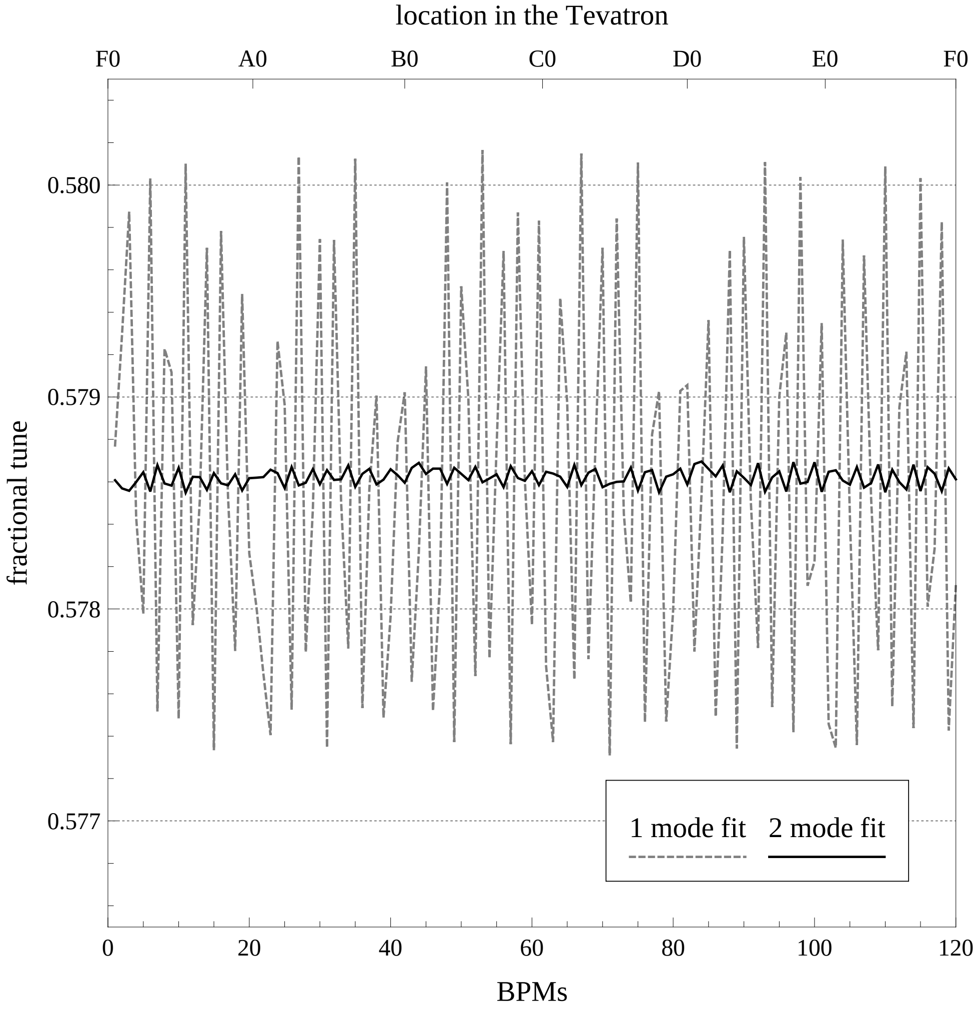

Figure 6.6: Free oscillation tunes determined as fit parameters of the amplitude responses at each BPM locations around the Tevatron. Inclusion of the secondary driving term in the fits gives a much consistent result for the machine free oscillation tune (global parameter).

is well known, there is another way to extrapolate the amplitude function of the free oscillations from data sets of the driven motions at several different frequencies of the AC dipole, without depending on measurement of the current in the AC dipole magnet. This analysis will be discussed in the next chapter.

6.4 Summary

Because of the synchrotron's periodicity, the sinusoidally-varying AC dipole's field effectively produces the two driving tunes to the circulating beam particles. The existence of the two driving tunes makes the beam particles' driven motions different from their free oscillations, as if there is a thin quadrupole field error at the location of the AC dipole, changing the amplitude function and phase advance depending on the difference between the driving tune and free betatron tune, δ_d. Figures 6.4 and 6.6 show such difference between the driven oscillations and free oscillations can be observed in the Tevatron as expected. If such difference is not properly accounted for, the measurement of the amplitude function and phase advance with an AC dipole may have significantly large errors, depending on δ_d.

Chapter 7

Linear Optics Measurement Using an AC Dipole

To sustain the luminosity of a collider, it is ideal to constantly monitor the amplitude function at interaction points. When the amplitude function is seen to change from its desired value, we have to make ring-wide measurement of the amplitude function or phase advance to find locations of the errors.

To date, two methods are mainly used to measure the amplitude function in the two interaction regions of the Tevatron. One is the (differential) orbit response measurement [51, 52], where we intentionally change the central orbit by varying known dipole magnets and construct a detailed model which reproduces the observed central changes. The parameters in the interaction region are inferred from the model. The other method uses the physics detectors [53]: by reconstructing the locations of collision events, we can observe shape and location of the luminous region inside a detector and thus can determine the amplitude function and emittance. This method assesses the amplitude function only in the interaction region, however. Both methods are time-consuming, requiring many hours of experimental data acquisition and lengthy off-line data analyses.

This chapter discusses techniques to measure linear optical parameters of a synchrotron using the AC dipole. The techniques presented here utilize the results of Chapter 6, in which a suite of measurements are made with the AC dipole at several frequencies near the betatron tune. The measurements require only a few minutes of time, permitting frequent feedback.

7.1 Diagnosis of an Interaction Region

Figure 7.1 shows a schematic layout of an interaction straight region in the Tevatron. The two interaction regions in the Tevatron are identical. Between a pair of the quadrupole triples, squeezing the transverse beam size and thus maximizing the luminosity (Equation 1.4), there is no magnetic elements[1]. As seen in Sections 2.2.3 and 2.3.4, in a drift space, the amplitude function is described by a parabolic function:

$$\beta(\tilde{s}) = \beta^* + \frac{1}{\beta^*}(\tilde{s} - \tilde{s}^*)^2 \ , \tag{7.1}$$

where β^* is the minimum value of the amplitude function and $\tilde{s}^*$ is the location of the beam waist, as depicted in Figure 7.1. In the design of a collider, the beam waist is located at the center of a physics detector. Quadrupole field errors change the amplitude function, including β^* and the location of the beam waist s^*, and thus may degrade the luminosity (Equation 1.4). Hence, in operations of a collider, it is desired to monitor β^* and s^* as often as possible.

As depicted in the figure, there are two BPM's in the straight region

---

[1] An exception is solenoids of the physics detectors. Because influence of these solenoids' field is small [54], we simply ignore them in the following.

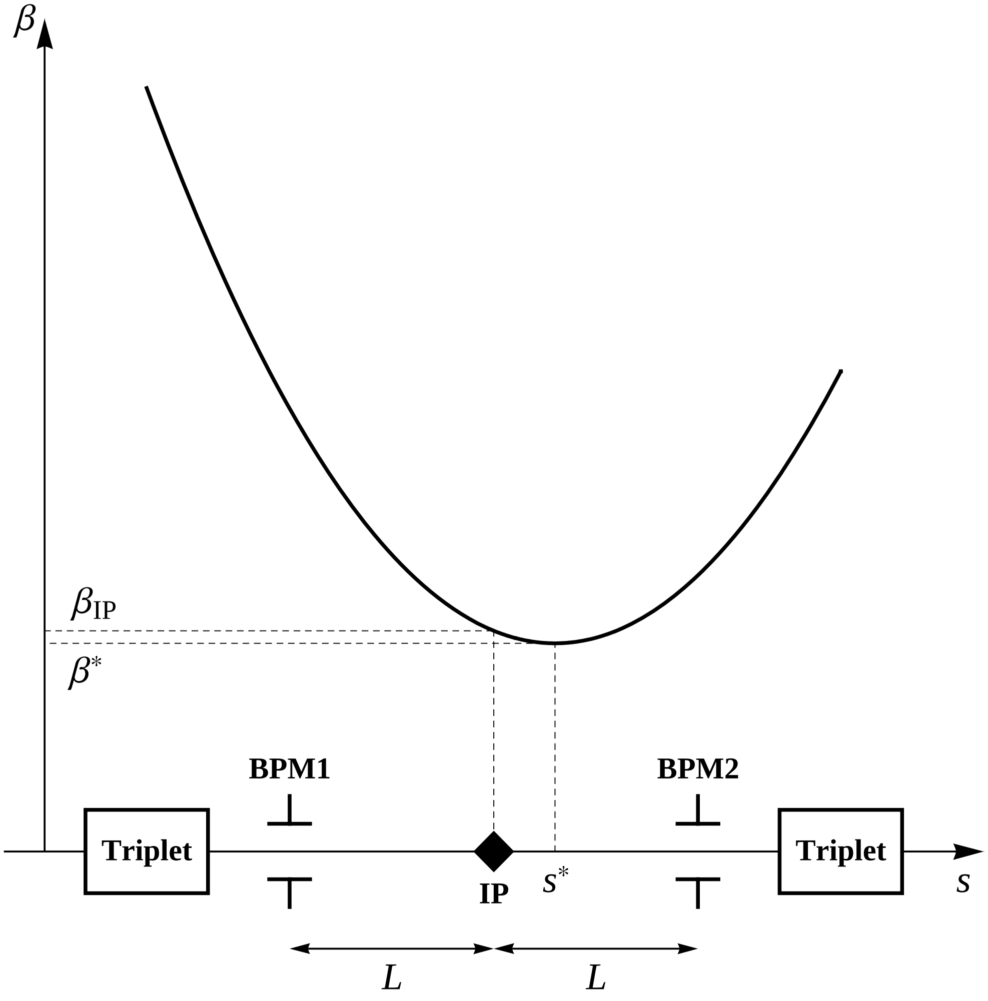

Figure 7.1: Schematic layout an interaction region in the Tevatron. Between the quadrupole triplets, squeezing the transverse beam sizes for collisions, no magnetic element exists and particles travel on straight lines. In such a region, the amplitude function changes as a parabolic function (Sections 2.2.3 and 2.3.4). From data of the two BPM's, **BPM1** and **BPM2**, we can reconstruct the phase space mapping, and thus can determine the minimum value of the amplitude function, β^*, and the beam waist location, s^*.

between the quadrupole triplets[2]. Because particles travel on straight lines in a magnet free straight region, we can measure the beam's angle in this region by using these two BPM's. The beam angle at these two location, x'_1 and x'_2, are given by

$$x'_1 = x'_2 = \frac{1}{2L}(x_2 - x_1) \ , \tag{7.2}$$

where x_1 and x_2 are beam positions at **BPM1** and **BPM2**, L is the distance from the interaction point to each BPM. For the Tevatron, $L = 7.483$ m in the horizontal plane and $L = 7.363$ m in the vertical plane. By simultaneously observing position and angle for multiple revolutions, we can reconstruct the phase space and, thus, the Courant-Snyder parameters[54, 56].

There are several analysis methods to determine the minimum value of the amplitude function, β^*, and offset of the beam waist location from the desired value, Δs^*, from data of the turn-by-turn oscillations, observed by the two BPM's in the interaction region. Here, we discuss an analysis to determine β^* and Δs^* from the amplitudes and phases of these turn-by-turn oscillations. In data of turn-by-turn oscillations, such as Figure 4.5, we can determine the amplitude and phase by fitting a sinusoidal function to the data points. From Equation 6.5, when the beam is driven by the AC dipole, the beam's positions observed by these two BPM's are given by

$$x_d(nC + \tilde{s}_{1,2}) = A_d\sqrt{\beta_d(\tilde{s}_{1,2})}\cos(2\pi\nu_d n + \psi_d(\tilde{s}_{1,2}|\tilde{s}_{\mathrm{ac}}) + \chi_d) \ , \tag{7.3}$$

where $\tilde{s}_1$ and $\tilde{s}_2$ are locations of the two BPM's, **BPM1** and **BPM2**, and $\tilde{s}_{1,2}$ is a shorthand notation indicating either $\tilde{s}_1$ or $\tilde{s}_2$. We rewrite this equation in

---

[2] The figure shows only one transverse plane and there are four BPM's in total: two in horizontal plane and two in vertical plane.

the following way:

$$x_d(nC+\tilde{s}_1) = a_{d,1}\cos(2\pi\nu_d n + \bar{\chi}_d) \tag{7.4}$$

$$x_d(nC+\tilde{s}_2) = a_{d,2}\cos(2\pi\nu_d n + \psi_d(\tilde{s}_2|\tilde{s}_1) + \bar{\chi}_d)\ . \tag{7.5}$$

These amplitudes, $a_{d,1} \equiv A_d\sqrt{\beta_d(\tilde{s}_1)}$ and $a_{d,2} \equiv A_d\sqrt{\beta_d(\tilde{s}_2)}$, and phases, $\psi_d(\tilde{s}_2|\tilde{s}_1)$ and $\bar{\chi}_d \equiv \psi_d(\tilde{s}_1|\tilde{s}_{\mathrm{ac}}) + \chi_d$, are the quantities directly determined from data of the turn-by-turn oscillations. We note that, because the phase $\bar{\chi}_d$ depends on an arbitrary phase χ_d, any physical quantity should be independent of $\bar{\chi}_d$ and should only depend on the relative phase difference of the two BPM locations $\psi_d(\tilde{s}_2|\tilde{s}_1)$. Given these amplitudes and phases, the quantities corresponding to β^* and $\mathit{\Delta} s^*$ for driven betatron oscillations, β^*_d and $\mathit{\Delta} s^*_d$, are determined from the following equations:

$$\beta^*_d = \frac{2a_{d,1}a_{d,2}\sin(\psi_d(\tilde{s}_2|\tilde{s}_1))}{a_{d,1}^2 + a_{d,2}^2 - 2a_{d,1}a_{d,2}\cos(\psi_d(\tilde{s}_2|\tilde{s}_1))}L \tag{7.6}$$

$$\mathit{\Delta} s^*_d = \frac{a_{d,1}^2 - a_{d,2}^2}{a_{d,1}^2 + a_{d,2}^2 - 2a_{d,1}a_{d,2}\cos(\psi_d(\tilde{s}_2|\tilde{s}_1))}L\ . \tag{7.7}$$

The constant A_d is also determined from these amplitudes and phases:

$$A_d = \sqrt{\frac{a_{d,1}a_{d,2}\sin(\psi_d(\tilde{s}_2|\tilde{s}_1))}{2L}}\ . \tag{7.8}$$

The last step to determine β^* and $\mathit{\Delta} s^*$ of free betatron oscillations is to make measurements of β^*_d and $\mathit{\Delta} s^*_d$ at several different frequencies of the AC dipole and to extrapolate to the case $\delta_d = 0$. Figure 7.2 shows β^*_d and $\mathit{\Delta} s^*_d$ of several different δ_d, measured in one interaction region of the Tevatron, referred to as B0 interaction region. The curves represent the fits to these data

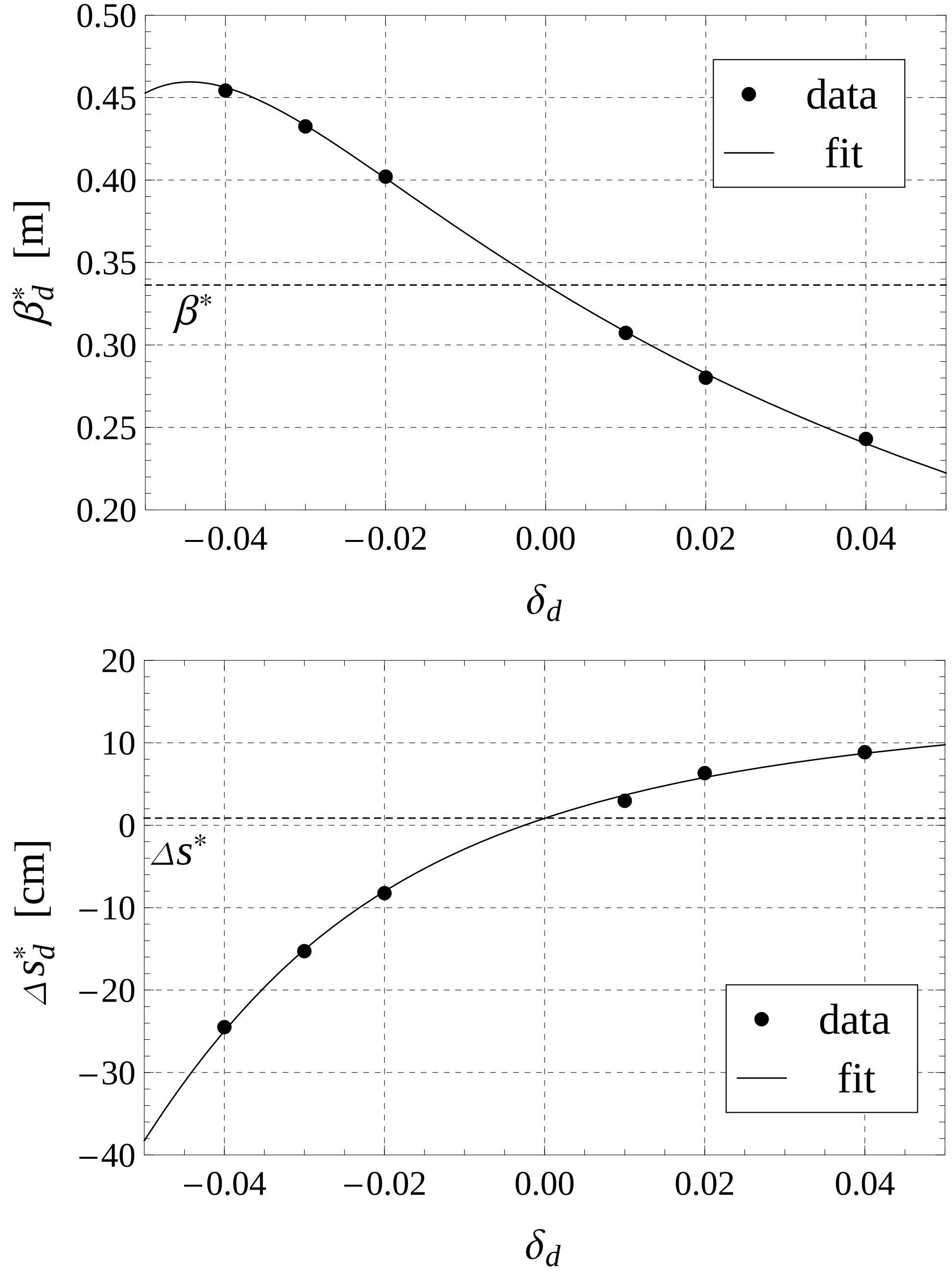

Figure 7.2: β_d^* and Δs_d^* vs. δ_d. For the free betatron oscillations' β^* and s^* can be extrapolated from the driven oscillations' β_d^* and Δs_d^* of several different frequencies. In the figure, β^* and s^* corresponds to the values when $\delta_d = 0$.

points using Equations 2.54, 2.55, 6.11, and 6.12:

$$\begin{aligned}
\beta_d^* &= \frac{1}{\gamma_d(\tilde{s}^*)} \\
&= \frac{1-\lambda_d^2}{1+\lambda_d^2+2\lambda_d\cos(2\psi(\tilde{s}^*|\tilde{s}_{\mathrm{ac}})-2\pi\nu\,\mathrm{sgn}(\tilde{s}^*-\tilde{s}_{\mathrm{ac}}))}\,\beta^* \qquad (7.9)\\
\mathit{\Delta} s_d^* &= \frac{\alpha_d(\tilde{s}^*)}{\gamma_d(\tilde{s}^*)} \\
&= \mathit{\Delta} s^* - \frac{2\lambda_d\sin(2\psi(\tilde{s}^*|\tilde{s}_{\mathrm{ac}})-2\pi\nu\,\mathrm{sgn}(\tilde{s}^*-\tilde{s}_{\mathrm{ac}}))}{1+\lambda_d^2+2\lambda_d\cos(2\psi(\tilde{s}^*|\tilde{s}_{\mathrm{ac}})-2\pi\nu\,\mathrm{sgn}(\tilde{s}^*-\tilde{s}_{\mathrm{ac}}))}\,\beta^* \ . \qquad (7.10)
\end{aligned}$$

In these equations, the free parameters are β^*, $\mathit{\Delta} s^*$, and $\psi(\tilde{s}^*|\tilde{s}_{\mathrm{ac}})$, which is the phase advance from the location of the AC dipole to the location of the beam waist. In the figure, we can see these functions fit well to the data points. The extrapolated minimum value of the amplitude function and offset of the beam waist location are $\beta^* = 0.34$ m and $\mathit{\Delta} s^* = 0.086$ cm.

7.2 Ring-wide Measurement

When the measured values of β^* and $\mathit{\Delta} s^*$ are different from the desired values, we have to make ring-wide measurements of the amplitude function or phase advance to find locations of the error sources.

We again start from the equation to describe the position of the turn-by-turn oscillations when the beam is driven by the AC dipole (Equation 6.5):

$$x_d(nC+\tilde{s}) = A_d\sqrt{\beta_d(\tilde{s})}\cos(2\pi\nu_d n+\psi_d(\tilde{s})-\psi_d(\tilde{s}_{\mathrm{ac}})+\chi_d) \ . \qquad (7.11)$$

We suppose the reference of the longitudinal coordinate $\tilde{s}=0$ is location of a particular BPM[3]. Then, the phase $\psi_d(\tilde{s})$ describes the phase advance of the driven betatron oscillations from the location of this reference BPM to the

---

[3] We choose the first BPM encountered by the proton beam after it is injected into the Tevatron.

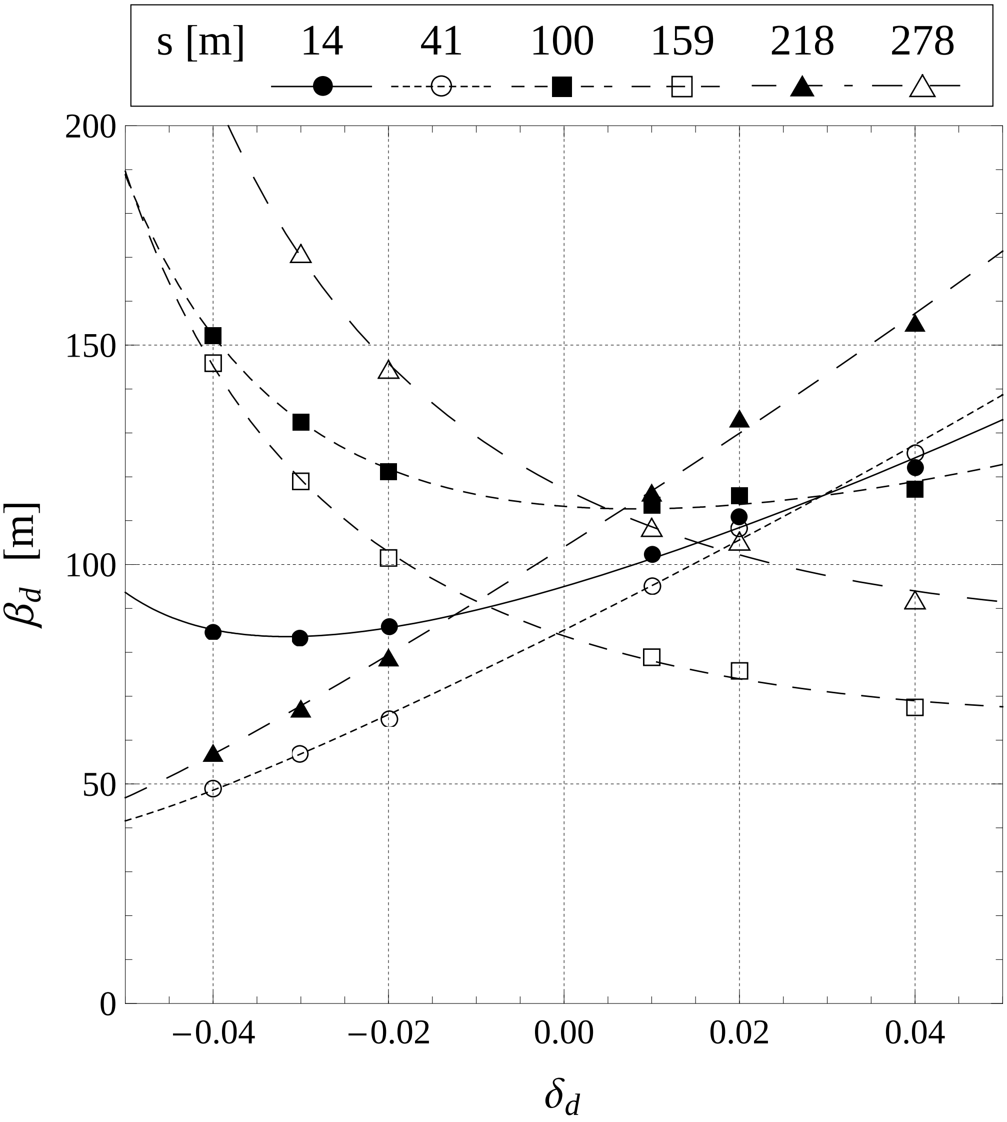

Figure 7.3: $\beta_d(\tilde{s})$ vs. δ_d at six consecutive BPM locations. The legend shows longitudinal position s of each BPM. The values of the amplitude function of the free betatron oscillations, $\beta(\tilde{s})$ at each BPM locations are the values of the fit curves when $\delta_d = 0$.

location $\tilde{s}$. As we did in the analysis of Section 7.1, by fitting this equation to the data of the turn-by-turn oscillations observed by each of the BPM's, we can determine the amplitude $A_d\sqrt{\beta_d(\tilde{s})}$ and phase $\psi_d(\tilde{s}) - \psi_d(\tilde{s}_{\rm ac}) + \chi_d$ at all the BPM locations. Here, the constant A_d can be determined by using the two BPM's in the interaction straight region, as given in Equation 7.8. We also note that the measured phase of the first BPM is $-\psi_d(\tilde{s}_{\rm ac}) + \chi_d$ since $\psi_d(0) = 0$. Hence, from the turn-by-turn oscillations excited by the AC dipole, we can determine the amplitude function and phase advance of the driven betatron oscillations, $\beta_d(\tilde{s})$ and $\psi_d(\tilde{s})$, at all the BPM locations.

Figure 7.3 shows $\beta_d(\tilde{s})$ of several different frequencies of the AC dipole, measured by the first six BPM's after the reference BPM. The curves show the fits of Equation 6.7 to the data points. The free parameters of the fits are the amplitude function at the BPM location, $\beta(\tilde{s})$, and the phase advance from the AC dipole's location to the BPM location, $\psi(\tilde{s}|\tilde{s}_{\rm ac})$. In Figure 7.3, $\beta(\tilde{s})$ at each BPM are the values of the fit curves when $\delta_d = 0$. The figure indicates that, if the difference of $\beta_d(\tilde{s})$ and $\beta(\tilde{s})$ is not properly accounted, measurement of the amplitude function may have large errors, depending on the longitudinal position and δ_d. Figure 7.4 shows ring-wide $\beta(\tilde{s})$, measured in this way, and also shows ring-wide $\beta_d(\tilde{s})$ when $\delta_d = 0.01$ and 0.04, as comparisons. As discussed in Section 6.2, compared to $\beta(\tilde{s})$, $\beta_d(\tilde{s})$ has a structure like the beta-beat and the effect gets larger when the magnitude of δ_d gets larger. As estimated in Section 6.2, even when $\delta_d = 0.01$, the maximum difference between $\beta(\tilde{s})$ and $\beta_d(\tilde{s})$ is about 10 m, corresponding to 10%. Hence, if the require measurement accuracy is better than this, we have to properly account the difference between $\beta(\tilde{s})$ and $\beta_d(\tilde{s})$.

Figure 7.5 shows $\psi_d(\tilde{s})$ of several different frequencies of the AC dipole, measured by first six BPM's after the reference BPM. In the figure, the phase

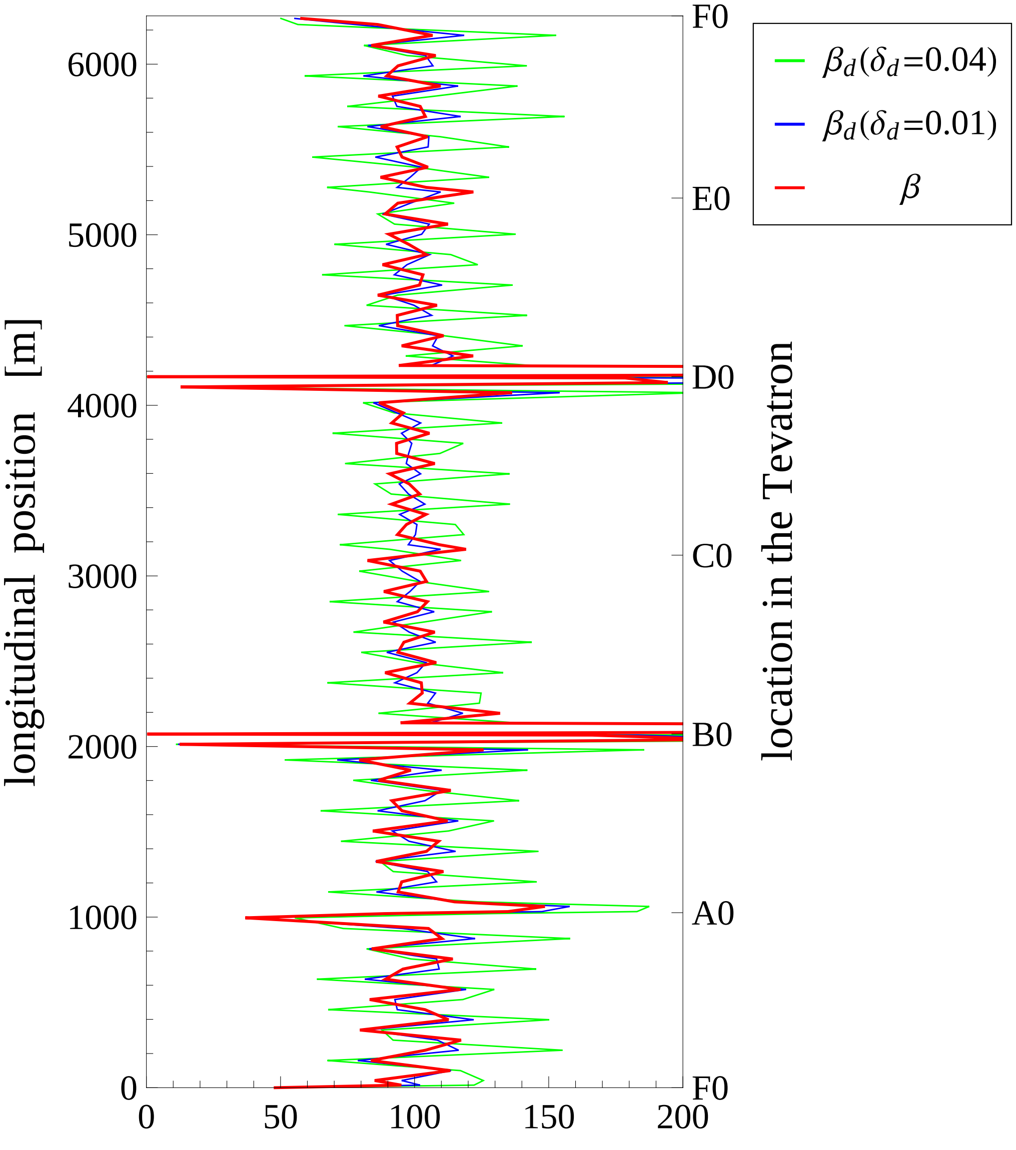

Figure 7.4: $\beta(\tilde{s})$ and $\beta_d(\tilde{s})$ vs. longitudinal position. Compared to the amplitude function of the free oscillations, $\beta(\tilde{s})$, the amplitude function of the driven oscillations $\beta_d(\tilde{s})$ has a structure like the beta-beta. The effect depend on the magnitude of δ_d.

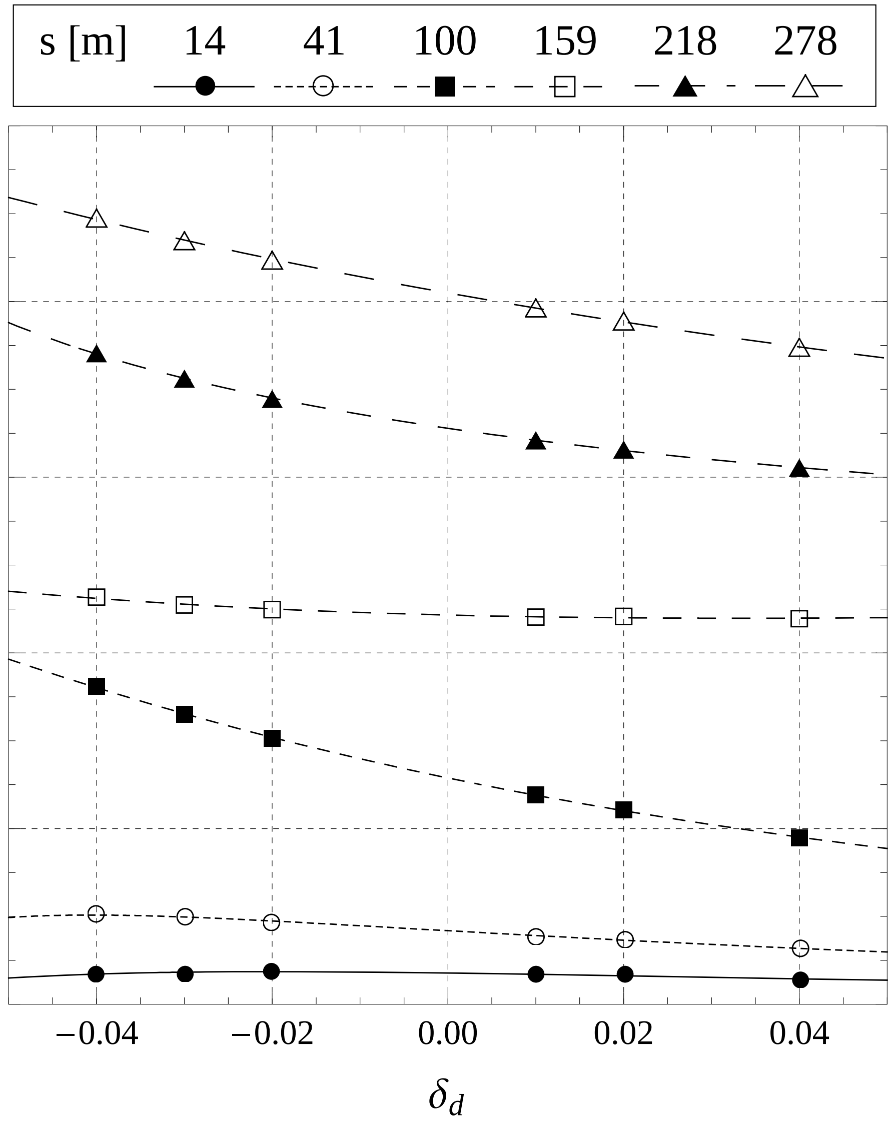

Figure 7.5: $\psi_d(\tilde{s})$ vs. δ_d at six consecutive BPM locations (The same BPM's as Figure 7.3). The legend shows longitudinal position $\tilde{s}$ of the BPM locations. The phase advance of the free oscillations $\psi(\tilde{s})$ can be extrapolated from the phase advance of the driven oscillations $\psi_d(\tilde{s})$, measured at several different frequencies of the AC dipole. The values of $\psi(\tilde{s})$ at each BPM locations are the values of the fit curves when $\delta_d = 0$.

advance is given in units of rad/2π. The curves show the fits of Equation 6.9 to the data points. The free parameter of the fit is the phase advance from the AC dipole's location to the BPM location $\psi(\tilde{s}|\tilde{s}_{\rm ac})$. In the figure, the phase advances of the free betatron oscillations to these BPM locations, $\psi(\tilde{s})$, are the values of the fit curves when $\delta_d = 0$. We can see, if the difference of $\psi_d(\tilde{s})$ and $\psi(\tilde{s})$ is not properly accounted for, the measurement of the phase advance may have large errors, depending on the longitudinal position and δ_d. Figure 7.6 shows deviation of the phase advance of the free betatron oscillations, compared to its design value $\psi_{\rm design}(\tilde{s})$, measured at all the BPM locations in the Tevatron. Here, the phase advance $\psi(\tilde{s})$ is determined as in Figure 7.5, from $\psi_d(\tilde{s})$ of several different AC dipole frequencies. For comparisons, Figure 7.6 also shows deviations of $\psi_d(\tilde{s})$ from $\psi_{\rm design}(\tilde{s})$ when $\delta_d = \pm 0.02$ and ± 0.04. Compared to $\psi(\tilde{s}) - \psi_{\rm design}(\tilde{s})$, $\psi_d(\tilde{s}) - \psi_{\rm design}(\tilde{s})$ has a structure like the phase-beat and the effect gets larger when the magnitude of δ_d gets larger. Similar to the case of the amplitude function measurement, accurate measurement of the phase using the AC dipole requires to properly account the difference between $\psi(\tilde{s})$ and $\psi_d(\tilde{s})$. We can also observe, for $\psi_d(\tilde{s}) - \psi_{\rm design}(\tilde{s})$, the mean value of the phase-beat undergoes a constant shift at the location of the AC dipole. This is a characteristic effect of a quadrupole field error and the AC dipole also produces a similar effect. The phase advance of the free betatron oscillations $\psi(\tilde{s}) - \psi_{\rm design}(\tilde{s})$ (black curve) also undergoes constant shifts at the two locations around $\tilde{s} \simeq 2{,}000$ m and 4,000 m. These are due to real quadrupole field errors at the location of the AC dipole. These two locations corresponds to the two interaction regions of the Tevatron.

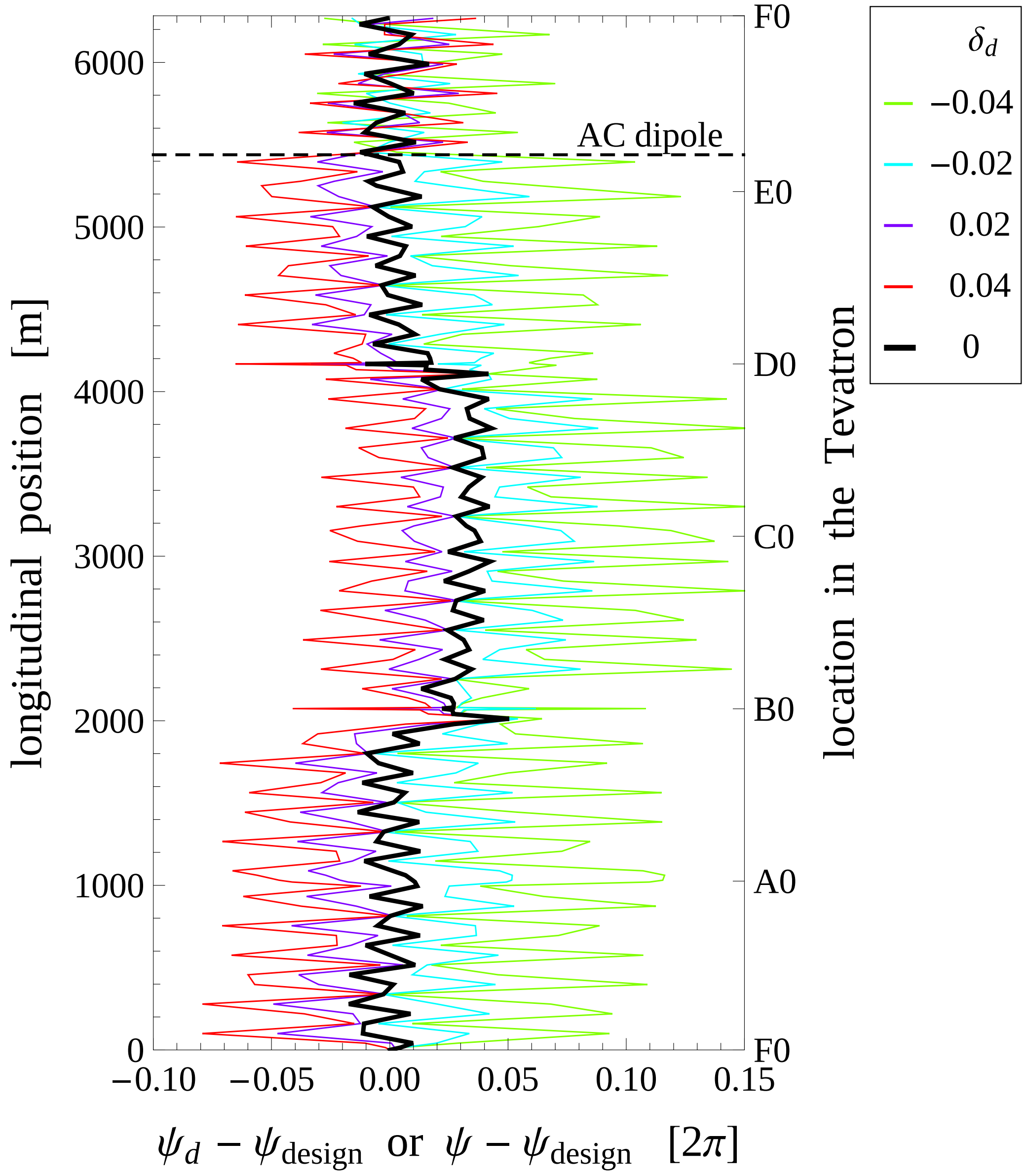

Figure 7.6: $\psi(\tilde{s}) - \psi_{\rm design}(\tilde{s})$ and $\psi_d(\tilde{s}) - \psi_{\rm design}(\tilde{s})$ vs. longitudinal position. Compared to the phase advance of the free oscillations, $\psi(\tilde{s})$, the phase advance of the driven oscillations, $\psi_d(\tilde{s})$, has a structure like the phase-beta and also undergoes a constant shift at the location of the AC dipole. The effect depend on the magnitude of δ_d. The shifts of the free oscillations' phase advance, $\psi(\tilde{s}) - \psi_{\rm design}(\tilde{s})$, around $\tilde{s} \simeq 2{,}000$ m and 4,000 m indicate existence of the quadrupole field errors.

7.3 Systematic Uncertainties

We conclude this Chapter with discussion about influence of systematic uncertainties on the measurement of the amplitude functions. Most notably, there are several error sources in the BPM measurements themselves, such as the electronics noise, misalignment (offset and tilt), and nonlinear response. Among these, the scaling error resulted from the tilt and nonlinearity are the largest, and here we study the impact on our measurements of machine optics from this type of systematic error sources [54, 56].

We suppose the two BPM's, used to diagnose the interaction region, have scaling errors. Then, in Equation 7.4 and 7.5, the amplitudes determined from the observations of these two BPM's change to $(1+\epsilon_1)a_{d,1}$ and $(1+\epsilon_2)a_{d,2}$, where ϵ_1 and ϵ_2 are constant parameters to denote the scaling errors. When the measured amplitudes change in this way, $\beta_d^*(\tilde{s})$ and $s_d^*(\tilde{s})$ determined from Equations 7.6 and 7.7 also change. Up to first order in ϵ_1 and ϵ_2, the changes of β_d^* and s_d^* are given by

$$\beta_d^* \to \left[1 - \frac{1}{4}(\epsilon_1 + \epsilon_2)^2\right] \beta_d^* \tag{7.12}$$

$$\varDelta s_d^* \to \varDelta s_d^* + \frac{L}{2}(\epsilon_1 - \epsilon_2) \ . \tag{7.13}$$

If the source of the scaling error is the BPM's nonlinearity, for a typical BPM in the Tevatron, the magnitude of the scaling error is less than a few percent $\epsilon_1, \epsilon_2 \lesssim 0.02$ (see [27, 25]). From Equation 7.12, the influence is very small since the effect is proportional to $(\epsilon_1 + \epsilon_2)^2$. For instance, to change measured value of β^* by 1%, one of the BPM must have as much as 20% scaling error. Whereas, from Equation 7.13, measurement of the beam waist location is very sensitive to these errors. For instance, if $\epsilon_1 \simeq 0.02$ and $\epsilon_1 \simeq 0$, the measured s_d^* and thus the extrapolated s^* has an additional 7 cm. We note that the method using the physics detector [53] can measure the beam waist location with better accuracy (less than ±1 cm). As a possible improvement in future, the result from the physics detector may give constrains to the scaling errors of the BPM's in the Tevatron's interaction regions.

In the measurement of the ring-wide amplitude function in Section 7.2, we also used the two BPM's in the interaction region to calculate the constant A_d. With the same scaling error described by ϵ_1 and ϵ_2, the measured value of this constant changes to

$$A_d \to \left[1 + \frac{1}{2}(\epsilon_1 + \epsilon_2)\right] A_d \ . \tag{7.14}$$

In the measurement, the amplitude function of the driven oscillations at each BPM location, $\beta_d(\tilde{s})$, is determined from square of the amplitude $A_d\sqrt{\beta_d(\tilde{s})}$. Hence, this scaling error changes the measured value of $\beta_d(\tilde{s})$ to

$$\beta_d(\tilde{s}) \to \left[1 + (\epsilon_1 + \epsilon_2)\right] \beta_d(\tilde{s}) \ . \tag{7.15}$$

The equation indicates that the ring-wide amplitude function measurement, discussed in Section 7.2, has global scaling error of $\epsilon_1 + \epsilon_2$, which is estimated less than a few percent. Such is acceptable and, furthermore, does not affect measurements of the relative amplitude function between any two points around the synchrotron.

7.4 Summary

In this chapter, we discussed measurements of the Tevatron's linear optical parameters using the AC dipole, both in the interaction region and in the entire synchrotron. From the data of the AC dipole excitations at several different frequencies of the AC dipole, we can extrapolate the parameters of the free oscillations in the limit $\delta_d \rightarrow 0$. In this way, we can make direct measurements of the Tevatron's linear optical parameters, relatively faster than the types of measurements relying on the synchrotron's model. In the presented measurements here, no significant error is found. For the measurements presented in this chapter, the largest error source is the BPM's scaling error. Section 7.3 shows our measurements are not sensitive to typical scaling errors of the BPM's in the Tevatron, except the measurement of the beam waist location.

Chapter 8

Nonlinear Optics Measurement

In Chapter 3, we discussed influences of perturbative magnetic fields to motions of beam particles in a synchrotron and these influences are summarized in Table 3.1. Perturbative fields whose orders are higher than the second order (quadrupole) may affect the stability of the beam in the synchrotron due to resonance effects (see Chapter 3). Therefore, it is ideal if we can measure influences of nonlinear fields in the synchrotron. In situ measurements, furthermore, would be a significant advantage over dedicated experiments, such as [57], to measure such nonlinear effects.

The AC dipole permits in situ measurements in a synchrotron, and furthermore the large, sustained oscillations it produces should enable nonlinear effects to become measurable. In this chapter, we discuss measurements of nonlinear perturbations due to sextupole and octupole fields. In Section 8.1, we discuss measurements of the perturbative effects due to sextupole fields and, in the following Section 8.2, we discuss measurements of the perturbative effects due to octupole fields. In both Sections 8.1 and 8.2, we focus on the effects summarized in Table 3.1.

8.1 Perturbation Due to Sextupole Field

Sextupole fields distort the central orbit of the beam particles, and also drive modes with tune $2\nu_0$. From Equation 3.56 and Table 3.1, these effects are nonlinear and depend on the square of the constant A, which determines the amplitude of the leading order free oscillations (Equation 2.29).

To observe such effects, measurements are performed with low intensity (2-3$\times 10^{11}$) proton beams of 150 GeV in the Tevatron. In the measurements, the strength of a single sextupole magnet[1] is set to various values and large amplitude beam oscillations, produced by the vertical AC dipole in the Tevatron, are observed by a BPM system to detect the effects due to this controlled sextupole magnet. In Section 8.1.1, we discuss measurements of the central orbit distortion due to this controlled sextupole and, in Section 8.1.2, we discuss measurements of the modes with tune $2\nu_0$ excited by this sextupole.

8.1.1 Central Orbit Distortion

Figure 8.1 shows an example of turn-by-turn oscillations in the vertical plane excited with the vertical AC dipole in the Tevatron during the sextupole study. In the figure, the initial vertical position of the central orbit before the AC dipole excitation, $y_{\mathrm{co,initial}}$, is subtracted from the data. When the oscillation amplitude grows, the average position of the oscillations changes (in this case upward) due to the influences of sextupole fields. We calculate the difference between the position of the initial central orbit and the position of the central orbit while the amplitude of the AC dipole's field is maximum, Δy_{co}, which

---

[1] In measurements discussed in this section, coherent oscillations of beam particles are always excited with the vertical AC dipole. Hence, the controlled sextupole in our measurements is actually skew sextupole magnet which produces a force proportional to the square of a particle's vertical displacement from the center of the magnet.

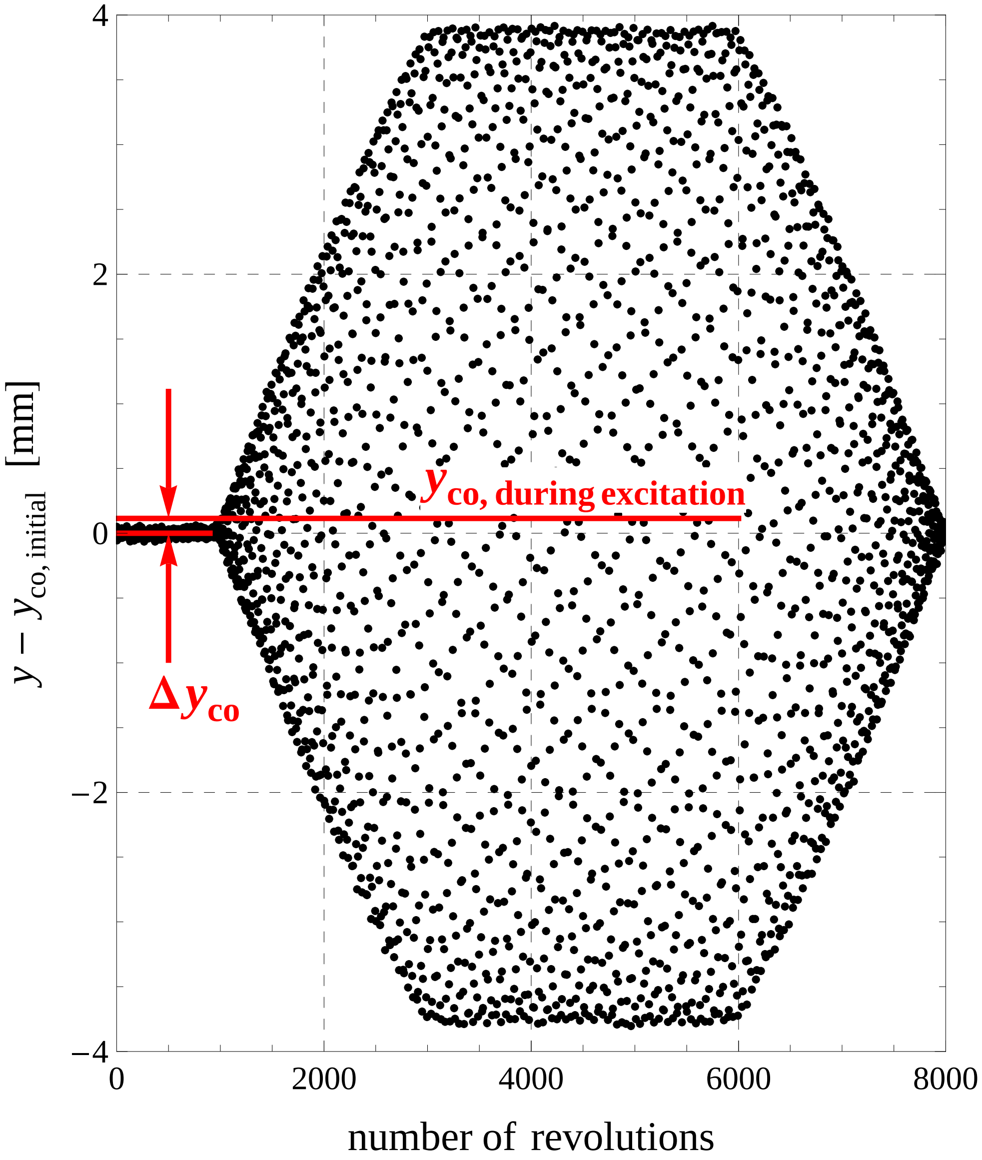

Figure 8.1: Orbit distortion due to sextupole fields observed in the turn-by-turn oscillations of the AC dipole's excitation. During the excitation, the average position of the beam particles are shifted by Δy_{co} from the initial position of the central orbit due to the influence of sextupole fields.

is described by the second term of Equation 3.56. We note that, when the beam particles are driven with the AC dipole, the orbit distortion due to sextupole fields is determined by the parameters of the driven oscillations defined in Chapter 6, A_d^2 and $\beta_d(\tilde{s}_3)^{3/2}$, instead of the parameters of the free betatron oscillations, A^2 and $\beta_0(\tilde{s}_3)^{3/2}$. Here, $\tilde{s}_3$ $(0 \leq \tilde{s}_3 < C)$ is the location of the sextupole magnet as in Equation 3.56. Because the constant A_d is proportional to the current going through the AC dipole (Equation 5.13), the orbit distortion due to sextupole fields is proportional to the square of the current going through the AC dipole. We also note that, since the second term of Equation 3.56 is proportional to the effective strength of a sextupole magnet k_3, and since k_3 is proportional to the current going through the sextupole magnet, the orbit distortion due to a single sextupole magnets is linearly proportional to the current going through the sextupole magnet.

Figure 8.2 shows distortions of the central orbit measured at all the BPM locations in the Tevatron, when the average oscillation amplitude of the AC dipole excitation is about 4.75 mm in the arc and the oscillation amplitude at the location of the given sextupole magnet is about 4 mm. The measurements were performed with the low intensity proton beam in the nominal condition of the Tevatron at its injection energy 150 GeV, corresponding to the magnetic rigidity $(B\rho) \simeq 500$ Tm. We note that the rms beam size at this energy is about 1.3 mm and the amplitude of the excited oscillations 4.75 mm corresponds to roughly 3.5σ beam size. The dotted line and solid line represent the two cases of the current going through a given sextupole magnet, 0 A (the nominal value) and 30 A. The figure shows that the distortion of the central orbit grows with the current going through the given sextupole magnet and the case of 30 A also shows the cusp structure at the nearest BPM to the sextupole magnet, as discussed in Section 3.2.1. For the sextupole magnet

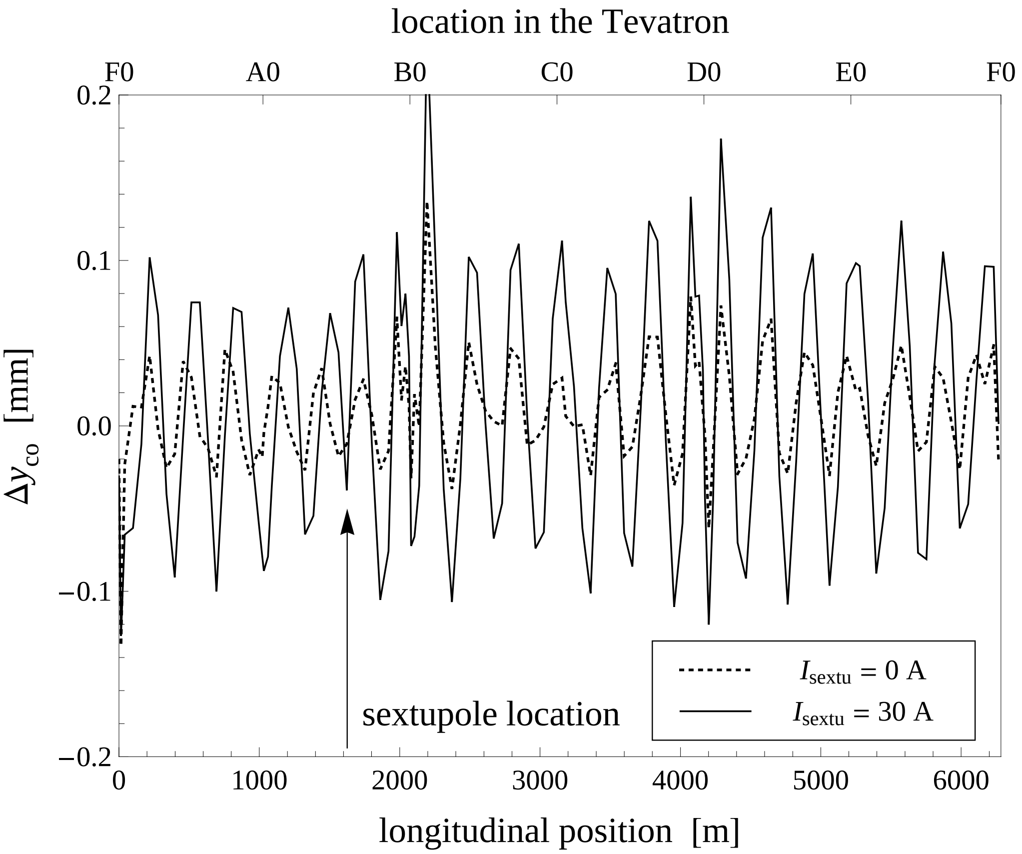

Figure 8.2: Distortions of the central orbit due to a single sextupole magnet when the current going through the sextupole magnet is the nominal 0 A and when it is increased to 30 A. The current going through the AC dipole is 280 A, corresponding to 5-6 mm oscillation amplitudes in the arc of the Tevatron. We can see a cusp structure (see Section 3.2.1) near the location of the sextupole magnet.

used in these measurements, the amplitude function at the location is about $\beta(\tilde{s}_3) \simeq 94$ m (design value), and the relation between the effective strength $k_3 = B_{y,2}\ell/(B\rho)$ and the current going through the sextupole magnet $I_{\rm sextu}$ is given by [3]

$$k_3 \simeq 14\, I_{\rm sextu}\ {\rm nrad/mm}^2\ , \tag{8.1}$$

where the current of the sextupole $I_{\rm sextu}$ is in units of Ampere. This equation indicates that, when the current of this sextupole magnet is $I_{\rm sextu} \simeq 30$ A and the oscillation amplitude at the location of this sextupole magnet is $A_d\sqrt{\beta(\tilde{s}_3)} \simeq 4$ mm, this sextupole magnet is equivalent to a dipole magnet with deflection angle $\frac{1}{4}k_3A_d^2\beta(\tilde{s}_3) \simeq 1.7$ μrad. Hence, from either Equation 3.36 or Equation 3.56, under these conditions, the maximum central orbit distortion is expected to be about 80 μm at the locations of the BPM's in the arc, where the amplitude function is $\beta(s) \simeq 95$ m. In the figure, we can see this estimate is not far from the measurement. We note that, because some sextupoles are used in the nominal condition of the Tevatron, the orbit distortion is not zero even when the current in the given sextupole $I_{\rm sextu}$ is zero. The figure indicates that the maximum orbit distortion due to these residual sextupole fields are about 40 μm. This is the case when the oscillation amplitude is about 3.5σ beam size. We note that, with no AC dipole excitation, beam particles are undergoing free betatron oscillations with the rms oscillation amplitude σ, determining the beam size σ. If we scale this 40 μm to the case of 1σ beam size oscillations, the orbit distortion is about 3 μm, which is only 0.2% of the beam size. Hence, the contribution to the beam size from these residual sextupole fields can be negligible, as long as we keep the tunes of the beam particles off the resonant condition $\nu_0 = N$, where N is an arbitrary positive integer.

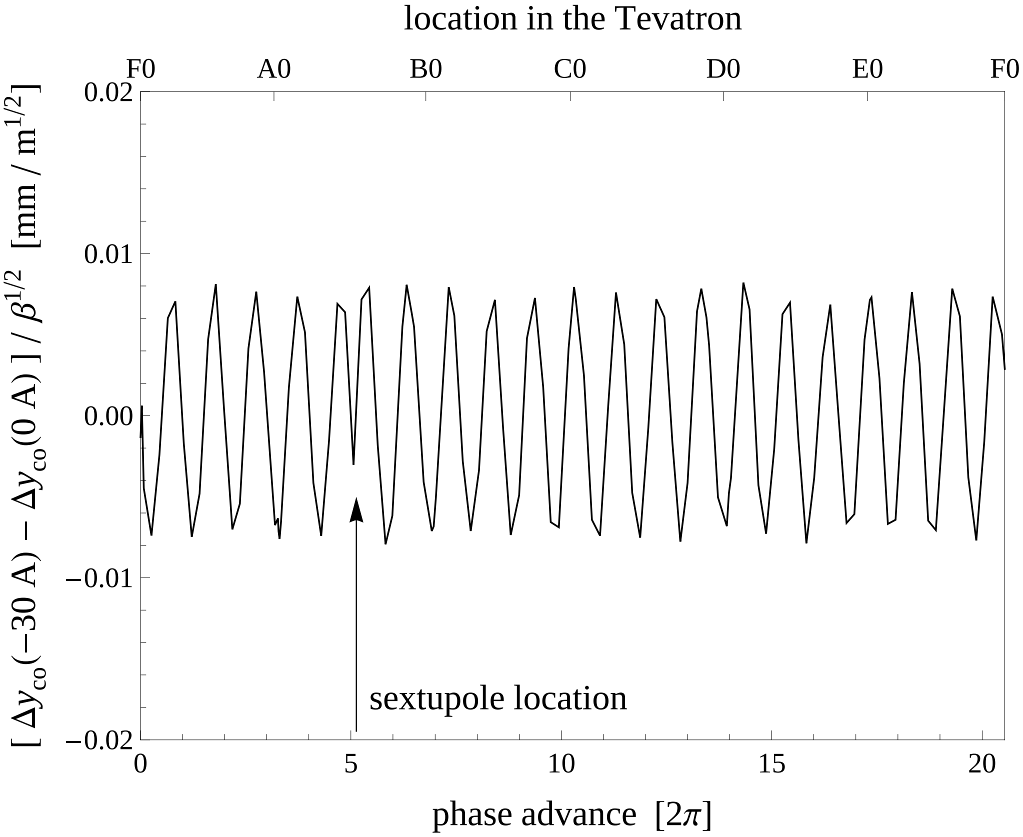

Figure 8.3: Difference of the central orbit distortions when the current in the given sextupole is 30 A and 0 A, normalized by the amplitude function. The horizontal axis is also changed from the longitudinal position to the phase advance. This figure shows only the effect due to the change of the given sextupole magnet.

Figure 8.3 shows the difference of the central orbit distortions in Figure 8.2, when the current in the given sextupole magnet is 30 A and 0 A. The vertical axis is normalized by the amplitude function at each BPM location and the horizontal axis is changed from the longitudinal position to the phase advance measured from the first BPM. From the second term of Equation 3.56, in this case, we predict a pure sinusoidal change with a constant amplitude

$$\frac{k_3 A_d^2 \beta_d(\tilde{s}_3)^{3/2}}{8\sin(\pi\nu_d)} \simeq 0.008 \text{ mm/m}^{1/2} \tag{8.2}$$

and the measurement agrees well to the prediction. In this figure, the cusp structure at the nearest BPM to the source can be seen clearer than Figure 8.2 and this quantity on the vertical axis is useful to find locations of the error sources.

The central orbit distortion due to a sextupole magnet is linearly proportional to the current going through the sextupole magnet and is proportional to the square of the current going through the AC dipole. To test this, we set the current of the same sextupole magnet used in Figure 8.2 to several different values, holding the AC dipole's current at constant 280 A. Figure 8.4 shows measured central orbit distortions as functions of the current going through the sextupole magnet, observed at three consecutive BPM's in the Tevatron. Because the central orbit distortion depends on the phase advance through the term $\cos(\psi_0(\tilde{s}) - \psi_0(\tilde{s}_3) - \pi\nu_0 \operatorname{sgn}(\tilde{s} - \tilde{s}_3))$ (see the second term of Equation 3.56), it may shift upward or downward depending on a location, and indeed different responses to the sextupole effect are seen at the locations of BPM#52, BPM#53, and BPM#54. We note that, at the locations of these

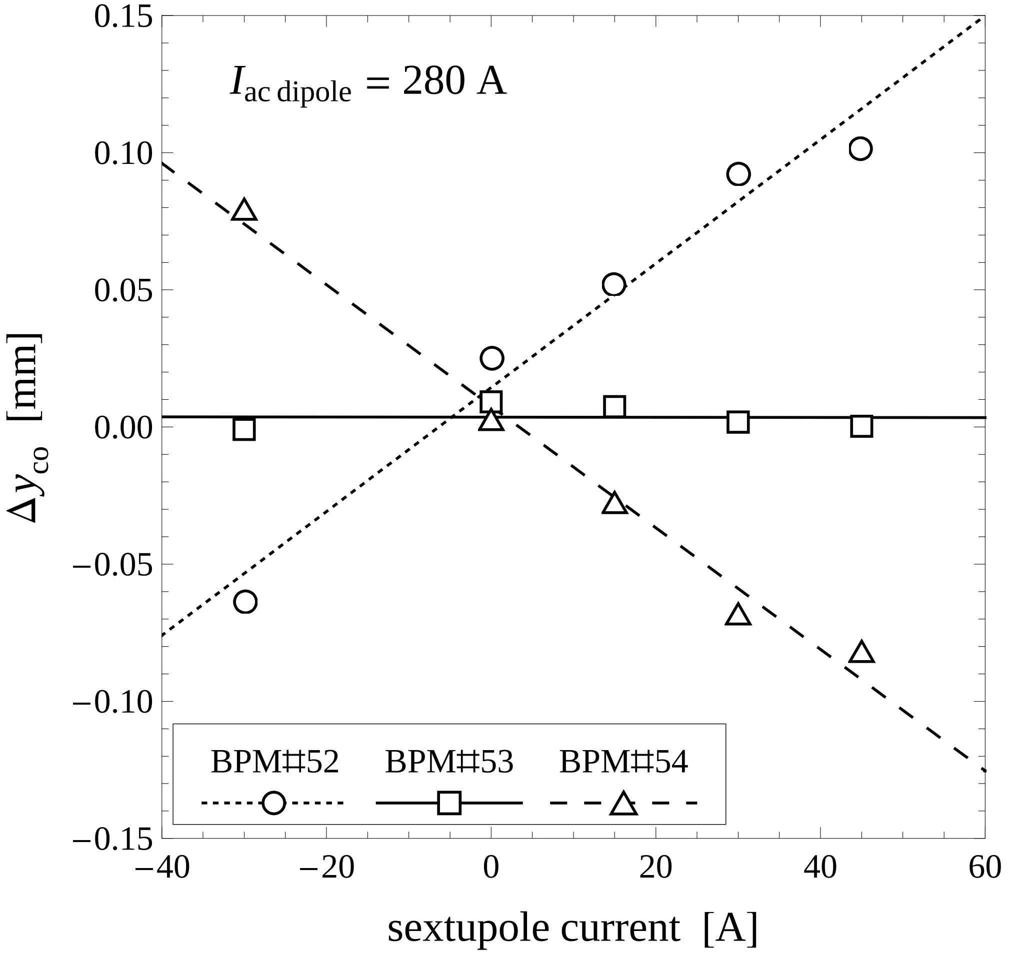

Figure 8.4: central orbit distortion vs. current of the sextupole magnet observed at three BPM locations in the Tevatron. In the measurements, current of the AC dipole is kept to a constant value, 280 A, and so the oscillation amplitude of the leading order mode is kept to a constant value. Then, the orbit distortion is linearly proportional to the current of the sextupole magnet.

BPM's,

$$\cos(\psi_0(\tilde{s}) - \psi_0(\tilde{s}_3) - \pi\nu_0 \,\mathrm{sgn}(\tilde{s} - \tilde{s}_3)) \tag{8.3}$$

$$\simeq \begin{cases} 0.91 & \text{for } \psi_0(\tilde{s}) - \psi_0(\tilde{s}_3) \simeq 130 \text{ deg (BPM\#52)} \\ -0.06 & \text{for } \psi_0(\tilde{s}) - \psi_0(\tilde{s}_3) \simeq 199 \text{ deg (BPM\#53)} \\ -0.94 & \text{for } \psi_0(\tilde{s}) - \psi_0(\tilde{s}_3) \simeq 160 \text{ deg (BPM\#54)}\ . \end{cases} \tag{8.4}$$

The amplitude of the central orbit distortion, modulated by the phase term $\cos(\psi_0(\tilde{s}) - \psi_0(\tilde{s}_3) - \pi\nu_0 \,\mathrm{sgn}(\tilde{s} - \tilde{s}_3))$ in Equation 3.56, is 80 μm, and is consistent with observations. Because there are other sextupole magnets, the central orbit distortion is not zero even when the current of the given sextupole magnet is zero and hence the fit lines in Figure 8.4 are not crossing zero when the sextupole's current is zero. In this way, we can observe the central orbit distortion due to a single sextupole magnet is linearly proportional to the current in the sextupole magnet, as expected[2].

The central orbit distortion due to sextupole fields is proportional to the amplitude of the beam's motion through the sextupole, as derived in Equation 3.56. As a result, the central orbit distortion should be proportional to the square of the AC dipole's current. To test this, we performed measurements in which this same sextupole was activated similarly to measurements in Figure 8.4, but now the current of the AC dipole is set to several different values. Figure 8.5 shows the measured central orbit distortion for different values of the AC dipole's current, observed at the same three consecutive BPM locations, BPM#52, BPM#53, and BPM#54. Because the central orbit distortion de-

---

[2] When we change a sextupole magnet, changes of dipole and quadrupole fields are involved through the feeddown effects (Section 3.1.5) and the coupling between the two transverse planes are also induced (Section 3.2.3). Hence, it is very hard to add only a nonlinear field without changing linear properties of the synchrotron. The deviations of the data points from the fits are expected due to such systematic changes of linear parameters when we change the sextupole magnet.

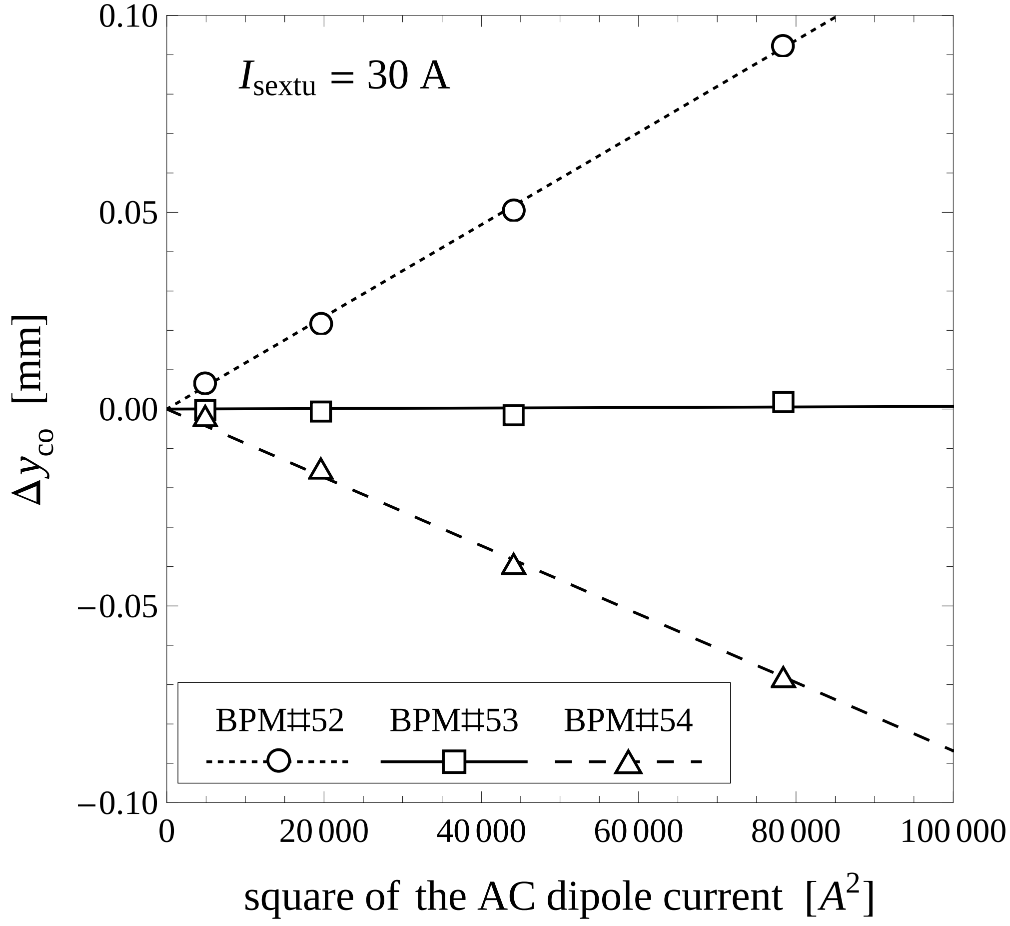

Figure 8.5: Central orbit distortion vs. current of the AC dipole observed at three BPM locations in the Tevatron. In the measurements, current of the given sextupole magnet is kept to a constant value, 30 A, and so the net sextupole field in the synchrotron is kept the same. In such cases, the orbit distortion is proportional to the square of the AC dipole's current.

pends on the phase advance, the central orbit may shift up or down, or may not be affected depending on a location in the synchrotron. The central orbit distortion goes to zero when the current of the AC dipole approaches zero. The central orbit distortion is proportional to the square of the AC dipole's current and, hence,the square of the amplitude of the beam's motion, A_d, as expected.

8.1.2 Higher Tune Mode

From the third and fourth terms of Equation 3.56, sextupole fields are expected to drive modes whose tune is twice of the leading order oscillations. The magnitudes of these modes are linearly proportional to the current of a sextupole and are proportional to the square of the current going through the AC dipole. In this section, we discuss measurements of such modes utilizing the Fourier spectra of the beam particles' oscillations excited by the AC dipole similar to measurements in [58, 59, 60, 61].

We note that, when the leading order oscillations is the free betatron oscillations, the modes driven by sextupole fields have the tune $2\nu_0$ as shown in Equation 3.56. When the leading order oscillations is the driven oscillations excited by an AC dipole, the two modes have the tune $2\nu_d$, instead of $2\nu_0$. When the leading order oscillations is the driven oscillations, the amplitudes of these two modes are proportional to parameters of the driven oscillations $A_d^2\beta_d(\tilde{s}_3)^{3/2}$ instead of $A^2\beta_0(\tilde{s}_3)^{3/2}$, as in the case of the central orbit distortion. We also note that, with one BPM, we can only observe the combined effects corresponding to the third and fourth terms of Equation 3.56.

Figure 8.6 shows Fourier spectra of the turn-by-turn oscillations observed at two BPM locations in the Tevatron, when the beam particles are driven by the AC dipole. The data is from the measurements in Figure 8.2, namely, the beam is excited twice with the AC dipole powered at 280 A when the sextupole magnet is set to 0 A and 30 A. We note that, for discrete Fourier transformations, the spectrum is always symmetric around the mid point and the upper and lower regions represent physically the same modes (see for instance Appendix B-I of [8]). Peaks at ν_d and $1 - \nu_d$ correspond to the oscillations driven by the AC dipole[3]. Here, we are using a convention of normalization, in which the sum of these two peak heights at ν_d and $1 - \nu_d$ is equal to the amplitude of the oscillations driven by the AC dipole. The spectrum at BPM#52 shows that the peaks at $2\nu_d$ and $1-2\nu_d$ grows when we increase the current in the given sextupole magnet from 0 A to 30 A. Whereas, in the spectrum of BPM#53, the peaks at $2\nu_d$ and $1 - 2\nu_d$ have much smaller changes. The situation is analogous to the central orbit distortion seen in Figure 8.4, where the effect depends on the phase advance term in Equation 3.56 and differs over locations of the BPM's[4].

The magnitudes of the modes with tune $2\nu_d$ are linearly proportional to sextupole fields. To observe this, we performed measurements in which the beam was excited by the AC dipole powered at 280 A, and the sextupole current was varied from -30 A to +45 A. Figure 8.7 shows the net oscillation amplitudes of the two $2\nu_d$ modes, when the current of the sextupole magnet is are set to several different values, while the current of the AC dipole is kept to a constant 280 A. These are in fact the same data as the measurements in Figure 8.4. The lines in the figure represent linear fits to the data. As

---

[3] We note that these two peaks do not correspond to the primary and secondary driving tunes discussed in Chapter 6. Both of the peaks in the Fourier spectrum include the effects of both the primary and secondary modes of the driven oscillations.

[4] We note that the peaks at $3\nu_d$ and $1 - 3\nu_d$ correspond to the modes driven by octupole fields. The spectra show these peaks since octupole magnets are used in the nominal condition of the Tevatron when the beam is at its injection energy 150 GeV.

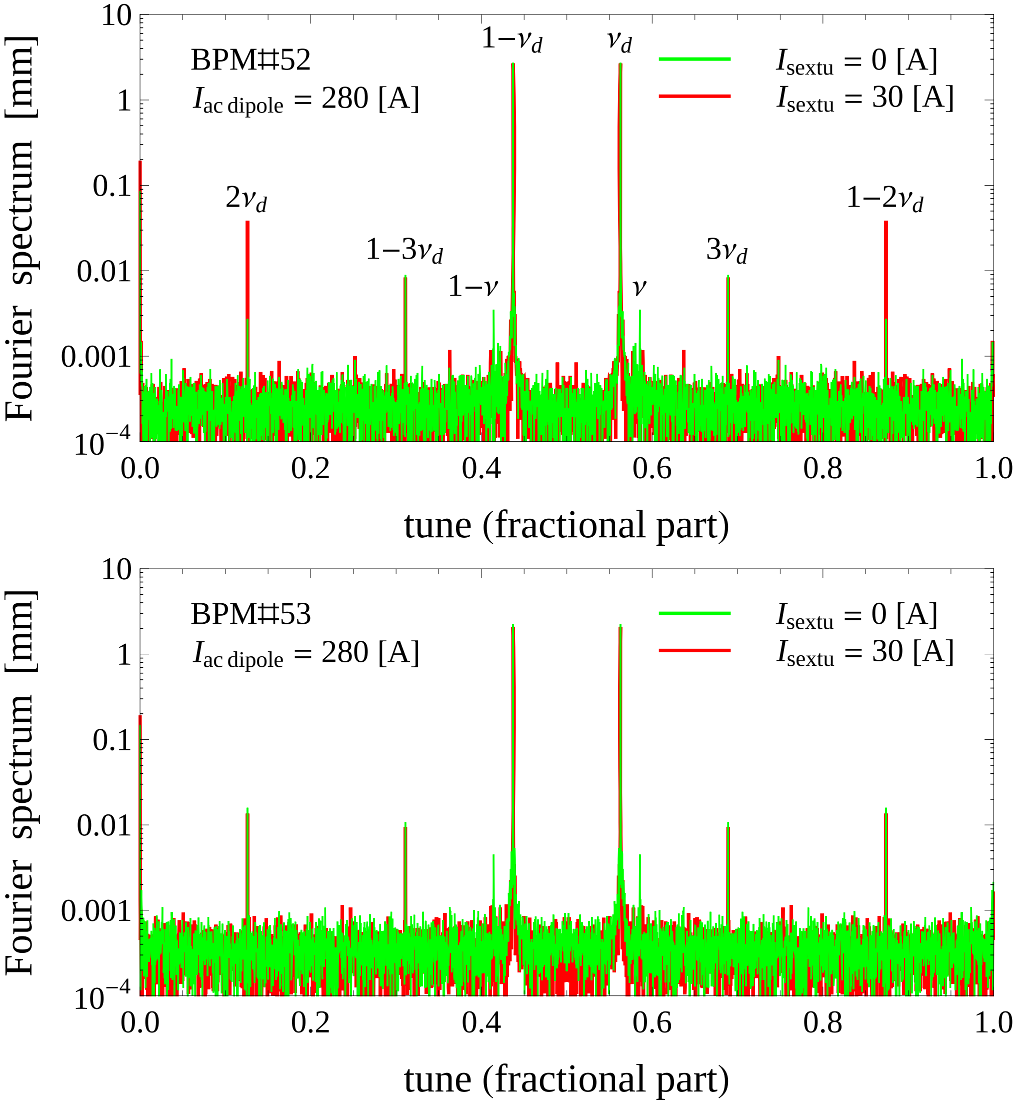

Figure 8.6: Fourier spectra of the oscillations driven by the AC dipole for two different currents in the given sextupole magnet, observed at two BPM locations in the Tevatron. Because sextupole fields drive modes with tune $2\nu_d$, in the Fourier spectrum observed by BPM#52, the peaks at $2\nu_d$ and $1-2\nu_d$ grow when the current in the given sextupole is increased. However the effect depends on the phase advance, and so the peaks at $2\nu_d$ and $1-2\nu_d$ does not grow at BPM#53, where the phase modulation cosine is approximately zero.

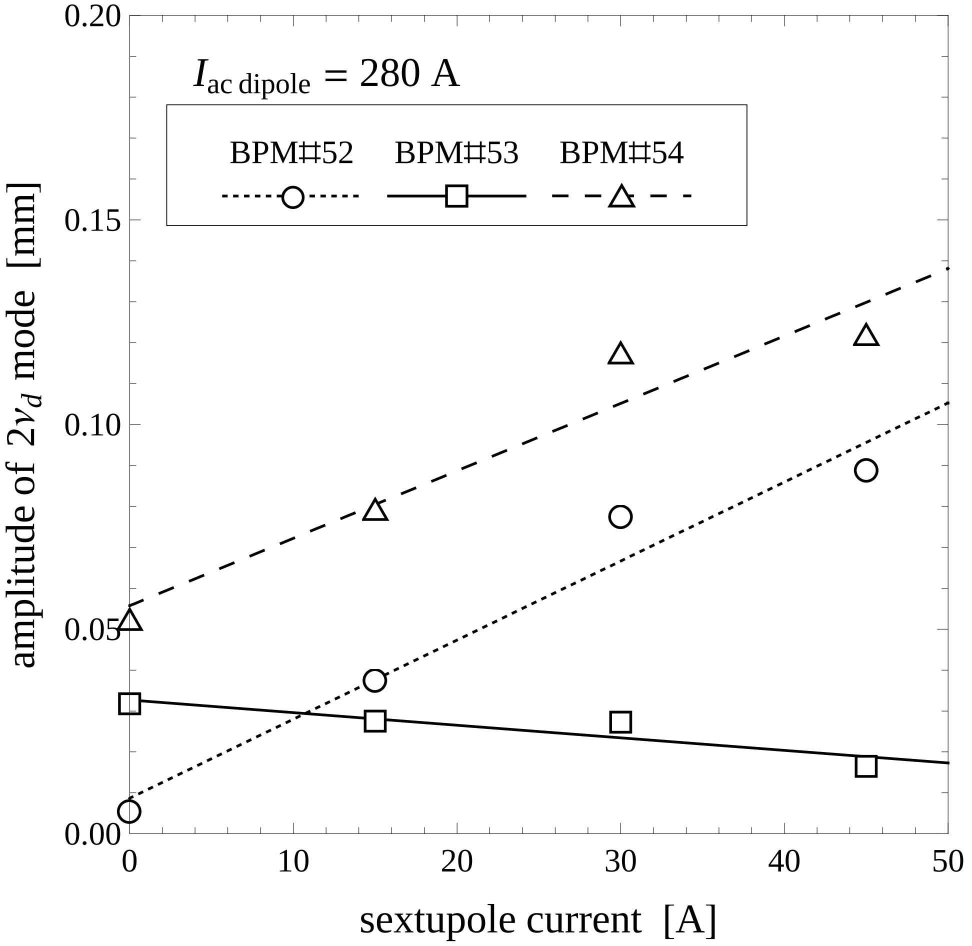

Figure 8.7: Net amplitude of the two modes with tune $2\nu_d$ vs. current of the sextupole magnet, observed at three BPM locations in the Tevatron. In the measurements, current of the AC dipole is kept to a constant value, 280 A, and so the oscillation amplitude of the leading order mode is kept to a constant value. As expected from Equation 3.56, the amplitude is linearly proportional to the current of the sextupole magnet.

already discussed, the slopes of the fits are different because the net effect of the two modes depend on the phase advance. The intercepts in the figure represents the effects of such residual sextupole magnets from elsewhere in the Tevatron. In this way, we can see the magnitude of the modes with tune $2\nu_d$ has linear dependence on sextupole fields. We note that the deviations of the data points from the fits are expected due to changes of linear parameters of the synchrotron induced by the changes of the sextupole magnet.

As indicated in Table 3.1 and in Equation 3.56, the appearance of this $2\nu_d$ mode should also depend upon the square of the amplitude of the beam's motion A_d^2 and, hence, the square of the AC dipole current. To test this, we performed a test in which the current of the given sextupole is kept to a constant value 30 A while the AC dipole excitation is varied between 70 A and 280 A. Figures 8.8 and Figure 8.9 show that, when the current of the AC dipole increases, the peaks at $2\nu_d$ and $1 - 2\nu_d$ indicating that these sextupole modes driven are proportional to A_d^2 in Equation 3.56. As expected from Equation 3.56, Figure shows the amplitude is proportional to the square of the AC dipole's current.

In this section, from Fourier spectra measured with BPM's, we observed sextupole fields drive the modes whose tune is twice of the tune of the leading order oscillations. Through the measurements with the AC dipole in the Tevatron, we tested that the amplitudes of these modes are linearly proportional to strength of sextupole fields and proportional to the square of the constant A_d of the driven oscillations. The appearance of such modes in the Fourier spectrum may be used as a quick diagnostic of the applied and parasitic sextupole fields in a synchrotron, and the magnitudes of these Fourier peaks may be quickly interpreted in terms of parasitic sextupole field strength.

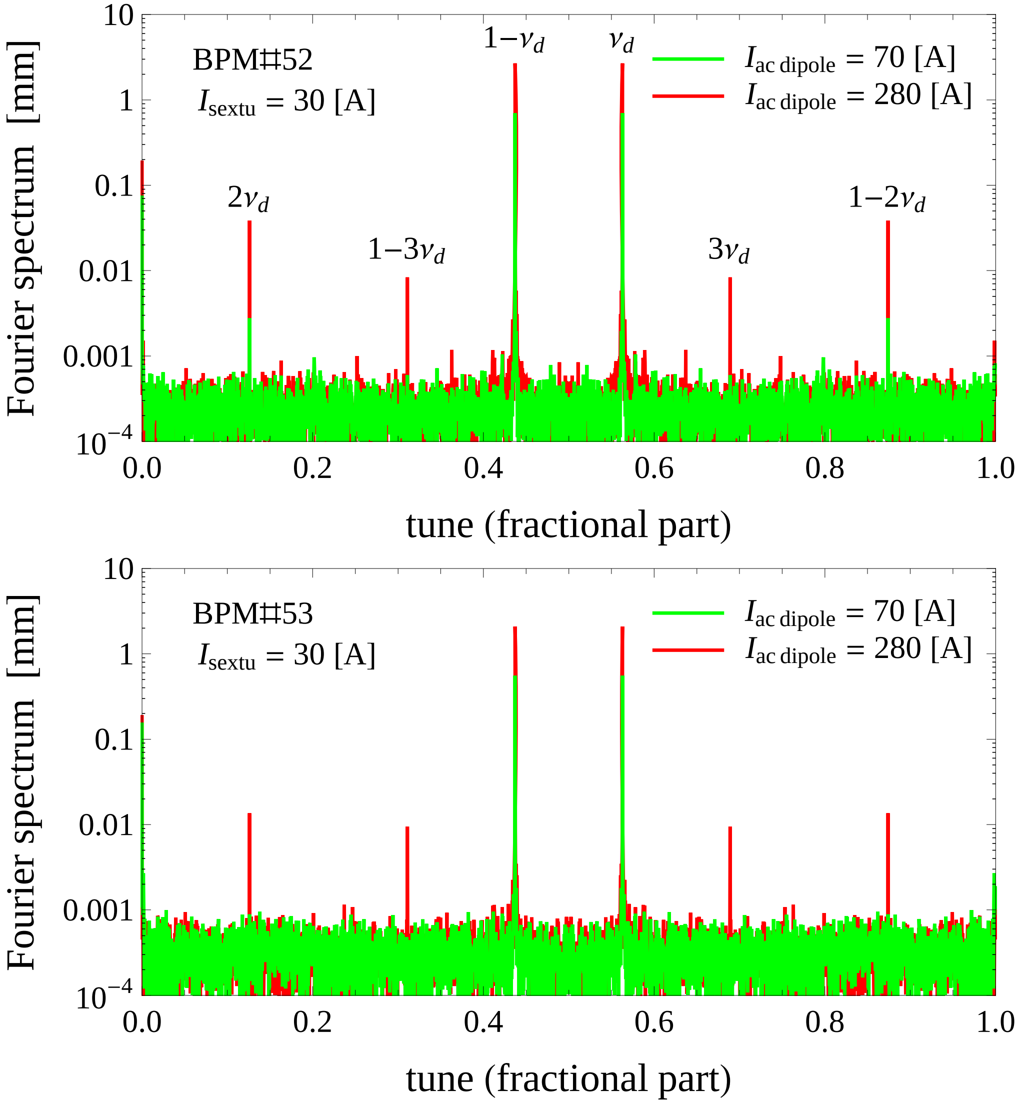

Figure 8.8: Fourier spectra of the oscillations driven by the AC dipole for two different AC dipole's currents, while current of a given sextupole magnet is kept to a constant value, observed at two BPM locations in the Tevatron. Sextupole fields drive the modes with tune $2\nu_d$ and so the peaks at $2\nu_d$ and $1-2\nu_d$ grow with current of the AC dipole. Because the magnitudes of these modes depend on the phase advance, the peak heights could be different such as the locations of BPM#52 and BPM#53.

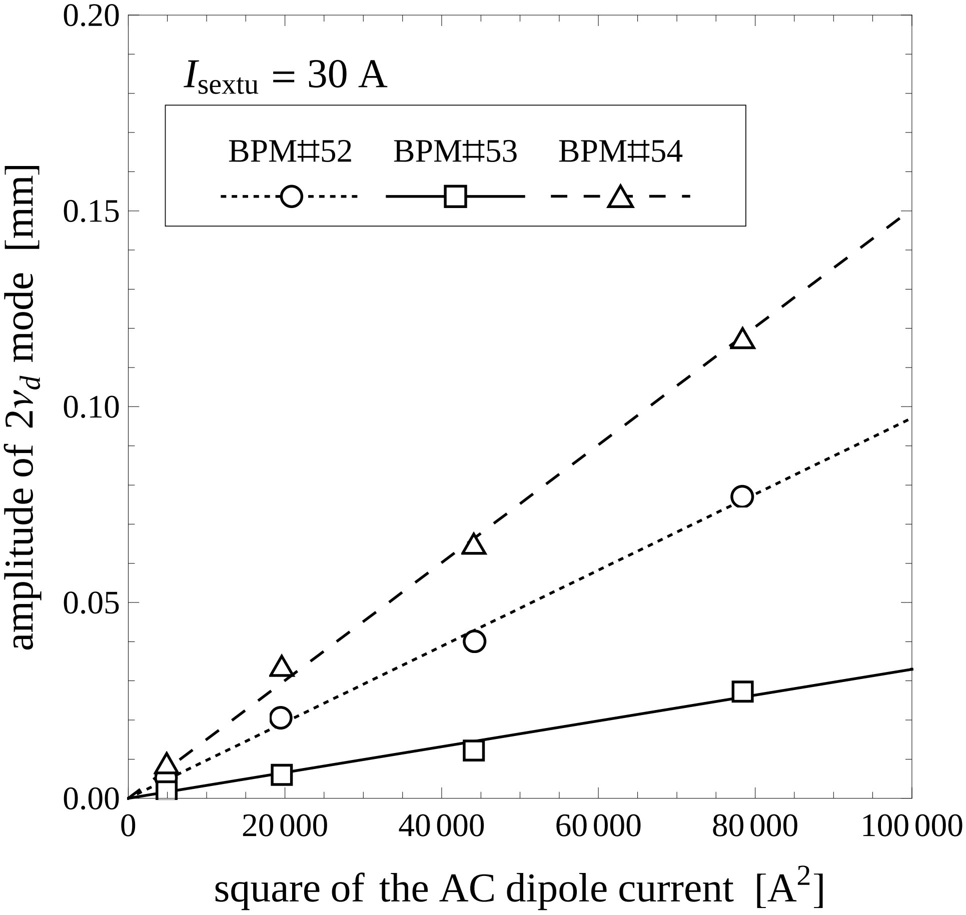

Figure 8.9: Net amplitude of the modes with tune $2\nu_d$ vs. current of the AC dipole, observed at three BPM locations in the Tevatron. In the measurements, current of the given sextupole magnet is kept to a constant value 30 A. As expected from Equation 3.56, the amplitude is proportional to the square of the AC dipole's current. The difference of the slopes come from the phase dependence of the net amplitude at the locations of the three BPM's plotted.

8.2 Perturbation Due to Octupole Field

In this section, we study the effects induced by octupole fields in an accelerator. From the discussions in Sections 3.2.4 and 3.1.4, we expect that octupole fields shift the tune ν of the accelerator and cause a beta-beating effect, much like quadrupole field errors. Furthermore, octupole fields are expected to drive modes with tune $3\nu_0$. From Equations 3.61 and 3.64, these effects are nonlinear and depend on cube of the constant A, which determines the amplitude of the leading order free oscillations (Equation 2.29), such as summarized in Table 3.1.

To observe such effects in the Tevatron, we performed measurements similar to those in Section 8.1 with low intensity (2-3$\times 10^{11}$) proton beams of 150 GeV. The Tevatron has four groups of octupole magnets [3], and all the octupoles in one group are controlled by a single power supply and produce the same field. In the measurements performed here, the strength of a group of octupole magnets, consisting of 18 octupole magnets, is set to various values, and large amplitude oscillations of the beam particles are excited with the vertical AC dipole to observe the perturbative effects due to this group of octupole magnets. From Equation 3.48, the strength of the beta-beat depends on the phase advance from the error source to the observation point, and so the net effect may be weakened when there are multipole sources canceling each others' effects, much like interference of multiple waves[5]. Hence, among three effects of octupole fields listed in Table 3.1, we discuss measurements only of the tune shift in Section 8.2.1 and also discuss measurements of the mode with tune $3\nu_0$ in Section 8.2.2.

---

[5] The groups of octupole magnets in the Tevatron are in fact arranged, so that they do not affect the amplitude function and phase advance and only cause the nonlinear tune shift.

8.2.1 Tune Shift

In this section, we discuss measurement of nonlinear tune shift due to octupole magnetic fields in the Tevatron, using the AC dipole. A tune shift due to nonlinear field is also referred to as detuning. As discussed in Chapters 4 and 6, the tune of beam particles is analogous to the intrinsic frequency of a driven harmonic oscillator system. When the beam is driven by a harmonic force such as an AC dipole, the amplitude of the driven motion grows large as the driving frequency approaches the intrinsic tune.

When a system has nonlinear forces which alter the intrinsic frequency of a particle depending on the particle's oscillation amplitude, such as forces of octupole magnetic fields, the resonant response of the driven motion is modified as seen in Figure 8.10 (see for instance Section 29 of [32]). This figure shows schematic amplitude responses of the beam particles' oscillations driven by the AC dipole in cases with and without a nonlinear force causing detuning. The black curve represents the amplitude response when particles with larger oscillation amplitudes have higher tunes. Suppose, in such a system, we drive the beam particles with an AC dipole from the lower side of the intrinsic tune, $\nu_d < \nu_0$. Here, the intrinsic tune of the system ν_0 is the tune when an oscillation amplitude of a particle approaches to zero. If we shift the driving tune ν_d, keeping the amplitude of the AC dipole's field the same, toward the intrinsic tune ν_0, the amplitude grows but this amplitude growth also shifts the free oscillation's tune higher. Hence, if the beam is driven in the lower side of the intrinsic tune, the detuning makes the amplitude less compared to the case without nonlinear fields causing the detuning (gray curve). In the same synchrotron with the detuning, if we drive the beam with the AC dipole from the upper side of the intrinsic tune $\nu_0 < \nu_d$, the detuning makes the

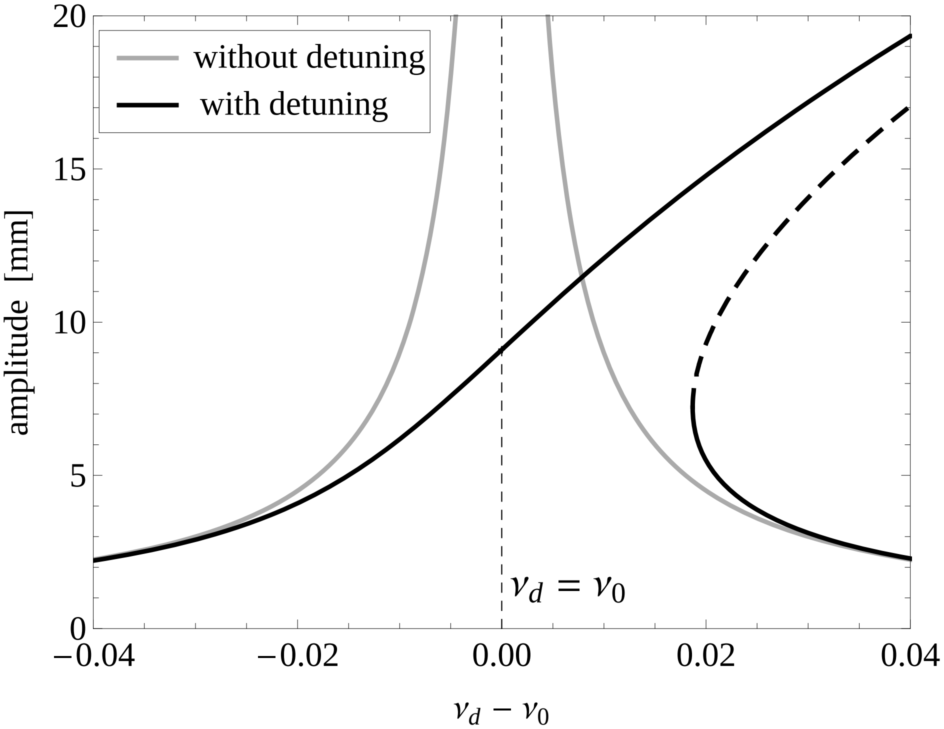

Figure 8.10: Schematic amplitude response of the beam driven by an AC dipole with and without the detuning effect caused by an octupole field. The curves represent the amplitudes of the driven beam for a fixed current of the AC dipole. The black curve corresponds to the case when particles with large oscillation amplitudes have larger free oscillation tunes. When the driving tune is smaller than the intrinsic tune, $\nu_d < \nu_0$, the detuning makes the amplitude smaller compared to the case without the detuning and vise versa.

amplitude larger compared to the case without nonlinear fields causing the detuning (gray curve). In this case, if we lower the driving tune ν_d keeping the amplitude of the AC dipole's field, the particle's amplitude diverges as $\nu_d \to \nu_0$ since the free oscillations' tune also moves higher.

Figure 8.11 shows a demonstration that the determine tune is affected by large amplitude motion in octupole fields. In the upper plot, we performed a measurement in which the beam is excited with the AC dipole seven times, with different AC dipole's frequency and the same AC dipole's current. These data may be fit for the free oscillations' tune, which is the central position of the resonance, as discussed in Section 6. Such a fit can be performed using data from each BPM location around the ring, and is shown in the lower plot of Figure 8.11. The solid curve in the lower plot shows the tunes determined in this way, using all seven data points from the upper plot. Here, if the curve of the amplitude response is deformed due to the detuning, the data point of the maximum amplitude is affected most. The dashed curve represents the tune determined in the same way as the solid curve, but using only the bottom six data points. As expected, there is a slight shift (∼0.003) in determined tune. We note that the expected uncertainty of the tune determined in this method is on the order of ∼0.001, which is smaller than the difference between the averages of solid line and dashed line, ∼0.003. Note that the lower graph in Figure 8.11 plots the fitted tunes from 118 different BPM's, each determined from a graph like that in the upper graph in Figure 8.11. Thus, the shift $\Delta\nu = 0.003$ is significant. Hence, in this way, we can observe the detuning effect in the amplitude response of the driven motion.

Next, we show that the tune shifts observed at large AC dipole amplitudes are in fact due to the octupole fields. In a separate test, we vary the current of a group of octupole magnets, consisting of 18 octupole magnets, to

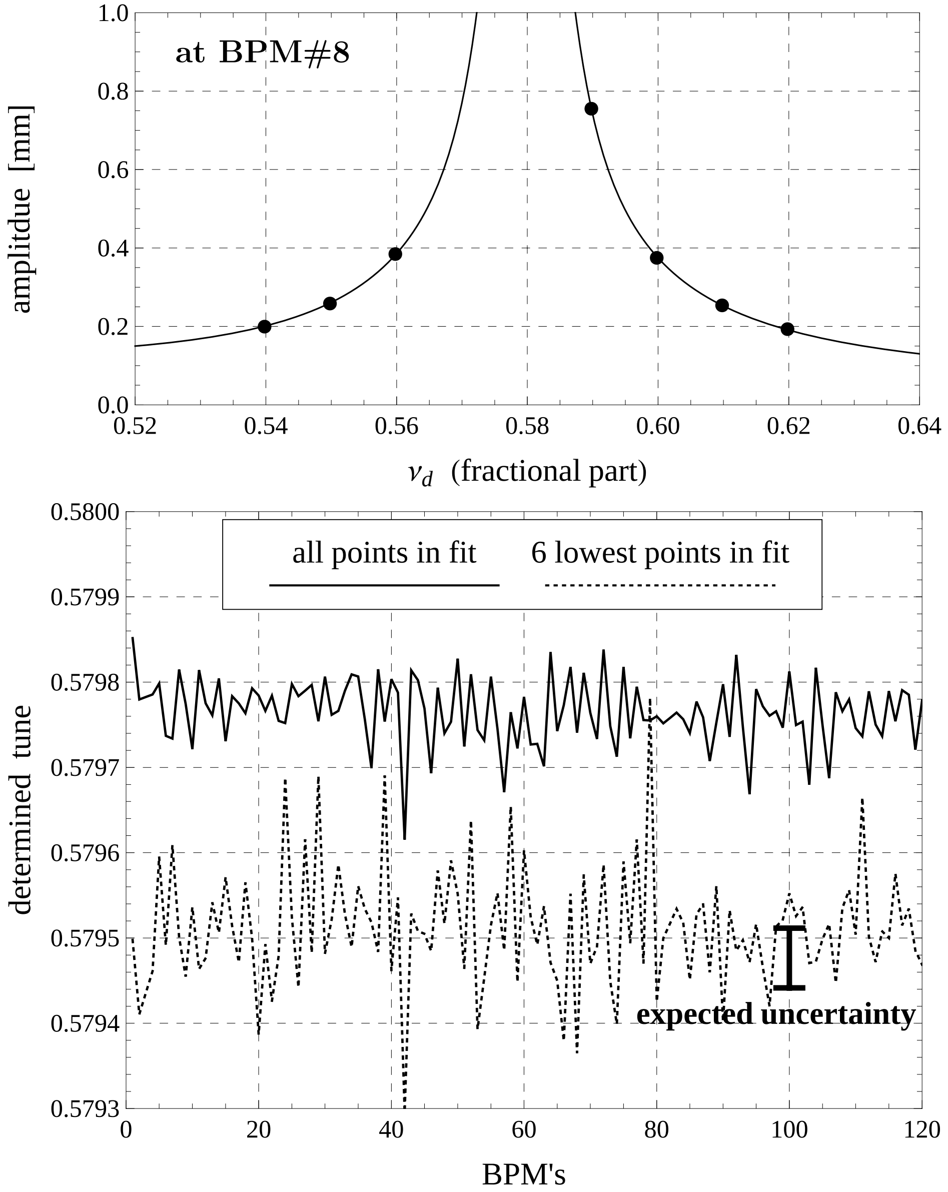

Figure 8.11: Detuning affecting the determined tune from the amplitude response of the driven motion. As done in Figure 6.6, the tune of the free oscillations is determined at all the BPM's, from the amplitudes of the driven oscillations with different frequencies of the AC dipole and with the same current of the AC dipole. The detuning affects the data of the maximum amplitude most, and dropping the point from the analysis shifts the determined tune, more than the expected uncertainty of the measurements.

various values. During this test, we excite the beam with the AC dipole, whose current is set to a constant value of either 140 A or 280 A. For the octupole magnets used in our measurements, the amplitude functions of their locations are about $\beta(\tilde{s}) \simeq 90$ m (design value). For the octupole magnets, the effective strength of the octupole field $k_4 = B_{y,3}\ell/(B\rho)$ and the current going through the octupole magnet I_{octu} are related by [3]

$$k_4 \simeq 1.2\, I_{\text{octu}}\ \mu\text{rad/mm}^2\text{/m}\ , \tag{8.5}$$

where the current I_{octu} is given in units of Ampere. This equation and Equation 3.64 indicate that, when the current of this group of octupole magnets is its nominal 7 A, for a particle with an oscillation amplitude 1 mm, each octupole magnet acts as a quadrupole magnet with the effective field gradient 1.05×10^{-6} m^{-1} or equivalently a quadrupole magnet with the focal length 950 km.

Figure 8.12 shows the turn-by-turn oscillations of the beam driven by the AC dipole, observed by a single BPM in the Tevatron, when the current of the group of octupole magnets is either 1 A or 10 A. In the measurements, the beam is driven from the lower side of the intrinsic tune ($\nu_d < \nu_0$). At this driving frequency, we would expect that detuning shifts the free oscillations' tune higher for the beam with larger oscillation amplitudes. As indicated in Figure 8.10, the amplitude of the driven oscillations in such a case is suppressed compared to the case with no detuning effect. When the current of the octupole magnets is 1 A, the detuning effect is relatively weak and the amplitude becomes roughly twice when the current of the AC dipole is increased from 140 A to 280 A. Whereas, when the current of the octupole magnets are increased to 10 A, the detuning effect becomes stronger and the amplitude of the case when the AC dipole's current is 280 A is suppressed.

Figure 8.13 shows a similar experiment, now repeated for the beam

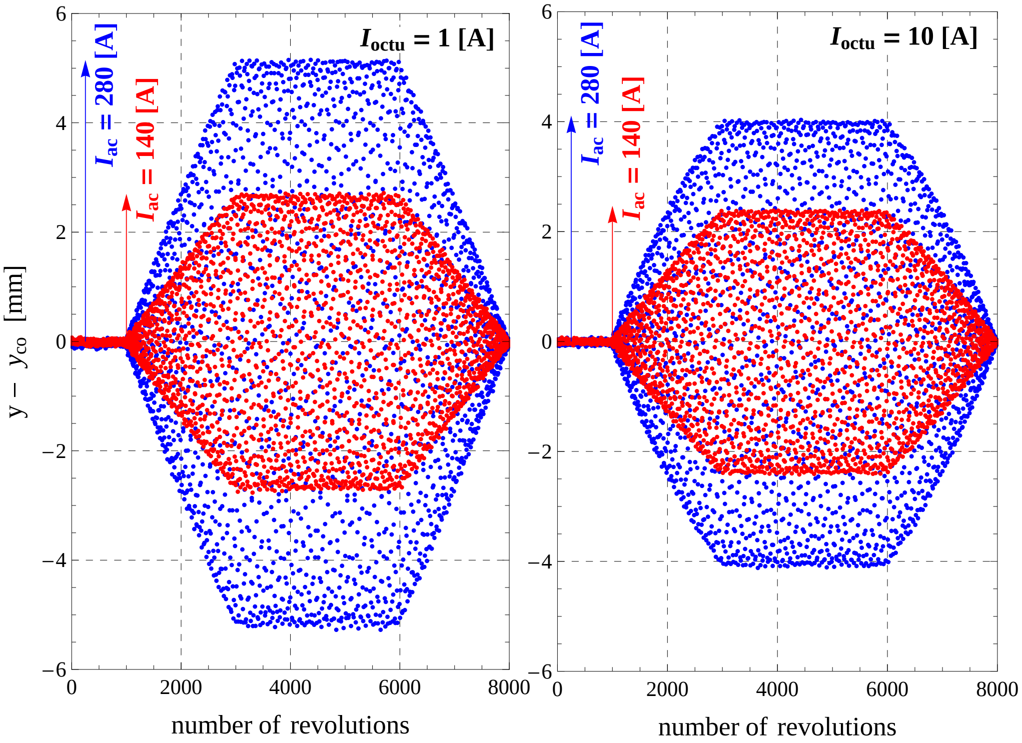

Figure 8.12: Turn-by-turn oscillations excited by the AC dipole, observed at one BPM location in the Tevatron, when current in a given group of octupole magnets is 1 A and 10 A. In both of the cases, the beam is driven from the lower side of the intrinsic $\nu_d - \nu_0 = -0.015$. When the detuning effect is relatively weak ($I_{\text{octu}} = 1$ A), the amplitude is linearly proportional to the current in the AC dipole. When the detuning effect is stronger ($I_{\text{octu}} = 10$ A), the amplitude is suppressed for larger currents of the AC dipole. If the beam is driven from the upper side of the intrinsic tune, the amplitude is enhanced for larger currents of the AC dipole.

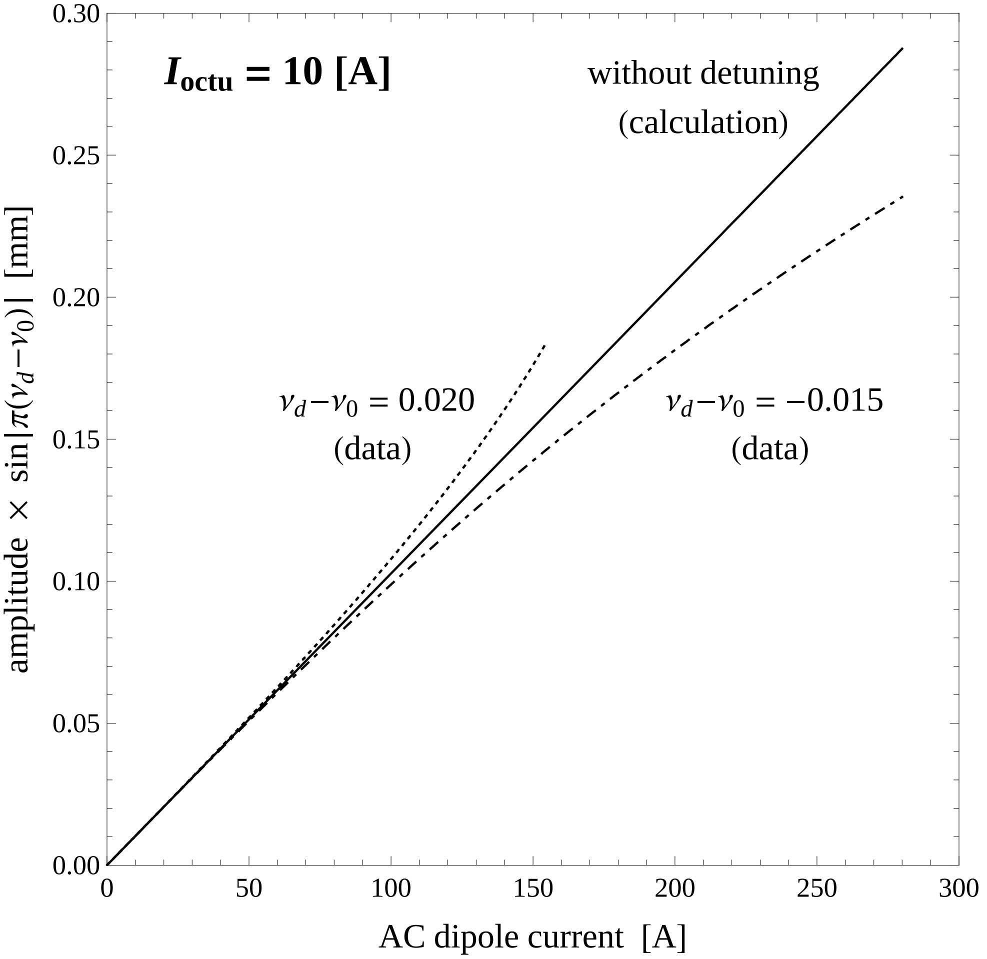

Figure 8.13: Current of the AC dipole vs. amplitude of the driven oscillations, multiplied by a factor sin $|\pi(\nu_d - \nu_0)|$, measured with one BPM in the Tevatron. The amplitudes are determined from the envelope of the linear ramp up of the turn-by-turn oscillations, such as shown in Figure 8.12. Depending on whether the driving ν_d is larger or smaller than the intrinsic tune ν_0, the detuning enhance or suppress the amplitude of the driven oscillations.

driven below ($\nu_d < \nu_0$) and above ($\nu_d < \nu_0$) the intrinsic tune. Figure 8.13 shows the relation between the amplitude of the beam's motion and the current of the AC dipole when the current in the group of octupole magnets is 10 A[6]. As expected, the amplitude is suppressed or enhanced depending on whether the beam is driven from the lower or the upper side of the intrinsic tune. The data in Figure 8.13 was acquired by one BPM in the Tevatron. From these curves, we can determine the detuning for a given oscillation amplitude (See for instance Section 29 of [32]). Figure 8.14 shows the detuning thus measured at all the BPM locations in the Tevatron, when the current and driving tune of the AC dipole is fixed to 280 A and $\nu_d - \nu_0 = -0.015$ and the current in the group of octupole magnets are changed from 1 A to 10 A. Under these conditions, the amplitudes of the excited oscillations are about 5 mm in the Tevatron arcs. Hence, from Equations 3.61 and 8.5, when the current in the given group of octupole magnets are changed by 3 A, the estimated tune shift is about 0.0015, which is roughly consistent with the gaps between curves. As seen in Figure 8.12, for a fixed driving tune ($\nu_d < \nu_0$) and a fixed current of the AC dipole, the amplitude gets smaller when the current of the octupoles gets larger. Because, as described in Equation 3.61, the detuning effect is proportional to the square of the oscillation amplitude, not the current of the AC dipole, the detuning effect becomes smaller when the current of the octupoles becomes larger, and thus the gap between adjacent curves in Figure 8.14 becomes smaller for larger currents of the octupoles[7].

---

[6] The beam's amplitude has been multiplied by $\sin|\pi(\nu_d - \nu_0)|$ to scale out differences between the low- and high- side frequency chosen.

[7] The detuning in this figure is determined from the change of the amplitude response, assuming the amplitude is proportional to $1/\sin|\pi(\nu_d - \nu)| \simeq 1/|\pi(\nu_d - \nu)|$. However, from Equation 6.4, the amplitude of the beam particles' driven oscillations depends on the tune of the free oscillations through the other terms, such as the amplitude function of the driven betatron oscillations $\beta_d(s)$. As discussed in Section 6.2, the amplitude function of the driven oscillations $\beta_d(s)$ depends on the difference $\nu_d - \nu$ and changes the amplitude as there is the

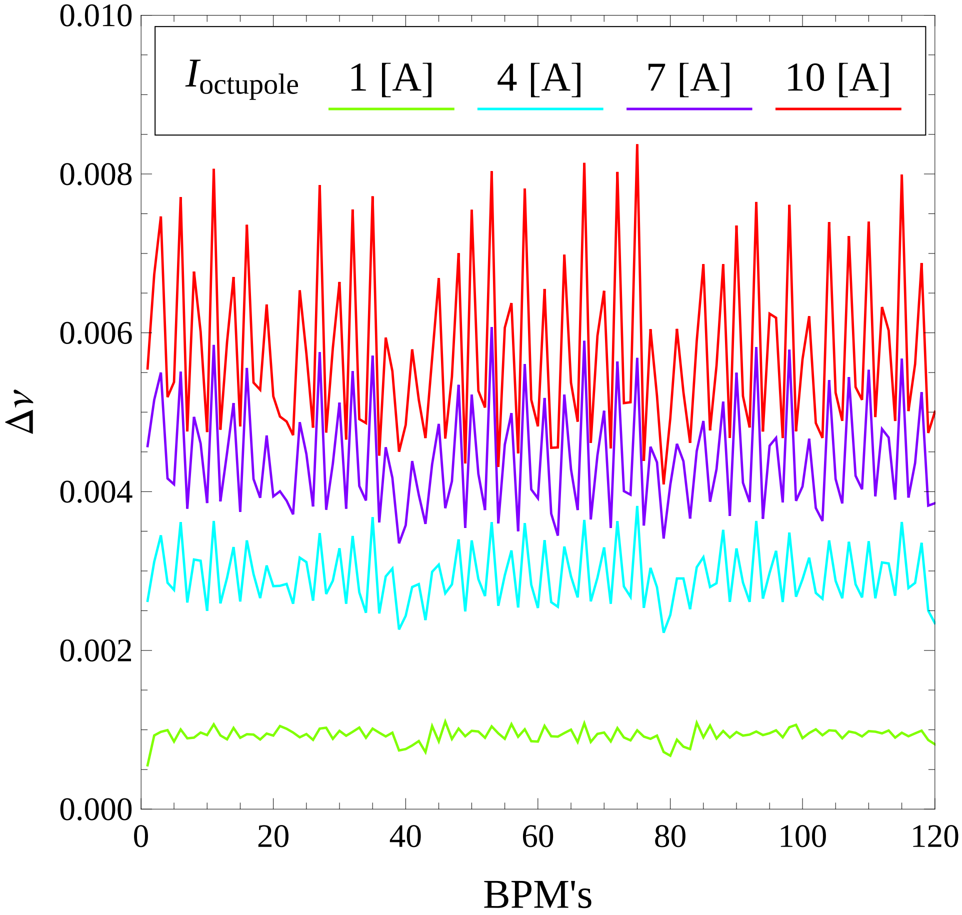

Figure 8.14: Detuning effect measured at all the BPM locations in the Tevatron, from the amplitude response of the driven oscillations. In the measurements, the driving tune and current of the AC dipole are fixed to $\nu_d - \nu_0 = -0.015$ and 280 A. When the detuning effect becomes larger, the amplitude function of the driven oscillations $\beta_d(s)$ is also changed, making the deviations over BPM's in the measurement.

In this section, we studied the detuning effect due to octupole fields. This tune shift grows with increasing amplitude of the oscillations driven by the AC dipole. When the amplitude of the driven oscillations is increased under presence of the detuning effect, the free oscillations' tune either goes away from the driving tune or comes close to the driving tune, and the amplitude is either suppressed or enhanced, as shown in Figure 8.13. By observing such changes of the driven oscillations' amplitudes, we can measure the detuning effect in the synchrotron.

8.2.2 Higher Tune Mode

Octupole magnetic fields drive modes whose tune is three times of that for the leading order oscillations. The second and third terms of Equation 3.64 correspond to those modes but, when the leading order oscillations is the driven oscillations, the tune is $3\nu_d$ instead of 3ν and the factor $A^3\beta(\tilde{s}_4)^2$ must be replaced with $A_d^3\beta_d(\tilde{s}_4)^2$. From Equation 3.64, the magnitudes of these modes driven by octupole fields are linearly proportional to octupole fields and are proportional to cube of the beam's oscillation amplitude A_d. In this section, we discuss measurements to demonstrate such features of higher tune modes.

Figure 8.15 shows Fourier spectra of driven oscillations observed at two BPM locations in the Tevatron, for two cases of the current in the octupole magnets. The same group of octupole magnets as Section 8.2.1 is used in the measurements. The peaks at $3\nu_d$ and $1 - 3\nu_d$ correspond to the modes driven by octupole fields. We note that the height of these peaks depends on the phase advance and hence differs between the two locations in the synchrotron.

---

beta-beat due to quadrupole field errors. In Figure 8.14, the growth of the deviations over BPM's in the measured detuning is due to this change of $\beta_d(s)$

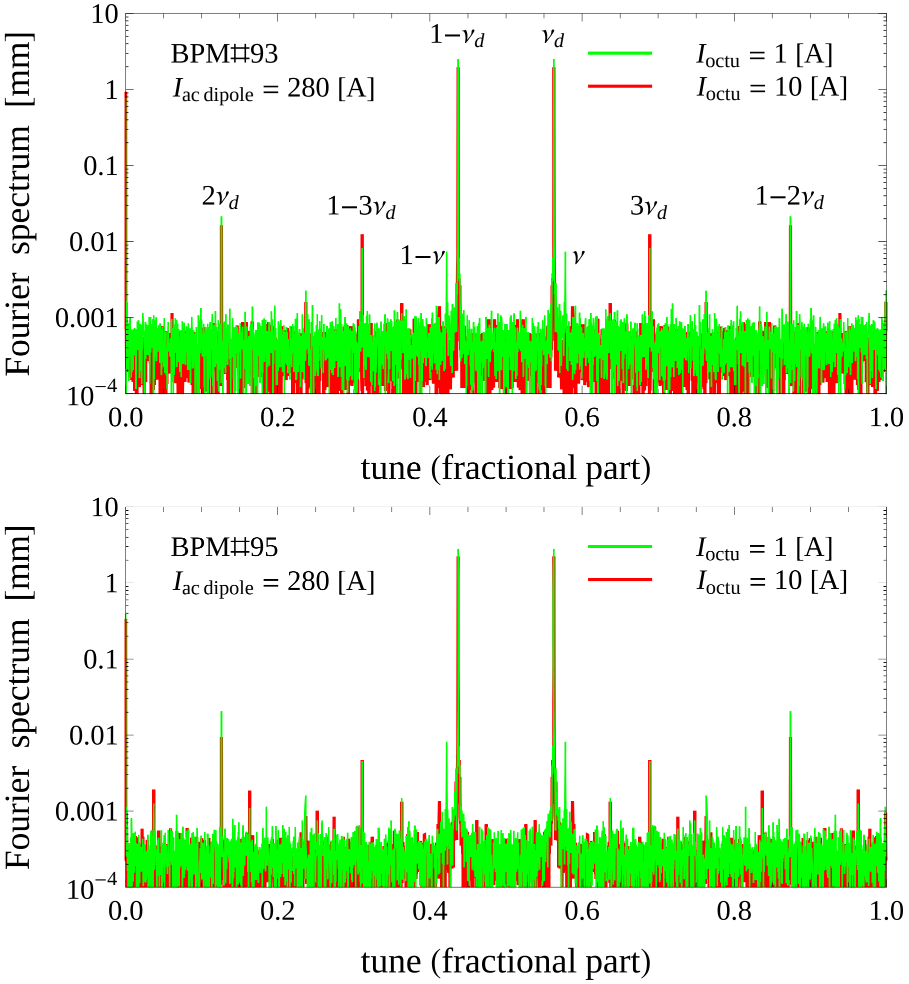

Figure 8.15: Fourier spectra of the driven oscillations observed by two BPM's in the Tevatron, when current in the given octupoles is 1 A and 10 A. The peaks at $3\nu_d$ and $1-3\nu_d$ correspond to the modes driven by octupole fields. When the current of the octupole magnets are changed, change of the peaks heights differs over the locations.

At the location of BPM#93, these peaks grow when the current of the octupole magnets is increased, whereas at the location of BPM#95, the peak heights remain almost the same.

Figure 8.16 shows the relation between the current of the given octupole magnets and the combined amplitude of the modes with the tune $3\nu_d$. Measurements are done with low intensity proton beam of 150 GeV. As expected, the figure shows that the net amplitude of these $3\nu_d$ modes grows linearly with the current of the octupole magnets but the slopes differ over BPM locations.

Figure 8.17 shows Fourier spectra of the driven oscillations observed at the same two BPM locations, but for two different currents of the AC dipole. When the current of the AC dipole is 70 A, no peak is observed at $3\nu_d$ and $1 - 3\nu_d$. When the current of the AC dipole is increased to 280 A, the spectra show the peaks at $3\nu_d$ and $1 - 3\nu_d$. Figure 8.18 shows the measured relation between the net amplitudes of the $3\nu_d$ modes and the current of the AC dipole. As expected, the net amplitude of $3\nu_d$ modes is roughly proportional to cube of the AC dipole's current. Similar to the case of Figure 8.17, the difference of the slopes is due to the phase dependence of the net amplitude of these modes.

In this section, we observed that, when the beam is driven with the AC dipole, octupole magnetic fields drive the modes with tune $3\nu_d$ and these modes appear as peaks at $3\nu_d$ and $1 - 3\nu_d$ in the Fourier spectra of the driven oscillations. We also showed that the net amplitude of these modes is linearly proportional to the current of the octupole magnets and is also proportional to the cube of the AC dipole's current.

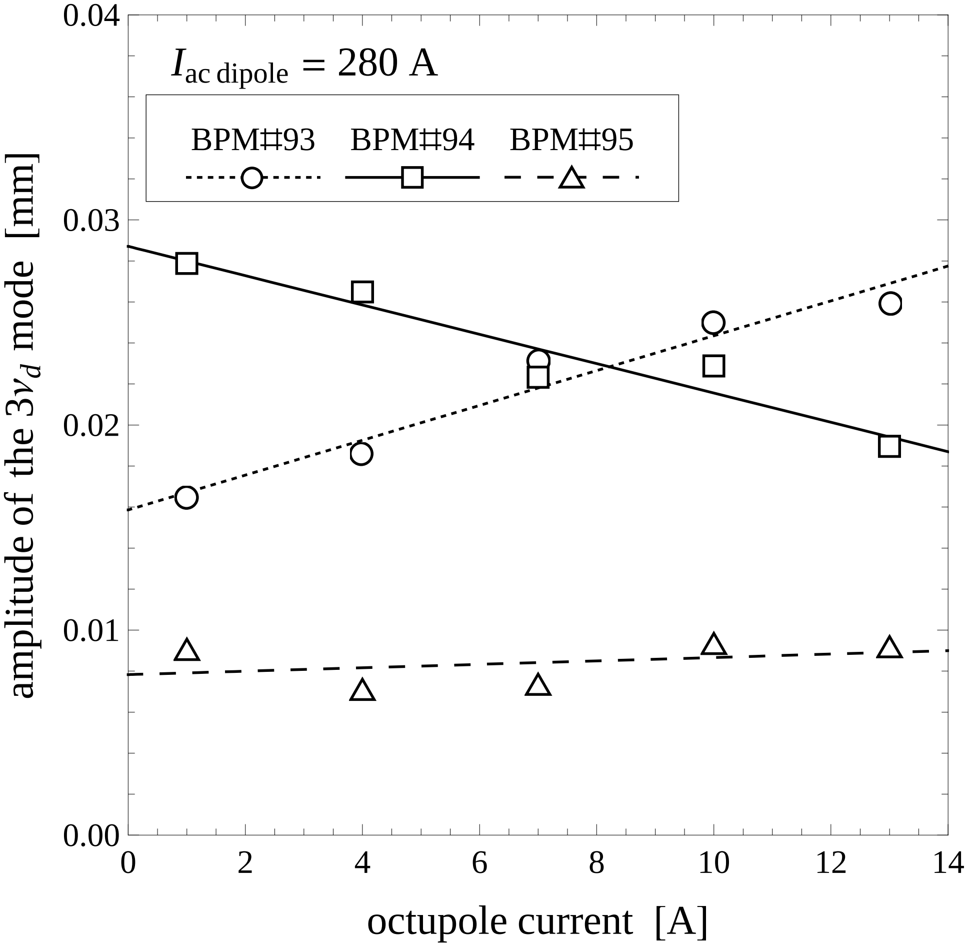

Figure 8.16: Net amplitude of the modes with tune $3\nu_d$ vs. current of the octupole magnets, observed at three consecutive BPM locations in the Tevatron. In the measurements, current of the AC dipole is kept to a constant value 280 A. As expected from Equation 3.64, the amplitude is linearly proportional to the current of the octupole magnets but differs over the locations.

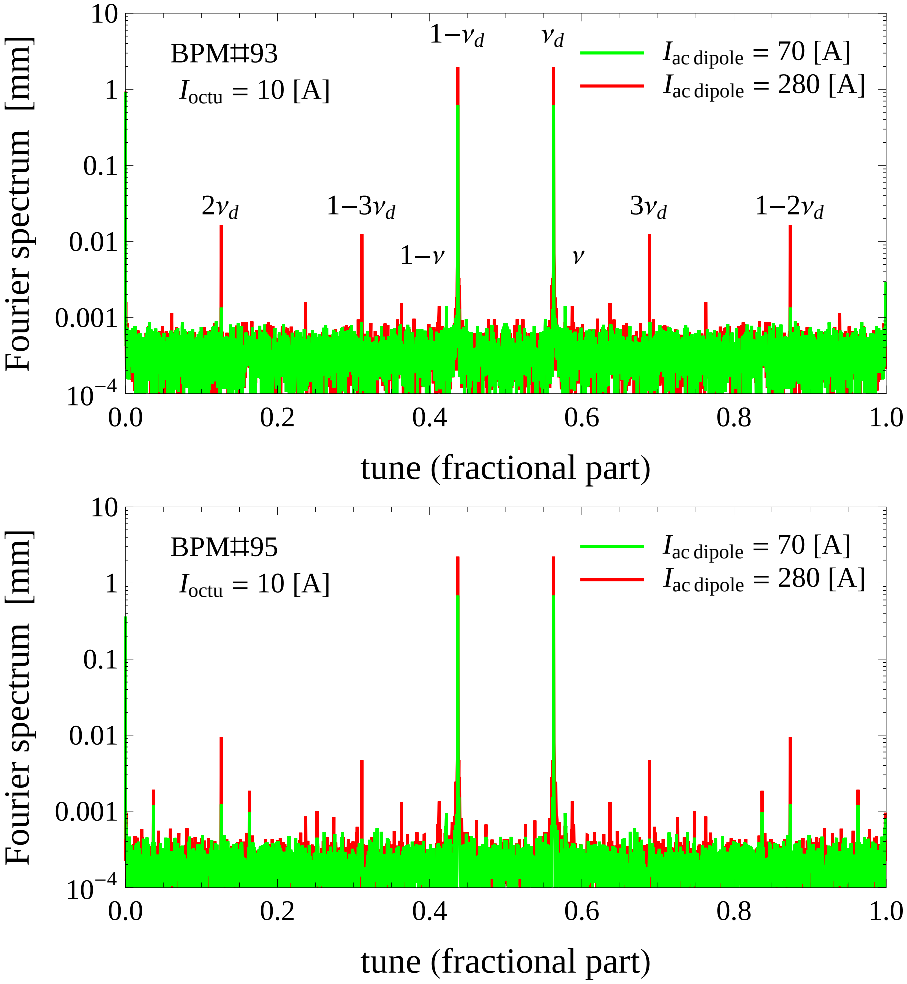

Figure 8.17: Fourier spectra of the driven oscillations observed by two BPM's in the Tevatron, when the current of the AC dipole is 70 A and 280 A. The peaks at $3\nu_d$ and $1-3\nu_d$ correspond to the modes driven by octupole fields. The difference of the peak heights comes from the phase dependence of the net amplitude.

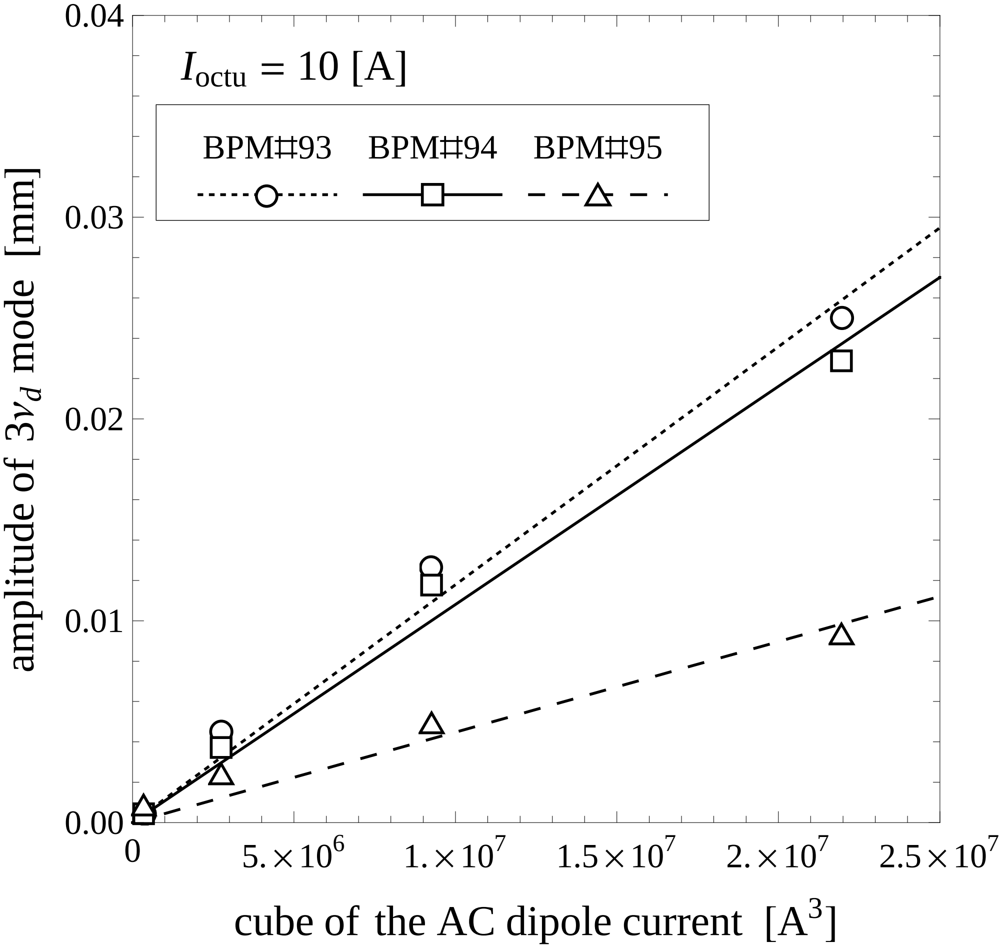

Figure 8.18: Net amplitude of the modes with tune $3\nu_d$ vs. current of the AC dipole, observed at three BPM locations in the Tevatron. In the measurements, the current of the given octupole magnets is kept to a constant 10 A. As expected from Equation 3.64, the amplitude is proportional to cube of the AC dipole's current but the slopes are different over the locations.

8.3 Summary

In this chapter, we discussed direct measurements of the nonlinear fields of sextupole and octupole magnets and their influences on the transverse motions of the beam in the Tevatron. As summarized in Table 3.1, the sextupole fields result in the central orbit distortion and also drive higher tune modes, and the octupole field cause the tune shift and also drive higher tune modes. We showed that all of these effects can be directly observed when the beam is driven to large amplitude oscillations with the AC dipole. Such simple tests can be performed on a routine basis throughout the operation of a synchrotron and are non-destructive to the beam.

Chapter 9

Conclusions

High energy and high intensity charged particle accelerators have been successful probes to study physics of subatomic particles. In modern circular synchrotron accelerators, the charged particle beams are guided by bending dipole magnets and accelerated by longitudinal electric fields of radio frequency cavities. A collider synchrotron is a type of a circular accelerator, which accelerates two particle beams in counter-rotating directions and produces head-on collisions of the beam particles. The Fermilab Tevatron has been the world's highest energy collider synchrotron, accelerating beams of protons and antiprotons up to 1 TeV and producing head-on collisions of these particles with the center-of-mass energy of 2 TeV. To produce higher energy particle beams with the bending dipole magnets of a given strength, we need a synchrotron with a larger radius, making the sizes of high energy accelerators in the present day quite large. The particle beams in the Tevatron are guided by superconducting dipole magnets with the maximum filed of 4.4 T and yet its radius must be as large as 1 km to form a circular trajectory.

In modern synchrotrons, transverse motions of the beam particles are stabilized with linear restoring forces of quadrupole magnets and, as a consequence, the beam particles undergo transverse oscillations around the central orbit, referred to as the betatron motion. The betatron motion of a beam particle is determined by the Hill's equation of motion, which is analogous to an equation of motion for a simple harmonic oscillator, and is characterized by the amplitude function and the phase advance. In a synchrotron, transverse beam sizes are determined by this amplitude function as well as initial distributions of the beam particles in the transverse planes, characterize by the transverse emittances. If there are quadrupole field errors, the transverse beam sizes are changed through modulations of the amplitude function and a collider's luminosity may be degraded. Hence, the primary purpose of a collider's diagnostics using the AC dipole is to measure the amplitude function and to find locations of the quadrupole field errors.

Modern accelerators utilize magnets producing higher order nonlinear fields, such as sextupole and octupole magnets, to compensate certain multi particle effects. Imperfections of bending dipole magnets and focusing quadrupole magnets also produce higher order nonlinear magnetic fields. These nonlinear fields perturb the betatron motion of the beam particles, and a perturbation becomes larger when the betatron frequency gets closer to a certain frequency corresponding to the perturbation. The phenomenon is analogous to driven harmonic motion in classical mechanics and is referred to as resonance. For instance, the sextupole magnetic fields shift the central orbit of the beam particles, much like dipole field errors, and also drive modes with frequency twice of the betatron frequency. These perturbative effects grow when fractional part of the betatron tune becomes close to zero or one third. The octupole magnetic fields modulate the amplitude function, the phase advance, and the betatron tune, much like quadrupole field errors, and also drive modes with frequency three times of the betatron frequency. These perturbative effects grow when fractional part of the betatron tune becomes close to half or one forth. If the betatron frequency is too close to one of the resonant frequencies, the corresponding perturbative effect may become large, blowing up the transverse beam size, or may even diverge, making the beam particles' transverse motions unstable. For a slow cycled collider synchrotron like the Tevatron, where the beam particles keep circulating and colliding about a day (∼4 billion revolutions), it is ideal to know the distribution of the nonlinear fields and to avoid the resonances, for stabilizing transverse motions of the beam particles and for maximizing the integrated luminosity. For instance, distributions of the sextupole fields and the octupole fields can be measured by observing their corresponding perturbative effects.

An AC dipole is a diagnostic tool which produces a sinusoidally oscillating dipole magnetic field with frequency close to the betatron frequency. Under the presence of such a field, all the beam particles undergo coherent driven oscillations around a synchrotron, which are analogous to the driven harmonic oscillations in classical mechanics. By observing such oscillations with a system of beam position monitors, we can measure ring-wide parameters of a synchrotron's magnet lattice. Synchrotron diagnostics using the AC dipole was first tested in BNL AGS [4], has been employed in the BNL RHIC [14, 15], the CERN SPS [16, 17], and the FNAL [18, 19, 20, 21], and will be also used in CERN LHC [22]. If we adiabatically ramp up and ramp down the amplitude of the AC dipole's oscillating field, before and after an observation, we can produce large sustained oscillations with no emittance growth. Compared to the kick excitation with the decoherence, the sustained signal produced by the AC dipole excitation enables more precise data analyses. The non-destructive nature of the AC dipole excitation allows multiple measurements using the same beam. This makes the AC dipole particularly useful for tuning up a slow cycled synchrotron, compared to the destructive kick excitation, for which we have to use the new beam every two to three measurements. These properties of the AC dipole excitation, the analogy to the classical driven oscillator, no decoherence, and no emittance growth, are demonstrated in the Tevatron.

The AC dipole system in the Tevatron utilizes an existing kicker magnet, which has been already installed. Because the betatron frequency of the beam particles in the Tevatron is approximately 20 kHz, the magnet is powered by a high power audio amplifier. To optimize the system for the audio amplifier, a resonant circuit is formed with the magnet. By utilizing the existing magnet and the audio amplifier, the Tevatron's AC dipole system is constructed relatively inexpensively without sacrificing performance. For the 1 TeV beam in the Tevatron, the Tevatron's AC dipole can produce oscillations with amplitude of 2-3σ beam size. After our successful design and construction of the Tevatron's AC dipole system, we initiated collaborations with CERN to develop similar AC dipole systems, utilizing existing kicker magnets and higher power audio amplifiers for the CERN LHC.

Because of a synchrotron's periodicity, an AC dipole excites not only a mode with tune ν_{ac} but also another mode with tune $1 - \nu_{\text{ac}}$. The existence of the two modes makes the driven betatron motion excited by an AC dipole different from the free betatron motion excited by a kicker magnet, as if there is a quadrupole field error at the location of the AC dipole. Hence, the driven motion of the AC dipole is well characterized by introducing the new amplitude function and the new phase advance, which are functions of the AC dipole's tune. This predicts rotation of the phase space ellipse depending on the AC dipole's tune and also asymmetric amplitude responses depending on locations with different phase advances. These effects are demonstrated in the Tevatron and explained well with our model. From the analogy to the quadrupole field error, if we simply ignore the difference between the driven and free betatron motions, we observe the false beta-beat and the false phase-beat. The magnitudes of these effects depend on conditions of a synchrotron and, for instance, the false beta-beat is 10-20% and the false phase-beat is about 0.05-0.10 rad in typical conditions of the Tevatron. These effects can be removed, without depending on a machine model, by simultaneously analyzing data sets of the driven betatron motions with different frequencies of the AC dipole. In this dissertation, we demonstrated applications of this technique to the Tevatron in measurements of the ring-wide amplitude function and phase advance as well as in measurements of the minimum value of the amplitude function and the beam waist location in the interaction region.

When the sustained large oscillations of the AC dipole excitation are recorded by a system of beam position monitors with an adequate resolution, we can also directly observe nonlinear motions of the beam particles. We performed studies to measure the effects in the Tevatron due to the sextupole and octupole magnetic fields. The central orbit distortion due to sextupole fields can be observed by comparing the average positions before and during the AC dipole excitation. The detuning effect, mainly due to the octupole magnetic fields, can be observed through modulation of the driven motion's amplitude. The other higher tune modes excited by the sextupole and octupole magnets can be observed as peaks at the corresponding frequencies in the Fourier spectrum of the AC dipole excitation. We demonstrated that these effects can be observed as expected in the Tevatron.

In this dissertation, we demonstrated improved techniques to measure linear and nonlinear lattice parameters in the Tevatron using the AC dipole.

The established measurement techniques will be useful for the Tevatron to maintain its performance and will be useful as well as for the LHC, where its lattice must be controlled with an unprecedented level of precision not only to raise the luminosity but also to protect the machine itself from its high intensity beam.

Bibliography

[1] M. S. Livingston, *High-Energy Accelerators* (Interscience, New York, 1954), p. 151.

[2] The Pierre Auger Collaboration, "Correlation of the Highest-Energy Cosmic Rays with Nearby Extragalactic Objects", Science **318** (5852), p. 938 (2007).

[3] H. T. Edwards, "The Tevatron Energy Doubler: A Superconducting Accelerator", Ann. Rev. Nucl. Part. Sci. **35**, p. 605 (1985).

[4] M. Bai, S. Y. Lee, J. W. Glenn, H. Huang, L. Ratner, T. Roser, M. J. Syphers, and W. van Asselt, "Experimental Test of Coherent Betatron Resonance Excitations", Phys. Rev. E **56**, p. 6002 (1997).

[5] E. Wilson, *An Introduction to Particle Accelerators* (Oxford University Press Inc., New York, 2001).

[6] W. K. H. Panofsky and M. Breidenbach, "Accelerators and Detectors", Rev. Mod. Phys. **71**, p. S121 (1999).

[7] D. A. Edwards and M. J. Syphers, *An Introduction to the Physics of High Energy Accelerators* (John Wiley & Sons, Inc., New York, 1993).

[8] S. Y. Lee, *Accelerator Physics Second Edition* (World Scientific, Singapore, 2004).

[9] V. Shiltsev, “CPT Theorem for Accelerators”, Fermilab Preprints No. FERMILAB-CONF-04-126 (2004).

[10] V. Shiltsev, A. Jansson, and R. Moore, “Tevatron Instrumentation: Boosting Collider Performance”, in *Proceedings of the 12th Beam Instrumentation Workshop, Batavia, Illinois, 2006* (AIP, Melville, New York, 2006), p. 65.

[11] D. Broemmelsiek, M. Hu, and S. Nagaitsev, “Stochastic Cooling in Barrier Buckets at the Fermilab Recycler”, in *Proceedings of the 9th European Particle Accelerator Conference, Lucerne, Switzerland, 2004* (EPS-IGA and CERN, Geneva, 2004), p. 794.

[12] A. Shemyakin, A. Burov, K. Carlson, M. Hu, T. Kroc, J. Leibfritz, S. Nagaitsev, L. R. Prost, S. Pruss, G. Saewert, C. W. Schmidt, M. Sutherland, V. Tupikov, and A. Warner, “Performance of the Fermilab’s 4.3 MeV Electron Cooler”, in *Proceedings of the 10th European Particle Accelerator Conference, Edinburgh, Scotland, 2006* (EPS-IGA and CERN, Geneva, 2006), p. 1654.

[13] N. Gelfand, “Summary of Tevatron Spool Data”, Fermilab Beams Division Note No. Beams-doc-1160-v1, 2004.

[14] M. Bai, M. Meth, C. Pai, B. Parker, S. Peggs, T. Roser, R. Sanders, D. Trbojevic, and A. Zaltsman, “RHIC AC Dipole Design and Construction”, in *Proceedings of the 19th Particle Accelerator Conference, Chicago, Illinois, 2001* (IEEE, Piscataway, NJ, 2001), p. 3606.

[15] M. Bai, J. Delong, L. Hoff, C. Pai, S. Peggs, J. Piacentino, B. Oerter, P. Oddo, T. Roser, T. Satogata, D. Trbojevic, and A. Zaltsman, “RHIC Vertical AC Dipole Commissioning”, in *Proceedings of the 8th European Particle Accelerator Conference, Paris, France, 2002* (EPS-IGA and CERN, Geneva, 2002), p. 1115.

[16] O. Berrig, W. Hofle, R. Jones, J. Koopman, J. P. Koutchouk, H. Schmickler, and F. Schmidt, “Excitation of Large Transverse Beam Oscillations without Emittance Blow-up Using the AC-Dipole Principle”, in *Proceedings of the 5th European Workshop on Beam Diagnostics and Instrumentation for Particle Accelerators, Grenoble, France, 2001* (ESRF, Grenoble, 2001), p. 82.

[17] F. Schmidt, R. Tomás, N. Catalán, G. Crockford, M. Hayes, W. Hofle, and J. P. Koutchouk, “Completion of the Sextupole Driving Terms Measurement at the SPS”, CERN Report No. AB-Note-2003-031 MD, 2003.

[18] R. Miyamoto, A. Jansson, S. Kopp, and M. Syphers, “Initial Tests of an AC Dipole for the Tevatron”, in *Proceedings of the 12th Beam Instrumentation Workshop, Batavia, Illinois, 2006* (AIP, Melville, New York, 2006), p. 402.

[19] R. Miyamoto, S. E. Kopp, A. Jansson, and M. J. Syphers, “Tevatron Optics Measurements Using an AC Dipole” in *Proceedings of the 22nd Particle Accelerator Conference, Albuquerque, New Mexico, 2007* (IEEE, Piscataway, NJ, 2007), p. 3465.

[20] R. Miyamoto, S. E. Kopp, A. Jansson, and M. J. Syphers, “Tevatron AC Dipole System”, in *Proceedings of the 22nd Particle Accelerator Confer-*

ence, Albuquerque, New Mexico, 2007 (IEEE, Piscataway, NJ, 2007), p. 3868.

[21] R. Miyamoto, S. E. Kopp, A. Jansson, and M. J. Syphers "Parametrization of the Driven Betatron Oscillation", Phys. Rev. ST Accel. Beams **11**, 084002 (2008).

[22] M. Bai, R. Calaga, W. Fischer, P. Oddo, H. Schmickler, J. Serrano, A. Jansson, M. J. Syphers, S. Kopp, and R. Miyamoto, "Considerations for AC Dipoles at the CERN LHC", in *Proceedings of the 22nd Particle Accelerator Conference, Albuquerque, New Mexico, 2007* (IEEE, Piscataway, NJ, 2007), arXiv:physics.acc-ph/0709.2753.

[23] R. E. Shafer, "Characteristics of Directional Coupler Beam Position Monitors", *IEEE. Trans. Nucl. Sci.* NS-**32**, p.1933 (1985).

[24] S. Wolbers, B. Banerjee, B. Barker, S. Bledsoe, T. Boes, M. Bowden, G. Cancelo, B. Forster, G. Duerling, B. Haynes, B. Hendricks, T. Kasza, R. Kutschke, R. Mahlum, M. Martens, M. Mengel, M. Olson, V. Pavlicek, T. Pham, L. Piccoli, J. Steimel, K. Treptow, M. Votava, B. West, R. Webber, and D. Zhang, "Tevatron Beam Position Monitor Upgrade", in *Proceedings of the 21st Particle Accelerator Conference, Knoxville, Tennessee, 2005* (IEEE, Piscataway, NJ, 2005), p. 410.

[25] R. Miyamoto, S. E. Kopp, A. Jansson, and M. J. Syphers, "Geometrical Interpretation of Nonlinearities from a cylindrical Pick-up" in *Proceedings of the 22nd Particle Accelerator Conference, Albuquerque, New Mexico, 2007* (IEEE, Piscataway, NJ, 2007), p. 3862.

[26] M. A. Martens, “Position Scan of Tev VPA33 BPM with Upgraded Electronic”, Fermilab Beams Division Notes No. Beams-doc-1516-v1, 2004.

[27] R. K. Kutschke, “Third Order Calculation of Beam Position”, Fermilab Beams Division Notes No. Beams-doc-1893-v3, 2005.

[28] J. V. José and E. J. Saletan, *Classical Dynamics* (Cambridge University Press, Cambridge, UK, 1998).

[29] K. G. Steffen, *High Energy Beam Optics* (John Wiley & Sons, Inc., New York, 1973).

[30] G. W. Hill, “On the Part of the Motion of the Lunar Perigee Which is a Function of the Mean Motions of the Sun and Moon”, Acta Mathematica **8**, p. 1 (1886).

[31] E. D. Courant and H. S. Snyder, “Theory of the Alternating-Gradient Synchrotron”, Ann. Phys. **3**, p. 1 (1958).

[32] L. D. Landau and E. M. Lifshitz, *Mechanics Third Edition* (Butterworth-Heinemann, Oxford, UK, 1982).

[33] G. B. Arfken and H. J. Weber, *Mathematical Methods for Physicists Sixth Edition* (Academic Press, San Diego, 2005).

[34] H. Kleinert, *Path Integrals in Quantum Mechanics, Statistics, Polymer Physics, and Financial Markets* (World Scientific, Singapore, 2006).

[35] A. W. Chao, *Physics of Collective Beam Instabilities in High Energy Accelerators* (John Wiley & Sons, Inc., New York, 1993)

[36] M. G. Minty and F. Zimmermann, *Measurement and Contral of Charged Particle Beams* (Springer-Verlag, Berline, 2003).

[37] Y. Alexahin and E. Gianfelice-Wendt, "Determination of Linear Optics Functions from Turn-by-turn Data", Fermilab Preprints No. FERMILAB-PUB-06-093-AD (2006).

[38] P. Castro, "Applications of the 1000-turns Orbit Measurement System at LEP", in *Proceedings of the 18th Particle Accelerator Conference, New York, New York, 1999* (IEEE, Piscataway, NJ, 1999), p. 456.

[39] T. Satogata, J. Cardona, V. Ptitsyn, S. Tepikian, J. van Zeijits, "Linear Optics during the RHIC 2001-2 Run", in *Proceedings of the 8th European Particle Accelerator Conference, Paris, France, 2002* (EPS-IGA and CERN, Geneva, 2002), p. 1187.

[40] A. Franchi, R. Tomás, and F. Schmidt, "Magnet Strength Measurement in Circular Accelerators from Beam Position Monitor Data", Phys. Rev. ST Accel. Beams **10**, 074001 (2007).

[41] A. W. Chao, J. M. Peterson, S. G. Peggs, and R. E. Meller, "Decoherence of Kicked Beams", SSC Report No. SSC-N-360, 1987.

[42] W. Blokland, G. Vogel, and J. Dey, "A New Flying Wire System For the Tevatron", in *Proceedings of the 17th Particle Accelerator Conference, Vancouver, British Columbia, Canada, 1997* (IEEE, Piscataway, NJ, 1997), p. 2032.

[43] R. Tomás, "Adiabaticity of the Ramping Process of an ac Dipole", Phys. Rev. ST Accel. Beams **8**, 024401 (2005).

[44] D. K. Cheng, *Field and Wave Electromagnetics Second Edition* (Addison-Wesley, 1989).

[45] H. Wiedemann, *Particle Accelerator Physics Basic Principles and Linear Beam Dynamics* (Springer-Verlag, Berline, 1993).

[46] C. Jensen (private communication).

[47] "I-Tech Series Operational Manual", Crown Audio® Inc., Indiana, 2005.

[48] S. Peggs, "Nonlinear Diagnostics Using AC Dipoles", in *Proceedings of the 18th Particle Accelerator Conference, New York, New York, 1999* (IEEE, Piscataway, NJ, 1999), p. 1572.

[49] C. Y. Tan, "Novel Tune Diagnostics for the Tevatron", in *Proceedings of the 21st Particle Accelerator Conference, Knoxville, Tennessee, 2005* (IEEE, Piscataway, NJ, 2005), p. 140.

[50] W. J. Corbett, M. J. Lee and V. Ziemann, "A Fast Model-Calibration Procedure for Storage Rings", in *Proceedings of the 15th Particle Accelerator Conference, Washinton D.C., 1993* (IEEE, Piscataway, NJ, 1993), p. 108.

[51] V. Sajaev, V. Lebedev and V. Nagaslaev, "Fully Coupled Analysis of Orbit Response Matrices at FNAL Tevatron" in *Proceedings of the 21st Particle Accelerator Conference, Knoxville, Tennessee, 2005* (IEEE, Piscataway, NJ, 2005), p. 3662.

[52] V. Lebedev, V. Nagaslaev, A. Valishev, and V. Sajaev, "Measurement and Correction of Linear Optics and Coupling at Tevatron Complex", Nucl. Instrum. Methods A **558**, p. 299 (2006).

[53] J. Slaughter, J. Estrada, K. Genser, A. Jansson, P. Lebrun, J.C. Yun, and S. Lai, "Tevatron Run II Luminosity, Emittance and Collision Point

Size", in *Proceedings of the 20th Particle Accelerator Conference, Portland, Oregon, 2003* (IEEE, Piscataway, NJ, 2003), p. 1763.

[54] M. J. Syphers, "A First Look at Direct Measurements of β^* in the Tevatron", Fermilab Beams Division Note No. Beams-doc-1880, 2005.

[55] M. J. Syphers, "Some Notes on Luminosity Calculations", Fermilab Beams Division Note No. Beams-doc-1348, 2004.

[56] M. J. Syphers and R. Miyamoto, "Direct Measurements of Beta-star in the Tevatron" in *Proceedings of the 22nd Particle Accelerator Conference, Albuquerque, New Mexico, 2007* (IEEE, Piscataway, NJ, 2007), p. 3495.

[57] A. Chao, D. Johnson, S. Peggs, J. Peterson, C. Saltmarsh, L. Schachinger, R. Meller, R. Siemann, R. Talman, P. Morton, D. Edwards, D. Finley, R. Gerig, N. Gelfand, M. Harrison, R. Johnson, N. Merminga, and M. Syphers, "Experimental Investigation of Nonlinear Dynamics in the Fermilab Tevatron", Phys. Rev. Lett. **61**, p. 2752 (1988).

[58] J. Bengtsson, "Non-linear Transverse Dynamics for Storage Rings with Applications to the Low-energy Antiproton Ring (LEAR) at CERN", Ph.D. thesis, Lund University, 1988; CERN Report No. CERN-YELLOW-88-05, 1988.

[59] R. Tomás, M. Bai, R. Calaga, and W. Fischer, "Measurement of Global and Local Resonance Terms", Phys. Rev. ST Accel. Beams **8**, 024001 (2005).

[60] M. Benedikt, F. Schmidt, R. Tomás, and P. Urschütz "Driving Term Experiments at CERN", Phys. Rev. ST Accel. Beams **10**, 034002 (2007).

[61] Y. Alexahin, V. Lebedev, D. Still, A. Valishev, and F. Schmidt, “Measurement and Correction of the 3rd Order Resonance in the Tevatron”, in *Proceedings of the 10th European Particle Accelerator Conference, Edinburgh, Scotland, 2006* (EPS-IGA and CERN, Geneva, 2006), p. 2140.

Vita

Ryoichi Miyamoto was born in Tokyo, Japan on November 17, 1975 and grew up in the city of Fussa under the direction of his parents: Yoshio Miyamoto and Akiko Miyamoto. He attended the Tokyo Metropolitan Tachikawa High School in Tokyo and graduated in 1994. He started as a student in Tokyo Science University 1995 and earned the degree of Bachelor of Science from the Tokyo Science University in the Spring of 1999. In the Fall of 1999, he started as a graduate student in the Department of Physics at the University of Texas at Austin. He worked with Professor Sacha E. Kopp in the field of Accelerator Physics. While he was at the University of Texas at Austin, he earned a travel grant to attend the 2007 Particle Accelerator Conference, and the United States Particle Accelerator School in the summer of 2005 and in the winters of 2006 and 2007.

Permanent Address: 711 Young Ave.
Batavia, IL 60510

This dissertation was typed by the author.